ISBN 978-82-326-0838-6 (printed version)
ISBN 978-82-326-0839-3 (electronic version)
ISSN 1503-8181

Doctoral theses at NTNU, 2015:91

Svein Edvardsen

MODELING MULTIPHASE FLOW IN DOWNHOLE VALVES

NTNU
Norwegian University of
Science and Technology
Faculty of Engineering
Science and Technology
Department of Energy andProcess Engineering

NTNU – Trondheim
Norwegian University of
Science and Technology

Doctoral theses at NTNU, 2015:91

NTNU

NTNU – Trondheim
Norwegian University of
Science and Technology

Svein Edvardsen

MODELING MULTIPHASE FLOW IN DOWNHOLE VALVES

Thesis for the degree of Philosophiae Doctor

Trondheim, June 2015

Norwegian University of Science and Technology

NTNU – Trondheim
Norwegian University of
Science and Technology

NTNU
Norwegian University of Science and Technology

Thesis for the degree of Philosophiae Doctor

ISBN 978-82-326-0838-6 (printed version)
ISBN 978-82-326-0839-3 (electronic version)
ISSN 1503-8181

Doctoral theses at NTNU, 2015:91

Printed by Skipnes Kommunikasjon as

Dedicated to my father Ole Jacob Istad Edvardsen (1934-1985)

Preface

This thesis has been submitted in fulfillment of the Ph.D. degree at the Norwegian University of Science and Technology (NTNU) under the supervision of Professor Carlos A. Dorao and co-supervision of Professor Ole Jørgen Nydal at NTNU and Professor Per Arne Sundsbø at Narvik University College. Senior specialist Dag Pedersen has been supervisor at Qinterra Technologies.

The present work was performed at the Department of Energy and Process Engineering, Faculty of Engineering Science and Technology in the period November 2010 to November 2014. The work was financed by my employer Qinterra Technologies with support from The Research Council of Norway with an industrial Ph.D scheme, project no. 208174.

Abstract

Oil and gas have been produced from onshore and offshore fields for more than 100 years, and production rates are falling for the most easily accessible fields. New oil fields are found at deeper and more remote areas, and exploration costs are increasing. A new tool that can enhance the well testing process is a wireline operated downhole shut-in valve. In order to get as precise as possible results from the well testing, the two-phase pressure drop across the shut-in valve must be known.

The flow path through this shut-in valve is however complex and cannot easily be compared to standard tubing parts and singularities. Frictional pressure losses in pipes are well understood now and have been studied by a number of authors since the late forties. Minor pressure losses arise from singularities like bends, contractions, expansions etc. Two-phase flow minor losses have also been studied by many authors, but only for well-defined and common shapes like bends, nozzles, sharp edged contractions etc. In a typical industrial application like the shut-in valve, the flow path is complex. More research is therefore needed in order to be able to predict the two-phase pressure drop in a complex flow path. The modeling methods developed here should hopefully be applicable to other two-phase flow systems as well.

The main objective for this work is therefore to find methods for modeling two-phase flow in complex geometries with several singularities and changes of cross section. The work has included design, construction and instrumentation of a full scale shut-in valve mock-up. A series of experiments have been performed with two-phase flow of air, water and two different oil types. This provides a valuable experimental data base for two-phase flow in a typical downhole valve. Furthermore an in-house simulation tool for 1-D models was implement, verified and

validated.

The first achievement in this thesis is the validation of 3-dimensional computational fluid dynamics (CFD) simulations of single-phase flow in the valve. Provided that the mesh is properly designed etc. the deviation in pressure drop is only 3-6% compared to experimental data.

The next achievement is the 1-D modeling of the flow in the valve. This 1-D model serves as a necessary basis for the two-phase simulations.

The main achievement is the implementation of two-phase flow in the 1-D model. Two approaches are used. First classical flow pattern independent correlations are applied, and then the state-of-the-art Unified Comprehensive Model formulation is introduced. The latter provides the best results with only some 10% deviation in pressure drop.

Acknowledgements

This doctoral study would not be possible without the support and encouragement from the people around me. Some people deserve to be mentioned especially.

Co-supervisor Professor Per Arne Sundsbø was the one who encouraged me to go on with a PhD study, and he also took part in establishing the project plan. My manager Stig Karlsen at Qinterra Technologies accepted the plan, and I am very grateful for his support through this project. I am also grateful for the funding from The Research Council of Norway.

Professor Ole Jørgen Nydal opened the doors at NTNU for me, and invited Professor Carlos Dorao to be my supervisor. He accepted, and I am very grateful for his guidance, patience and leadership. The numerical part of the project is a result of his expertise. The experimental part was inspired and guided by Professor Nydal, and I will express my gratitude to the whole staff at the Multiphase laboratory at NTNU for help and support. My daughter Tone was also assisting me in some of my multiphase flow experiments. The experimental results were vital for the understanding of multiphase flow in a valve section.

I would also like to thank all my colleagues at Qinterra Technologies and at NTNU. Their interest and help gave me energy to go on.

My wife Karina and our daughters Lena, Lise and Tone have also supported and encouraged me, waiting patiently for the day when this is over.

Contents

List of Tables

List of Figures

List of Symbols

A cross section area [m^2]

c constant

c_p specific heat capacity at constant pressure

D diameter [m]

f friction coefficient

G mass flux [kg/m^2s]

g gravitational acceleration [m/s^2]

h enthalpy

K_L minor loss coefficient

l length [m]

$\dot{m}$ mass flow rate [kg/s]

P pressure [Pa]

R_e Reynolds number

T temperature [K]

u internal energy

u_c uncertainty

V volume [m^3]

v velocity [m/s]

v_{SL} superficial liquid velocity [m/s]

v_{SG} superficial gas velocity [m/s]

x flow quality, mass flow of gas over total mass flow

z distance along flowline

Greek symbols

α void fraction

ε surface roughness

μ dynamic viscosity [Pa-s]

μ_t turbulent viscosity

ρ density

σ area ratio, $\frac{A_1}{A_2}$

τ_w wall shear stress

Subscripts

a air

G gas

H homogeneous (equal phase velocities)

h hydraulic

L liquid

o oil

s stagnation

TF two-phase

w water

Abbreviations

CFD computational fluid dynamics

RNG re-normalization group

PNA paraffin-naphthene-aromatic

SCN single carbon number

TBP true boiling point

STC stock tank condensate

$@SC$ at standard conditions

CCE constant composition expansion

CVD constant volume depletion

VLE vapor-liquid equilibrium

EOS equations of state

vdW van der Waals

SRK Soave-Redlich-Kwong

PR Peng-Robinson

MBE material balance equations

UCM Unified Comprehensive Model

POM Polyoxymethylene, hard plastic

$PMMA$ Polymethyl methacrylate, or acrylic glass

Chapter 1

Introduction and objectives

1.1 Introduction

Oil has been produced from drilled oil wells since the 4th century, when the Chinese were drilling with bamboo poles. The first oil well in modern times was drilled on the Aspheron Peninsula north-east of Baku in 1848. The motivation was to find a more efficient way to extract oil from the ground, and until then oil was collected from seeps. Oil and gas have become an absolute necessity for the modern society, powering every kind of transport and production. Oil and gas companies are continuously seeking for new oil fields, and exploration costs increases as the most easily accessible fields are depleted. Seismic data indicates where hydrocarbons can be found, in structures of typically porous sandstone, covered with a layer of impermeable rock. However, only an exploration well can confirm the existence of hydrocarbons. The recoverable amount of oil and gas will be quantified from well testing together with geophysical surveys, well logs, core analysis and PVT analysis. It is therefore important to improve equipment and procedures for well testing, as the quality of the well tests is crucial when evaluating whether a new field is viable. The economic consequences can be serious if a fields production rate drops more than expected, after spending huge resources on field development.

A well test can provide vital information about the whole reservoir, even if an exploration well only penetrates the reservoir at one spot. It is performed by logging pressure and temperature during subsequent periods of well flow and well shut-in. Memory gages will be located close to the well production tubing perforation, where the oil flows from the reservoir into the well.

A well test will start with opening a valve at the well head to let the well flow. The pressure at the well bottom during a well flow period will be governed by reservoir initial pressure and the flow resistance within the reservoir among other things. In the earliest part of the flow period the well produces because of the compressibility of the fluid in the well bore, but later a wider and wider area around the well will be affected with a pressure drop because of the flow towards the well bore. Total amount of recoverable oil and gas can be deducted by studying logarithmic pressure-time curves.

After a sudden well shut-in, the pressure at the well bottom starts to build up again. The shut-in can be performed with a valve at the well-head, or more preferably with a downhole shut-in valve. In the first case, the whole volume of the well bore itself must also be filled up in order to increase the pressure. This is known as the wellbore storage effect. This will give an uncertainty in the analysis, as the actual compressibility of the well volume is not known. This situation will be avoided with a downhole shut-in valve. During a well flow period of a well test, the downhole shut-in valve will be open, and thereby cause a minor pressure loss in the well. The well bottom pressure will increase, and in order to achieve a correct interpretation of the pressure curves it is necessary to get a detailed understanding of the two-phase pressure loss in a valve like this. The pressure loss across the shut-in valve can be also be used for calculation of the downhole flow. This is important, as a logging of the flow at the wellhead will not be real time compared to the pressure logging at the well bottom. The compressibility of the fluids in the well bore will cause a delay in flow at the well head. Simultaneous measurement of pressure and flow at the well bottom is also a necessary basis in order to use modern well test analysis based on pressure derivative plots. The so-called sand face flow rate can be directly related to the downhole pressure only if the volume under the shut-in valve is kept at a minimum, so that the compressibility of the fluids below the valve can be regarded as constant. This will be the case with a downhole shut-in valve. The pressure time-derivative curve can then be retrieved with high accuracy.

The use of a downhole shut-in valve is therefore an important improvement of the shut-in test. Knowledge on two-phase pressure loss is vital both for the use of it, and for the development of the valve also as a flow-meter.

1.2 Objectives

The main objective for this Ph.D. project are to increase the knowledge about multiphase flow in complex geometries like downhole shut-in valves. The main sub objectives for this work are:

- Develop a methodology for estimating the two-phase pressure drop along a complex geometry
- Develop a two-phase flow model for estimating the pressure drop in a downhole shut-in valve
- Investigate the characteristics of the flow in a full-scale model of a shut-in valve
- Validate the developed models with the experimental data base

1.3 Scope

Both experimental and numerical activities have been involved in this dissertation. A full scale mock-up of an existing downhole shut-in valve was made, with maximum internal diameter of 94mm, and a total length of 9.42 meters including inlet section. A series a different single phase and multiphase experiments were performed. All flow tests were performed at the multiphase laboratory at NTNU. A 1-D model based on CFD simulations was verified with single phase experiments. Multiphase experiments were performed with air, water and two different oil types; Exxsol D80 for low viscosity tests and NEXBASE 3080 for high viscosity tests. The majority of the experiments were performed with horizontal tubes, but some tests were done with 2.7 and 5 deg. inclination. Some experiments with oil/water phase inversion were also performed.

1.4 Thesis lay-out

The dissertation is structured as follows. Chapter 2 gives an introduction to petroleum reservoir rock and fluid properties. Chapter 3 gives State of the Art for two-phase pressure loss. Two different pressure drop calculation methods are presented: the black-box models and mechanistic models. The black-box models are the earliest systematic treatment of two-phase flow, and are flow pattern independent. In the mechanistic models, the flow patterns are predicted on an analytic basis. Pressure drop is calculated according to the predicted flow pattern. Downhole shut-in valves are presented in Chapter 4 together with the valve mock-up for the laboratory experiments. Minor losses throughout the valve are determined by use of CFD simulation in Chapter 5 . Chapter 6 presents the development and verification of the 1-D flow model. This is a least squares finite element model, based on spectral elements. Minor loss factors are determined from a CFD simulation, and the model is verified with single phase flow experiments. Chapter 7 has focus on pressure recovery at sudden expansions. It is shown that two-phase flow generates less pressure recovery than single phase flow. In Chapter 8 the 1-D model is expanded with two-phase compressible flow. Pressure drop calculation is based on

black box models and mechanistic two-phase flow models. Flow simulations with air, water and oil are compared to experimental results. Simulations of two-phase flow of real oil and gas are presented in Chapter 9. Chapter 10 gives summaries of papers that constitute parts of this thesis. Chapter 11 presents conclusions and outlook for future work.

Part I

Overview of two-phase flow modeling in complex geometries

Chapter 2

Petroleum reservoir rock and fluid properties

To understand the nature of the multiphase flow in an oil well, it is necessary to have insight into the nature of petroleum reservoir rock and fluid properties. The fluid itself has a complex nature, as it consists of a large number of different chemical fractions. It is flowing through a rock structure with limited free flowing area, causing rather high pressure drops. And moreover, the fluid is composed of liquid, gas or liquid with dissolved gas. This presentation is based upon Zolotukhin and Ursin (2000) and Dandekar (2006). In the end of this thesis simulations are presented based on flow of crude oil and gas.

2.1 Basic concepts of petroleum geology

2.1.1 Petroleum generation

Petroleum fluids originate from organic matter, buried millions of years ago under non-oxidizing conditions. According to present hypotheses, marine phytoplankton, algae and foraminifera (microorganisms) buried in mud and clay on the seafloor is the main sources for oil. Plants, trees and grass buried in terrestrial sedimentary basins are sources for mainly coal and gas. Mud samples from the continental shelves have shown a TOC (total organic carbon) of up to 8%.

If the sediments are exposed to burial pressure, they will slowly turn into *shale*. At temperatures below $50^{\circ}C$,the organic matter will be converted to *kerogen,* existing as particles inside the oil shale, and subsequently *bitumen.*

Petroleum fluids will be generated if the shale containing kerogen is exposed to

temperatures above $60°C$. At rock structure temperatures from $60°C$ to $175°C$ oil of different qualities will be generated. Higher temperatures will give lighter oil qualities. Above $175°C$, dry gas and wet gas will be produced.

The transformation process of organic material into petroleum is called *maturation.*

2.1.2 Accumulation in reservoir rocks

Petroleum liquid and gas generated in the source rock are less dense than formation water, and will therefore migrate upwards through cracks and permeable overlaying rocks. Typical porous and permeable reservoir rocks are *sedimentary* rocks, as sandstone, with 7-20% porosity. An oil reservoir will be created if the migrating petroleum fluids are stopped by an impervious rock type forming a so-called trap. Massive limestones, marls and mud rocks are common impermeable rocks constituting the overlying trap.

2.2 Reservoir engineering concepts and definitions

2.2.1 Continuum mechanics and filtration theory

When dealing with flow of water, oil and gas through saturated porous and permeable rocks, the physical concept of *continuum mechanics* is applied. That is, all components are expected to be continuous, or present in every region considered. Further, a *filtration theory* has been developed on this basis, for the calculation of average parameters for fluid flow in the rock.

2.2.2 Porosity

Rock porosity can be defined as *absolute porosity* or *effective porosity.* The absolute porosity ϕ_a is the ratio of all porous space in the rock to the bulk volume, whether it is interconnected (permeable) or not:

$$\phi_a = \frac{V_{p_a}}{V_b} \tag{2.1}$$

where V_{p_a} is the total void volume and V_b is the bulk volume of the rock.

Effective porosity ϕ is the ratio of interconnected porous space to bulk volume:

$$\phi = \frac{V_p}{V_b} \tag{2.2}$$

2.2.3 Saturation and wettability

If all (effective) pore volume in a rock is filled with fluids we have:

$$V_p = V_o + V_g + V_w \tag{2.3}$$

where V_o is oil volume, V_g is gas volume and V_w is gas volume. The saturation of the rock is then

$$S_i = \frac{V_i}{V_p}, \quad i = o, g, w$$

The adhesive force between rock-grain surface and the different reservoir fluids will vary. The fluid with the strongest adhesive force is the *wetting* fluid, and the other phases will be *non-wetting*. Most petroleum reservoirs are water-wet, and there is a minimum, or irreducible water saturation.

2.2.4 Permeability

The permeability k of a rock is a measure for its capability to transmit fluid :

$$k = \frac{\mu \Delta x}{A} \frac{q}{\Delta p} \tag{2.4}$$

where μ is viscosity, q is flow, A is flow cross subsection and Δp is pressure drop over distance Δx. This formula is derived from the Darcy Law for linear, horizontal flow of an incompressible fluid:

$$q = -A \frac{k}{\mu} \frac{dp}{dx} \tag{2.5}$$

Therefore, the unit of permeability is Darcy (D), and one Darcy permeability is defined as $1\frac{cm^3}{s}$ at $1cm^2$ flow cross subsection, $1cP$ viscosity and $1\frac{bar}{cm}$pressure drop.

Various flow directions in a rock sample will normally give various permeability. The *absolute permeability* is measured with only one fluid present in the rock sample, or $S_i = 1$. The effective permeability k_{ej} for phase j is a function of the saturation S_j.

2.2.5 Pressure and fluid phase distribution

The fluids inside a reservoir will mainly be distributed according to density, with a gas cap on the top, if present, and a water zone in the bottom. If the rock is water-wet, water will be found through the reservoir as grain surface wetting fluid.

The fluid levels in a reservoir are defined as follows:

Gas-Oil Contact (GOC) Interphase between oil and gas cap.

Oil-Water Contact (OWC) Interphase separating oil and water zone. This level is influenced by the capillary forces of the wetting fluid.

As water normally is present as wetting fluid, the water-saturation S_w will be gradually reduced above the OWC, where $S_w = 100\%$. The rocks effective permeability for oil is influenced by the water-saturation S_w , and therefore some more interfaces are defined:

Edge Water Level $S_o \approx 0$, oil immobile.

Productive OWC $S_o > \approx 15\%$, oil mobile.

Free-Oil Level (FOL) $S_o > \approx 70\%$,water immobile.

2.2.6 Capillary pressure

2.2.6.1 Fluid distribution in reservoir

At a particular depth in the reservoir, the total pressure d_{ov} is caused by the weight of the overlying rock-column, and is equal to the sum of the fluid-column pressure p_f and the rock grain column pressure p_m:

$$d_{ov} = p_f + p_m$$

Because the total pressure d_{ov} is constant at a given depth, a reduction in fluid pressure will give an increase in rock grain pressure:

$$dp_f = -dp_m$$

The reservoir pressure is normally taken to be the pressure at the GOC, where the pressures in the oil and gas phase are equal. Because of capillary forces, some oil will still be present in the rock pores above the GOC. The gas phase and the oil phase have different pressure gradients,

$$dp = \rho_i g dh$$

where g is gravitational constant and dh is depth increment. Now, as oil and gas are both present above the GOC, their pressure will be different, and the difference is called *capillary pressure,* denoted $(P_c)_{ij}$.

2.2.6.2 Fluid flow in reservoir

When considering fluid flow through porous channels in a reservoir, both pressure drop caused by viscous forces and capillary pressure must be evaluated. The capillary pressure is acting across fluid interfaces in pore channels. In fact, the capillary pressure is considerable. The capillary pressure is given as

$$P_c = \frac{2\sigma_{ow}\cos\theta}{r} \tag{2.6}$$

where σ_{ow} is interfacial tension between oil and water, r is channel radius and θ is wetting angel. See Figure 2.1.

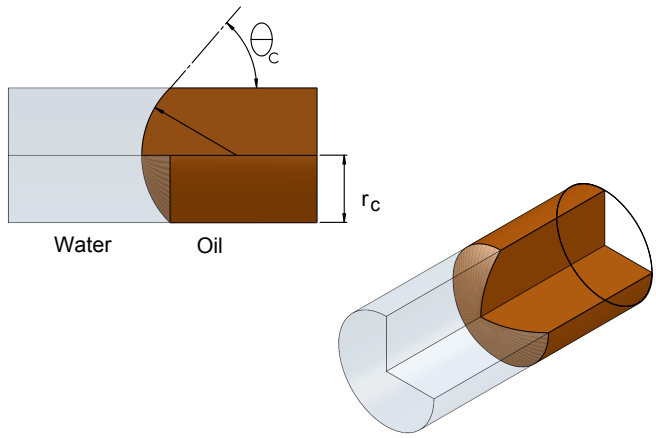

Figure 2.1: Interfacial tension between oil and water in a tube.

Because the capillary pressure is proportional to the inverse of the channel radius, there will be a channel radius size limit, below which there will be no oil flow.

2.2.7 Compressibility

The isothermal compressibility of a substance is defined as

$$c = -\frac{1}{V}\left(\frac{\partial V}{\partial p}\right)_T \tag{2.7}$$

For an oil reservoir the following compressibility must be taken into account:

Rock grain compressibility c_r.

Bulk rock compressibility c_bFor typical siliciclastic sandstone $c_{quartz} \approx 2.5 \times 10^{-6} bar^{-1}$.

Oil and water compressibility c_o and c_w. For heavy crude oil $c_o \approx 25 \times 10^{-5} bar^{-1}$. Live oil with dissolved gas has higher compressibility. For water $c_w \approx 4.6 \times 10^{-5} bar^{-1}$.

Gas compressibility c_gFor a perfect gas we have that $c_g = -\frac{1}{V}\left(\frac{\partial V}{\partial p}\right)_T = \frac{1}{p}$.

When dealing with petroleum gases at high pressures and temperatures, the deviation in behavior between real gases and ideal gases must be taken into account. For an ideal gas we have that

$$PV = nRT \tag{2.8}$$

where P is pressure, V is volume, n is number of moles, R is universal gas constant and T the temperature. For a petroleum gas we have that

$$PV = ZnRT \tag{2.9}$$

where Z is the *compressibility factor.* This factor is a function of pressure and temperature, $Z = Z(p, T)$.

The compressibility of a real gas at constant temperature is given as

$$c_g = \frac{1}{P} - \frac{1}{Z}\frac{dz}{dp}$$

2.2.7.1 Drive mechanisms

The rock compressibility is in fact a production-drive factor for oil reservoirs without gas-cap. The reason is that the confining stress, or overburden pressure, is constant. Further, the effective stress σ' in the rock is

$$\sigma' = \sigma - p \tag{2.10}$$

where σ is external stress and p is internal pore pressure, as defined by van Terzaghi (1923). That is, if the pore pressure is reduced, the effective rock stress is increased, as the sum is constant. The volume change in the rock is therefore

$$\frac{\Delta V}{V} = c_r \Delta\sigma \tag{2.11}$$

Or, assuming constant compressibility :

$$V = V_0 e^{-c_r(\sigma-\sigma_0)} \tag{2.12}$$

In this case, the rock is assumed to be without pores. A similar relationship is valid for liquids.

Both rock bulk volume and pore volume is affected by external and internal pressure:

$$V_b = V_b(\sigma, p) \tag{2.13}$$
$$V_p = V_p(\sigma, p) \tag{2.14}$$

A change in pore volume means that oil can be squeezed out of the reservoir. Porosity is defined as the ratio of pore volume V_p to bulk volume V_b, and the following relationship can be shown for change in porosity:

$$\Delta\phi = c_r \left(\frac{c_b}{c_r} (1 - \phi) - 1 \right) \Delta p \tag{2.15}$$

The bulk compressibility is normally much larger than the rock compressibility, and a pressure reduction Δp will therefore give a porosity reduction $\Delta\phi$.

If the oil is (gas-) saturated and a gas cap is present in the reservoir, the expansion of the gas will be the main production drive factor. The pressure in the reservoir can also be maintained by inflow of water from the underlaying formation.

2.3 Reservoir fluids

2.3.1 Petroleum chemistry

Hydrocarbon reservoir fluids are made up of large number of different chemical compounds. According to the International Union of Pure and Applied Chemistry (IUPAC), they are divided into:

Aliphatics alkanes, alkenes, alkynes, cycloaliphatics

Aromatics

In addition to these there might be nitrogen (N_2), carbon dioxide (CO_2) and hydrogen sulfide (H_2S). *Sour fluids* contain H_2S, and at levels above 5% precautions must be taken to avoid serious corrosion on well equipment.

Alkanes The general formula is C_nH_{2n+2} , also called paraffins. Chains of carbon atoms, saturated with hydrogen. For carbon number 1 to 4 they are gases at ambient conditions, carbon number 5-17 are liquids, and compound with carbon number above 17 are solids. For carbon number 4, butane, and above there are a number of different possible configurations of carbon and hydrogen atoms, called structural isomers. Molecules with different configurations have different physical properties. An example of structural isomers of hexane is given below Com (2014), see Figure 2.2.

The numbers of structural isomers increases for increasing carbon numbers. Alkanes are normally occurring in reservoir fluids.

Alkenes The general formula is C_nH_{2n} , also called olefins. Olefins does not occur in reservoir fluids, they are produced in petrochemical factories.

Alkynes The general formula is C_nH_{2n-2} , does normally not occur in reservoir fluids, they are produced in petrochemical factories. Example: Acetylene, used for gas welding.

Cycloaliphatics In *cyclic compounds*, like cykloalkanes (cycloparaffins, naphthalenes) and cycloalkenes the molecule is ring-shaped. The general formula is $C_nH_{2(n+1-g)}$, where g is the number of rings.

Aromatics Very toxic compounds with pleasant odors. Examples are Benzene (C_6H_6), toluene (C_7H_8) and xylene (C_8H_{10}).

N-Hexane:

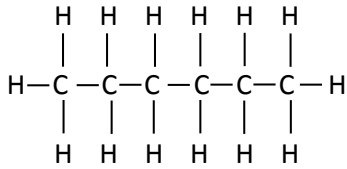

2-methylpentane:

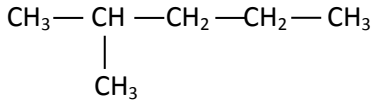

3-methylpentane:

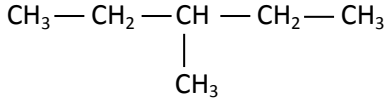

2,3-dimethylbuthane:

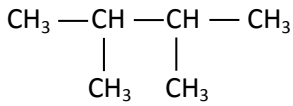

2,2-dimethylbuthane:

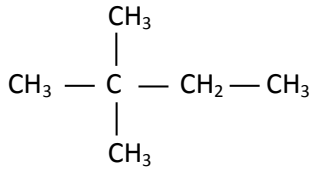

Figure 2.2: Hexane isomers.

Nonhydrocarbons Nitrogen (N_2), carbon dioxide (CO_2) and hydrogen sulfide (H_2S). The latter is extremely toxic, and even in small concentrations very corrosive.

2.3.2 Solid components in fluids

Crude oil contains some solid hydrocarbons, that are suspended in the oil at reservoir conditions. Altered temperature, chemical composition and pressure can cause them to precipitate inside production equipment. The consequence is reduced flow cross subsection area.

Gas hydrate Consists of methane, ethane and water at relatively high pressure and low temperature. Can be prevented by injection of methanol or glycol.

Waxes Heavy paraffins, deposited below a specific temperature

Asphaltenes Consists of hydrocarbons, nitrogen, sulfur and oxygen.

Diamondoids Saturated polycyclic organic compounds, rarely deposited.

Naphthenate salts Forms when naphthenic acids come in contact with metal ions.

2.3.3 Classification of reservoir fluids

2.3.3.1 Hydrocarbon classes

Reservoir fluids are classified as follows:

Reservoir fluids	API [°]	**Density [kg/m^3]**	**Viscosity [cP]**
Black oils	15-40	825-966	2-100
Volatile oils	45-55	759-802	0.25-3
Gas condensates	>50	<780	≈0.25
Wet gases	>60	<739	≈0.25
Dry gas			0.02-0.05

The density (°API) is measured at normal conditions, that is 1 *bar* absolute pressure and $15°C$. Volatile oils can be brown, orange or even green.

2.3.3.2 Formation water

As the rock formation in an oil reservoir is partly saturated with water, there will always be some water in the well stream. This is brine, with several types of dissolved chlorides.

2.3.4 Phase behavior

2.3.4.1 Singe component behavior

Water is known to be boiling at $100°C$, at normal pressure. At lower pressure however, the boiling temperature will be lower. At 98% vacuum e.g. (0.02 *bar* absolute pressure), water is boiling at $20°C$. A typical phase diagram is given in Figure 2.3 . The diagram illustrates that there is a critical point, where the properties of liquid and gas become indistinguishable.

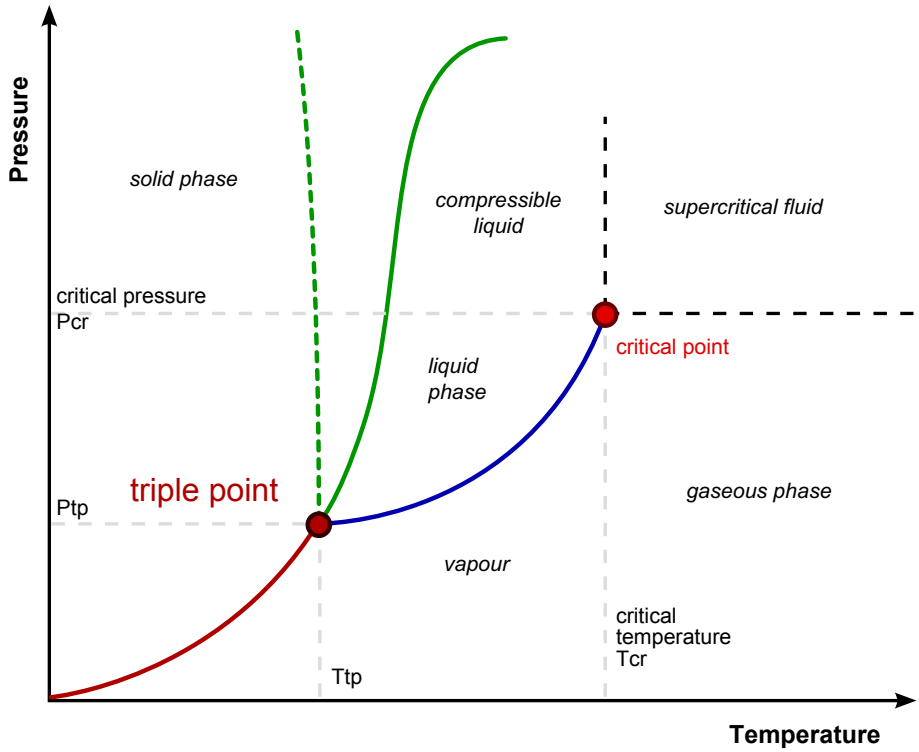

Figure 2.3: Typical single phase diagram.

The solid green line is typical transition from solid to liquid. The dotted green line indicates the behavior for water. The blue line represents the vapor pressure curve between the triple point and the critical point. Above the critical point the liquid becomes compressible. The triple point of water is approximately $0°C$, $0bar$ absolute pressure. Boiling point for water at normal conditions ($15°C$, 1 *bar* abs. pr.) is somewhere in the middle of the blue line, and the critical point for water is $374°C$ and 220,6 *bar* abs. pressure.

A pressure-specific volume diagram for a pure component is shown in Figure 2.4. We can see that transition from liquid to vapor happens at constant pressure for constant temperature, from the bubble point line to the dew point line. When boiling, the first bubble appears when crossing the bubble point line, and the last drop of liquid turns into vapor when crossing the dew point line.

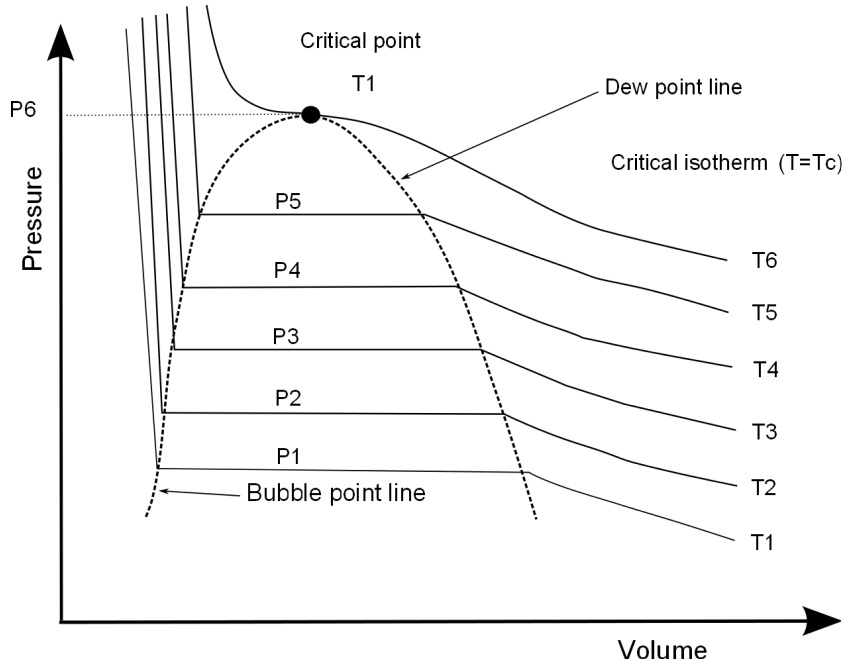

Figure 2.4: Pressure-specific volume isotherms for a single component. (University 2008)

2.3.4.2 Multi-component behavior

Reservoir fluids consists of a large number of components, and each of them might have its own vapor pressure curve. A typical pressure-temperature diagram for a multi component system is shown in Figure 2.5 . This is a typical reservoir fluid. It is now clear that evaporation/condensing no longer happens at a fixed pressure, depending on temperature. Inside the phase envelope, consisting of the bubble-point curve and the dew point curve there is both liquid and gas.

A possible process is indicated in the diagram, starting at A: 225 *bar*, 25°C, where the fluid is in liquid state. This state is also called *under-saturated*, as all gas now is dissolved in the liquid, and the oil has capability to dissolve more gas. If now the pressure drops, at constant temperature, to app. 175 *bar*, the condition is at the

bubble-point. The liquid is saturated, an the first bubble of gas appears. As the pressure continues to drop, more and more gas is released from the liquid. At 50 *bar*, the remaining liquid volume is 7%, and consequently 93% of the volume is gas.

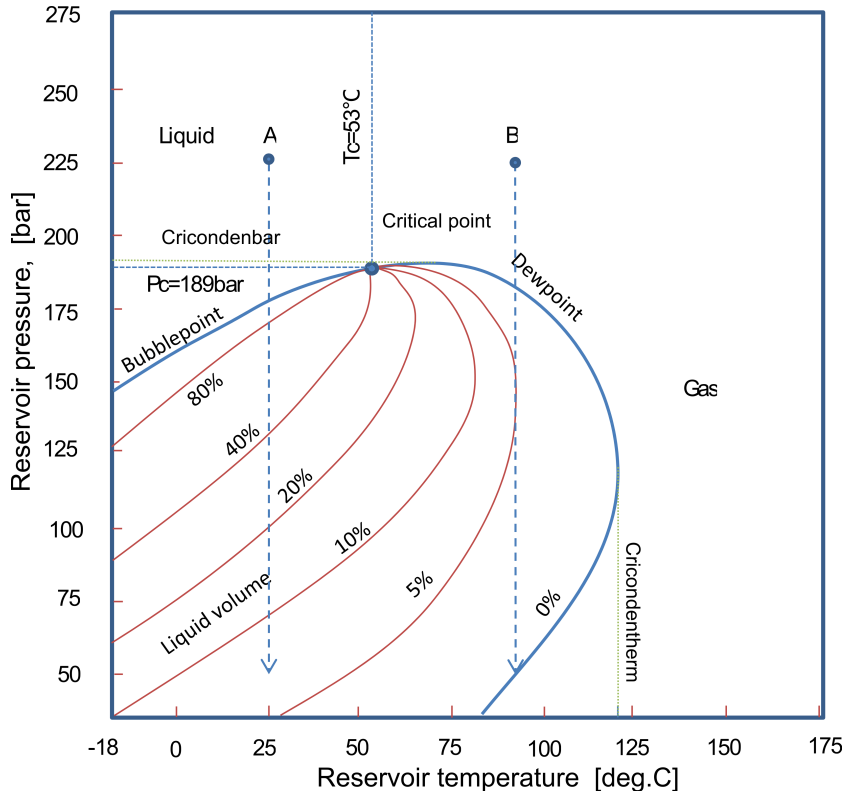

Figure 2.5: P-T diagram of reservoir fluid. (After Whitson and Brulé (2000))

Another isotherm process is indicated from point B: 225 *bar*, 90°C. The fluid is now in supercritical gas-like state. At 182 *bar*, the condition is now on the dew-point, and the first drop of liquid appears. This is called retrograde condensation, being opposite of what one should expect. At 140 *bar*, there is 5% liquid, or retrograde condensate, and 95% gas in equilibrium. At further pressure drop, the liquid part evaporates again, and at 50 *bar* there is only gas.

2.3.4.3 Types of depletion reservoirs

The different types of depletion reservoirs are indicated in Figure 2.6.

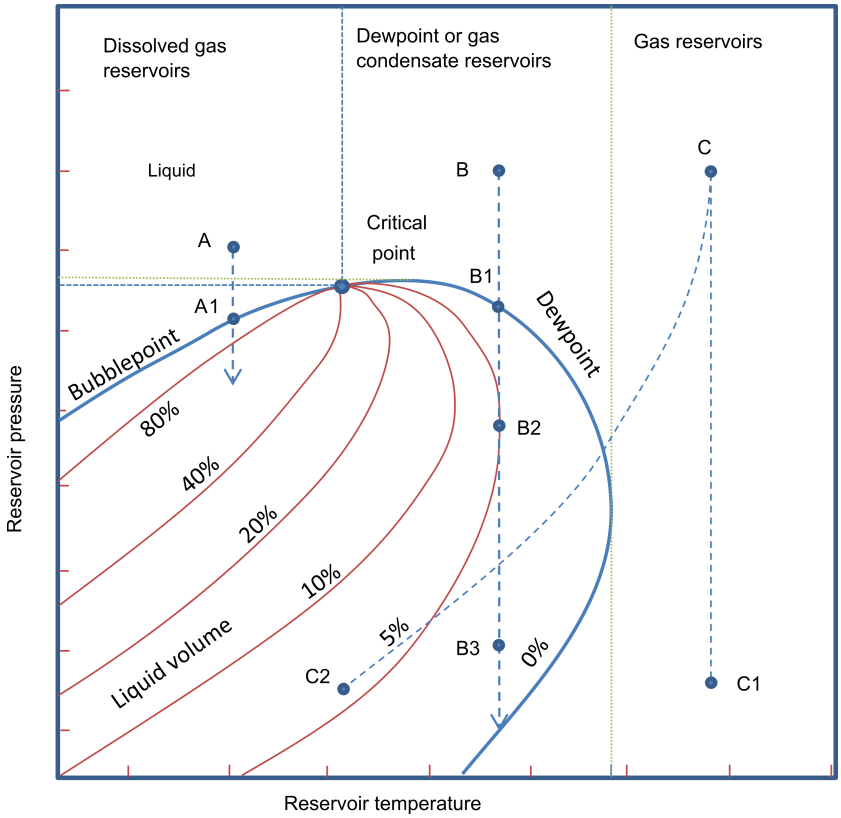

Figure 2.6: Types of depletion reservoirs (After Whitson and Brulé (2000))

2.3.4.4 Reservoir classification

The most typical oilfield reservoir mixtures are described below (Whitson and Brulé 2000).

Black oil If the reservoir temperature is much lower than the fluid critical temperature, the fluid will be a black oil. See curve A in Figure 2.6. The amount of produced gas to produced oil (Gas-oil ratio) will be relatively low, and this is therefore sometimes called *low-shrinkage oils.* Even if the reservoir pressure might be above the bubble point, pressure drop in the production tubing in the well will cause the pressure to fall below the bubble point. The well stream will therefore contain both oil and gas.

Volatile oils In this case the temperature in the reservoir is still lower than the critical temperature, but closer to it. It contains fewer heavy hydrocarbons (C_7+) than black oil, and will give a higher GOR. For both black oil and volatile oil the preferable production pressure is equal to or above the bubble point. The reason is that liberated gas at pressures below the bubble point is more mobile than oil, and will be produced at higher quantities. The relative amount of heavy hydrocarbons will increase in the reservoir, and a part of it will eventually be unrecoverable (Zolotukhin and Ursin 2000, page 164).

Gas condensate For gas condensates the reservoir temperature is above the critical temperature, but below the cricondentherm. See curve B in Figure 2.6. Production will give a pressure reduction in the reservoir, and at point B1 retrograde condensation will occur. As pressure continues to fall, more and more liquid is generated, until point B2. However, the phase envelope will in fact be changed during production, as the lightest hydrocarbons is produced, leaving heavier hydrocarbons in the reservoir. The overall composition of the reservoir is therefore changed. A revaporization of the liquid phase will therefore not happen.

Wet gas For wet gases, the reservoir temperature is higher than the cricondentherm for the reservoir fluid, see curve C-C2. At the surface, the gas is cooled enough to condense a liquid phase (Whitson and Brulé 2000, page 14).

Dry gas The dry gases produces very little condensates at the surface production equipment, and the production path stays outside the phase envelope, see curve C-C1.

2.3.4.5 Classification of reservoir fluid constituents

Reservoir fluids consists of a large number of components. The well defined components are:

Non-hydrocarbons Nitrogen, hydrogen sulfide and carbon dioxide.

Hydrocarbons Methane, ethane, propane, i-butane, n-butane, i-pentane an n-pentane.

The physical and chemical properties of these components are well known. The heavier components are lumped together:

Pseudo fractions The components heavier than pentane are grouped together after their number of carbon atoms, normally in the range C_6 to C_{19}. Each of these pseudo-fractions are characterized by average boiling point, average molecular weight etc. Each *single carbon number (SCN)* is sometimes analyzed to determine the paraffin-naphthene-aromatic (PNA) distribution. Critical pressure, critical temperature etc. can then be predicted based on average molecular weight and specific gravity (Dandekar 2006, page 314).

Plus fraction The heaviest components are grouped together in a *plus fraction*. If the pseudo fraction is covering SCN C_6 to C_{19}, the rest is grouped together in a C_{20+} fraction. As for the pseudo fraction, critical pressure, critical temperature etc. can be predicted based on average molecular weight and specific gravity.

Gas and liquids compositions with carbon numbers up to C_{80} are analyzed with *gas chromatography*. Liquids can also be analyzed with *true boiling point distillation (TBP)*. The latter is necessary to get accurate values for average molecular weight and specific gravity (density).

2.4 PVT analysis

2.4.1 Properties of petroleum reservoir fluids

2.4.1.1 Petroleum gases - Principle of corresponding states

Reduced pressure is defined as a ratio of pressure to critical pressure:

$$P_r = \frac{P}{Pc} \tag{2.16}$$

Reduced temperature is defined similarly:

$$T_r = \frac{T}{Tc} \tag{2.17}$$

Compressibility factor Z as function of reduced pressure and reduced temperature is nearly equal for all pure gases.

2.4.1.2 Formation volume factor

The *formation volume factor* B_g for dry gases is defined as the ratio of gas volume at reservoir conditions $V_{P,T}$ to volume at standard condition V_{SC}:

$$B_g = \frac{V_{P,T}}{V_{SC}} \tag{2.18}$$

The *formation volume factor* B_{wg} for wet gases is defined as the ratio of gas volume at reservoir conditions $V_{P,T}$ per volume of stock tank condensate $V_{STC}@SC$:

$$B_{wg} = \frac{V_{P,T}}{V_{STC}@SC} \tag{2.19}$$

2.4.1.3 Black oil and volatile oil

Due to liberation of dissolved gas, black oil and volatile oil shrinks when it is transported from the reservoir to the surface. Temperature and pressure also affects the volume, but to a minor extent. The *formation volume factor* B_o is defined as the volume of oil at reservoir condition $(V_o)_{P,T}$ to the volume at standard condition $(V_o)_{sc}$:

$$B_o = \frac{(V_o)_{P,T}}{(V_o)_{sc}} \tag{2.20}$$

2.4.1.4 Solution gas-oil ratio

The *solution gas-oil ratio* R_S is the number of standard m^3 of gas which will dissolve per standard m^3 of oil in the reservoir:

$$R_S = \frac{V_{ogn}}{V_{on}} \tag{2.21}$$

Note that when industry units are used, gas volume is given as *cubic feet* (0.02832 m^3), and oil volume is given as *barrels* (0.1590 m^3). The value of the solution gas-oil ratio will therefore be different.

2.4.2 PVT equipment

To be able to evaluate reserves and to develop a recovery plan, Pressure-Volume-Temperature (PVT) analysis are performed on test samples of reservoir fluids. These tests simulate the recovery of hydrocarbon fluids by varying pressure and temperature, in order to find especially volumetric data at surface and reservoir conditions. The mechanical PVT test cell has to chambers, one on top of the other. Each chamber has a mechanically driven piston in the end, so that the volume can be changed. The connection channel between them has inspection windows, and a stirrer inside can speed up the homogenization. It is equipped with instruments for measuring density and viscosity, and the temperature of the cell can be controlled. Surface tension can also be determined with a pendant drop device, if equipped.

2.4.2.1 Constant composition expansion - flash expansion

In a Constant Composition Expansion (CCE) test, the fluid sample is first exposed to reservoir temperature and pressure equal to or above the initial reservoir pressure. The volume of the test cell is then increased by moving the pistons, step by step. At each step, phase volumes and total volume are recorded together with pressure. No parts of the test sample is removed during the test. The physical properties of the phases can also be measured. The bubble-point pressure can be determined from the plot of pressure versus volume. For dry gases, the CCE-test can be used to measure the *compressibility factor.* (Z-factor).

2.4.2.2 Differential liberation

This test is carried out on reservoir oils, at reservoir temperature. Volumetric and compositional changes are evaluated at declining pressures, resembling the depletion process in the reservoir. At each pressure step, liberated gas is removed from the cell. Therefore, the composition of the test fluid in the cell is changing for each step. As the lightest components are removed as gas, the average molecular weight in the cell is increasing, and consequently the phase envelope is moving down. Based on test results the Z-factor, formation volume factor B_{oD} ,total formation volume factor B_{tD} and solution gas-oil ratio (GOR), R_{sD} can be determined as function of pressure. The subscript D indicates a value from the differential liberation test.

2.4.2.3 Constant volume depletion

The purpose of the Constant Volume Depletion (CVD) test is to simulate the pressure depletion in gas reservoirs. Initially the gas is compressed and heated to reservoir conditions. At each test step, the pressure is reduced by expanded the test cell. Next, gas is let out of the cell while moving the test cell piston to keep the pressure constant until initial volume is reached. The retrograde condensate is assumed to stay in the reservoir, and it is therefore accumulated in the test cell. The CVD test give information about amount and quality of retrograde condensate.

2.4.2.4 Separator test

The purpose of the separator test is to simulate potential separator stages. The temperature is therefore reduced at each test step. Formation volume factor B_{oS} , solution gas-oil ratio R_{sS} and specific gravity are determined.

2.5 Vapor-liquid equilibrium

2.5.1 Ideal solution principle

2.5.1.1 Equilibrium ratio

The *equilibrium ratio* K_i for component with index i can be expressed as

$$K_i = \frac{Y_i}{X_i} = \frac{P_{vi}}{P} \tag{2.22}$$

where

Y_i mole fraction of component i in the vapor phase, $\sum_{i=1}^{n} Y_i = 1$

X_i mole fraction of component i in the liquid phase $\sum_{i=1}^{n} X_i = 1$

P total system pressure

P_{vi} vapor pressure of component i at actual temperature.

This relation is based on Raoult´s law for the partial pressure P_i in an ideal solution:

$$P_i = X_i P_{vi} \tag{2.23}$$

and Dalton´s law for the partial pressure P_i in an ideal gas mixture:

$$P_i = Y_i P \tag{2.24}$$

2.5.1.2 Concept of PT flash

The concept of PT flash is based on a process where a stream of n moles of material with composition Z_i is divided into n_L moles of vapor and n_V moles of gas. For the sum of material flow we have that

$$n = n_L + n_V \tag{2.25}$$

For each component with index i we also have that

$$Z_i = X_i n_L + Y_i n_v \tag{2.26}$$

2.5.1.3 Calculation of bubble-point pressure

The bubble-point pressure of an ideal liquid solution is

$$P_b = \sum_{i=1}^{n} Z_i P_{vi} \tag{2.27}$$

2.5.1.4 Calculation of dew-point pressure

The dew-point pressure of an ideal gas mixture is

$$P_d = \frac{1}{\sum\limits_{i=1}^{n} Z_i / P_{vi}} \tag{2.28}$$

2.5.1.5 Restrictions of the ideal solution principle

The ideal solution principle is based on

1. There is a mutual solubility.
2. Mixing of components does not result in chemical reaction.
3. Equal intermolecular forces.

These conditions holds only for very similar components, at moderate temperatures below about 7 bar. But first of all, the VLE equations are only valid if all the components have defined vapor pressure. This is not true if the actual temperature is above the critical temperature for any of the components. Methane is present in every reservoir fluid, and has a critical temperature of $-82°C$.

2.5.2 Empirical correlations

Many correlations are made for the prediction of equilibrium ratio for hydrocarbon mixtures. They are a function of composition, temperature and pressure:

$$K_i = f(P, T, Z_i) \tag{2.29}$$

2.5.2.1 Wilson equation

The Wilson equation for the prediction of equilibration ratio is

$$K_i = \frac{P_{ci}}{P} \exp\left[5.37(1+\omega_i)\left(1-\frac{T_{ci}}{T}\right)\right] \tag{2.30}$$

where

P_{ci} critical pressure of component i

T_{ci} critical temperature of component i

P, T pressure and temperature

ω_i acentric factor of component i ,

$$\omega_i = \frac{3\left[\log\left(P_c/14.70\right)\right]}{7\left[T_c/T_b - 1\right]} - 1 \tag{2.31}$$

2.5.2.2 Concept of convergence pressure

The *equilibrium ratio* K_i is defined as the ratio of mole fraction in vapor phase to mole fraction in liquid phase. When pressure and temperature is inside the phase envelope, and approaching the critical point, the mole fractions in liquid and vapor phase for each components converges to equal values. That is, composition of vapor and liquid becomes equal, and the equilibrium ratio K_i converges to unity.

2.5.2.3 Whitson-Torp correlation

The Whitson-Torp Correlation is a modification of the Wilson correlation,

$$K_i = \left[\frac{P_{ci}}{P_k}\right]^{A-1}\left[\frac{P_{ci}}{P}\right]\frac{P_{ci}}{P}\exp\left[5.37A(1+\omega_i)\left(1-\frac{T_{ci}}{T}\right)\right] \tag{2.32}$$

where

$$A = 1 - \left[\frac{P - 14.7}{P_k - 14.7}\right]^{0.6} \tag{2.33}$$

and

P, T system pressure [*psia*] and temperature [$^\circ R$]

P_k convergence pressure [*psia*], from Standings correlation: $P_k = 60MW_{C_{7+}} - 4200$

ω_i acentric factor

$MW_{C_{7+}}$ molecular weight of C_{7+} fraction

Equilibrium ratios for PT flash calculations can be carried out directly. Bubble-point and dew-point pressure calculations involves iteration procedures, as the pressure is implicit in the formula.

2.5.3 Equations-of-state models

Equations-of-state (EOS) models are expressions that relates pressure, temperature and volume at extended ranges of pressure and temperature. Several families of EOS models exists, but only the van der Waals family will be used here.

2.5.3.1 van der Waals Equation of State

The van der Waals (vdW) equation of state is

$$\left(P + \frac{a}{V^2}\right)(V - b) = RT \tag{2.34}$$

where

P, T system pressure [*psia*] and temperature [$^\circ R$]

R gas constant (10.73 $psi - ft^3/lb - mol^\circ R$)

V molar volume ($ft^3/lb - mol$)

a and b are constants for the component in question.

At low pressures the equation is reduced to the ideal gas equation $PV = nRT$.

The vdW EOS gives a qualitatively correct description of phase behavior of a pure component in gaseous and liquid states, but the precision is inadequate for practical use.

2.5.3.2 Redlich-Kwong equation of state

The Redlich-Kwong equation of state is a modification of the vdW EOS:

$$P = \frac{RT}{V-b} - \frac{a}{V\left(V+b\right)T^{0.5}} \tag{2.35}$$

Constants a and b can be determined by inserting critical pressure and temperature, and then

$$a = 0.42727\frac{R^2T_c^{2.5}}{P_c} \tag{2.36}$$

and

$$b = 0.08664\frac{RT_c}{P_c} \tag{2.37}$$

This equation can be expressed in terms of compressibility as

$$Z^3 - Z^2 + (A - B - B^2)Z - AB = 0 \tag{2.38}$$

where

$$A = \frac{aP}{(R^2T^{2.5})} \tag{2.39}$$

$$B = \frac{bP}{RT} \tag{2.40}$$

In the two-phase region, 3 real roots are obtained. The largest root is compressibility for gas, and the smallest for liquid. The middle root has no physical significance.

This equation is only accurate for predicting of molar volumes of pure substances.

2.5.3.3 Soave-Redlich-Kwong equation of state

The Soave-Redlich-Kwong (SRK) equation of state is a modification of the Redlich-Kwong equation of state:

$$P = \frac{RT}{V-b} - \frac{a\alpha}{V\left(V+b\right)} \tag{2.41}$$

where

$$\alpha = \left[1 + m\left(1 - T_r^{0.5}\right)\right]^2 \tag{2.42}$$

and

$$m = 0.48 + 1.574\omega - 0.176\omega^2 \tag{2.43}$$

The SRK EOS is commonly used for petroleum fluids, and a and b can be determined as for the Redlich-Kwong equation of state.

2.5.3.4 Peng-Robinson equation of state

The Peng-Robinson (PR) equation of state is a modification of the SRK EOS:

$$P = \frac{RT}{V-b} - \frac{a\alpha}{V\left(V+b\right) + b\left(V-b\right)} \tag{2.44}$$

where

$$a = 0.45724\frac{R^2T_c^{2.5}}{P_c} \tag{2.45}$$

$$b = 0.07780\frac{RT_c}{P_c} \tag{2.46}$$

and α is defined as for the SRK EOS, but

$$m = 0.379642 + 1.48503\omega - 0.1644\omega^2 + 0.016667\omega^3 \tag{2.47}$$

2.5.3.5 EOS models used on mixtures

Although EOS models are developed for pure components, they can be used on mixtures as well by using mixing rules, like

$$(a\alpha)_m = \sum_{i=1}^{n}\sum_{j=1}^{n} Z_i Z_j (a_i a_j \alpha_i \alpha_j)^{0.5}(1 - k_{ij}) \tag{2.48}$$

and

$$b_m = \sum_{i=1}^{n} Z_i b_i \tag{2.49}$$

Densities, equilibrium ratios, bubble-point pressures etc. can then be calculated.

2.6 Material balance and drive mechanisms

2.6.1 The golden principle

Material Balance Equations (MBE) are based on the assumption that the reservoir can be viewed as a closed volume. This volume has the only outlet through the well, and a possible inlet for water in the bottom. The fluid and rock formation inside the volume will expand if pressure is reduced. The bulk volume of the reservoir will also be compressed by the overburden pressure when the inside pressure in the reservoir is reduced. The following equation is commonly referred to as *the golden principle:*

$$V_i - V = \Delta V \tag{2.50}$$

where:

V_i initial hydrocarbon volume at initial pressure p_i

V current hydrocarbon volume at pressure p

ΔV produced volume

By studying production decline curves, the reservoir drive mechanisms can be identified.

2.6.2 Gas reservoirs

In case of a gas reservoir driven only by the expansion of gas we have that the reservoir net (pore) volume is unchanged, as there is no influx of water:

$$G_i \cdot B_{gi} = (G_i - G_p)\, B_g \tag{2.51}$$

where

G_i is initial volume of gas in reservoir $\left[Sm^3\right]$

G_p produced volume of gas $\left[Sm^3\right]$

B_{gi} initial gas formation volume factor, reservoir volume per Sm^3 $\left[Rm^3/Sm^3\right]$

B_g current gas formation volume factor, reservoir volume per Sm^3 $\left[Rm^3/Sm^3\right]$

It can be rewritten as

$$\frac{B_{gi}}{B_g} = 1 - \frac{G_p}{G_i} \tag{2.52}$$

For a real gas we have that

$$p_i V_i = z_i n_i R T_i \tag{2.53}$$

The formation volume factor B_{gi} is relating the volumes of the same mass of gas as reservoir (initial) and standard conditions (1 *bar*/15$^\circ C$):

$$B_{gi} = \frac{V_i}{V_n} = \frac{z_i n_i R T_i}{p_i} \div \frac{z_n n_i R T_n}{p_n} \tag{2.54}$$

$$= \frac{p_n}{Z_n T_n} \cdot \frac{Z_i T_i}{p_i} \tag{2.55}$$

For the current formation volume factor we have

$$B_g = \frac{V_r}{V_n} = \frac{p_n}{Z_n T_n} \cdot \frac{Z_r T_r}{p_r} \tag{2.56}$$

Where V_r is current volume of gas in reservoir.

Inserting this into Equation (2.52) we get

$$\frac{B_{gi}}{B_g} = \frac{Z_i T_i}{p_i} \div \frac{Z_r T_r}{p_r} \tag{2.57}$$

The initial and current reservoir temperature T_i and T_r are normally equal, so that

$$\frac{B_{gi}}{B_g} = \frac{Z_i}{p_i} \div \frac{Z_r}{p_r} \tag{2.58}$$

$$\Downarrow \tag{2.59}$$

$$\frac{p_r}{Z_r} = \frac{p_i}{Z_i}\left(1 - \frac{G_p}{G_i}\right) \tag{2.60}$$

The only variable on the right side is *produced volume of gas* G_p , so this must be the function of a straight line. If the production decline curve follows this line, it is evident that there is no influx of water, and the drive mechanism is *gas expansion.*

2.6.3 Oil reservoir

There are many factors contributing to expelling oil from reservoirs. Figure 2.7 below displays the production mechanisms.

Nomenclature is as for gas reservoirs, and as follows:

HCPV - hydrocarbon-filled pore volume

N - initial resources of oil, Sm^3

$\mathbf{N}_p$ - produced resources of oil, Sm^3

m - ratio gas/oil, at reservoir pressure and temperature, $m = \frac{GB_{gi}}{NB_{oi}}$

G - initial gas in place, in Sm^3

$\mathbf{N}_p$ - volume of oil produced

As pressure is declining in the reservoir, water, oil and gas is expanding. On the other side, available pore volume is reduced. When a gas cap is present, the oil in the reservoir is saturated, and when the pressure is reduced more gas will be liberated from the oil. We have that

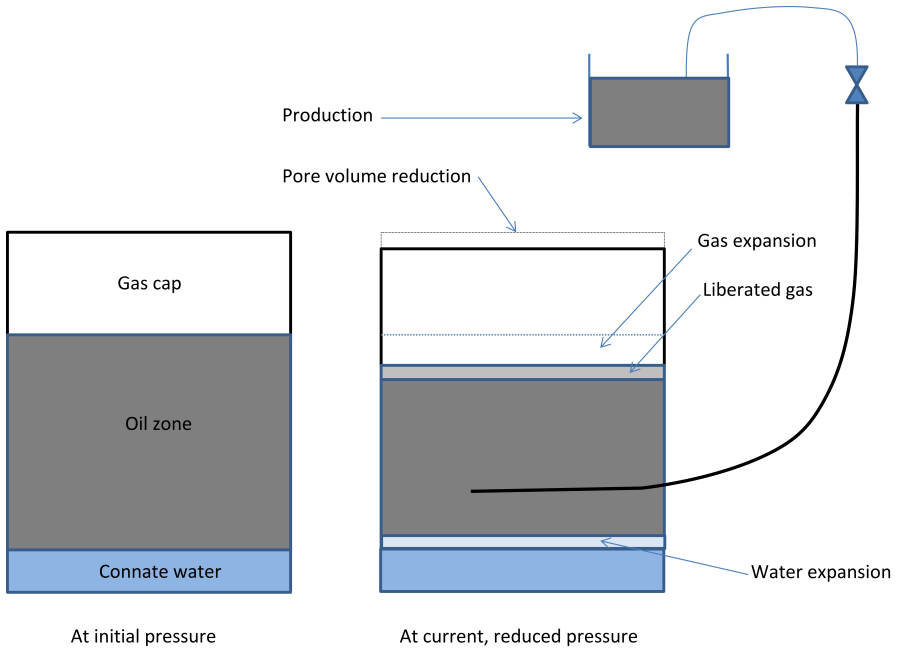

Figure 2.7: Drive mechanisms in an oil reservoir with gas cap. (Zolotukhin and Ursin 2000, p. 187)

Production = Gas expansion + Vol. of liberated gas
+ connate water expansion + pore-volume reduction + oil expansion

2.6.3.1 Oil expansion

The formation volume factor B_o is the ratio of oil (with dissolved gas) volume at reservoir condition to volume at stock tank condition. B_o at initial condition is denoted B_{oi} . Due to liberation of gas the oil will shrink at pressure drop. If the pressure is above the bubble-point, the oil will expand at pressure drop. With the presence of a gas cap, the pressure is at the bubble-point, so we have that

$$\Delta V_{oil} = N\left(B_{oi} - B_o\right) \tag{2.61}$$

This volume is given as reservoir volume.

2.6.3.2 Liberated gas expansion

The *solution gas-oil ratio* R_S is the number of standard m^3 of gas which will dissolve per standard m^3 of oil in the reservoir, and initial value is given by R_{si}. Obviously, this value is at its maximum when the pressure is at the bubble point. Then we have that

$$\Delta V_{liberated\_gas} = N\left(R_{si} - R_s\right) B_g \tag{2.62}$$

2.6.3.3 Gas cap expansion

The gas cap will expand when the pressure is falling, and for the volume change we have that

$$\Delta V_{gas\_cap} = G\left(B_g - B_{gi}\right) = mNB_{oi}\left(\frac{B_g}{B_{gi}} - 1\right) \tag{2.63}$$

2.6.3.4 Hydrocarbon pore volume

Falling pressure causes connate (irreducible saturation) water to expand. As the pore volume itself is compressible we have that

$$\Delta V_{HCPV} = \left(c_w V_w + c_p V_p\right) \Delta p \tag{2.64}$$

Since $V_w = S_w V_p$ and $V_{HCPV} = V_o + V_g = (1+m)\, NB_{oi}$

$$\Delta V_{HCPV} = (1+m)\, NB_{oi} \left(\frac{c_w S_w + c_p}{1 - S_w} \right) \Delta p \tag{2.65}$$

2.6.3.5 Material balance equation

The above given equations can be summarized as follows in the MBE:

$$N_p \left[B_o + (R_p - R_s)\, B_g \right] = NB_{oi} \left[\frac{(B_o - B_{oi}) + (R_{si} - R_s)\, B_g}{B_{oi}} + m \left(\frac{B_g}{B_{gi}} - 1 \right) + (1+m) \left(\frac{c_w S_w + c_p}{1 - S_w} \right) \Delta p \right] + (W_e - W_p)\, B_w \tag{2.66}$$

where

W_e - water influx

W_p - produced water

B_w - water formation volume factor

2.6.3.6 Drive mechanisms

Drive mechanisms can occur in various combinations:

Oil reservoir without gas cap - expansion of oil, water and dissolved gas, water influx and pore volume reduction.

Gas cap drive - expansion of gas cap, oil and dissolved gas. Water and pore compressibility are normally insignificant.

Natural water drive with gas cap - water influx , expansion of gas cap, oil and dissolved gas. Water influx reduces pressure drop, and causes high recovery factor.

Each drive mechanism has its own specific production-pressure curve. By plotting historical data, the main reservoir drive mechanism can be identified.

2.6.3.7 Water injection

Water injection is used to maintain reservoir pressure. The MBE then reduces to:

$$N_p \left[B_o + (R_p - R_s)\, B_g\right] = (W_e - W_p)\, B_w \tag{2.67}$$

2.7 Well testing

2.7.1 Methods

Well testing is used to help identifying the reservoir model. The typical methods are:

Shut-in test Composed of a pressure *drawdown test* and a pressure *buildup test*. The well is flowing at constant rate until the pressure is stabilized, followed by a sudden closing, causing the pressure to build up.

Falloff test Injecting (water) through an injection well at constant rate, followed by a shut in. Pressure falloff is then logged.

Multiple rate gas well test The gas well is flowing at several increasing flow rates, followed by a shut-in period.

System of units used in well test analysis:

Parameter	Nomenclature	SI-Unit
Flow rate	q	Sm^3/d
Form. vol. factor	B	Rm^3/Sm^3
Thickness	h	m
Permeability	k	μm^2
Viscosity	μ	$mPs \cdot s$
Pressure	p	kPa
Distance	r	m
Tot. compr.	c_t	$(kPa)^{-1}$
Time	t	hrs

2.7.2 Wellbore effects

Well testing may be disturbed by several wellbore effects.

Wellbore storage effects is the result of shutting in a well by a surface valve. The reservoir will be flowing for a period after shutting in, caused by the compressibility of fluid in the wellbore. This can be avoided by shutting in at the bottom of the well, close to the casing perforation. For the period of the wellbore storage effect we have that

$$p_i - p_{wf} = \frac{qB}{24C_{ws}}t \tag{2.68}$$

where the well constant $C_{ws} = c_l V_w$.

Skin effect is caused by drilling mu particles that have penetrated a distance r_s into the reservoir due to necessary overbalance.

Induced fractures are reducing the flow resistance in the formation, especially close to the well.

2.7.3 Reservoir model

The near wellbore region is a cylinder, with diffusivity equation for a liquid

$$\frac{1}{r}\frac{\partial}{\partial r}\left(r\frac{\partial p}{\partial r}\right) = \frac{1}{\eta}\frac{\partial p}{\partial t} \tag{2.69}$$

where $\eta = k/\left(\mu\phi c_t\right)$ is the diffusivity constant and

k - permeability

μ - viscosity

ϕ - porosity

c_t - total compressibility as sum of liquid compressibility c_l and matrix compressibility c_m

2.7.4 Dimensionless variables

Dimensionless variables are used to simplify well test analysis. The following groups are used :

Dimensionless radius:

$$r_D = \frac{r}{r_w} \tag{2.70}$$

Dimensionless time, SI-units:

$$t_D = 0.0036 \frac{kt}{\phi \mu C_t r_w^2} \tag{2.71}$$

Dimensionless pressure, SI-units

$$p_D = \frac{kh}{1.842 qB\mu} \left[p_i - p\left(r,t\right) \right] \tag{2.72}$$

2.7.5 Transient flow regime

During the *transient period*, the pressure in the wellbore for a drawdown test can be calculated by

$$p_i - p_w = \frac{qB\mu}{2\pi hk} \frac{1}{2} \left(\ln \frac{kt}{\phi \mu C_t r_w^2} + 0.80907 + 2S \right) \tag{2.73}$$

where S is the skin factor. The well acts as if it is an infinite reservoir. Plotting the data in a diagram with logarithmic time as horizontal axis versus pressure, a curve with declining trend can be observed. When the trend in late period deviates from the straight line, the reservoir boundary effect is seen.

2.7.6 Pseudo steady state flow

At the end of the transient flow regime, the pressure is falling in the whole reservoir. The time-dependent pressure drop is constant as function of radius :

$$\frac{\partial p(r)}{\partial t} = const. \tag{2.74}$$

By integration of the diffusivity Equation (2.69) we get for the pseudo steady state period:

$$p_i - p_w = \frac{qB\mu}{2\pi hk} \left(\frac{2\pi k}{\phi A C_t \mu} t + \frac{1}{2} \ln \frac{4A}{e^{\gamma} C_A r_w^2} + S \right) \tag{2.75}$$

where $\gamma = 0.5772$ is Euler´s constant. C_A is the Dietz shape factor.

2.8 Well test analysis

2.8.1 Shut-in test curves

A typical well shut-in test sequence consists of a pressure drawdown period followed by a sudden shut-in. Downhole pressure and temperature will be logged during the whole test sequence. A representative diagram of logged pressure and temperature with a downhole shut-in valve is shown in Figure 2.8. From the ho-

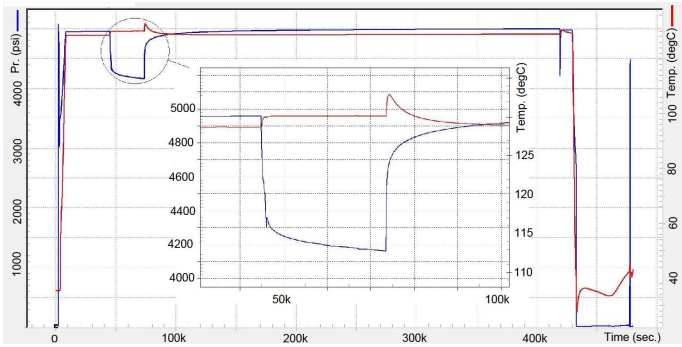

Figure 2.8: Pressure and temperature curves from shut-in test (Qinterra Technologies).

rizontal axis we can see that the whole test was lasting for about 440.000 s, or some 122 hours. Logging started at the surface, and at about 45.000 s the pressure suddenly dropped. At this moment a valve at the surface was opened to let the well flow. The pressure before this moment can be regarded as the average reservoir (initial) pressure $\bar{p}$. After some 70.000 s the flowing bottomhole pressure p_{wf} approached a constant value, probably about 4100 psi. The detailed shape of this curve and its time-derivative is important for the well analysis. At about 74.000 s the shut-in valve closed, and the bottomhole pressure suddenly increased. The shape of the first part of this curve after shut-in reveals much information about the reservoir. Compared to topside shut-in, it has been shown by Guerrero and Lessi (2007) that a fast downhole shut-in reveals more information about the near wellbore region. Also, a detailed knowledge about the two-phase pressure drop across the valve can be used for calculating the flow from a measured pressure difference.

The diagram also shows that the downhole temperature increased $1 - 2°C$ when well was flowing. The reason might be frictional work by compressing the well fluid.

2.8.2 Pressure drawdown test

A semi-logaritmic plot of a drawdown test is shown in Figure 2.9. These data are derived from the curve shown in Figure 2.8.

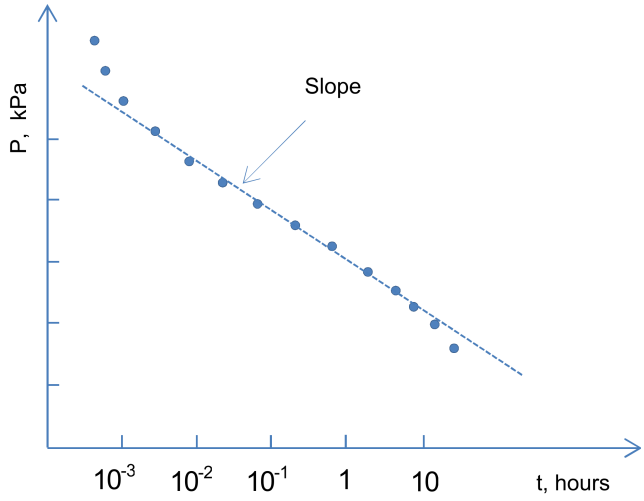

Figure 2.9: Semi-logarithmic plot of pressure drawdown test (After Zolotukhin and Ursin (2000, p. 232)).

From the straight part of the curve, a line with slope m can be found, where

$$m = 2.1208\frac{qB\mu}{hk} \tag{2.76}$$

The permeability can then be found:

$$k = \frac{2.1208qB\mu}{mh} \tag{2.77}$$

The skin-factor can also be identified:

$$S = 1.151\left[\frac{p_i - p_{wf}\,(1hr)}{m} - \log\frac{k}{\phi\mu C_t r_w^2} + 2.0923\right] \tag{2.78}$$

2.8.3 Horner plot

The Horner plot is used for analyzing the pressure buildup tests shown in Figure 2.8, and an example is shown in Figure 2.10.

After an infinite long period, $\Delta t \to \infty$, we have that $\Delta t/(t + \Delta t) = 1$, and initial reservoir pressure can be found from the Horner plot.

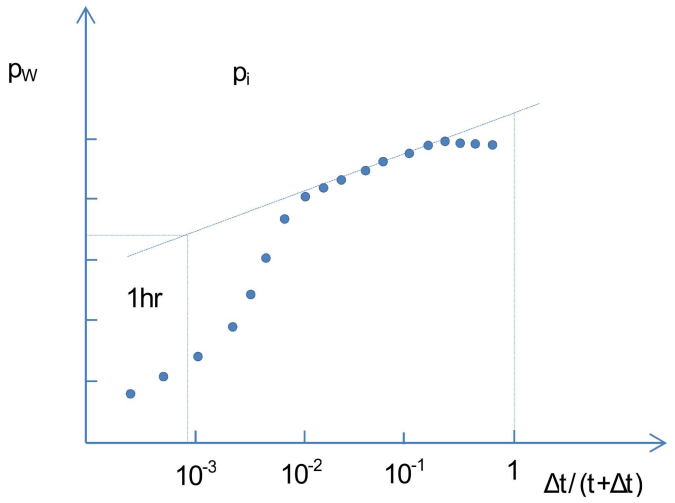

Figure 2.10: Horner plot (After Zolotukhin and Ursin (2000, p. 234)).

2.8.4 Type curves

Type curves are log-log plots of dimensionless pressure and derivative of dimensionless pressure versus dimensionless time.

The pressure derivative is more sensitive to reservoir characteristics than the Horner plot, and can give the wanted information in shorter well flowing time. Type curves can be given for dimensionless parameters as given in Equations (2.71) and (2.72) and by dimensionless wellbore storage coefficient:

$$C_D = 2.308 \frac{C}{\phi h C_t r_w^2} \tag{2.79}$$

Reservoir data can be matched with type-curves to estimate reservoir parameters as skin factor, wellbore storage coefficient and permeability-thickness product kh. An example is given in Figure 2.11.

2.9 Summary

The rock and fluid properties described in this chapter constitutes the boundary condition for the two-phase flow in the wellbore. The mass flows of liquid and gas are governed by initial composition, reservoir pressure, formation permeability etc. Also, as the pressure is dropping along the wellbore towards the surface the mass balance will change.

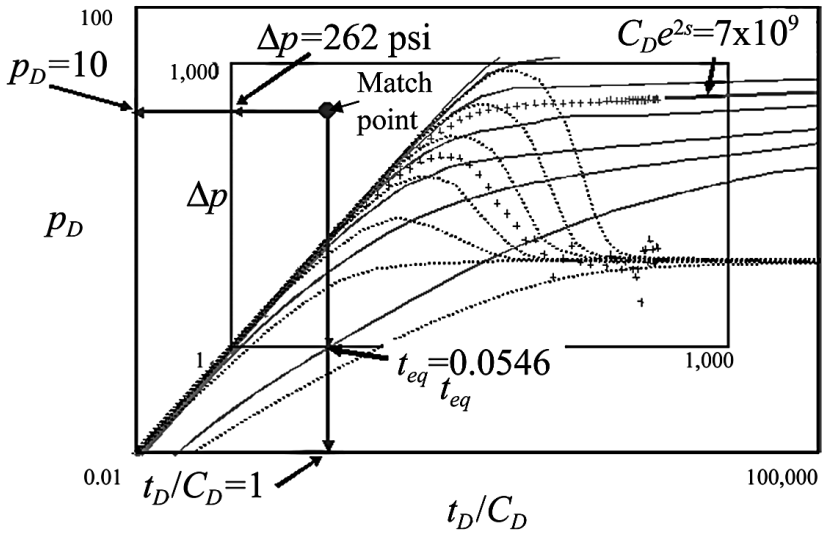

Figure 2.11: Curve-fitting with type-curves (After Zolotukhin and Ursin (2000, p. 248))

Chapter 3

State of the art for two-phase pressure losses

The flow passage in a downhole shut-in valve used in oil wells can be considered as a combination of different geometries which results in a major challenge when estimating the pressure drop across the valve. In this section, a summary of the modeling of frictional pressure drop on complex flow geometry will be presented. First a summary of the most used correlation for pipe flow will be summarized, followed by the review of pressure drop across restrictions.

3.1 Flow pattern independent correlations

3.1.1 Chisholm C-correlation

The correlations by Lockhart and Martinelli (1949) have been the starting point for the greater part of subsequent work in this area. They expressed the two-phase pressure drop Δp_{TF} as a function of the single phase gas pressure drop Δp_G or liquid flow pressure drop Δp_L:

$$\Delta p_{TF} = \varphi_{FL}^2 \Delta p_L \tag{3.1}$$
$$\Delta p_{TF} = \varphi_{FG}^2 \Delta p_G \tag{3.2}$$

The two-phase multipliers φ_{FL} and φ_{FL} were correlated with flow quality x, densities ρ and viscosities μ without considering the flow pattern. The flow quality is defined as

$$x = \frac{\dot{m}_G}{\dot{m}_G + \dot{m}_L} \tag{3.3}$$

where $\dot{m}_G$ and $\dot{m}_L$ is mass flow rate of gas and liquid. The Lockhart-Martinelli parameter X is defined as

$$X = \sqrt{\frac{\Delta p_L}{\Delta p_G}} \tag{3.4}$$

and they plotted the two-phase multipliers to a base of X. Later, Chisholm. (1967) developed analytic expressions representing these curves:

$$\varphi_{FL}^2 = 1 + \frac{C}{X} + \frac{1}{X^2} \tag{3.5}$$

$$\varphi_{FG}^2 = 1 + CX + X^2 \tag{3.6}$$

This will therefore be called the Chisholm C-correlation. For Reynolds numbers from 2000 to 100000, with frictional coefficient

$$\lambda = \frac{0.314}{R_e^n} \tag{3.7}$$

where $n = 0.25$ is the Blasius exponent we get that

$$X = \left(\frac{\mu_L}{\mu_G}\right)^{\frac{n}{2}} \left(\frac{1-x}{x}\right)^{\frac{2-n}{2}} \sqrt{\frac{\rho_G}{\rho_L}} \tag{3.8}$$

For turbulent flow of both the liquid and the gas, setting $C = 21$ will give a two-phase pressure drop multiplier equal to the curves presented by Lockhart and Martinelli.

3.1.2 Chisholm B-correlation

The B coefficient method (Chisholm 1983) is given by

$$\varphi_{FLO}^2 = 1 + \left(\Gamma^2 - 1\right)\left[Bx^{\frac{2-n}{2}}(1-x)^{\frac{2-n}{2}} + x^{2-n}\right] \tag{3.9}$$

where

$$\Gamma^2 = \frac{\Delta p_{FG0}}{\Delta p_{FL0}} = \left(\frac{\mu_G}{\mu_L}\right)^n \frac{\rho_L}{\rho_G} \tag{3.10}$$

Here Δp_{FG0} and Δp_{FL0} are pressure drops for total mass flow as gas and liquid respectively. When $\Gamma > 8.9$ the B coefficient is given by

$$B = \frac{21\Gamma - 2^{2-n} + 2}{\Gamma^2 - 1} \tag{3.11}$$

If $\Gamma < 8.9$ and Blasius coefficient $n = 0.25$ we have that $B = 2.364$.

3.1.3 Friedel correlation

The Friedel (1979) correlation is recommended by Hewitt and Whalley (1980, 1983) for viscosity ratios $\frac{\mu_L}{\mu_G} < 1000$ and mass velocities below $G = 2000 \frac{kg}{m^2 s}$:

$$\varphi_{FR}^2 = E + \frac{3.24FH}{FR_H^{0.045} We_L^{0.035}} \tag{3.12}$$

$$FR_H = \frac{G_{Total}^2 d_i}{\sigma \rho_H} \tag{3.13}$$

$$E = (1-x)^2 + x^2 \frac{\rho_L f_G}{\rho_G f_L} \tag{3.14}$$

$$F = x^{0.78}(1-x)^{0.224} \tag{3.15}$$

$$H = \left(\frac{\rho_L}{\rho_G}\right)^{0.91} \left(\frac{\mu_G}{\mu_L}\right)^{0.19} \left(1 - \frac{\mu_G}{\mu_L}\right)^{0.7} \tag{3.16}$$

$$We_L = \frac{G_{Total}^2}{g d_i \rho_H^2} \tag{3.17}$$

The homogeneous density is

$$\rho_H = \left(\frac{x}{\rho_G} + \frac{1-x}{\rho_L}\right) \tag{3.18}$$

3.1.4 Homogeneous theory

In the old homogeneous theory the two-phase viscosity was assumed to be equal to the liquid density. With a homogeneous density defined as above, the frictional pressure gradient is (Chisholm 1983):

$$\Delta p_{TF} = \lambda_{TF} \frac{G^2}{2 d_i \rho_H} \tag{3.19}$$

The friction factor λ_{TF} can be calculated using the Reynolds number with a two-phase viscosity defined by a formulae by Cicchitti (1960):

$$Re = \frac{G d_i}{\mu_{TP}} \tag{3.20}$$

and

$$\mu_{TP} = x\mu_G + (1-x)\mu_L \tag{3.21}$$

The two-phase multiplier is then given as

$$\varphi_{FLO}^2 = \frac{\Delta p_{TF}}{\Delta p_{FL0}} \tag{3.22}$$

3.1.5 Bankoff correlation

The Bankoff (1960) correlation for two-phase pressure drop is given by

$$\varphi_{BF} = \frac{1}{1-x}\left(1-\gamma\left(1-\frac{\rho_G}{\rho_L}\right)\right)^{3/7}\left(1+x\left(\frac{\rho_L}{\rho_G}-1\right)\right) \tag{3.23}$$

where

$$\gamma = \frac{0.71+2.35\left(\frac{\rho_G}{\rho_L}\right)}{1+\left(\frac{1-x}{x}\right)\left(\frac{\rho_G}{\rho_L}\right)} \tag{3.24}$$

This two-phase multiplier is used in the following way:

$$\Delta p_{TF} = \varphi_{BF}^{7/4}\Delta p_{L0} \tag{3.25}$$

where

$$\Delta p_{L0} = f_L\frac{\Delta z}{d_i}\frac{G_{Total}^2}{2\rho_L} \tag{3.26}$$

$$f_L = \frac{0.314}{Re_L^{0.25}} \tag{3.27}$$

$$Re_L = \frac{G_{Total}d_i}{\mu_L} \tag{3.28}$$

3.1.6 Müller-Steinhagen and Heck

This empirical correlation by Müller-Steinhagen and Heck (1986) is given by

$$\left(\frac{dp}{dz}\right)_{TF} = G\left(1-x\right)^{1/3}+Bx^3 \tag{3.29}$$

where

$$G = A+2\left(B-A\right)x \tag{3.30}$$

$$A = \left(\frac{dp}{dz}\right)_L = f_L\frac{G_{Total}^2}{2d_i\rho_L} \tag{3.31}$$

$$B = \left(\frac{dp}{dz}\right)_G = f_G\frac{G_{Total}^2}{2d_i\rho_G} \tag{3.32}$$

The liquid friction coefficient is given by Eq. (3.27). The gas friction coefficient is given similarly:

$$f_G = \frac{0.314}{Re_G^{0.25}} \tag{3.33}$$

$$Re_L = \frac{G_{Total}d_i}{\mu_G} \tag{3.34}$$

The two-phase multiplier is given as

$$\varphi_{FLO}^2 = \frac{\left(\frac{dP}{dz}\right)_{TP}}{A} \tag{3.35}$$

The two-phase flow of air and water in a downhole shut-in valve has been simulated using these correlations (Edvardsen et al. 2014), and a plot of the result is given in Figure 3.1.

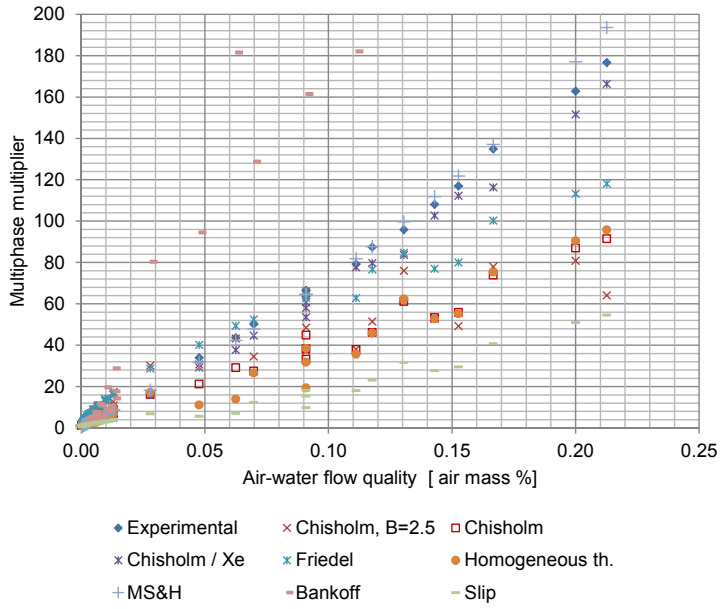

Figure 3.1: Two-phase pressure drop (Edvardsen et al. 2014).

The single phase pressure drop was simulated using computational fluid dynamics (CFD). The correlations were applied to data for total single phase pressure drop for liquid and gas, and the results shows a very high deviation for some of the correlations. The Müller-Steinhagen and Heck correlation is best with a deviation of -17%.

3.2 Unified Comprehensive Model formulation

The Unified Comprehensive Model (UCM) formulation used in this work is taken from Gomez et al. (2000) and Shoham (2006), and is explained here.

3.2.1 Unified flow pattern prediction model

Flow patterns of type stratified, slug (intermittent), annular, bubble and dispersed bubble can be indicated with the Unified Comprehensive model, see Figure 3.2.

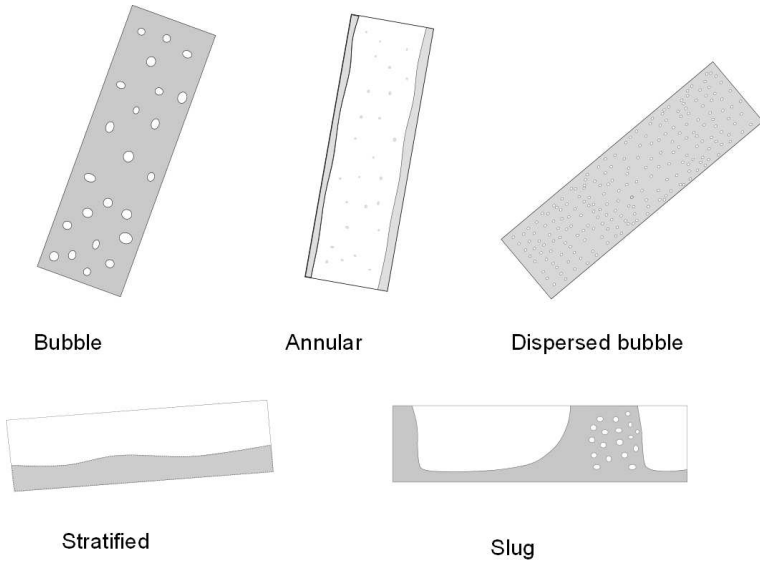

Figure 3.2: Flow patterns.

3.2.1.1 Stratified to non-stratified transition

An equilibrium liquid level can be calculated from a given liquid and gas flow rate, see Figure 3.3.

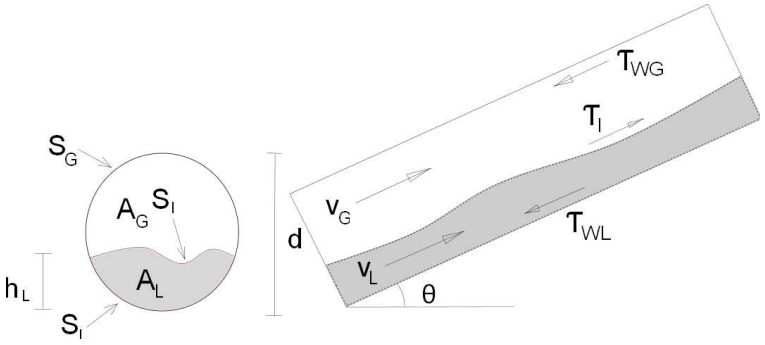

Figure 3.3: Stratified flow pattern.

It is assumed first that the flow is stratified, and that the liquid level is such that the two phases will have equal pressure gradients. By expressing cross-sections and

inter-phases in terms of the equilibrium liquid level height, the liquid level can be found from a combined momentum equation for the gas and liquid phase:

$$\frac{\tau_{WL}}{\tau_{WG}}\frac{S_L}{A_L} - \left(\frac{S_G}{A_G} + \frac{S_I}{A_L} + \frac{S_I}{A_G}\right) + \frac{(\rho_L - \rho_G)\, g \sin\theta}{\tau_{WG}} = 0 \tag{3.36}$$

For simplicity the interfacial shear stress is assumed to be equal to the wall shear stress. On basis of the identified equilibrium level, a simplified Kelvin-Helmholtz stability analysis is applied in order to determine whether the flow is stratified or not. The final criterion for instability is:

$$v_G \geq \left(1 - \frac{h_L}{d}\right)\left[\frac{(\rho_L - \rho_G)\, g \cos\theta A_G}{\rho_G S_I}\right]^{0.5} \tag{3.37}$$

The definition of stratified flow includes also stratified-wavy flow pattern.

3.2.1.2 Slug to dispersed bubble transition

At high liquid flow rates, turbulent forces breaks the gas bubbles into smaller bubbles. The diameter of the dispersed bubbles can be obtained from a correlation by Barnea et al. (1985):

$$d_{\max} = \left[0.725 + 4.15\left(\frac{v_{SG}}{v_M}\right)^{0.5}\right]\left(\frac{\sigma}{\rho_L}\right)^{0.6}\left(\frac{2 f_M v_M^3}{d}\right)^{-0.4} \tag{3.38}$$

If the bubbles becomes small enough, they will form a stable dispersed bubble flow. In that case the bubble diameter must be below the critical diameter for agglomeration, given by:

$$d_{CD} = 2\left[\frac{0.4\sigma}{(\rho_L - \rho_G)\, g}\right]^{0.5} \tag{3.39}$$

The turbulent forces must also be strong enough to keep the bubbles dispersed. The rising velocity of a bubble in a liquid increases with increasing bubble diameter, and to avoid accumulation of bubbles in the upper part of horizontal pipes, the dispersed bubbles must have a diameter below:

$$d_{CB} = \frac{3}{8}\frac{\rho_L}{(\rho_L - \rho_G)}\frac{f_M v_M^2}{g\cos\theta} \tag{3.40}$$

The flow patter will change from slug (intermittent) to dispersed if

$$d_{\max} < d_{CD} \text{ and } d_{\max} < d_{CB} \tag{3.41}$$

However, if the void fraction α is larger than 0.52 , the flow transition from slug to dispersed bubble will not occur. This void fraction limit is equal to the maximum packing of spheres in a cubic lattice.

3.2.1.3 Annular to slug transition

For annular flow, a dimensionless equation is presented by Gomez et al. (2000):

$$Y = \frac{1 + 75H_L}{(1 - H_L)^{2.5} H_L} - \frac{1}{H_L^3} X^2 \tag{3.42}$$

Here *X* is the Lockhart and Martinelli parameter, and using the Blasius formula for the friction factor we get that:

$$X = \frac{\frac{dP_{SL}}{dL}}{\frac{dP_{SG}}{dL}} = \frac{\frac{4C_L}{d}\left(\frac{\rho_L v_{SL} d}{\mu_L}\right)^{-n} \frac{\rho_L v_{SL}^2}{2}}{\frac{4C_G}{d}\left(\frac{\rho_G v_{SG} d}{\mu_G}\right)^{-n} \frac{\rho_G v_{SG}^2}{2}} \tag{3.43}$$

Y is a dimensionless group based on the inclination angle:

$$Y = \frac{(\rho_L - \rho_G)\, g \sin\theta}{\frac{dP_{SG}}{dL}} \tag{3.44}$$

Transition from annular to slug flow occurs when the liquid film on the pipe wall becomes unstable. The condition for liquid film instability is:

$$Y \geq \frac{2 - 1.5H_L}{H_L^3 (1 - 1.5H_L)} X^2 \tag{3.45}$$

It is also found that annular flow can only exist if the liquid holdup $H_L < 0.24$.

3.2.1.4 Bubble to slug transition

Bubble flow exists only in pipes with inclination angles of 60° or more, provided that the pipe diameter is larger than

$$d_{\min} = 19 \left[\frac{(\rho_L - \rho_G)\,\sigma}{\rho_L^2 g} \right]^{0.5} m \tag{3.46}$$

If the void fraction is larger than $\alpha = 0.25$, transition from annular to slug flow will occur due to coalescence of bubbles if the superficial liquid velocity is larger than (Shoham 2006):

$$v_{SL} = 3v_{SG} - 1.15 \left[\frac{g\,(\rho_L - \rho_G)\,\sigma}{\rho_L^2} \right]^{0.25} \sin\theta \tag{3.47}$$

3.2.2 Flow pattern transition discontinuities

3.2.2.1 Transition from slug to bubble and dispersed bubble flow

Even if slug flow is predicted, the flow pattern can transform into bubble or dispersed bubble flow. As the flow conditions approach the boundary between slug and bubble or dispersed bubble flow, the gas pocket region L_f of the slug unit becomes small. Gomez et al. (2000) presents the following constraints:

$$\text{If } L_f \leq 1.2d \text{ and } v_{SL} \leq 0.6\ m/s \text{ , bubble flow exists} \tag{3.48}$$

$$\text{If } L_f \leq 1.2d \text{ and } v_{SL} > 0.6\ m/s \text{ , dispersed bubble flow exists} \tag{3.49}$$

3.2.2.2 Transition from slug to annular flow

For slug flow at conditions close to the border to annular flow, the UCM formulation includes a transition zone where the calculation of pressure gradient is averaged between pressure gradient for slug flow and gradient for annular flow. In this transition zone the superficial gas velocity is larger than

$$v_{SG(crit)} = \frac{3.1\,[\sigma g \sin\theta\,(\rho_L - \rho_G)]^{0.25}}{\rho_G^{0.5}} \tag{3.50}$$

3.2.3 Flow models

After predicting the flow pattern for the current flow conditions, the UCM formulation gives separate flow models for each flow pattern, with calculation of liquid

holdup and pressure gradient.

3.2.3.1 Unified stratified flow model

For stratified flow, the interfacial and cross section areas can be expressed in terms of the liquid height, see Figure 3.3. The momentum balances for the two phases are

$$-A_L\frac{dP_L}{dL} - \tau_{WL}S_L + \tau_I S_I - \rho_L A_L g\sin\theta = 0 \quad (3.51)$$

$$-A_G\frac{dP_G}{dL} - \tau_{WG}S_G + \tau_I S_I - \rho_G A_G g\sin\theta = 0 \quad (3.52)$$

By combining these we get that

$$\tau_{WG}\frac{S_G}{A_G} - \tau_{WL}\frac{S_L}{A_L} + \tau_I S_I\left(\frac{1}{A_L}+\frac{1}{A_G}\right) - (\rho_L-\rho_G)\,g\sin\theta = 0 \quad (3.53)$$

This equation can be solved for the liquid level h_L , and the pressure gradient can then be found from one of the momentum equations.

3.2.3.2 Stratified flow closure relationships

Wall shear stresses are given by

$$\tau_{WL} = f_L\frac{\rho_L v_L^2}{2} \text{ and } \tau_{WG} = f_G\frac{\rho_G v_G^2}{2} \quad (3.54)$$

Fanning friction factors are used here, and the Reynolds numbers are

$$Re_L = \frac{d_L v_L \rho_L}{\mu_L} \text{ and } Re_G = \frac{d_G v_G \rho_G}{\mu_G} \quad (3.55)$$

The hydraulic diameters used here are

$$d_L = \frac{4A_L}{S_L} \text{ and } d_G = \frac{4A_G}{S_G+S_I} \quad (3.56)$$

The friction factor for the gas phase is for turbulent flow

$$f_G = 0.001375 \left[1 + \left(2 \times 10^4 \frac{\varepsilon}{d} + \frac{10^6}{Re_G} \right)^{1/3} \right] \tag{3.57}$$

For the liquid phase, the UCM formulation uses the correlation developed by Ouyang and K.Aziz (1996):

$$f_L = \frac{1.6291}{Re_L^{0.5161}} \left(\frac{v_{SG}}{v_{SL}} \right)^{0.0926} \tag{3.58}$$

The stress along the interface between liquid and gas is defined by the UCM formulation as

$$\tau_I = f_I \rho_G \frac{(v_G - v_L)^2}{2} \tag{3.59}$$

The interfacial friction factor is different for smooth and wavy flow. For pipe diameters smaller than $0.127\ m$, as here,the superficial gas transition velocity between stratified smooth and stratified wavy flow pattern is defined as

$$v_{SG,T} = 5\sqrt{\frac{101325}{p}} \tag{3.60}$$

Here p is absolute pressure in Pa. Then we have that

$$v_{SG} < v_{SG,T} : f_I = f_G \tag{3.61}$$

$$v_{SG} < v_{SG,T} : f_I = f_G \left[1 + 15\sqrt{\frac{h_L}{d}} \left(\frac{v_{SG}}{v_{SG,T}} - 1 \right) \right] \tag{3.62}$$

3.2.3.3 Unified slug flow model

Slug flow is shown schematically in Figure 3.4, and is modeled with the following simplifications:

1. The liquid film along the gas pocket zone has constant thickness.
2. Pressure drop calculated from a global momentum balance on the slug unit.

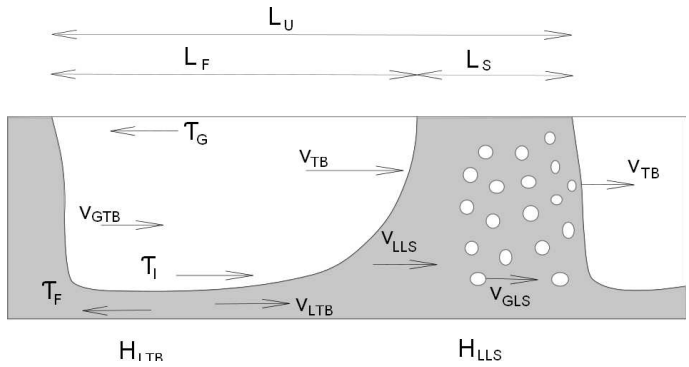

Figure 3.4: Slug flow pattern.

3. Liquid holdup in the slug body given by the Gomez et al. (2000) correlation.

The overall liquid mass balance is

$$v_{SL} = v_{LLS} H_{LLS} \frac{L_S}{L_U} + v_{LTB} H_{LTB} \frac{L_F}{L_U} \tag{3.63}$$

Looking at two parallel cross sections in the slug body and in the liquid film region, moving with the velocity v_{TB} , we have that

$$(v_{TB} - v_{LLS})\, H_{LLS} = (v_{TB} - v_{LTB})\, H_{LTB} \tag{3.64}$$

As the volumetric flow rate must be constant everywhere, we also have that

$$v_m = v_{SL} + v_{SG} = v_{LLS} H_{LLS} + v_{GLS}\,(1 - H_{LLS}) \tag{3.65}$$

and

$$v_m = v_{LTB} H_{LTB} + v_{GTB}(1 - H_{LTB}) \tag{3.66}$$

The slug body velocity v_{LLS} can now be determined from Eq. (3.65), as closure relationships gives the other variables. The hight h_F of the assumed equilibrium liquid film can be found from an momentum balance for this region

$$\tau_F \frac{S_F}{A_F} - \tau_G \frac{S_G}{A_G} + \tau_I S_I \left(\frac{1}{A_F} + \frac{1}{A_G} \right) - (\rho_L - \rho_G)\, g \sin\theta = 0 \tag{3.67}$$

Shear forces, areas and cross section areas are functions of the liquid level h_F , and this equation can be solved in the same way as the combined momentum equation for stratified flow. For a given liquid height the liquid holdup H_{LTB} in the gas pocket/film region is as follows from geometrical relationships

$$H_{LTB} = \frac{1}{\pi}\left[\pi - \cos^{-1}\left(2\frac{h_F}{d} - 1\right) + \left(2\frac{h_F}{d} - 1\right)\sqrt{1 - \left(2\frac{h_F}{d} - 1\right)^2}\right] \tag{3.68}$$

The slug unit lenght L_U can be found from Equation 3.63, using that $L_U = L_F + L_S$

$$L_U = L_S\frac{v_{LLS}H_{LLS} - v_{LTB}H_{LTB}}{v_{SL} - v_{LTB}H_{LTB}} \tag{3.69}$$

From a global force balance over a slug unit we get the pressure gradient:

$$-\frac{dP}{dL} = \rho_U g\sin\theta + \frac{\tau_S \pi d}{A_p}\frac{L_S}{L_U} + \frac{\tau_F S_F + \tau_G S_G}{A_P}\frac{L_F}{L_U} \tag{3.70}$$

Average slug unit density is given by

$$\rho_U = H_{LSU}\rho_L + (1 - H_{LSU})\rho_U \tag{3.71}$$

The slug unit average holdup H_{LSU} can be found from Equations 3.63, 3.64 and 3.65, and we get that

$$H_{LSU} = \frac{v_{TB}H_{LLS} + v_{GLS}\left(1 - H_{LLS}\right) - v_{SG}}{v_{TB}} \tag{3.72}$$

3.2.3.4 Slug flow closure relationships

The UCM formulation for slug flow includes the following closure relationships:

1. For horizontal pipes the fully developed slug unit length $L_S = 30d$, and for vertical pipes $L_S = 20d$. For pipes with inclination angles between $\pm 1^\circ$ and diameters above 0.075m, a correlation by Scott et al. (1989) is used, with d and L_S in meter:

$$\ln\left(L_S\right) = -26.6 + 28.5\left[\ln\left(d\right) + 3.67\right]^{0.1} \tag{3.73}$$

2. The Gomez et al. (2000) correlation for liquid holdup in the slug body is used:

$$H_{LLS} = \exp\left[-\left(7.85 \times 10^{-3}\theta + 2.48 \times 10^{-6} Re_{LS}\right)\right] \text{ for } 0^\circ \leq \theta \leq 90^\circ \tag{3.74}$$

where

$$Re_{LS} = \frac{\rho_L v_M d}{\mu_L} \tag{3.75}$$

3. The Bendiksen (1984) correlation is used for slug translational velocity, where $c_o = 1.2$ for turbulent flow:

$$v_{TB} = c_o v_M + 0.54\sqrt{gd}\cos\theta + 0.35\sqrt{gd}\sin\theta \tag{3.76}$$

4. The gas bubble velocity is given by

$$v_{GLS} = 1.2 v_M + 1.53\left[\frac{g\left(\rho_L - \rho_G\right)}{\rho_L^2}\right]^{0.25} H_{LLS}^{0.5}\sin\theta \tag{3.77}$$

3.2.3.5 Unified annular flow model

The Alves et al. (1991) model for annular flow is used in the UCM formulation, and covers inclination angles from -10° to 90°, see Figure 3.5.

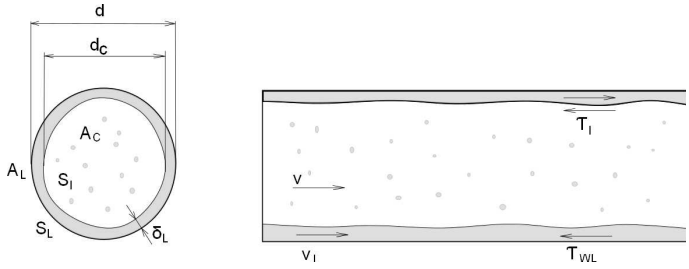

Figure 3.5: Annular flow pattern.

Momentum balances for the liquid film on the pipe wall and for the gas core are

$$-\tau_{WL}\frac{S_L}{A_F} + \tau_I\frac{S_I}{A_F} - \frac{dP_L}{dL} - \rho_L g\sin\theta = 0 \tag{3.78}$$

and

$$-\tau_I \frac{S_I}{A_C} - \frac{dP_C}{dL} - \rho_C g \sin\theta = 0 \tag{3.79}$$

By combining these two equations we get that

$$-\tau_{WL} \frac{S_L}{A_F} + \tau_I S_I \left(\frac{1}{A_F} + \frac{1}{A_C} \right) - (\rho_L - \rho_C) g \sin\theta = 0 \tag{3.80}$$

The liquid film thickness δ_L can be found by solving this equation, as shear stresses and areas are implicit functions of δ_L. The velocities can be determined from mass balance equations:

$$v_F = v_{SL} \frac{(1 - f_E) d^2}{4\delta_L (d - \delta_L)} \tag{3.81}$$

$$v_C = \frac{(v_{SG} + v_{SL} f_E) d^2}{(d - 2\delta_L)^2} \tag{3.82}$$

The gas core has entrained liquid droplets, and the entrainment fraction is given by the variable f_E. This model formulation assumes homogeneous flow in the core, and the void fraction, average density and viscosity in the core are then

$$\alpha_C = \frac{v_{SG}}{v_{SG} + v_{SL} f_E} \tag{3.83}$$

$$\rho_C = \rho_G \alpha_C + \rho_L (1 - \alpha_C) \tag{3.84}$$

$$\mu_C = \mu_G \alpha_C + \mu_L (1 - \alpha_C) \tag{3.85}$$

The total void fraction is

$$\alpha_T = \alpha_C \left(1 - 2\frac{\delta_L}{d} \right)^2 \tag{3.86}$$

3.2.3.6 Unified annular flow closure relationships

The shear stress along the pipe wall is calculated using the principle of hydraulic diameter:

$$d_L = \frac{4A_L}{S_L + S_I} = 2\delta_L \tag{3.87}$$

As before we have that $Re_L = \frac{d_L v_L \rho_L}{\mu_L}$ and $\tau_{WL} = f_L \frac{\rho_L v_L^2}{2}$. The interfacial shear stress between the gas core and the annular liquid film is defined as

$$\tau_I = f_I \frac{\rho_C \left(v_C - v_F\right)^2}{2} \tag{3.88}$$

where

$$f_I = I_\theta f_{SC} = I_\theta \left(0.046 Re_{SC}^{-0.2}\right) \tag{3.89}$$

The core superficial velocity takes account for the liquid entrainment in the core:

$$v_{SC} = v_{SG} + v_{SL} f_E \tag{3.90}$$

The core superficial Reynolds number is

$$Re_{SC} = \frac{\rho_C v_{SC} d}{\mu_C} \tag{3.91}$$

The interfacial friction correction parameter I_θ depends on the inclination angle:

$$I_\theta = I_H \cos^2 \theta + I_V \sin^2 \theta \tag{3.92}$$

A correlation by Henstock and Hanratty (1976) is used for the horizontal interfacial correction parameter:

$$I_H = 1 + 850F \tag{3.93}$$

$$F = \frac{\left(0.42 Re_F^{1.25} + 2.8 \times 10^{-4} Re_F^{2.25}\right)^{0.4}}{Re_{SG}^{0.9}} \frac{\mu_L}{\mu_G} \left(\frac{\rho_G}{\rho_L}\right)^{0.5} \tag{3.94}$$

The definition of the liquid film Reynolds number is

$$Re_F = \frac{\rho_L v_F d_F}{\mu_L} \tag{3.95}$$

and the superficial gas Reynolds number is

$$Re_{SG} = \frac{\rho_G v_{SG} d}{\mu_G} \tag{3.96}$$

A correlation by Wallis (1969) is used for the vertical interfacial correction parameter:

$$I_V = 1 + 300\frac{\delta_L}{d} \tag{3.97}$$

Wallis has also provided the entrainment correlation:

$$f_E = 1 - \exp\left[-0.125\left(\phi - 1.5\right)\right] \tag{3.98}$$

$$\phi = 10^4 \frac{v_{SG}\mu_G}{\sigma}\left(\frac{\rho_G}{\rho_L}\right)^{0.5} \tag{3.99}$$

3.2.3.7 Unified bubble flow model

If bubble flow is indicated, the void fraction $\alpha = 1 - H_L$ is taken from a correlation by Hasan and Kabir (1988):

$$1.53\left[\frac{g\left(\rho_L - \rho_G\right)\sigma}{\rho_L^2}\right]^{0.25}(1-\alpha)^{0.5}\sin\theta = \frac{v_{SG}}{\alpha} - 1.2v_M \tag{3.100}$$

The pressure gradient is then calculated from mixture properties as follows:

$$\rho_M = \rho_L H_L + \rho_G(1 - H_L) \tag{3.101}$$

$$\mu_M = \mu_L H_L + \mu_G(1 - H_L) \tag{3.102}$$

$$v_M = v_{SL} + v_{SG} \tag{3.103}$$

The mixture Reynolds number is

$$Re_M = \frac{\rho_M v_M d}{\mu_M} \tag{3.104}$$

The pressure gradient is then

$$-\frac{dP}{dL} = \rho_M g\sin\theta + 2f_M\rho_M\frac{v_M^2}{d} \tag{3.105}$$

where f_M is a standard pipe Fanning friction factor.

3.2.3.8 Unified dispersed bubble flow model

For dispersed bubble flow, the void fraction $H_L = \lambda_L = \frac{v_{SL}}{v_{SL}+v_{SG}}$. The calculation of pressure gradient is for the rest as for bubble flow.

3.3 Two-phase minor losses

Pressure losses due to contractions, expansions, bends etc. are generally called minor losses. Some recent work on two-phase minor losses are presented in Table 3.1. Schmidt and Friedel (1997) give an improved model for two-phase flow in

Table 3.1
Two-phase minor losses

D [mm]	Authors	Fluids	System
50	Alimonti et al. (2010)	Water/air	Multiple orifices
0.8-1.6	Roul and Dash (2011)	Water/air	Expansion, contraction
0.33-0.85	Zhou et al. (2008)	Nitrogen/water	Expansion, contraction
0.83	Coleman (2004)	R134a	Minor loss, contraction
50	Kim et al. (2010)	Water/air	Minor loss, elbows
<60	Schmidt and Friedel (1997)	Water, air, R12, glycerol	Minor loss, contraction

contractions, but for relatively high flow qualities with annular flow. It is worth noting that they prove that there is no *vena contracta* (streamline concentration) downstream a sudden contraction, unlike the case for single phase flow. Kim et al. (2010) gives an interesting model for overall two-phase pressure loss in a system with minor losses. An alternative two-phase pressure loss multiplier is calculated with an extra term for minor losses. However, they calculated a minor loss factor that differs from recommended values for single phase flow. They also showed that the overall pressure loss could be predicted using the Chisholm C-correlation with C=30, instead of using the normal value of C=21 for turbulent gas/turbulent liquid flow.

3.3.1 Pressure change in contractions

Coleman (2004) investigated experimentally the minor losses for contractions in micro tubes with 0.83 *mm* hydraulic diameter. He found the pressure loss to be larger than expected from common correlations, and established a simple mathematical model for the mass flux in the *vena contracta* without taking slip into consideration. Zhuo et al. (2008) also investigated single- and two-phase flow in contractions, and found that introducing a slip-ratio of $S = (\rho_L/\rho_G)^{1/3}$ gave predicted pressure drops corresponding to experimental values. Roul and Dash (2011) also performed experiments with abrupt area changes in mini-channels,

and concluded that the same slip-ratio applies. Alimonti et al. (2010) performed experiments with multiple orifice valves, and correlated multiphase pressure drop with a measured void fraction. However, they did not correlate flow quality and void fraction, and information on slip ratio is therefore missing.

3.3.2 Pressure change in expansions

Two-phase flow in sudden expansions are also studied by a number of authors. A schematic model is shown in Figure 3.6.

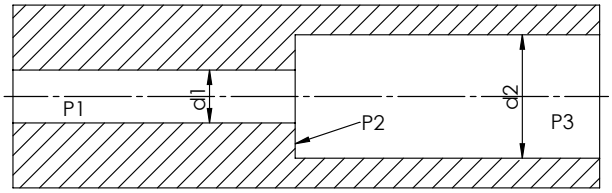

Figure 3.6: Sudden expansion.

The pressure recovery for a two-phase flow can be modeled by calculating an average two-phase density ρ_h, and in its simplest form it is without slip velocity (Wadle 1989):

$$p_3 - p_1 = \frac{\sigma_A \left(1 - \sigma_A\right) G^2}{\rho_h} \tag{3.106}$$

where the homogeneous density is

$$\frac{1}{\rho_h} = \frac{x}{\rho_G} + \frac{1 - x}{\rho_L} \tag{3.107}$$

Here area ration is $\sigma_A = (d1/d3)^2$, G $[kg/m^2 s]$ is mass flux and flow quality $x = m_G/(m_G + m_L)$ is mass flow of gas over total mass flow. A model by Lottes (1961) and attributed to Romie (1958) uses the void fraction for calculating the pressure recovery. In this formulation the void fraction at inlet and outlet is assumed to be equal.

$$p_3 - p_1 = \frac{\sigma_A \left(1 - \sigma_A\right) G^2}{\rho_s} \tag{3.108}$$

where the slip density is

$$\frac{1}{\rho_s} = \frac{x^2}{\rho_G \alpha} + \frac{\left(1 - x\right)^2}{\rho_L \left(1 - \alpha\right)} \tag{3.109}$$

Here α is void fraction. Lottes (1961) also proposed a simplified model where loss in dynamic pressure in the gas phase is not included:

$$p_3 - p_1 = \sigma_A \left(1 - \sigma_A\right) G^2 \left[\frac{1}{\rho_L \left(1-\alpha\right)^2}\right] \tag{3.110}$$

The model by Attou and Bolle (1997) is based on the momentum balance, where the jet emerging from the sudden expansion is treated as a conical section. For an incompressible flow with constant quality and mean void fraction they got that:

$$p_3 - p_1 = G^2 \sigma_A \left(1 - \sigma_A\right) \left[\Phi\theta^r + \frac{\left(1-\theta^r\right)}{\rho_L}\right] \tag{3.111}$$

where the quantities Φ and θ are defined as

$$\Phi = \frac{x^2}{\alpha\rho_G} + \frac{(1-x)^2}{(1-\alpha)\rho_L} \tag{3.112}$$

$$\theta = \frac{3}{1+\sqrt{\sigma}+\sigma} \tag{3.113}$$

The correction factor r is dependent on the involved fluids and pressures. For air-water mixtures at low qualities and low pressures r is estimated to -7/5.

Chisholm and Sutherland (1969) gives a general procedure for calculating pressure drop in pipeline components. The two-phase pressure drop is given as a function of the single phase liquid flow pressure drop:

$$\frac{\Delta p_{TP}}{\Delta p_L} = 1 + \frac{C}{X} + \frac{1}{X^2} \tag{3.114}$$

where

$$X = \left(\frac{1-x}{x}\right)\sqrt{\frac{\rho_G}{\rho_L}} \tag{3.115}$$

and

$$C = \left[1 + \left(C_2 - 1\right)\left(\frac{\rho_L - \rho_G}{\rho_L}\right)^{0.5}\right]\left(\sqrt{\frac{\rho_L}{\rho_G}} + \sqrt{\frac{\rho_G}{\rho_L}}\right) \tag{3.116}$$

For a pipe enlargement the factor $C_2 = 0.5$. Starting with the momentum equation we have that

$$p_3 - p_1 = \sigma\left(1-\sigma\right) G^2 \left(1-x\right)^2 \left[1 + \frac{C}{X} + \frac{1}{X^2}\right]\frac{1}{\rho_L} \tag{3.117}$$

Wadle (1989) also proposed a model which is not based on the momentum equation. The pressure recovery is here given as a fraction of the reduction in dynamic pressure head:

$$p_3 - p_1 = \left(1 - \sigma^2\right) \frac{G^2}{2} K \left[\frac{x^2}{\rho_G} + \frac{(1-x)^2}{\rho_L}\right] \tag{3.118}$$

The factor K was experimentally found to be 0.83.

Schmidt and Friedel (1996) presented a model for two-phase flow pressure recovery considering also the liquid entrainment in the gas phase:

$$p_3 - p_1 = \frac{G^2 \left[\frac{\sigma_A}{\rho_{eff}} - \frac{\sigma_A^2}{\rho_{eff}} - f_e \rho_{eff} \left(\frac{x}{\rho_G \alpha} - \frac{(1-x)}{\rho_L (1-\alpha)}\right)^2 \left(1 - \sigma_A^{0.5}\right)^2\right]}{1 - \Gamma_e \left(1 - \sigma_A\right)} \tag{3.119}$$

where

$$\frac{1}{\rho_{eff}} = \frac{x^2}{\rho_G \alpha} + \frac{(1-x)^2}{\rho_L (1-\alpha)} + \frac{\alpha_E \rho_L (1-\alpha)}{1-\alpha_E} \left[\frac{x}{\rho_G \alpha} - \frac{1-x}{\rho_L (1-\alpha)}\right]^2 \tag{3.120}$$

$$\alpha = 1 - \frac{2(1-x)^2}{1 - 2x + \sqrt{1 + 4x(1-x)\left(\frac{\rho_L}{\rho_G} - 1\right)}} \tag{3.121}$$

$$\alpha_E = \frac{1}{S}\left[1 - \frac{1-x}{1 - x\left(1 - 0.05 We^{0.27} Re^{0.05}\right)}\right] \tag{3.122}$$

$$S = \frac{x}{1-x} \frac{(1-\alpha)}{\alpha} \frac{\rho_L}{\rho_G} \tag{3.123}$$

$$We = G^2 x^2 \frac{d}{\rho_G \sigma} \frac{(\rho_L - \rho_G)}{\rho_G} \tag{3.124}$$

$$Re = \frac{G(1-x)\,d}{\mu_L} \tag{3.125}$$

$$\Gamma_e = 1 - \sigma_A^{0.25} \tag{3.126}$$

$$f_e = 4.9 \times 10^{-3} x^2 (1-x)^2 \left(\frac{\mu_L}{\mu_G}\right)^{0.7} \tag{3.127}$$

One of the earliest pressure recovery equations is presented by Richardson (1958). He includes only the liquid phase in his equation, modeling the real liquid velocity:

$$p_3 - p_1 = \frac{\sigma_A \left(1-\sigma_A^2\right) G^2}{2\rho_L} \left[\frac{(1-x)^2}{(1-\alpha)}\right] \tag{3.128}$$

Another equation by Delhaye (1981) is also based on the mechanical energy balance, but here the gas phase is included, with slip velocity:

$$p_3 - p_1 = \frac{G^2\left(1-\sigma_A^2\right)}{2} \left[\frac{(1-x)^3}{\rho_L^2 (1-\alpha)^2} + \frac{x^3}{\rho_G^2 \alpha^2}\right] \left[\frac{(1-x)}{\rho_L} + \frac{x}{\rho_G}\right]^{-1} \tag{3.129}$$

In most cases the gas velocity is larger than the liquid velocity, and several models exist for the calculation of the void fraction. The Drift Flux model by Zuber and Findlay (1965) is a well known model for void fraction prediction, and also Wallis (1969) and Ishii (1977) have taken part in its development. The general drift flux void fraction equation is given by

$$\alpha = \frac{x}{\rho_G} \left[C_0 \left(\frac{x}{\rho_G} + \frac{1-x}{\rho_L}\right) + \frac{\bar{U}_{GU}}{G}\right]^{-1} \tag{3.130}$$

where $\bar{U}_{GU}$is the weighed mean drift velocity. For horizontal flow it is given by

$$\bar{U}_{GU} = 1.18 (1-x) \left[\frac{g\sigma(\rho_L - \rho_G)}{\rho_L^2}\right] \tag{3.131}$$

where $C_0 = 1 + c_0 (1-x)$ and $c_0 = 0.12$. This void fraction correlation is recommended by Thome (2014).

A number of void fraction correlations have been evaluated by Dalkilic et al. (2008), and one of the best was that by Thom (1964):

$$\alpha = \frac{\gamma x}{1 + x(\gamma - 1)} \tag{3.132}$$

where

$$\gamma = Z^{1.6}, Z = \left(\frac{\rho_L}{\rho_G}\right)^{0.555} \left(\frac{\mu_G}{\mu_L}\right)^{0.0.111} \tag{3.133}$$

3.3.3 Two-phase pressure loss in singularities

For a singularity in a liquid flow the pressure drop is expressed as

$$\Delta p = K_L \rho_L \frac{v^2}{2} = K_L \frac{G^2}{2\rho_L} \tag{3.134}$$

where K_L is a loss factor. Minor losses in two-phase flow can be predicted in several ways. One option is to use a two-phase pressure drop multiplier from one of the correlations given above. , e.g. from the Chisholm B-correlation. Then we get that

$$\Delta p = \varphi_{FLO}^2 K_L \rho_L \frac{v_{LO}^2}{2} \tag{3.135}$$

where v_{LO} is the velocity if the total mass flow rate was liquid. Chisholm (1983, Table 12.2) gives recommendations for approximate B coefficients for plates, bends, valves etc.

Another possibility is to define an average density ρ_H assuming equal phase velocities. We have that

$$\rho_H = \rho_L (1-\alpha) + \rho_G \alpha \tag{3.136}$$

$$v_H = \frac{\dot{m}_L + \dot{m}_G}{A \rho_H} \tag{3.137}$$

where α is void fraction and A is flow cross-section. The homogeneous void fraction is given by the superficial velocities of gas and liquid as

$$\alpha = \frac{v_{SG}}{v_{SG} + v_{SL}} \tag{3.138}$$

and

$$v_{SG} = \frac{\dot{m}_G}{A \rho_G} \tag{3.139}$$

$$v_{SL} = \frac{\dot{m}_L}{A \rho_L} \tag{3.140}$$

The two-phase pressure drop in a singularity can then be expressed as

$$\Delta p = K_L \rho_H \frac{v_H^2}{2} \tag{3.141}$$

3.4 Two-phase flow in complex geometry

The nature of two-phase flow in pipelines has been studied since the late forties, starting with the work of Lockhart and Martinelli (1949). Two-phase flow in standard singularities has also been studied by a number of authors. Kim et al. (2010) studied two-phase flow in elbows and gives some recommendations for calculation of pressure loss. Alimonti et al. (2010) performed experiments with multiple orifice valves, and correlated multiphase pressure drop with a measured void fraction. However, they did not correlate flow quality and void fraction, and information on slip ratio is therefore missing. Coleman (2004) investigated experimentally the minor losses for contractions in micro tubes with 0.83 *mm* hydraulic diameter. He found the pressure loss to be larger than expected from common correlations, and established a simple mathematical model for the mass flux in the *vena contracta* without taking slip into consideration. Zhuo et al. (2008) also investigated single- and two-phase flow in contractions, and found that introducing a slip-ratio of $S = v_G/v_L = (\rho_L/\rho_G)^{1/3}$ gave predicted pressure drops corresponding to experimental values. Roul and Dash (2011) also performed experiments with abrupt area changes in mini-channels, and concluded that the same slip-ratio applies. In agreement with Schmidt and Friedel (1997) it is observed that a *vena contracta* do not exist in two-phase flow.

There are also some publications on CFD simulation of two-phase flow. Eskin and Deniz (2012) studied experimentally two-phase flow of air and water in a smooth expansion section. It was found that the pressure drop along the pipe and over the expansion was well predicted at lower void fractions. Bubble interaction at higher void fractions could not be simulated with the software.

The shut-in valve provides however an even more complicated geometry that cannot be compared to standard singularities like those mentioned above. Also, the shut-in valve has an internal flow path with a series of minor losses and frictional losses. The increased turbulence created by valve ports etc. can possibly have an impact on following minor losses and frictional losses. Details of the flow path in the shut-in valve are given in Figure 3.7 and Figure 3.8.

From these figures it is clear that the shut-in valve contains a number of different unusual flow cross-sections and minor losses. Two-phase pressure losses in flow geometries like this are not investigated before. Moreover, a method for solving pressure loss problems like this is also missing.

This work has therefore focused on two-phase pressure losses in non-standard geometries where no correlations for neither single-phase nor two-phase pressure loss are available. An experimental research method was applied with focus on the

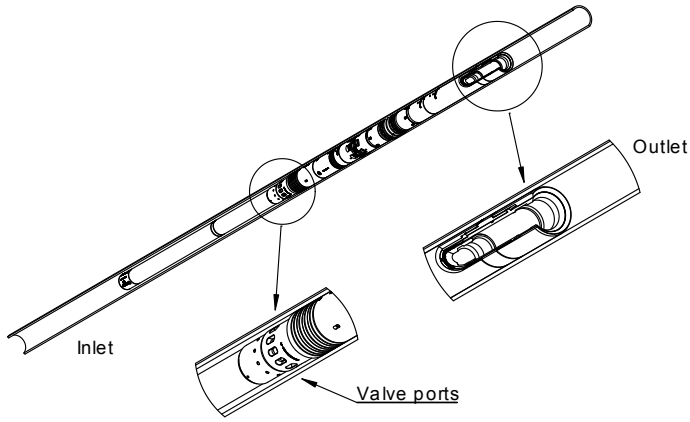

Figure 3.7: The Qinterra STC downhole shut-in valve assembled with packer, shown inside production tubing.

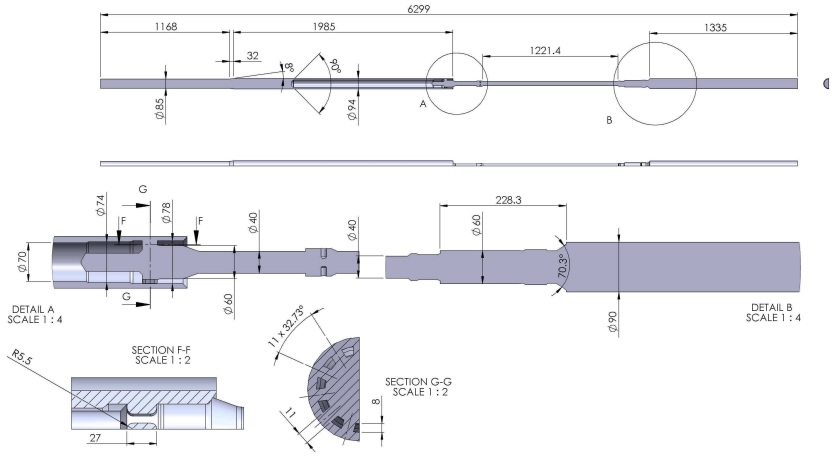

Figure 3.8: Flow path inside shut-in valve.

following research questions:

- How is the pressure drop across this valve type related to two- or three-phase composition?
- How will a downhole valve affect the multiphase flow regime?
- Will the turbulence created inside the complex valve geometry have an impact on e.g. phase inversion and phase distribution?

The first question was found to be the most important one, and the activities have been limited to the two main points from the project description:

1. Experimental two- and three-phase flow of oil, gas and water in downhole valves.
2. Numerical modeling of flow in downhole shut-in valve, based on observed flow regimes and pressure drops.

The following scheme was followed in order to find answers to the research questions:

1. Develop detailed 3-D model of shut-in valve.
2. Perform 3-D CFD simulations for single phase flow.
3. Build full-scale mock-up of shut-in valve.
4. Validate CFD simulations with single phase experiments.
5. Develop and validate 1-D model for single phase flow.
6. Develop and validate 1-D model for two-phase flow.

For the final item, two different methods were tested with respect to two-phase frictional losses. The first was based on flow-pattern independent correlations, and the second was based on mechanistic modeling. The sudden expansion at the valve outlet was found to be particularly important for the overall pressure loss, and a separate article was written about that.

Part II

Experimental work

Chapter 4

Downhole shut-in valves and experimental setup

Shut-in operations can be performed at the well-head or downhole. The benefit of downhole shut-in will here be discussed and some typical downhole shut-in valves are presented. The Qinterra STC shut-in valve has been chosen as a representative valve type and the internal flow-path is described. A laboratory mock-up was built in order to do experiments with single phase and two-phase flow in this valve and the laboratory setup is described here.

4.1 Downhole shut-in

Oil and gas are typically found in rock formations of porous and permeable sandstone. Due to the tiny spaces between the grains of the stone, the flow resistance is considerable. There will therefore be a difference between the average reservoir pressure $\bar{p}$ and the flowing bottomhole pressure p_{wf}, dependent of the flow rate q. Within production testing this pressure difference is called the pressure drawdown. The productivity index PI is defined as

$$PI = \frac{q}{\bar{p} - p_{wf}} \tag{4.1}$$

As can be seen from this equation, the pressure and the flow rate must be measured simultaneously to get a correct value for the productivity index. The shut-in operation should also be performed downhole, in order to avoid problems with the unknown compressibility of the wellbore volume. In Figure 4.1 the use of a downhole shut-in valve is depicted.

In this figure it is indicated that the shut-in valve is run in hole on a drill string,

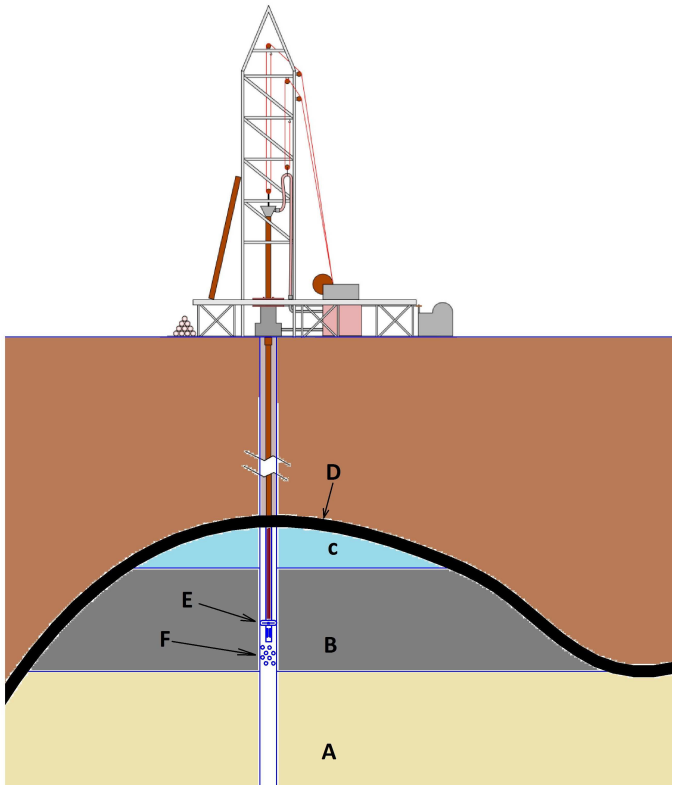

Figure 4.1: Drill rig and well. A: Rock, B: Oil in reservoir formation, C: Gas cap, D: Impermeable caprock, E: Packer with shut-in valve, F: Production tubing perforation

but it is also possible to use wireline. The Qinterra STC shut-in valve is shown in Figure 3.7.

The valve will be in open position when run in hole (placed inside well), and the sliding sleeve valve will close quickly at a predetermined time. Below the valve ports the flow cross-section is annular, and inside the valve ports the flow is led into a narrow channel through the packer section. The packer unit has an outside seal that expands when the packer is "set", forcing the flow through the valve. A pressure-temperature curve from a downhole shut-in test is given in Figure 2.8.

4.2 Shut-in valves

Downhole shut-in valves are available from a number of companies. The Spartek Systems SS3100 and SS3110 are multi-cycle downhole shut-in tools with 1.75” (44.5 *mm*) and 2,5” (63,5 *mm*) outer diameter (Spa 2015). They are electrically operated and have a sliding sleeve type valve. They are designed for differential pressures up to 690 *bar*, see Figure 4.2. The Omega shut-in tools are of a similar

Figure 4.2: Spartek Systems shut-in valves (Spartek Systems).

type with sliding sleeve valve, but are only able to close once (Ome 2015). This tool is offered in sizes from 2" (50,8 *mm*) to 4.3" (109.2 *mm*), see Figure 4.3.

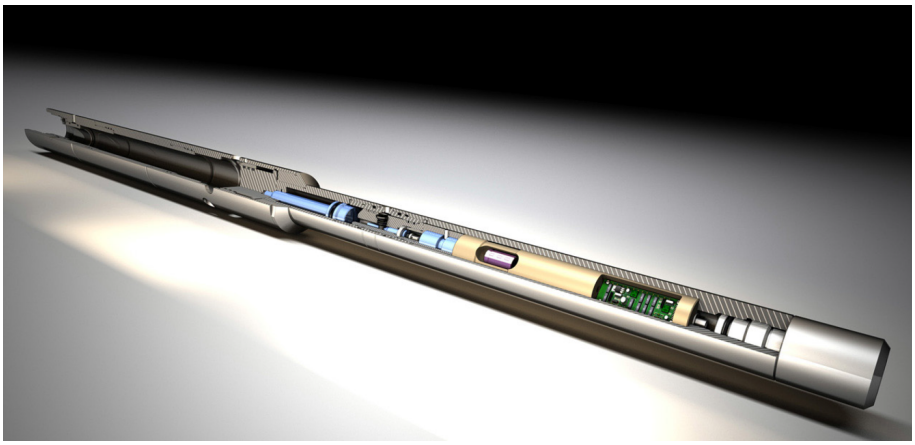

Figure 4.3: Omega shut-in tools (Omega Completion Technology Ltd.).

The Halliburton eRED valve is a similar type of downhole valve, with valve flow ports in the side of the tool. Here a ball valve is used, but the resulting flow path is comparable to the tools with sliding sleeve valve, see Figure 4.4.

Figure 4.4: Halliburton shut-in valve (Halliburton).

The maximum differential pressure for these valves is 400 to 700 *bar*. None of the companies offers pressure drop data for single phase or two-phase flow, and no scientific articles have been found about two-phase flow in such valves. The Qinterra Technologies STC shut-in valve investigated here is shown in Figure 3.7. All these valves are facing the same kind of problem regarding finding two-phase pressure drop.

The co*mm*on problem when modeling two-phase flow in valves is finding a correlation between minor pressure loss factors for single phase flow and for two-phase flow. The special problem for this type of shut-in valve is modeling a series of two-phase minor losses within a short distance. Singularities giving intense turbulence can be expected to have impact on downstream flow pattern and downstream overall friction factor. The degree of such impact is unknown. The annulus type flow cross section around the upstream part is also unco*mm*on and must be modeled. Yet another type of pressure loss is the convective acceleration and deceleration. These depends among others on the effective density, which in turn is a function of the slip velocity. As far as possible, all these pressure losses due to singularities will be expressed in terms of the pressure loss factors derived from CFD simulation of single phase flow.

4.3 The STC shut-in valve

The shut-in valve that has been investigated has a complex inner flow path. The flow cross-sections and the interconnections between them is such that neither the single phase nor the two-phase pressure drop can be determined with analytical methods or correlations. The flow volume across the shut-in valve is shown in Figure 3.8.

The upper part of the figure shows an axial cross-section of the valve as installed in the multiphase laboratory flow loop. At the left side there is a conical expansion from 85 to 94 *mm* diameter due to practical reasons. The first singularity is a kind of inverse contraction to an annulus section. Then there are two annular contractions, where the ring-shaped cross section is reduced. Inner diameter increases from 70 *mm* to 74 *mm*, and from 74 *mm* to 78 *mm*. The next singularity is the deflection of the flow through the valve ports into the valve chamber. From this point the flow cross-sections are circular. The following minor loss is a contraction from 60 *mm* to 40 *mm* diameter. Some distance downstream there is a short section with 50 *mm* diameter where four pins are protruding into the flow. At the outlet there are double expansions: from 40 *mm* to 60 *mm* diameter, and from 60 *mm* to 90 *mm* diameter.

The main goal of this study is to gain knowledge within modeling two-phase flow in complex geometries. Consequently a laboratory mock-up of the shut-in valve was needed for validation of the single-phase and two-phase flow simulations. The details of this mock-up are given in Figure 4.5. In the upper left side of the figure the inlet pipe is shown with a length of 4700 *mm*. The length was chosen in order to allow the flow pattern to stabilize before entering the valve mock-up. The pipe outside the lower valve part was made of transparent polycarbonate in order to be able to observe the flow pattern here. In detail B a 6 *mm* pipe is show that

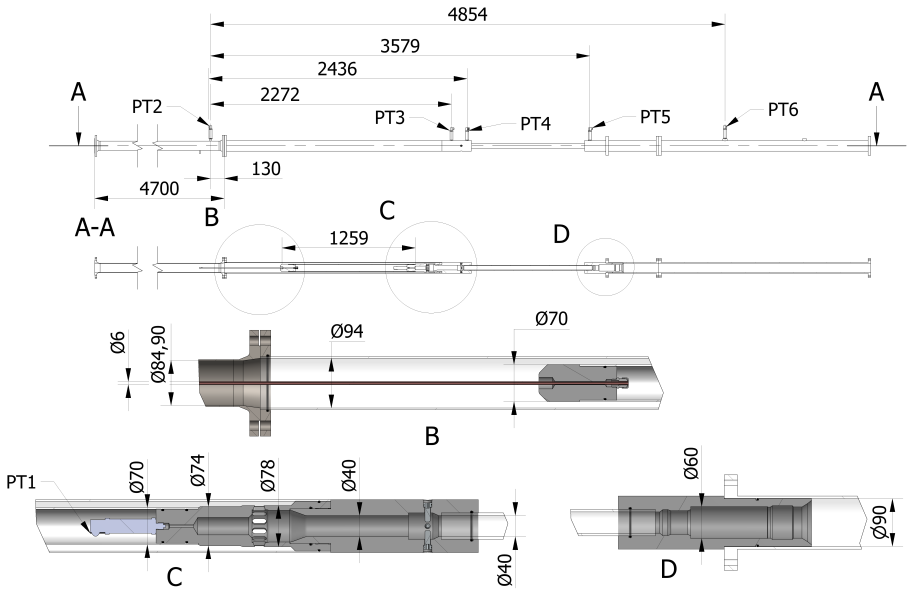

Figure 4.5: Shut-in valve mock-up.

was used for guiding the sensor cables for pressure sensor PT1. Detail C and D shows the valve port section and the outlet section. These parts were made of Polyoxymethylene (POM). The central 40 *mm* pipe was also made of transparent polycarbonate. Figure 4.6 shows a picture of the valve mock-up in the multiphase laboratory. The inlet end is at the left hand side, and the outlet is at the upper right

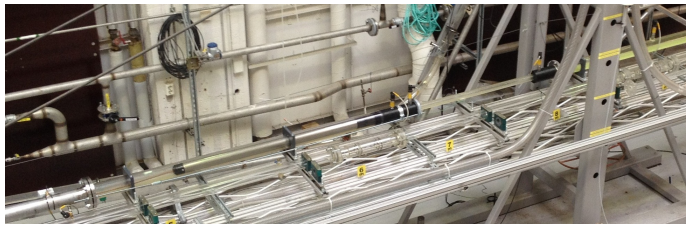

Figure 4.6: Shut-in valve mock-up in multiphase laboratory.

hand side. In Figure 4.7 the valve section is shown filled with green dyed water. The inlet end is shown in Figure 4.8. This end of the shut-in valve was centered inside the tubing with 3 screws, see the left hand side of the picture. Figure 4.9 shows the valve ports. The flow direction is from left to right, and to the left of the valve ports the flow cross-section is ring-shaped. Figure 4.10 shows the 40 *mm* section found inside the packer.

Figure 4.7: Shut-in valve mock-up with green dyed water.

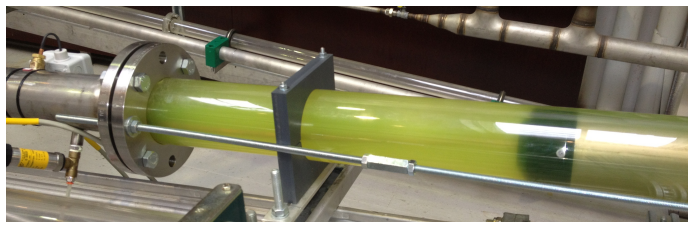

Figure 4.8: Shut-in valve mock-up inlet.

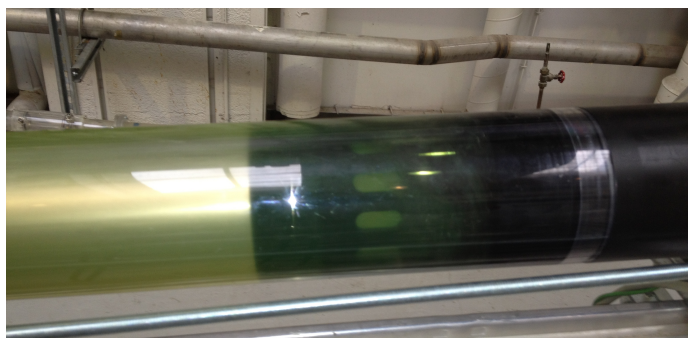

Figure 4.9: Shut-in valve mock-up valve ports.

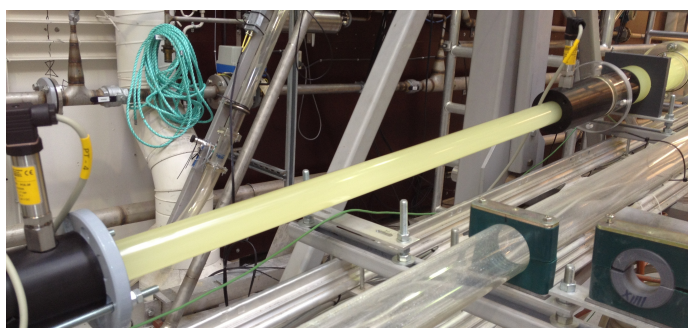

Figure 4.10: 40 *mm* pipe in shut-in valve mock-up.

4.4 Multiphase laboratory and instrumentation

Six pressure sensors were fitted to the shut-in valve mock-up in order to find the partial pressure losses in as much detail as possible. These are identified in the upper part of Figure 4.5. Note that sensor PT1 is placed inside the valve front end, see detail C. The details of the pressure sensors are given in Table 4.1. Sensor PT2

Table 4.1
Pressure sensors.

No.	Range	Uncertainty
PT1	0-6 *bar*	±1.2 *kPa*
PT2	0-6 *bar*	±1.2 *kPa*
PT3	0-6 *bar*	±1.2 *kPa*
PT4	-1/ +1 *bar*	±0.4 *kPa*
PT5	-1/ +1 *bar*	±0.4 *kPa*
PT6	-1/ +1 *bar*	±0.4 *kPa*

at the inlet, PT1 in the valve chamber and PT3 in the center tube had a pressure range of 0 - 600 *kPa*. For sensor PT4 and PT5 along the center tube and PT6 on the outlet tube a range of -100 to +100 *kPa* was chosen, as pressure below atmospheric pressure was expected. All sensors had an accuracy of 0.2% of the full range.

Figure 4.11 shows a simplified diagram of the flow loop in the multiphase laboratory at NTNU. The multiphase flow loop is designed for continuous circulation

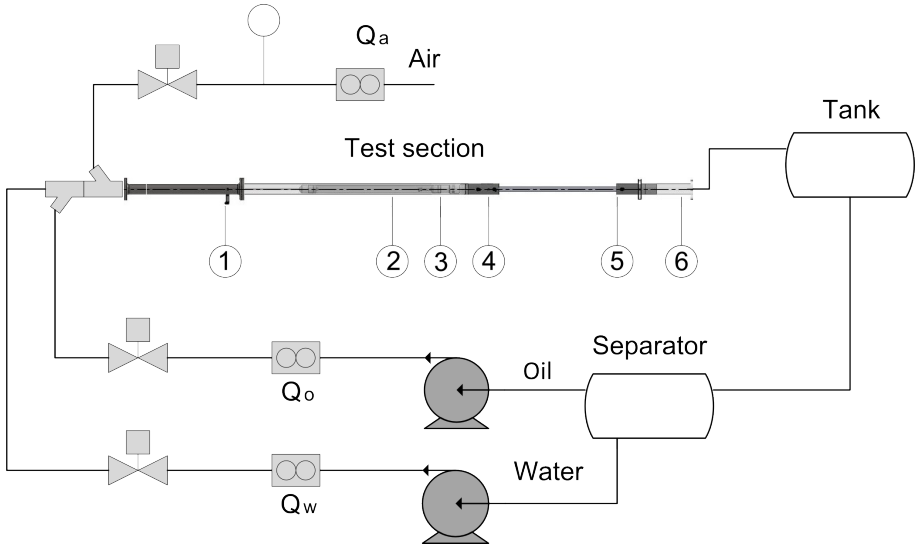

Figure 4.11: Multiphase flow loop at NTNU.

of oil, water and air. At high liquid flow rates however, there is a risk of improper oil-water separation if the test lasts too long. Experiments with high liquid flow rates were therefore limited to a few minutes. Fluids used in the experiments are given in Table 4.2.

Table 4.2
Fluids for two-phase flow test rig.

Fluid	Density, 1 atm, 20°C [kg/m^3]	Viscosity at 20°C [$Pa\text{-}s$]	Surface tension in air [N/m]
Air	1.2	1.79E-05	
Water	998	1.00E-03	7.20E-02
Exxsol D80	798	1.80E-03	2.63E-02

The maximum liquid pumping pressure was approximately 3 *bar* and flow rate was approximately 10 *kg/s* for oil and water, and flow meter details are given in Table 4.3. Air was supplied with a compressor, and maximum air flow rate was 0.33 *kg/s*.

Table 4.3
Flowmeter specifications

Flowmeter	Type	Range	Uncertainty	Repeatability
Air, small	Coriolis	0-0.022 *kg/s*	±0.1% of rate combined	
Air, large	Vortex	0.024-0.612 *kg/s*	±1% of rate	±0.25% of rate
Water	Electromagnetic	10 *kg/s*	±0.5% of rate	±0.15% of rate
Oil	Coriolis, liquid	10 *kg/s*	±0.15% of rate combined	

All signals from pressure sensors and flow meters were logged with a computer. The pressure signals at high speed multiphase flow were fluctuating, and the reported pressures are averages for a period of several seconds. The values for flow and pressure were sampled with a frequency of 5 *kHz*, and average values were logged to a data file 5 times per second.

High speed videos were used in some cases in order to identify the flow pattern. The flow velocity in the 40 *mm* pipe shown in Figure 4.10 was too high for direct observations.

For uncorrelated input quantities the combined uncertainty is

$$u_c^2(y) = \sum_{i=1}^{N} \left(\frac{\partial f}{\partial x_i} \right)^2 u^2(x_i) \tag{4.2}$$

or

$$\left[\frac{u_c(y)}{y} \right]^2 = \sum_{i=1}^{N} \left[p_i u(x_i)/x_i \right]^2 \tag{4.3}$$

where (JGCM/WG1 1995)

$$y = cX_1^{p1}X_2^{p2}....X_N^{pN} \tag{4.4}$$

For a total pressure difference from PT2 to PT6 we have that

$$u_c^2(y) = 1.2^2 + 0.4^2 \tag{4.5}$$

and then the uncertainty is $u_c(y) = \pm 1.3kPa$.

Part III

Modeling and simulation

Chapter 5

Determination of minor loss coefficients

The two-phase flow pressure drop in the shut-in valve will be simulated using a 1-D model. The approach here is to develop this 1-D model by means of CFD simulation of single phase flow in the valve. In this chapter the minor loss coefficients for the singularities will be derived by studying curves for pressure drop along the valve.

5.1 CFD simulation and minor losses

A full 3-dimensional CFD simulation was used as a tool for establishing the minor losses for the 1D model. In order to reduce the computational cost only incompressible simulations were performed, and the governing equations to be solved are the continuity equation:

$$\nabla \cdot (\rho \overline{v}) = 0 \tag{5.1}$$

and the momentum equation:

$$\nabla \cdot (\rho \overline{v}\overline{v}) = -\nabla P + (\mu + \mu_t) \nabla^2 \overline{v} + \rho \overline{g} \tag{5.2}$$

where μ is absolute viscosity and μ_t is turbulent viscosity.

The absolute viscosity of water is dependent on the temperature. It changes from 1.0 *cP* at 20°*C* to 0.5 *cP* at 55°*C*. The maximum possible temperature rise can be calculated from the workflow W_t performed by the flow per mass unit. The maximum pumping pressure available in the laboratory setup is 3 *bar*. For a volume of $0.001m^3$ we get that $W_t = V(P_1 - P_2) = 0.001 * 300000 = 300J/kg$. The specific heat capacity of water at 20°*C* is 4180 $J/kg \cdot K$, and maximum temperature

rise for water flow is therefore $\Delta T = 300/4180 = 0.07K$. Here it is assumed that all workflow is transformed into heat by frictional work on the fluid. The absolute viscosity is therefore regarded to be constant since the temperature change will be very little.

Specific heat capacity for oil type Exxsol D80 has not been found, but for kerosene and light oils the heat capacity is approximately 2000 $J/Kg \cdot K$. With a density of 798 kg/m^3 and a pressure drop of 3 *bar* we get $\Delta T = 300/(2000 * 0.798) = 0.19K$. The possible temperature rise is higher for oil than for water, but it is still very low.

Three different turbulence models were tested: standard $k-\varepsilon$ model, the RNG $k-\varepsilon$ model and the realizable $k-\varepsilon$ model. In the standard semi-empirical 2-equation $k-\varepsilon$ model by Launder and Spalding (1974) , the turbulent viscosity μ_t is given by turbulent kinetic energy k and turbulent dissipation rate ε as $\mu_t = \rho C_\mu \frac{k^2}{\varepsilon}$, where $C_\mu = 0.09$ is a constant. The RNG k-ε turbulence model by Yakhot and Orszag (1986) is derived from the Navier-Stokes equations using the renormalization group theory. The equation for turbulent dissipation rate ε has an extra term for rapidly strained flows, and the effect of swirl on turbulence is added. The Prandtl number in the turbulence transport equation is given by an analytical formula, and the calculation of the effective viscosity is done with respect to both high and low Reynolds numbers. This turbulence model is recommended by Amirante et al. (2006).

In the realizable k-ε model by Shih et al. (1995) , the number C_μ in the equation for turbulent viscosity is a function of the mean strain and rotation rates, the turbulence fields and the angular velocity of the system rotation. This model has been tested and found to perform better than the standard k-ε model in many cases, e.g. channel flow, as demonstrated by Leutwyler and Dalton (2008).

A 3-dimensional model of the flow volume was created with the SOLIDWORKS (Sol 2014) software package and loaded into ANSYS Fluent (ANSYS), and a part of the generated unstructured mesh is shown in Figure 5.1. The design of the mesh is essential in order to get reliable results from the CFD simulations. The main parameters are the number of inflated layers (prismatic boundary layers) and the number of cells across gaps. After a series of experiments it was found that two inflated layers was sufficient together with scalable wall functions. The pressure drop was simulated with high accuracy with at least 6 cells across gaps.

The first part of the simulations was performed on a symmetrical half-section. The mesh was refined until the simulated pressure drop did not change with further refinement. The final mesh had maximum 0.005 *m* cell size, with maximum 0.004

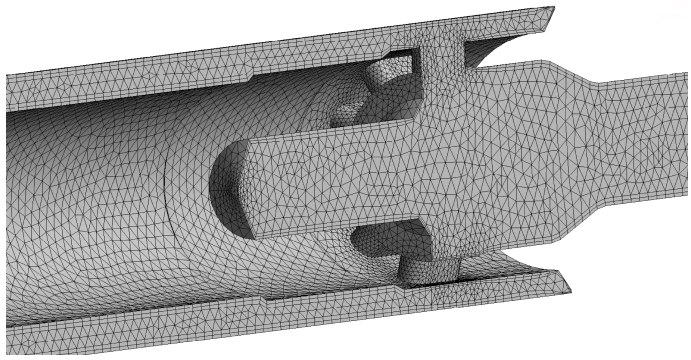

Figure 5.1: Unstructured mesh for CFD simulation.

m face size. As shown on the figure, a mesh with prismatic boundary elements was selected In order to limit the total number of cells, the final mesh had 6 inflated layers, and automatic adjustable wall functions were used. In order to allow for build-up of turbulence, the inlet section was extended 1 m in front of the first pressure sensor. Turbulence intensity at the inlet was set to 5%.

A maximum normalized residual of 10^{-4} was used as convergence criteria for all equations. CFD simulations were also performed on a full cross-section model.

5.2 Results from CFD simulations and determination of minor losses

Simulation results are presented together with experimental results for total pressure loss for water and oil flow in Figure 5.2. These simulations were done on a symmetrical half-section model, using the RNG k-ε turbulence model. For water flow the deviation between simulations and experimental values is 2-3%. For oil flow, the deviation is 4-6% at high flow rates. As the simulated pressures in both cases are so close to the experimental pressure values, the water flow simulations were chosen for calculating representative partial pressure drops inside the STC shut-in valve.

Figure 5.3 shows the flow velocity inside the shut-in valve along a symmetry plane, for a water mass flow of 9.83 *kg/s*. This flow rate corresponds to the maximum flow rate for the laboratory experiments.

From the inlet at the left-hand side we can see that the flow first changes to annular flow, and that the annular cross-section is reduced in two steps towards the valve inlet at detail A. Inside the valve ports there is complicated turbulent flow, and in the right-hand part of detail A we can see the equalizing section. The function of

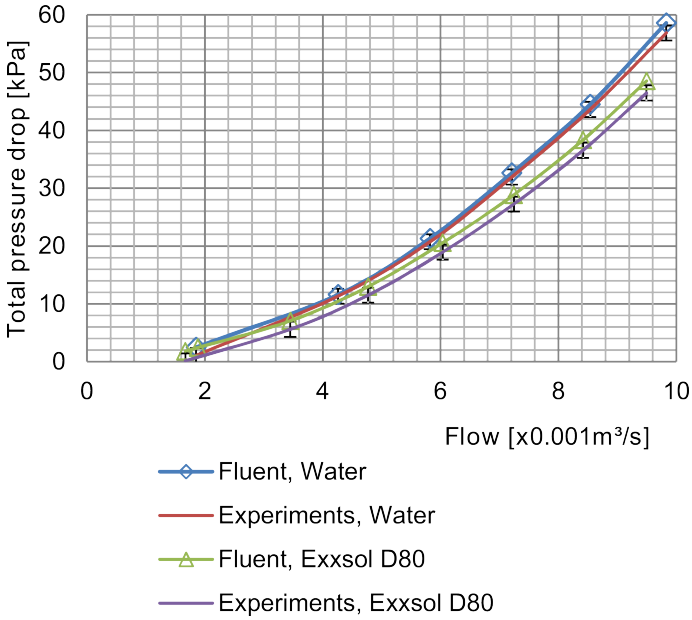

Figure 5.2: CFD simulation results and experimental results for total pressure drop over STC shut-in valve. Error bars of ± 1.3 *kPa* are indicated.

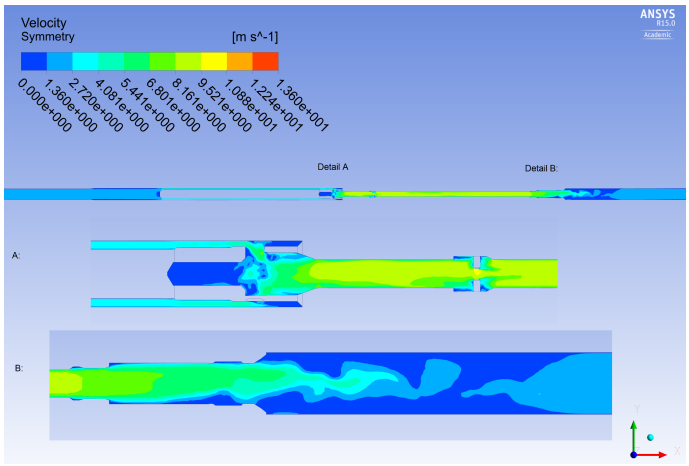

Figure 5.3: Velocity plot of ANSYS CFD simulation for high rate water flow, 9.83 *kg/s*.

this part is connected to the release of a closed valve from the well-bore. Detail B illustrates the outlet at the top of the valve, with a two-step expansion. Above the valve there is a wake section with turbulence which is similar to an oscillating Karman vortex street wake.

The pressures in Figure 5.4 are average pressures over the cross-sections along the valve, calculated with a built-in ANSYS program function. In this figure there are two pressure profiles. One profile is transversal, just upstream of the valve ports. The second profile is along the symmetry plane in the center of the valve. The two pressure profiles have the same pressure color scale.

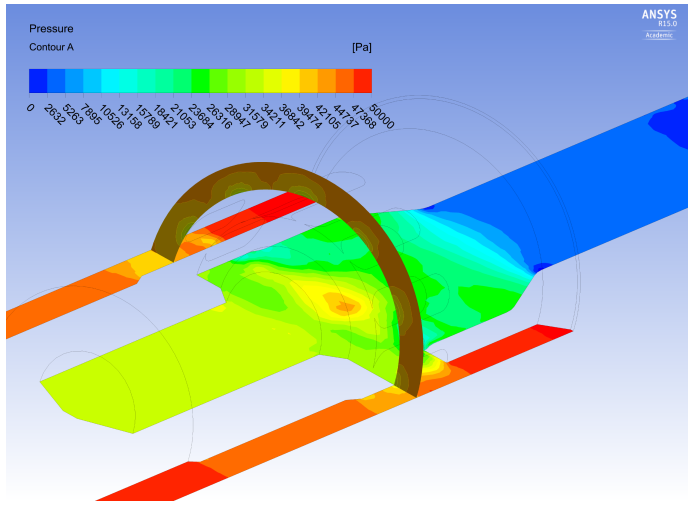

Figure 5.4: Cross-sectional pressure profile at valve ports at high water flow rate.

The pressure profile along the shut-in valve is shown in Figure 5.5 for three different simulation cases. All pressure values are taken from ANSYS cross-section average calculations. Simulations were performed on both symmetrical half-sections and full cross-section.

Several valve features can be observed from the pressure-position curve. The coordinate system used has its origin at 22 *mm* below the valve openings, with lowest valve point at -1.355 *m* and the top outlet at 1.883 *m*. The test section has inlet at -3.08 *m*, and outlet at 3,0 *m*. At -1.91 *m* there is a conical expansion from 84.9 to 94 *mm* diameter due to practical reasons in the laboratory. A small increase in pressure can be observed due to the reduced velocity. Annular flow occurs over the lower section of the valve, and a sudden pressure drop can be observed at the valve nose at -1.35 *m*. At -0.079 *m* there is an annular contraction, with a corresponding pressure drop. Another annular contraction follows at position 0, closely followed

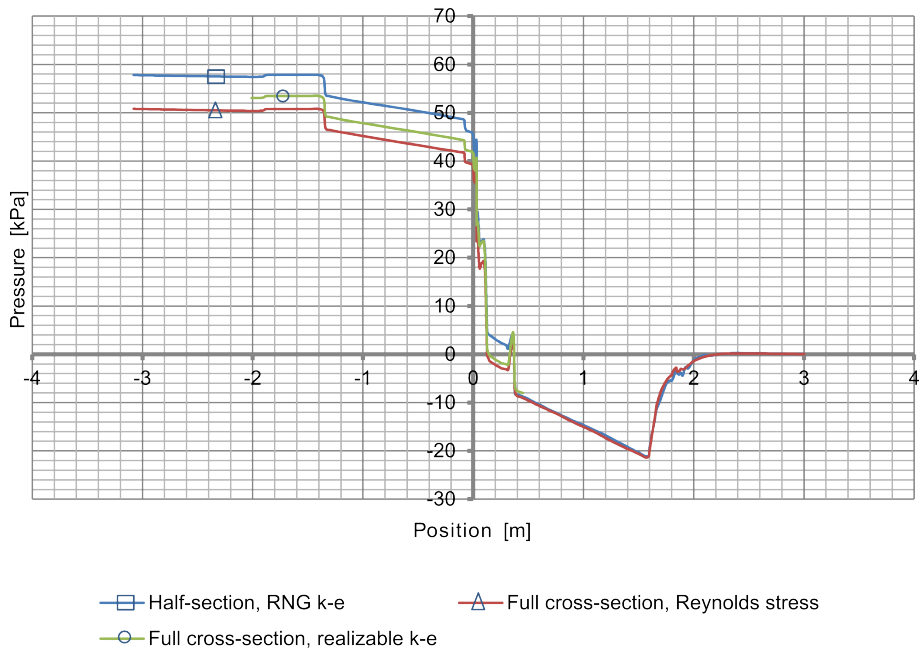

Figure 5.5: Pressure profile along the shut-in valve as simulated with ANSYS Fluent for half-section and full cross-section.

by the valve ports. The flow cross-section of the valve ports is 2981 mm^2, which is a little larger than the narrowest annular section. The outside pressure of 46 *kPa* drops to about 24 *kPa* inside the turbulent valve chamber. As the flow is guided further into the 40 *mm* diameter central section, pressure drops further. An additional pressure drop can be observed across the equalizing central. The outlet expansion section is between 1.595 *m* and 1.883 *m*, but the pressure continues to increase to about position 2.35 *m*. In other words, the pressure increases to a position about 0.45 *m* above the valve outlet, where a fully developed turbulent velocity profile can be expected.

The minor losses for each location along the valve can now be determined from the pressure curve, by applying the following equation:

$$P_1 + \rho\frac{v_1^2}{2} - K_L\rho\frac{v_1^2}{2} = P_2 + \rho\frac{v_2^2}{2} \tag{5.3}$$

The velocities v_1 and v_2 downstream of and upstream the minor loss location are calculated at the same positions as P_1 and P_2. Figure 5.6 shows how the pressure profile curve can be used for the calculation of a minor loss factor at the valve

outlet. As can be seen from Figure 5.3 and Figure 5.5, the two expansions at the outlet must be treated as one single loss factor. There are in fact several diameter changes at the outlet, with distances down to fractions of the local diameter. The expansion occurs between positions 1.595 *m* and 1.883 *m*, and this is marked with dashed lines in Figure 5.6. The linear pressure profile trend downstream of position 2.35 *m* is extrapolated back to the position of the valve outlet. The intersection with the vertical dashed line at position 1.883 *m* will now give the outlet pressure P_2 for calculation of a local minor loss factor. The pressure P_1 is taken from the intersection of the simulated pressure profile and the vertical dashed line at position 1.595 *m*, which is the start of the first expansion.

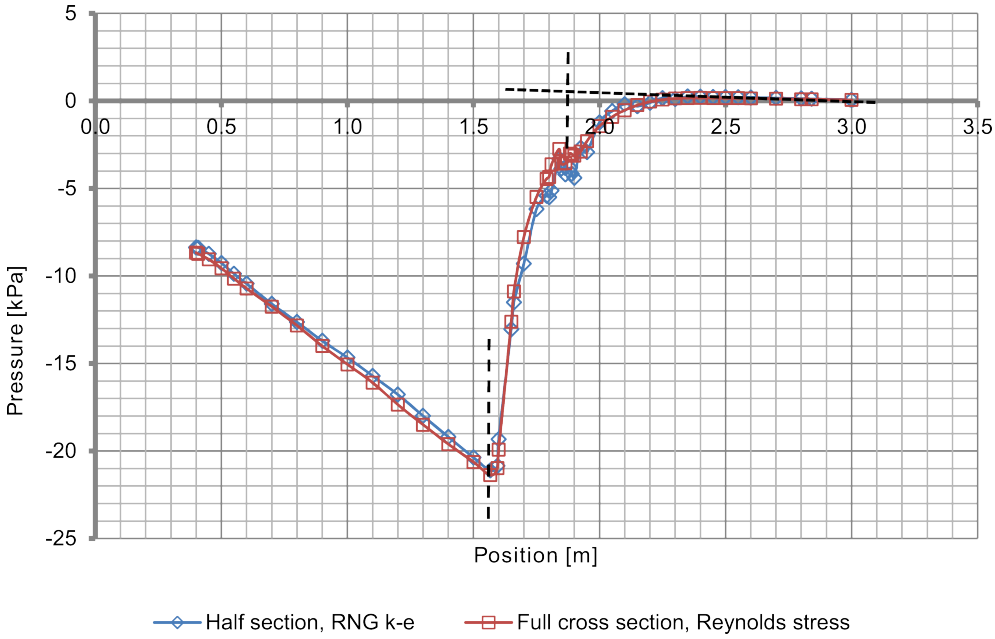

Figure 5.6: Pressure profile and calculation of valve outlet loss factor.

For the inlet expansion at -1.9 *m* from 84.9 *mm* to 94 *mm* diameter, the loss factor from the CFD simulation is calculated to 0.067, and this value is used in the simulations. The next minor loss is at -1.35 *m* with a contraction to an annular section, with 70 *mm* inner diameter, and the minor loss factor is calculated to 0.285. The minor loss factors for the two following annular contractions are calculated in the same manner to respectively 0.037 and 0.044. For the pressure drop across the valve inlet ports, the stagnation pressure P_s, as measured with sensor PT-1, was

used in the following way:

$$P_1 + \rho\frac{v_1^2}{2} - K_L\rho\frac{v_1^2}{2} = P_s \tag{5.4}$$

The valve inlet minor loss coefficient is found to be 1.74. The next change is a contraction from circular flow 60 *mm* to 40 *mm* diameter. As can be seen from detail C in Figure 2.5, there is a well rounded transition at the start and end of this contraction. From the CFD simulation results it can be concluded that the minor loss coefficient here is approximately zero. The reason might be that there is a heavy turbulence right in front of it, and that a contraction will help converting a part of the turbulent energy into kinetic energy in the flow direction.

The equalizing section has a short distance with an increased diameter, and four screws are protruding into the chamber. The minor loss coefficient across it is found to be 0.154. Treated as one single minor loss as described above, the minor loss factor at the valve outlet is found to be 0.255. The complete list of calculated minor loss coefficients K_L is given in Table 5.1.

Table 5.1
Frictional and singular losses in the downhole shut-in valve

No.	Description	Length S [m]	Minor loss coeff.	Hydraulic diameter 1 [m]	Hydraulic diameter 2 [m]	Flow cross-section in [m²]	Flow cross-section out [m²]
1	Friction	0.1		0.085	0.085	5.675E-03	5.675E-03
2	Diffuser, 16°	0.03	0.067	0.085	0.094	5.675E-03	6.940E-03
3	Friction	0.525		0.094	0.094	6.940E-03	6.940E-03
4	Annular contraction, 90°	0.015	0.28	0.094	0.024	6.940E-03	3.091E-03
5	Friction	1.261		0.024	0.024	3.091E-03	3.091E-03
6	Annular contraction, 90°	0.079	0.037	0.024	0.02	3.091E-03	2.639E-03
7	Annular contraction, 90°	0.02	0.044	0.02	0.016	2.639E-03	2.161E-03
8	Valve inlet	0.075	1.74	0.016	0.06	2.161E-03	2.827E-03
9	Contraction, 40°	0.03	0	0.06	0.04	2.827E-03	1.257E-03
10	Friction	0.192		0.04	0.04	1.257E-03	1.257E-03
11	Equalizing central	0.058	0.15	0.04	0.04	1.257E-03	1.257E-03
12	Friction	1.22		0.04	0.04	1.257E-03	1.257E-03
13	Expansion	0.288	0.255	0.04	0.09	1.257E-03	6.362E-03
14	Friction	0.958		0.09	0.09	6.362E-03	6.362E-03
	Total length	4.851					

Chapter 6

Development and verification of 1-D flow model

In this chapter the modeling and numerical study of the shut in valve is presented. The 1-D model of the shut-in valve consists of a row of elements where each element is either a frictional element or a singularity with a minor loss. Pressure losses in frictional elements are calculated by means of a Reynolds number dependent frictional coefficient. Minor pressure losses are calculated from the minor loss factors identified by means of CFD simulations. The 1-D model is simulated using an in-house Least Squares Spectral Element Method solver. The mathematical model is validated with the experimental data sets for single phase flow. The 1-D model will in the following sections be adapted to two-phase flow.

6.1 Mathematical model

For a slab Δx of the flow we have that the shear stress acts on the outer surface, and

$$\rho v \frac{\partial v}{\partial x} \Delta x = -\frac{\partial P}{\partial x} \Delta x - \frac{4}{D_i} \tau_w \Delta x \tag{6.1}$$

where ρ [kg/m^3] is density, v [m/s] is velocity, x [m] is distance along the pipe, P [Pa] is static pressure and D_i [m] is pipe internal diameter. The left hand side here is momentum change caused by convective acceleration. The first term on the right hand side is the derivative of the static pressure along the pipe, and the last term is the pressure loss caused by the shear stress τ_w [N/m^2] along the pipe wall.

There are several changes in cross section along the flow path in the STC shut-in valve, and area changes are approximated as conical sections. The derivative of velocity with respect to distance is therefore

$$\frac{\partial v}{\partial x} = \frac{\partial v}{\partial A}\frac{\partial A}{\partial x} = \frac{\partial}{\partial A}(\frac{\dot{m}}{A\rho})\frac{\partial A}{\partial x} \tag{6.2}$$

$$\frac{\partial v}{\partial x} = -\frac{\dot{m}}{A^2\rho}\frac{\partial A}{\partial x} \tag{6.3}$$

For simulation of compressible flow, the flow is regarded as isothermal. The shear stress along the surface of the slab is

$$\tau_w = f\rho\frac{v^2}{8} \tag{6.4}$$

and we get that the pressure gradient due to frictional losses can be expressed as

$$\frac{\Delta P}{\Delta x} = f\frac{1}{D}\rho\frac{v^2}{2}, \tag{6.5}$$

Here $f = f(R_e, \frac{\epsilon}{D})$ is the Darcy friction factor, $R_e = \frac{\rho v D}{\mu}$ is the Reynolds number, μ [*Pa s*] is dynamic viscosity, ϵ [m] is pipe roughness and D is pipe diameter. The friction factor can be approximated by the formula by Swamee and Jain (1976):

$$f = \frac{0.25}{\left(\log\left(\frac{\varepsilon}{3.7D} + \frac{5.74}{R_e^{0.9}}\right)\right)^2} \tag{6.6}$$

6.2 Least squares spectral element method

The dynamic equations for single phase flow are solved using the least-squares method with spectral element approximation (Proot and Gerritsma 2002). This method has also been used successfully by Chiapero (2013) for simulation of two-phase flow instabilities, and by Sporleder (2011) for simulation of chemical reactors.

The advantages of the least-squares method are low numerical diffusion and generic implementation amongst others, and it involves the minimization of a norm-equivalent functional. Generally we have that

$$L\mathbf{u} = \mathbf{g} \quad in\ \Omega \tag{6.7}$$

$$B\mathbf{u} = \mathbf{h} \quad on\ \partial\Omega \tag{6.8}$$

where Ω and $\partial\Omega$ are the domain and the boundary of the domain respectively. With the requirement that the system is well-posed and that the operators L and B being continuous mappings between the function space $X(\Omega)$ onto the solution space $Y(\Omega) \times Y(\partial\Omega)$, the norm equivalent functional becomes

$$I(u) = \frac{1}{2} \|L\mathbf{u} - \mathbf{g}\|^2_{Y(\Omega)} + \frac{1}{2} \|B\mathbf{u} - \mathbf{h}\|^2_{Y(\partial\Omega)} \tag{6.9}$$

Variational analysis gives that

$$\lim_{\epsilon \to 0} \frac{d}{d\epsilon} I(\mathbf{u} + \epsilon\mathbf{v}) = \mathbf{0} \; \forall \; \mathbf{u} \in \mathbf{X}(\mathbf{\Omega}) \tag{6.10}$$

I can now be minimized with the following necessary condition: Find $\mathbf{u} \in \mathbf{X}(\mathbf{\Omega})$ such that

$$A(\mathbf{u}, \mathbf{v}) = \mathbf{F}(\mathbf{v}) \; \forall \; \mathbf{v} \in \mathbf{X}(\mathbf{\Omega}) \tag{6.11}$$

and

$$\begin{aligned} A(\mathbf{u}, \mathbf{v}) &= \langle L\mathbf{u}, \mathbf{L}\mathbf{v} \rangle_{Y(\Omega)} + \langle B\mathbf{u}, \mathbf{B}\mathbf{v} \rangle_{Y(\partial\Omega)} & (6.12) \\ F(\mathbf{v}) &= \langle \mathbf{g}, \mathbf{L}\mathbf{v} \rangle_{Y(\Omega)} + \langle \mathbf{h}, \mathbf{B}\mathbf{v} \rangle_{Y(\partial\Omega)} & (6.13) \end{aligned}$$

$A : X \times X \rightarrow \mathbf{R}$ is a symmetric, continuous bilinear form. $F : X \rightarrow \mathbf{R}$ is a continuous linear form.

As for finite element formulations, the computational domain Ω is divided into N_e non-overlapping sub-domains Ω_e such that

$$\Omega = \cup_{e=1}^{N_e} \Omega_e \; with \; \Omega_e \cap \Omega_k = \emptyset, \; e \neq k \tag{6.14}$$

The unknown function u_h^e is approximated in each element Ω_e by the set of all polynomials P_Q of degree $\leq Q$. The global approximation u_h in Ω is

$$u_h = \cup_{e=1}^{N_e} u_h^e \tag{6.15}$$

Within each element, the solution is expanded in Φ_i basis functions

$$u_h^e(x) = \sum_{n=0}^{i} u_n^e \Phi_i(\xi) \tag{6.16}$$

with $(\xi) = X_e^{-1}(x)$ th local coordinate of (x) in the parent element, with $-1 \leq \xi \leq 1$, and u_h^e the coefficients in the expansion. This method requires linear equations, and the term $v\frac{\partial v}{\partial x}$ can be linearized using Newton-Raphson linearizion. With k defining the step in an iteration we have that

$$u_{k+1} = u_k + \delta u \tag{6.17}$$

$$u\frac{\partial u}{\partial x} = (u_k + \delta u)\left(\frac{\partial u_k}{\partial x} + \frac{\partial \delta u}{\partial x}\right) \tag{6.18}$$

$$u\frac{\partial u}{\partial x} \approx u_k\frac{\partial u_{k+1}}{\partial x} + u_{k+1}\frac{\partial u_k}{\partial x} - u_k\frac{\partial u_k}{\partial x} \tag{6.19}$$

Here step k is the known value from the previous iteration step, and $k+1$ is the new value.

The flow volume around and through the shut-in valve is depicted in Figure 6.1. For the purpose of a finite element simulation of the flow, the whole shut-in valve is divided into discrete elements. Detail A in Figure 6.1 gives example of how the valve is divided into 1-D elements.

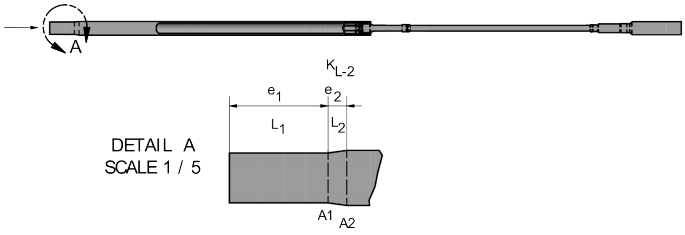

Figure 6.1: Flow volume around and through the shut-in valve, with indication of finite element representation.

This is the inlet section, showing a cylindrical section and a concentric expansion. The latter has also a loss factor, indicated as K_{L-2}. Straight sections are divided into several elements. The total test section length of 4.851 *m* was divided into a total of 79 elements, with element lengths between 0.033 *m* and 0.074 *m*. For the laboratory experiments, the outlet pressure was constant and equal to atmospheric

pressure. The mass flow and outlet pressure were therefore chosen as boundary conditions for the simulations. The spectral element method is a higher order method, and the order O is given as $O = P - 1$, where P is number of nodes per element including end nodes. Refinement tests were run with different orders, and the final simulations were performed with P=6 nodes per element. The following information is provided for each element, see Table 5.1:

Type Frictional or minor loss type. This parameter is read and interpreted by the computer program. The set of equations to be used will depend on the element type.

Length Length of element.

Inlet hydraulic diameter Calculated from $D_h = 4A/p$, where A is flow cross-section and p is perimeter. For annular flow. $D_h = D_{outer} - D_{inner}$

Outlet hydraulic diameter Calculated as above.

Inlet flow cross section This area is calculated, as the flow cross-section is not circular everywhere.

Outlet flow cross section Calculated for circular and annular sections.

Minor loss coefficient This value will be given only for elements of type "minor".

The details of the implementation of the method can be found in Sporleder (2011).

6.2.1 Numerical solution of 1-D model

The calculation of total pressure drop with the 1-D model was accomplished as an iteration for one element at a time, with frictional and minor losses as given by Table 5.1. As explained above, the least-squares method with spectral elements was used. Spectral elements are higher order elements, with internal nodes. The solution for each element will therefore be a column vector with pressure at each node in the element. The set of equations given above can now be formulated as $L\mathbf{u}= \mathbf{g}$ in Ω . The linear partial differential operator is

$$L = \left\{ \frac{\partial}{\partial x} \right\} \tag{6.20}$$

and

$$L\mathbf{u} = v_k \frac{\partial v_{k+1}}{\partial x} + v_{k+1} \frac{\partial v_k}{\partial x} + \frac{\partial P}{\partial x} \tag{6.21}$$

$$\mathbf{g} = -\frac{4}{D_i}\tau_w + v_k \frac{\partial v_k}{\partial x} \tag{6.22}$$

When solving for the pressure P we get that

$$\frac{\partial P}{\partial x} = -v_k \frac{\partial v_{k+1}}{\partial x} - v_{k+1} \frac{\partial v_k}{\partial x} - \frac{4}{D_i}\tau_w + v_k \frac{\partial v_k}{\partial x} \tag{6.23}$$

For minor pressure losses we have that

$$\mathbf{g} = -\frac{1}{\partial x} K_L \rho \frac{v^2}{2} + v_k \frac{\partial v_k}{\partial x} \tag{6.24}$$

The last term in the expression for g comes from the linearization of $v\frac{\partial v}{\partial x}$, and as given above we have that $\frac{\partial v}{\partial x} = -\frac{\dot{m}}{A^2\rho}\frac{\partial A}{\partial x}$.

The density ρ is calculated from a thermodynamic law in each iteration step and for each of the nodes inside the element. It is assumed that the temperature is constant and the velocities are then calculated from the updated densities. The simulations will be compared to laboratory experimental results, where the valve outlet is at atmospheric pressure. Consequently, the outlet pressure will be specified and the element pressures will be calculated counter current from outlet to inlet. A solution algorithm is given in Figure 6.2.

The 1-D model is applicable to compressible flow of air as well, as the density ρ is recalculated at each iteration step. The error evaluated in the decision step is in fact the change in calculated pressure. If the calculated pressure changes more than a decided limit, a new iteration loop is done, with recalculated pressure based upon updated density, velocity and friction factor.

6.3 Verification

The numerical accuracy of the 1-D model will here be verified. An incompressible liquid flow in a conical contraction is used as a suitable case as the non-linear pressure drop can be calculated analytically. Figure 6.3 shows an example of flow in a conical section.

If the flow is without friction the pressure drop is only due to convective acceleration:

$$\frac{\partial P}{\partial x} = -\rho v \frac{\partial v}{\partial x} \tag{6.25}$$

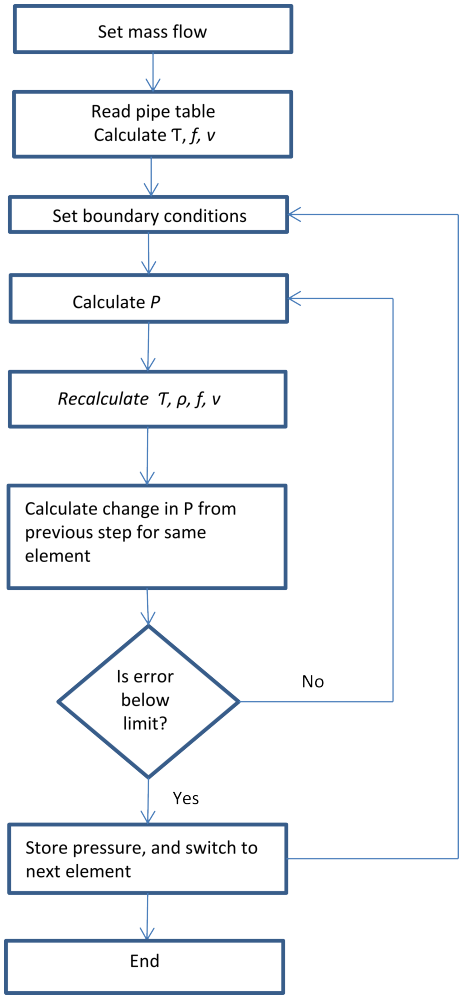

Figure 6.2: Solution algorithm for single-phase liquid flow.

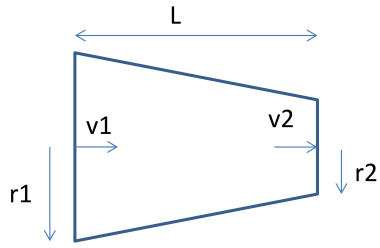

Figure 6.3: Flow in conical section.

By integrating we get the Bernoulli equation:

$$P_1 - P_2 = \rho/2 \left(v_2^2 - v_1^2\right) \tag{6.26}$$

The flow of water in a 1 *m* long section with 0.2 *m* inlet diameter and 0.1 *m* outlet diameter was simulated using the 1-D model. The simulated outlet pressure $P2_{sim}$ was compared to the analytical value $P2_{an}$, and the relative error err_{rel} was calculated as

$$err_{rel} = \frac{P2_{sim} - P2_{an}}{P2_{an}} \tag{6.27}$$

The relative error is given as function of number of elements in Figure 6.4 and we can see that the simulation is converging algebraically. The approximation order here is 3 (4 nodes per element). The relative error is given as function of approximation order in Figure 6.5 and here the simulations are converging exponentially as expected. In this case the model has 10 elements.

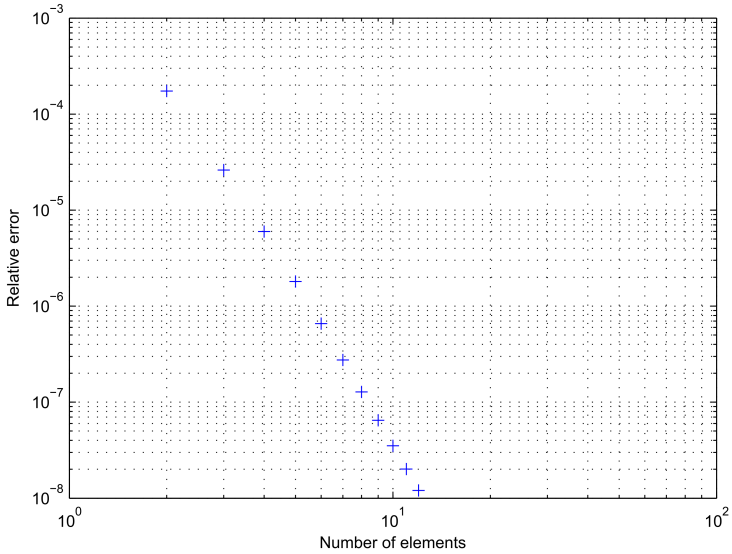

Figure 6.4: Relative error vs. number of elements.

6.4 Validation

A theoretical example of Fanno flow in a pipe is used for validating the 1-D model. Fanno flow is compressible flow with friction in a constant cross-sectional area duct. Here we have for the thermal energy that

$$c_p \frac{dT}{dx} + v \frac{dv}{dx} = 0 \tag{6.28}$$

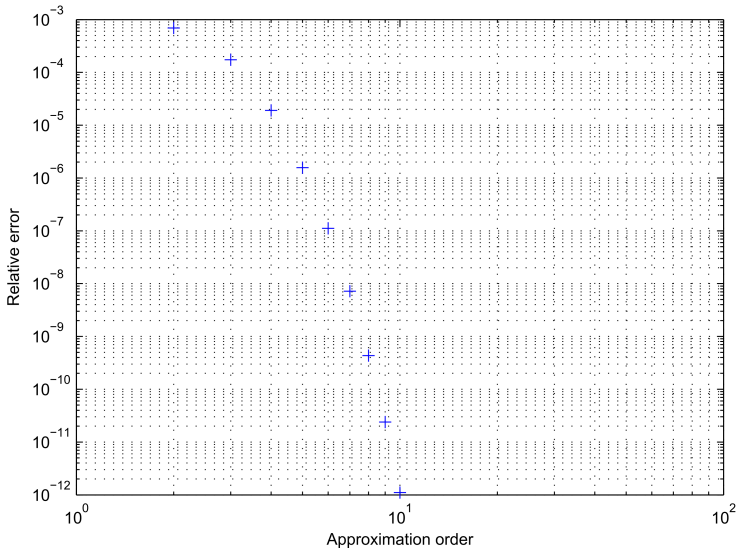

Figure 6.5: Relative error vs. approximation order.

where c_p is heat capacity at constant pressure, T is temperature $[K]$ and v is velocity. For an ideal gas we also have that

$$P = \rho RT \tag{6.29}$$

The motivation for this choice is that the pressure drop along the pipe is not linear. Using the 1-D model the calculated pressure drop over the pipe should therefore converge to some value as the number of elements increases. This kind of flow can be calculated analytically and will therefore also provide a check of the accuracy of the simulations with the 1-D model. This example also demonstrates the pressure drop difference between the analytical solution with temperature change and the 1-D model with constant temperature.

Figure 6.6 shows the dimensions chosen as an example of Fanno flow of air in a pipe. The pipe is 15 *m* long and the diameter is 0.1 *m*. At an imagined length of 20 *m* the flow is choked.

According to Munson et al. (2006, chapter 11.5) the Mach-number at the distance Δx from the imagined choked outlet can be calculated as follows:

$$\frac{1}{k}\frac{(1-Ma^2)}{Ma^2} + \frac{k+1}{2k} ln\left[\frac{[(k+1)/2]\,Ma^2}{1+[(k-1)/2]\,Ma^2}\right] = \frac{f\Delta x}{d} \tag{6.30}$$

where ratio of specific heat capacities at constant pressure and constant volume is $k = \frac{c_p}{c_v} = 1.4$, $f = 0.02$ is the friction coefficient and d is the pipe diameter. The

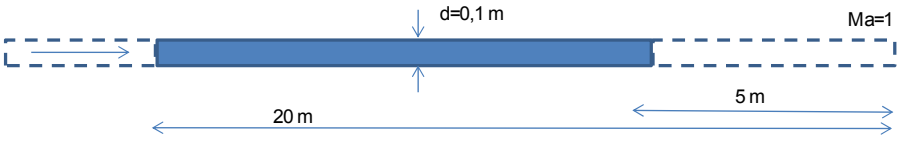

Figure 6.6: Fanno flow example.

friction coefficient is here set to be constant for the whole pipe. With the Mach-number calculated from the above given equation the ratio of pressure p at distance Δx over the pressure p^* at the exit is

$$\frac{p}{p^*} = \frac{1}{Ma}\left[\frac{(k+1)/2}{1+[(k-1)/2]\,Ma^2}\right]^{1/2} \tag{6.31}$$

The exit pressure at choked flow (*Ma*=1) is here set to 101 *kPa*≈1 *atm*. The ratio of temperature T [*K*] at distance Δx over the temperature T^* at the exit is

$$\frac{T}{T^*} = \frac{(k+1)/2}{1+[(k-1)/2]\,Ma^2} \tag{6.32}$$

The density ratio for the same positions is

$$\frac{\rho}{\rho^*} = \left[\frac{1+[(k-1)/2]\,Ma^2}{[(k+1)/2]\,Ma^2}\right]^{1/2} \tag{6.33}$$

For an ideal gas we also have that the velocity of sound is

$$c = \sqrt{RTk} \tag{6.34}$$

where $R = 287[J/Kg \cdot K]$ is the gas constant for air. The mass flow has been calculated to $3.52kg/s$ from the data and equations given above. The pressures, temperatures and velocities at the different sections are given in Table 6.1.

Table 6.1
Fanno flow in pipe.

	Dx=20 *m*	Dx=5 *m*	Exit, choked
Pressure [*Pa*]	330830	212890	101000
Temp [*K*]	298.2	289.6	253
Ma	0.3314	0.508	1
Velocity [*m/s*]	115.1	173.7	318.8

These data will now be used in order to validate the 1-D least squares spectral element model. From Table 6.1 we can see that the pressure is dropping from 3.31 to 2.13 bar and the temperature drops from 298.2 K to 298.6 K. The 1-D model calculates the pressure drop at constant temperature and this will cause a little

deviation. As the 1-D model calculates the flow with constant properties between the nodes the calculated pressure difference should converge to some value as the number of elements or nodes increases.

For the present verification test case the 1-D model uses the pressure at $x = 5m$ as the boundary condition. The Darcy friction factor is set to 0.02 as for the analytical calculation. The simulated pressure at $x = 20m$ is given in Figure 6.7 for different numbers of elements along the 15 m long pipe. Results are given for both first order and second order elements.

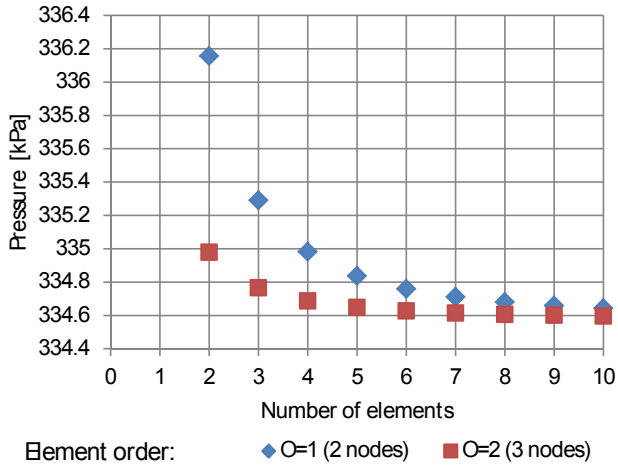

Figure 6.7: Convergence plot for simulated start pressure for Fanno flow example.

The figure shows that the simulations converges toward a pressure of 334.6 *kPa* with 10 first order elements. The same value is achieved with only 6 second order elements. The simulated pressure is only 1.1% higher than the pressure of 330.8 *kPa* from the analytical calculation.

6.4.1 Single-phase flow calibration

The single-phase pressure drop in a straight section between pressure sensors PT-4 and PT-5 on the mock-up was used for single-phase flow calibration, see Figure 6.8. The tube has 40 *mm* inside diameter and smooth surface, and it is made of PMMA (Polymethyl methacrylate, or acrylic glass). With an estimated roughness of ϵ =0.004·10^{-3} *m*, we have that D_h/ϵ=10000.

The experimental friction factor is compared with the well-known Colebrook cor-

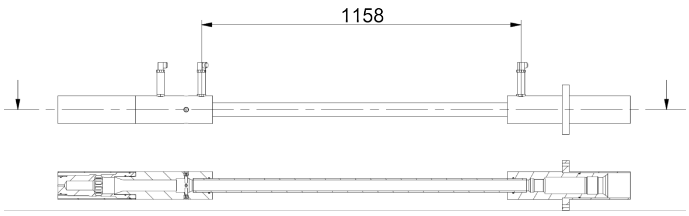

Figure 6.8: Central straight section of shut-in valve mock-up used for flow calibration.

relation.

$$\frac{1}{\sqrt{f}} = -2\log\left(\frac{2.51}{Re\sqrt{f}} + \frac{\epsilon}{3.7D_h}\right) \tag{6.35}$$

The experimental friction factor can be calculated from the following relation:

$$\begin{aligned} \Delta p &= f\frac{l}{D_h}\rho\frac{v^2}{2} \\ &\Updownarrow \\ f &= \frac{2D_h\Delta p}{\rho l v^2} \end{aligned}$$

Calibration tests were done with Reynolds numbers from 135600 to 312900 for water, and with Reynolds numbers from 23500 to 133990 for oil. The results are given in Figure 6.9 and Figure 6.10.

The uncertainty in friction factor measurement depends on the flow rate. At low flow rates, e.g. 2 *kg/s*, with about 3 *kPa* pressure drop the combined uncertainty is $\frac{u_c(y)}{y} = \sqrt{\left(-2\frac{0.005*10}{2}\right)^2 + \left(\frac{1.3}{3}\right)^2} = 44\%$, assuming there is no uncertainty in diameter measurement for the valve inlet. At high flow rates it is typically $\frac{u_c(y)}{y} = \sqrt{\left(-2\frac{0.005*10}{10}\right)^2 + \left(\frac{1.3}{55}\right)^2} = 2.6\%$ As can be seen from Figure 6.9 and 6.10, the experimental friction factor is about 10-20% higher than the theoretical values for both oil and water. Oil flow tests were done with flow rates from 1.67 to 9.5 *kg/s*, and water flow tests with rates from 4.26 to 9.83 *kg/s*.

For the tests with water at low flow rates (low Reynolds numbers), experimental friction factors were more than 20% higher than the Colebrook correlation theoretical values. The main part of the friction factor uncertainty comes from the relative uncertainty in the measurement of the pressure. For the lowest flow rates the pressure at the sensor location might be disturbed due to the contraction upstream, as

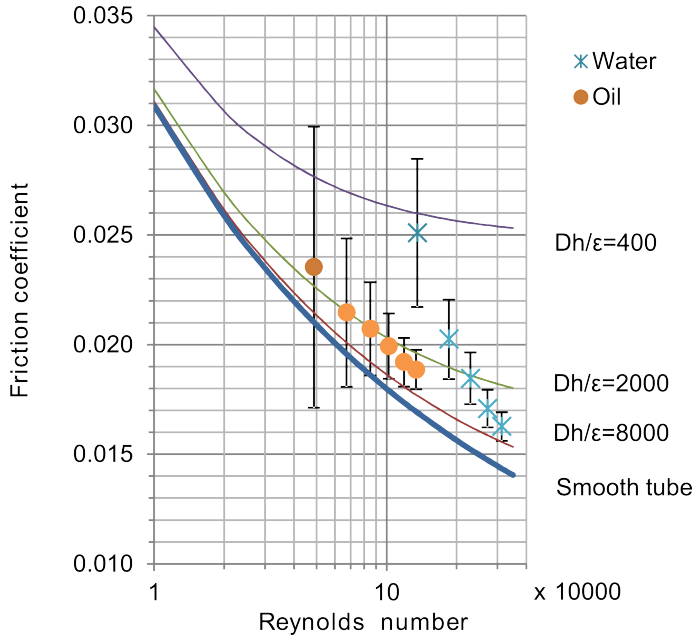

Figure 6.9: Experimental friction factor compared to the Colebrook correlation.

depicted in Figure 6.11. The pressure sensor tap is only 35 *mm* downstream a 50^o conical contraction. A reduction in effective flow area (vena contracta) can be expected, giving a reduced pressure where the pressure sensor is located. For low flow rates and low overall pressure drop, a small addition to the pressure drop will have a huge impact on the calculated friction factor. For oil flow, the higher viscosity is believed to reduce the effect of flow contraction behind the conical contraction.

6.4.2 Single-phase flow study - Water

The experimental pressure drop for single-phase flow of water is presented in Figure 6.12, together with (3-D) CFD simulated pressure drop and the 1-D model simulation. The curves reveal first of all that the pressure drop from the CFD simulation of incompressible liquid flow is very close to the experimental values. The deviation is -6.1% for the highest flow rate. This CFD simulation was performed with a full cross-section 3-D model and the realizable k-ε turbulence model.

Second, the curves show that the 1-D model also predicts the pressure loss quite accurately. The friction factor used in all MATLAB simulations was calculated with the Haaland equation, with an extra 10% due to the results from the calibration tests, see Figure 6.10. The deviation is -0.6 *kPa*, or -1.2% at the highest flow rate.

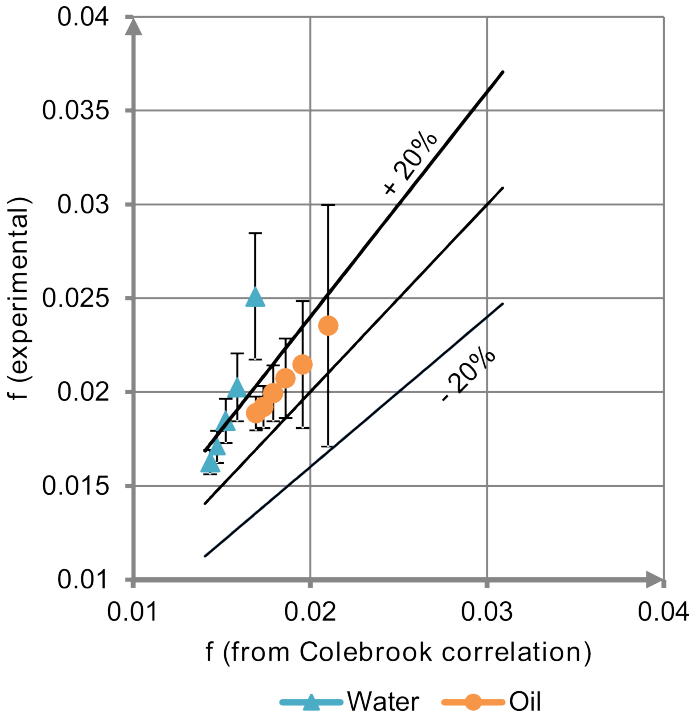

Figure 6.10: Comparison of experimental friction factor with result from the Colebrook correlation.

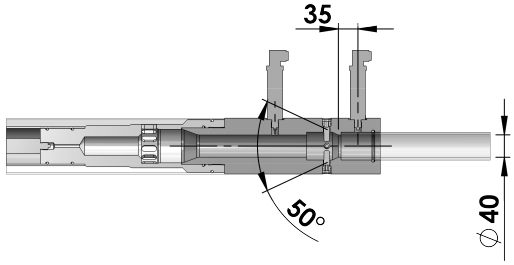

Figure 6.11: Internal details of STC shut-in valve.

The deviation is therefore of the same order as the measurement uncertainty of $\pm 1.3\ kPa$.

The procedure used for deriving the minor loss factors from the CFD simulations must therefore be correct, and the 1-D model as such is also working satisfyingly for liquid flow. The small deviation between the CFD simulation and the 1-D model might partly be due to the increased frictional coefficient.

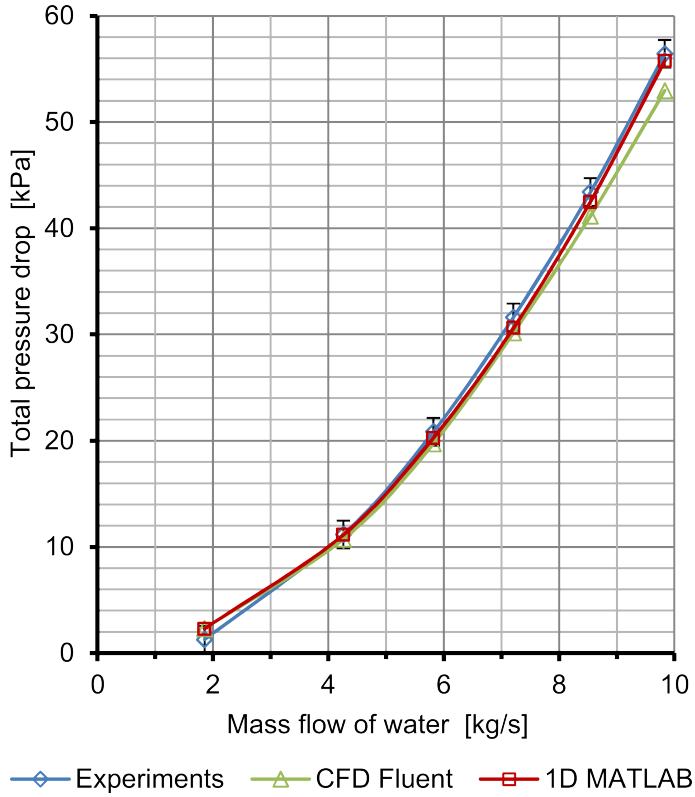

Figure 6.12: Experimental water flow pressure drop compared to CFD simulation and 1-D MATLAB model.

In Figure 6.13 the experimental pressure profile along the STC shut-in valve mock-up is shown together with simulation results from ANSYS Fluent and 1-D simulation results from MATLAB. The water flow rate is 9.83 *kg/s*. These curves are only correct at the sensor positions 1-6, and are only sketchy between these points.

Although the overall pressure loss is simulated with high accuracy, there are some small internal inaccuracies for both the CFD and the MATLAB 1-D simulations.

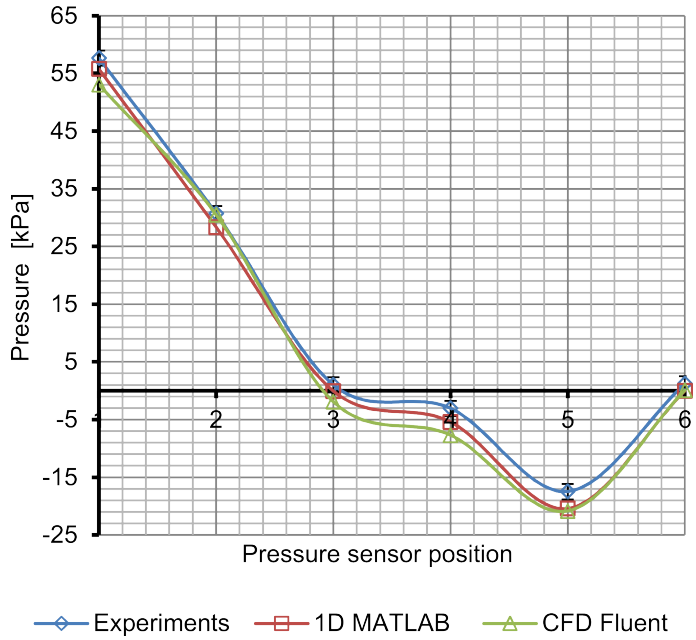

Figure 6.13: Pressure drop along the STC shut-in valve for a water-flow of 9.83 *kg/s*. Water flow experimental results compared to 3-D CFD full cross-section simulations and 1-D simulations. Measurement error bars of $\pm 1.3kPa$ indicated.

Between sensor PT3 and sensor PT4 the experimental results found a lower pressure drop. It is therefore believed that the complex flow geometry in the central part is not completely recreated with the CFD model. An even finer mesh resolution or some tuned turbulence parameters would probably be the solution.

The initial CFD simulations were performed on a 3-dimensional symmetrical half-section of the valve, but the simulated pressure drop across the equalizing section between PT3 and PT4 was much higher than the experimental value. A change to simulations on a 3-D model with full cross-section improved the results. The new model had about 3.3 million elements. Different turbulence models were also tested. Using the realizable $k-\varepsilon$ model (Shih et al. 1995) gave an overall pressure drop closer to experimental values than the $k-\varepsilon$ model and the Reynolds stress model. Figure 6.13 shows the results from the final CFD simulations with realizable $k-\varepsilon$ turbulence model on the full cross-section model.

6.4.3 Single-phase flow study - Oil type Exxsol D80

Experiments and 1-D simulations with oil type Exxsol D80 found the same trend as with water, see Figure 6.14. Here the pressure drop is over-predicted at low flow rates, and under-predicted by 2.3 *kPa* or 5% at the highest flow rate. The pressure

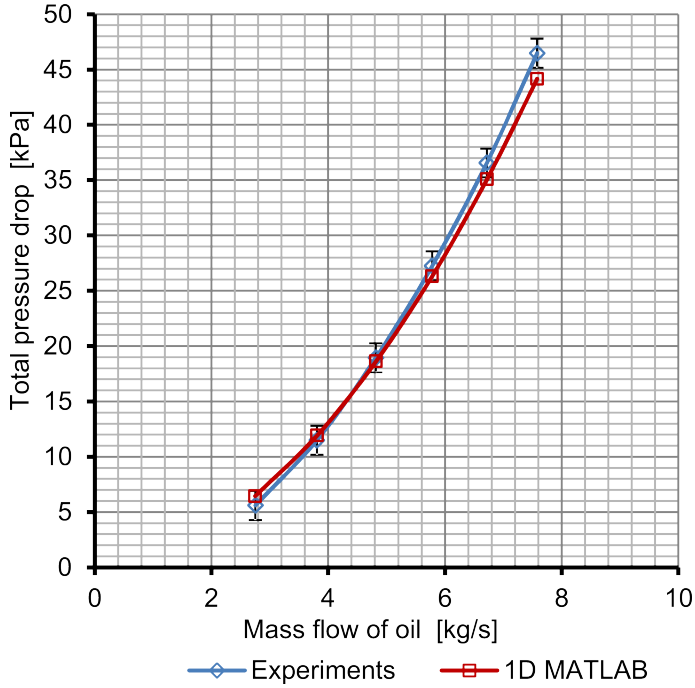

Figure 6.14: Experimental oil flow pressure drop compared to 1-D MATLAB model.

profile along the valve for Exxsol D80 is shown in Figure 6.15, and it reveals some interesting details. For the first part from the inlet to the valve chamber (PT1) the experimental pressure drop is a little higher than the 1-D MATLAB simulated value. One explanation might be that small amounts of water were mixed into the oil causing the viscosity to increase. The pressure drop from PT1 to PT3 is however lowest for the experimental value, and here the minor loss factor for the 40° contraction is found to be zero. This shows that the pressure drop across the valve ports from the MATLAB 1-D model is too low, or that the annular section in front of the valve ports creates a higher pressure drop than expected with oil flow.

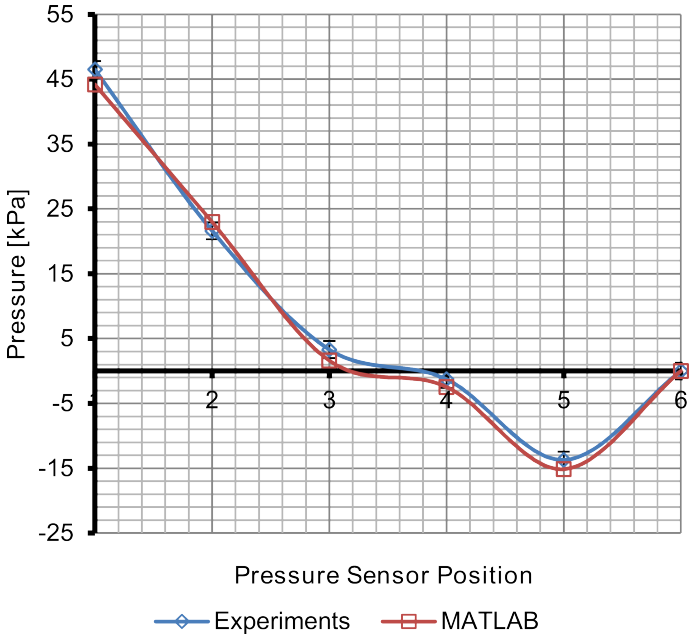

Figure 6.15: Pressure drop along the STC shut-in valve for an oil-flow of 7.45 *kg/s*. Oil flow experimental results compared to 1-D simulations. Measurement error bars of $\pm 1.3kPa$ indicated.

6.4.4 Single-phase flow study - Air

The 1-D flow model that is developed here will be used also for compressible two-phase flow, and it is therefore necessary to validate it for compressible flow of air. For experiments with air flow, the total pressure drop between sensors PT2 and PT6 was measured with a 0-100 *kPa* differential pressure transmitter, and the pressure drop from PT4 to PT5 was measured with a 0-10 *kPa* differential pressure transmitter. The first one had an accuracy of 0.5%, and the second one an accuracy of 1%.

The simulated pressure drop for airflow is shown together with the experimental results in Figure 6.16.

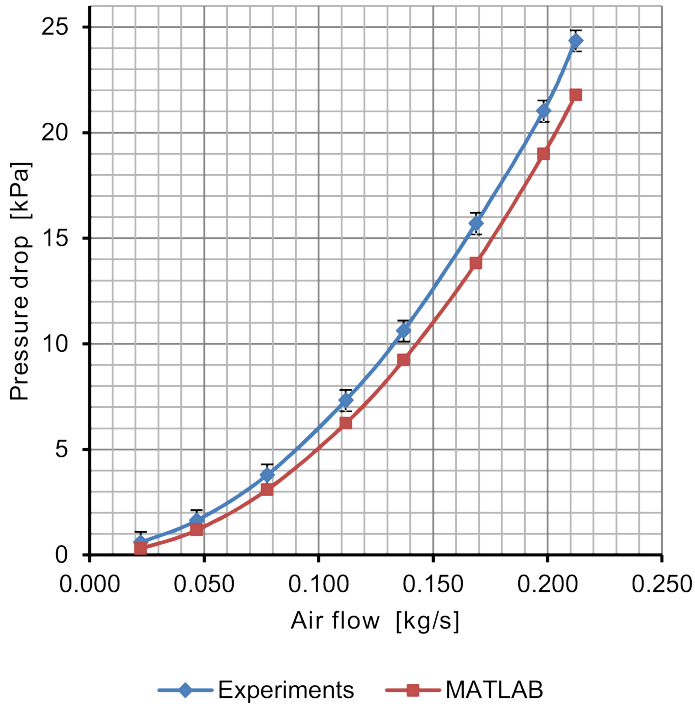

Figure 6.16: 1-D model simulated total pressure drop for airflow.

Experiments with the full-scale valve mock-up gave a total pressure drop of 24.4 *kPa* at maximum air flow rate of 0.212 *kg/s*. The 1-D model under-predict the pressure drop by 10.5% at maximum flow rate, and this trend is constant over the whole range of flows.

The pressure profile inside the valve mock-up for an airflow of 0.212 *kg/s* is given in Figure 6.17.

The most noticeable difference here is the pressure drop across the central section, where the experimental results find a higher pressure drop than the 1-D MATLAB simulations. This difference is the opposite of the result for water flow. One explanation might be that sensor PT4 is influenced by a vena contracta effect downstream of the central section. If that is the case, the increased experimental frictional pressure drop between sensors PT4 and PT5 can also be explained. For all air flow simulations the friction factor was as calculated from Equation (6.6), with 10% additional friction.

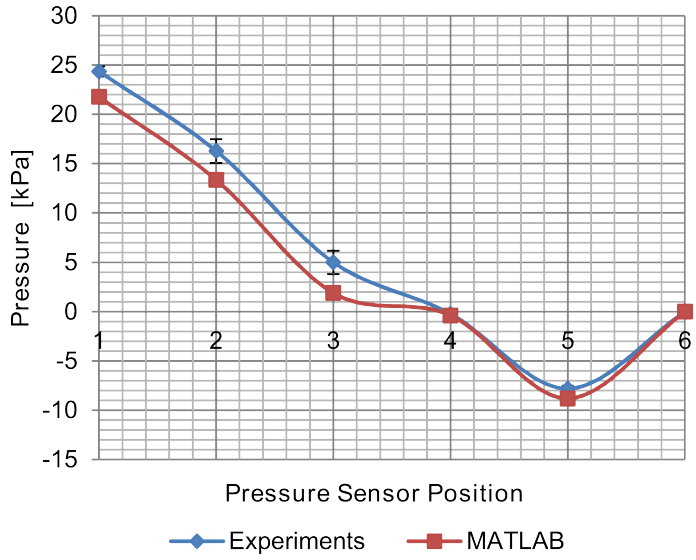

Figure 6.17: Pressure profile inside shut-in valve for airflow of 0.212 *kg/s*.

6.5 Summary

A downhole shut-in valve represents a complex flow geometry. The total pressure loss for single-phase water flow was simulated using the ANSYS Fluent CFD package. When comparing these simulations with the experimental results, it is proved that incompressible liquid flow can be simulated with a high degree of precision using a full cross-section 3-dimensional model. The realizable $k-\varepsilon$ turbulence model was found to perform better than the RNG $k-\varepsilon$ and the Reynolds stress turbulence model. At the highest flow rate the CFD simulated total pressure drop is less than 2% lower than experimental values. CFD simulations on a 3-dimensional symmetrical half-section was found to give too high pressure drop in some areas with high velocity and turbulence intensity.

In order to be able to simulate multiphase pressure drop, a 1-dimensional model is convenient. From the CFD-simulation, the axial pressure profile graph can be used for determination of all internal minor losses. Simulation of liquid flow with a novel 1-D least-squares spectral element method gives total pressure loss deviation comparable to the CFD simulation. The 1-D model can also be used for simulation of compressible flow, by regarding the flow as isothermal. At maximum air flow rate, the 1-D model understates the total pressure drop by 10% compared to experimental values.

Chapter 7

Two-phase flow in sudden expansions

The outlet section of the downhole shut-in valve can be compared to a sudden expansion. The flow cross-section changes abruptly, giving a sudden deceleration of the flow. The pressure losses for single phase flow with this kind of singularity is well known. For two-phase flow the situation is more complicated, and the first experiments indicated that the pressure recovery across the outlet section had to be investigated in more detail. This chapter describes first a validated method for simulation of single phase flow through the valve outlet. Then the results with two-phase flow is presented and compared to various known correlations.

7.1 Valve outlet geometry

The downhole shut-in valve will be mounted onto a well packer, and the geometrical detail of the valve-packer assembly are governed by functional needs. Some detail of the assembly are shown in Figure 3.7, and details from the valve mock-up as shown in detail D of Figure 4.5 and in Figure 7.1 below. The outlet section can be compared to a two-step sudden expansion. The first step is from 40 to 59 mm diameter, and the second step is from 59 to 90 *mm*. As the distance between these two steps is short, the single phase flow model has to be validated. The next section gives the theory for single phase pressure recovery in sudden expansions. Some correlations for two-phase pressure recovery in sudden expansions are also described.

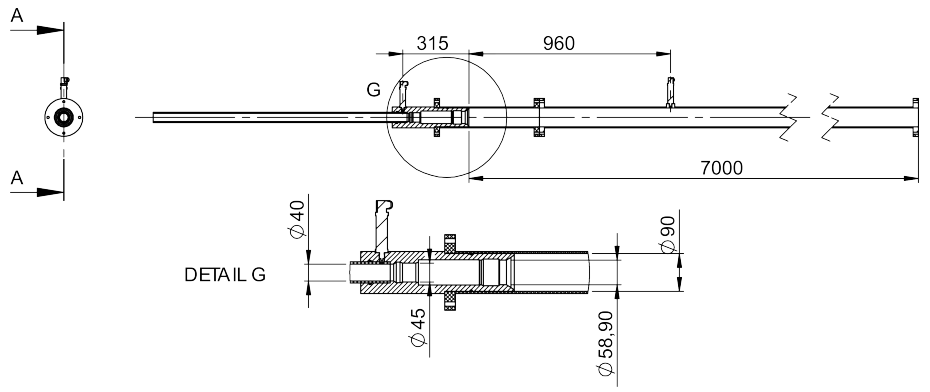

Figure 7.1: Shut-in valve outlet.

7.2 Theoretical background

7.2.1 Single phase

The flow of incompressible liquid through a sudden expansion can be modeled from two different view points. The first one is assuming that only the momentum is preserved, and that implies a loss of energy. The retardation of the flow at the expansion can in that case be compared to an inelastic collision, where kinetic energy is lost. The second view point is to assume that no energy is lost, so that the reduction in kinetic energy is equal to increased pressure energy. It is reasonable to assume that some energy will be lost, and the pressure recovery can be deduced by combining the equation for mass conservation:

$$A_1 v_1 = A_3 v_3 \tag{7.1}$$

and the momentum equation:

$$p_1 A_3 - p_3 A_3 = \rho A_3 v_3 (v_3 - v_1) \tag{7.2}$$

and the mechanical energy equation with energy loss:

$$p_1 + \rho \frac{v_1^2}{2} = p_3 + \rho \frac{v_3^2}{2} + K_L \rho \frac{v_1^2}{2} \tag{7.3}$$

Here ρ is density, u is velocity and p is pressure. By rearranging these equations it can be shown that the loss factor for incompressible liquid flow in a sudden expansion is $K_L = (1 - \sigma_A)^2$ where σ_A is the the ratio of upstream to downstream cross sectional area. This formula is approved by experimental data (Munson et al.

2006). For the pressure drop over the expansion with momentum conservation we also have that:

$$p_3 - p_1 = \frac{\sigma_A \left(1 - \sigma_A\right) G^2}{\rho} \tag{7.4}$$

As a further simplification, the radial pressure profile is assumed to be flat, and the pressure on the axial face at the expansion is taken as p_1.

If we have a kind of expansion without mechanical energy loss, we get from the energy conservation equation that:

$$p_3 - p_1 = \frac{\left(1 - \sigma_A^2\right) G^2}{2\rho} \tag{7.5}$$

7.2.2 Two phase pressure recovery

The pressure recovery for a two-phase flow can be modeled by calculating an average two-phase density, and in its simplest form it is without slip velocity (Wadle 1989):

$$p_3 - p_1 = \frac{\sigma_A \left(1 - \sigma_A\right) G^2}{\rho_h} \tag{7.6}$$

where the homogeneous density is

$$\frac{1}{\rho_h} = \frac{x}{\rho_G} + \frac{1 - x}{\rho_L} \tag{7.7}$$

Here x is mass flow of gas divided by total mass flow.

A model by Lottes (1961) and attributed to Romie (1958) uses the void fraction for calculating the pressure recovery. In this formulation the void fraction at inlet and outlet is assumed to be equal.

$$p_3 - p_1 = \frac{\sigma_A \left(1 - \sigma_A\right) G^2}{\rho_s} \tag{7.8}$$

where the slip density is

$$\frac{1}{\rho_s} = \frac{x^2}{\rho_G \alpha} + \frac{\left(1 - x\right)^2}{\rho_L \left(1 - \alpha\right)} \tag{7.9}$$

Lottes (1961) also proposed a simplified model where loss in dynamic pressure in the gas phase is not included:

$$p_3 - p_1 = \sigma_A \left(1 - \sigma_A\right) G^2 \left[\frac{1}{\rho_L \left(1 - \alpha\right)^2}\right] \tag{7.10}$$

The model by Attou and Bolle (1997) is based on the momentum balance, where the jet emerging from the sudden expansion is treated as a conical section:

$$p_3 - p_1 = G^2 \sigma_A \left(1 - \sigma_A\right) \left[\Phi\theta^r + \frac{\left(1 - \theta^r\right)}{\rho_L}\right] \tag{7.11}$$

where

$$\Phi = \frac{x^2}{\alpha\rho_G} + \frac{(1-x)^2}{(1-\alpha)\rho_L} \tag{7.12}$$

and

$$\theta = \frac{3}{1 + \sqrt{\sigma_A} + \sigma_A} \tag{7.13}$$

Here r is a correction factor dependent on the physical properties of the two-phase mixture.

Chisholm and Sutherland (1969) gives a general procedure for calculating pressure drop in pipeline components. The two-phase pressure drop is given as a function of the single phase liquid flow pressure drop:

$$\frac{\Delta p_{TP}}{\Delta p_L} = 1 + \frac{C}{X} + \frac{1}{X^2} \tag{7.14}$$

where

$$X = \left(\frac{1-x}{x}\right)\sqrt{\frac{\rho_G}{\rho_L}} \tag{7.15}$$

and

$$C = \left[1 + \left(C_2 - 1\right)\left(\frac{\rho_L - \rho_G}{\rho_L}\right)^{0.5}\right]\left(\sqrt{\frac{\rho_L}{\rho_G}} + \sqrt{\frac{\rho_G}{\rho_L}}\right) \tag{7.16}$$

For a pipe enlargement, $C_2 = 0.5$. Starting with the momentum equation we have that

$$p_3 - p_1 = \sigma\left(1 - \sigma\right) G^2 \left(1 - x\right)^2 \left[1 + \frac{C}{X} + \frac{1}{X^2}\right] \frac{1}{\rho_L} \tag{7.17}$$

Wadle (1989) also proposed a model which is not based on the momentum equation. The pressure recovery is here given as a fraction of the reduction in dynamic pressure head:

$$p_3 - p_1 = \left(1 - \sigma^2\right) \frac{G^2}{2} K \left[\frac{x^2}{\rho_G} + \frac{(1-x)^2}{\rho_L}\right] \tag{7.18}$$

The factor K was experimentally found to be 0.83.

Schmidt and Friedel (1996) presented a model for two-phase flow pressure recovery considering also the liquid entrainment in the gas phase:

$$p_3 - p_1 = \frac{G^2 \left[\frac{\sigma_A}{\rho_e} - \frac{\sigma_A^2}{\rho_e} - f_e \rho_e \left(\frac{x}{\rho_G \alpha} - \frac{(1-x)}{\rho_L (1-\alpha)}\right)^2 \left(1 - \sigma_A^{0.5}\right)^2\right]}{1 - \Gamma_e \left(1 - \sigma_A\right)} \tag{7.19}$$

where

$$\frac{1}{\rho_e} = \frac{x^2}{\rho_G \alpha} + \frac{(1-x)^2}{\rho_L (1-\alpha)} + \frac{\alpha_E \rho_L (1-\alpha)}{1-\alpha_E} \left[\frac{x}{\rho_G \alpha} - \frac{1-x}{\rho_L (1-\alpha)}\right]^2 \tag{7.20}$$

$$\alpha = 1 - \frac{2(1-x)^2}{1 - 2x + \sqrt{1 + 4x(1-x)\left(\frac{\rho_L}{\rho_G} - 1\right)}} \tag{7.21}$$

$$\alpha_E = \frac{1}{S}\left[1 - \frac{1-x}{1 - x\left(1 - 0.05 We^{0.27} Re^{0.05}\right)}\right] \tag{7.22}$$

$$S = \frac{x}{1-x} \frac{(1-\alpha)}{\alpha} \frac{\rho_L}{\rho_G} \tag{7.23}$$

$$We = G^2 x^2 \frac{d}{\rho_G \sigma} \frac{(\rho_L - \rho_G)}{\rho_G} \tag{7.24}$$

$$Re = \frac{G(1-x)\,d}{\mu_L} \tag{7.25}$$

$$\Gamma_e = 1 - \sigma_A^{0.25} \tag{7.26}$$

$$f_e = 4.9 \times 10^{-3} x^2 (1-x)^2 \left(\frac{\mu_L}{\mu_G}\right)^{0.7} \tag{7.27}$$

One of the earliest pressure recovery equations is presented by Richardson (1958). He includes only the liquid phase in his equation, modeling the real liquid velocity:

$$p_3 - p_1 = \frac{\sigma_A \left(1-\sigma_A^2\right) G^2}{2\rho_L} \left[\frac{(1-x)^2}{(1-\alpha)}\right] \tag{7.28}$$

Another equation by Delhaye (1981) is also based on the mechanical energy balance, but here the gas phase is included, with slip velocity:

$$p_3 - p_1 = \frac{G^2\left(1-\sigma_A^2\right)}{2} \left[\frac{(1-x)^3}{\rho_L^2 (1-\alpha)^2} + \frac{x^3}{\rho_G^2 \alpha^2}\right] \left[\frac{(1-x)}{\rho_L} + \frac{x}{\rho_G}\right]^{-1} \tag{7.29}$$

In most cases the gas velocity is larger than the liquid velocity, and several models exist for the calculation of the void fraction. The Drift Flux model by Zuber and Findlay (1965) is a well known model for void fraction prediction, and also Wallis (1969) and Ishii (1977) have taken part in its development. The general drift flux void fraction equation is given by

$$\alpha = \frac{x}{\rho_G} \left[C_0 \left(\frac{x}{\rho_G} + \frac{1-x}{\rho_L}\right) + \frac{\bar{U}_{GU}}{G}\right]^{-1} \tag{7.30}$$

where $\bar{U}_{GU}$is the weighed mean drift velocity. For horizontal flow it is given by

$$\bar{U}_{GU} = 1.18 (1-x) \left[\frac{g\sigma (\rho_L - \rho_G)}{\rho_L^2}\right] \tag{7.31}$$

where $C_0 = 1 + c_0 (1-x)$ and $c_0 = 0.12$. This void fraction correlation is recommended by Thome (2014).

A number of void fraction correlations have been evaluated by Dalkilic et al. (2008), and one of the best was that by Thom (1964):

$$\alpha = \frac{\gamma x}{1 + x(\gamma - 1)} \tag{7.32}$$

where

$$\gamma = Z^{1.6}, Z = \left(\frac{\rho_L}{\rho_G}\right)^{0.555} \left(\frac{\mu_G}{\mu_L}\right)^{0.111} \tag{7.33}$$

7.3 Experimental setup and testing procedure

Two-phase air-water and air-oil experiments were performed with air flow rate from 0-0.020 *kg/s*, water flow rate 0-9 *kg/s* and oil flow rate 0-8 *kg/s*. Air-oil experiments were performed with horizontal tubes, while air-water experiments were performed with horizontal and 2.7 and 5^o inclined tubes. Specifications of fluids used for two-phase experiments are given in Table 7.1.

Table 7.1
Two-phase flow fluids.

Fluid	Density, 1 atm, 20°C [kg/m^3]	Viscosity at 20°C [$Pa\text{-}s$]	Surface tension in air [N/m]
Air	1.2	1.79E-05	
Water	998	1.00E-03	7.20E-02
Exxsol D80	798	1.80E-03	2.63E-02

7.4 Validation and results

7.4.1 Single phase flow

The valve outlet section is now simplified to a two step expansion as described above, and the outlet pressure recovery is calculated with the momentum equation, see Equation 7.4. Calculated pressure recovery is compared to experimental results in Figure 7.2 for water flow, and in Figure 7.3 for oil flow.

Both curves provides very good comparison, and it is therefore justified to compare the shut-in valve outlet section with a two-step sudden expansion.

7.4.2 Two-phase flow

The upstream and downstream flow conditions will now be described before the data analysis. The sudden expansion studied here was a part of a valve section mock-up as shown in Figure 7.1. The 40 *mm* diameter upstream pipe in this study was therefore a mid-section of a large assembly. The two-phase flow was mixed at the inlet to a 5 *m* long, 85 *mm* diameter pipe upstream the valve mock-up. Slugs that were formed in this pipe could be tracked through the rest of the test section. The expected flow pattern in the 40 *mm* diameter upstream pipe was predicted by using the Unified Comprehensive Mechanistic (UCM) model for steady-state two-phase flow by Gomez et al. (2000). Figure 7.4 gives the predicted flow pattern for the 40 *mm* pipe upstream the expansions together with some observations by high-speed video filming.

Only slug flow was observed downstream the sudden expansion, as predicted by the UCM formulation. Two-phase flow pressure recovery is compared to the above

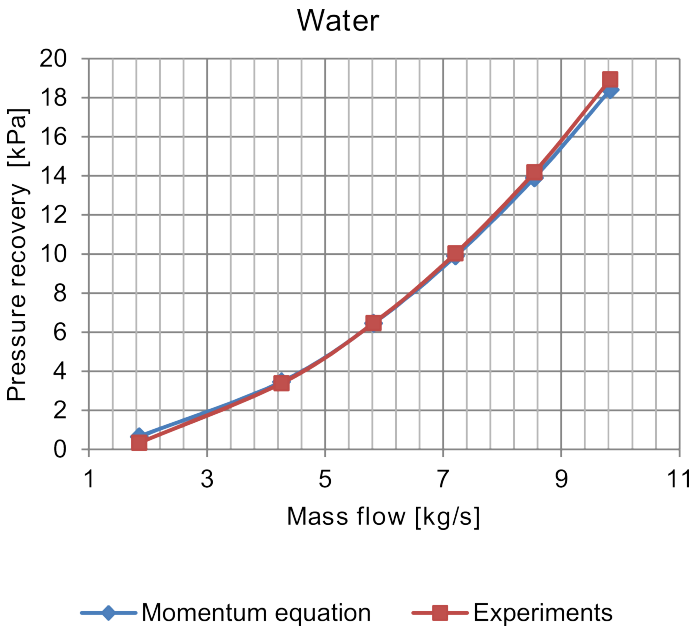

Figure 7.2: Pressure recovery with water flow.

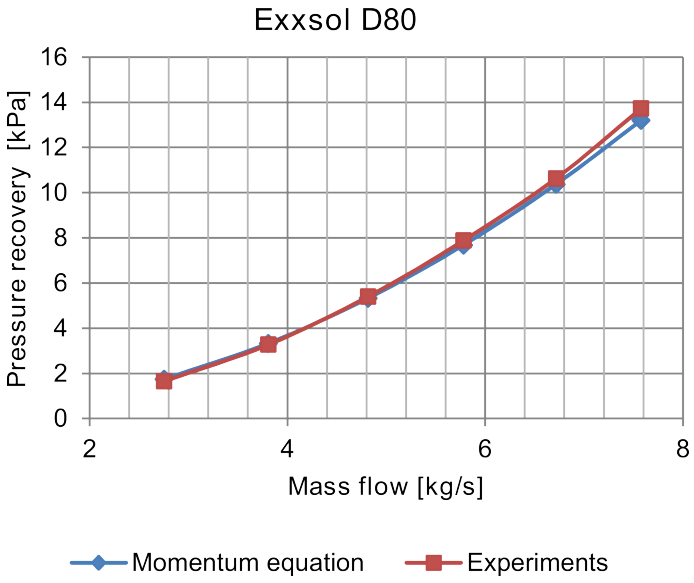

Figure 7.3: Pressure recovery with oil flow.

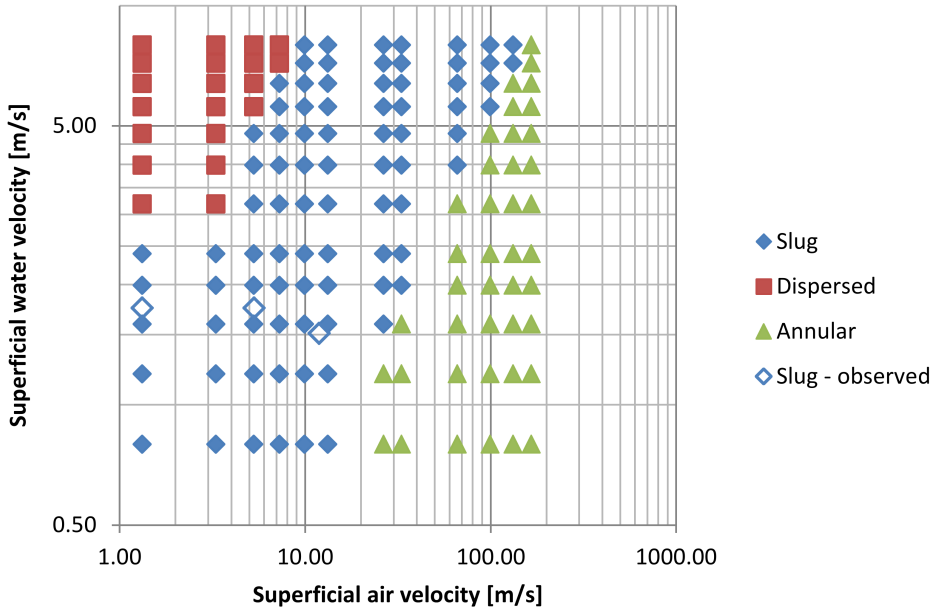

Figure 7.4: Predicted and observed flow patterns for 40 *mm* upstream pipe.

given correlations in the next figures. In Figures 7.5, 7.6 and 7.7 comparisons are given for water flows of 4, 6 and 8 *kg/s*. The pressure downstream the expansions is calculated using the UCM formulation for the flow in the 7 *m* long downstream pipe to the atmospheric outlet.

At all flow rates the pressure recovery at no air flow, or single phase liquid flow, coincides with the extrapolation of all the different correlations. For 4 *kg/s* water flow the pressure recovery drops as soon as air flow is introduced. A minimum is observed for 5 *g/s* air flow, and at higher air flows the pressure recovery is only around 1 *kPa*. A similar pattern can be observed for a water flow of 6 *kg/s*. With a water flow of 8 *kg/s* there is a maximum pressure recovery for 2 *g/s* air flow, and minimum for 8 *g/s* air flow. For all flow rates the Richardson correlation appears to be most representative.

The drop in pressure recovery is surprising, and in order to get a better understanding of this phenomenon the measured pressure recovery is given below for the different liquids and different flow rates. For horizontal tubes, the measured pressure recovery for air-water flow is given in Figure 7.8, and for air-oil flow in Figure 7.9. For oil flow of 2-5 *kg/s*, the pressure recovery is almost independent of air flow rate. For oil flow of 6 and 7 *kg/s*, there is a local maximum for pressure

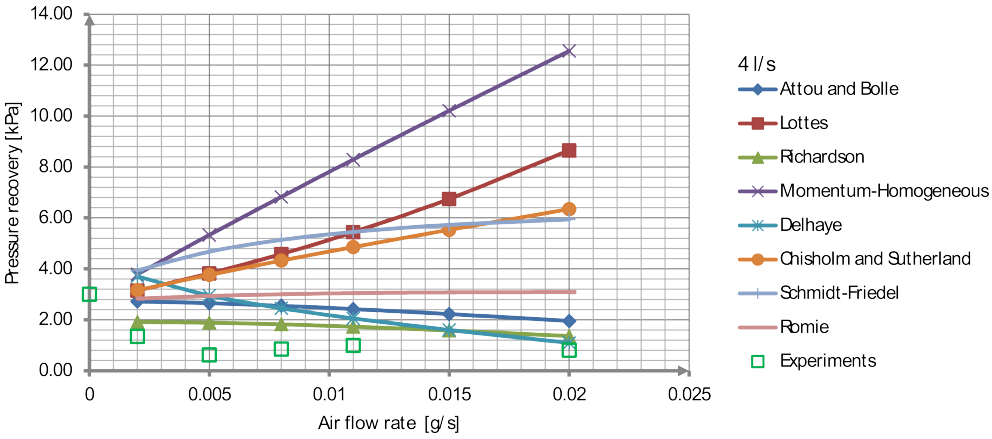

Figure 7.5: Measured and predicted pressure recovery as function of air flow rate, with constant water flow rate of 4 *kg/s*.

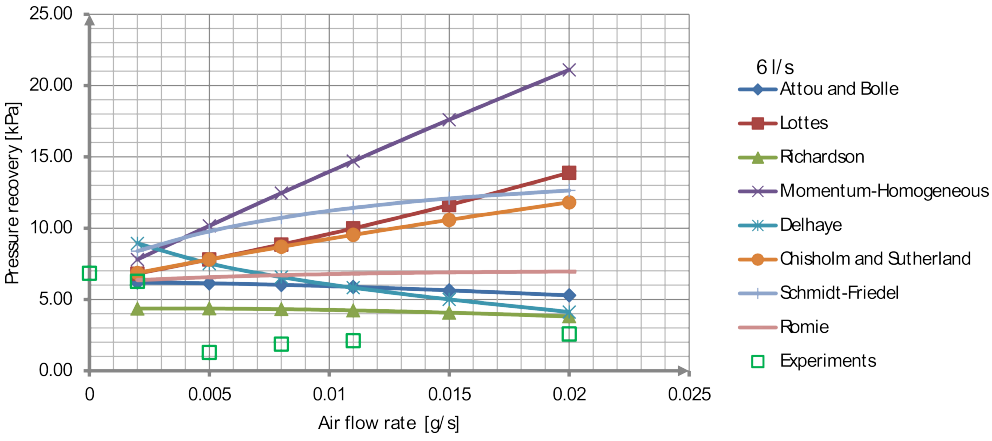

Figure 7.6: Measured and predicted pressure recovery as function of air flow rate, with constant water flow rate of 6 *kg/s*.

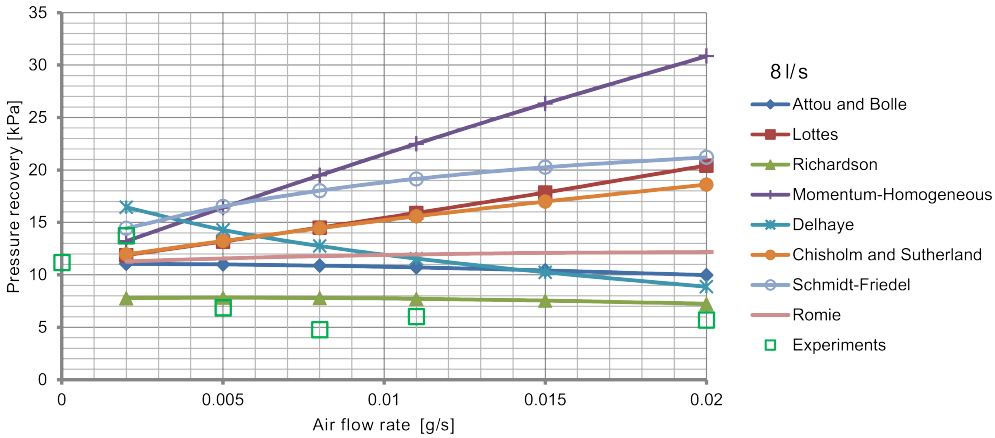

Figure 7.7: Measured and predicted pressure recovery as function of air flow rate, with constant water flow rate of 8 *kg/s*.

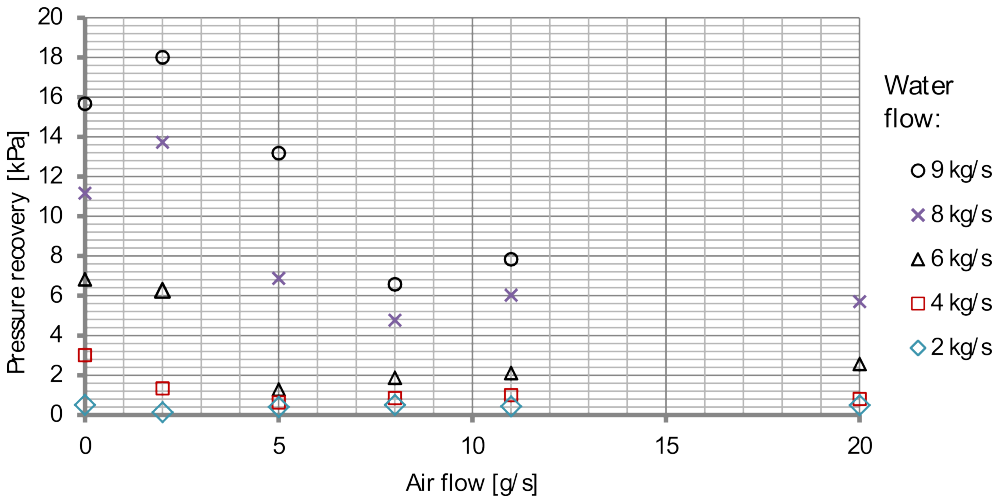

Figure 7.8: Pressure recovery with air-water two-phase flow, horizontal pipes.

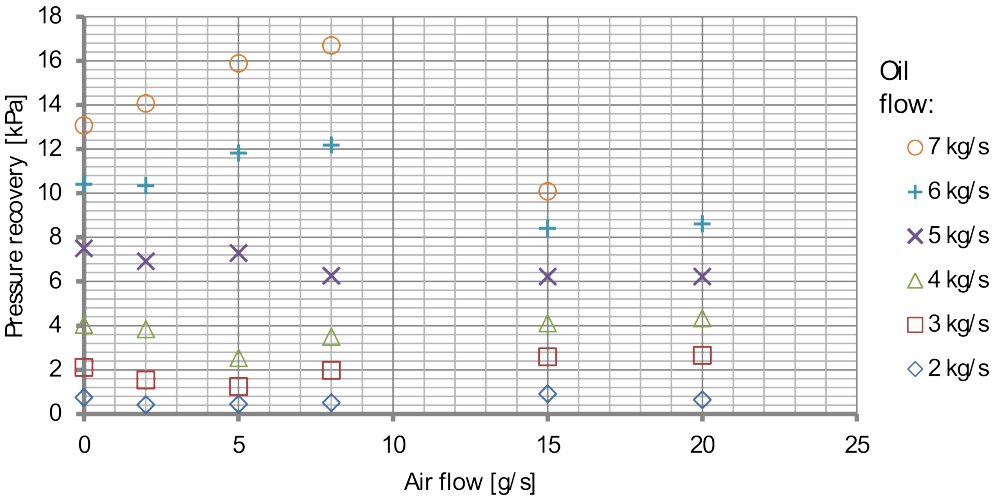

Figure 7.9: Pressure recovery with air-oil two-phase flow, horizontal pipes.

recovery at 8 *g/s* air flow rate. For air-water two-phase flow with horizontal tubes, the pressure recovery is reduced to a stable minimum for air flow rates above 8-11 *g/s*, only dependent on liquid flow rate. The same trend can be observed for oil flow. For oil flow of 2-7 *kg/s*, the pressure recovery is almost stable above 15 *g/s* air flow rate.

From Figures 7.8 and 7.9 is seems like the liquid part can be saturated with gas to some level before the gas is separated from the jet at the sudden expansion.

Pressure recovery was also studied for inclined pipe flow. Curves for pressure recovery vs. flow rates for air-water flow with horizontal pipes are given together with corresponding pressure recovery values at 2.7^o and 5^o inclination in Figure 7.10 and Figure 7.11 for 6 and 8 *kg/s* water flow. The whole test section with outlet pipe was bolted to a long table that was rotated. The tests with horizontal test section were repeated several times. The curves shows that the pressure recovery is changing little with these inclination angels. The outlet pressures downstream the sudden expansion are here calculated from height difference and frictional pressure drop in the outlet pipe. The data shows some minor differences, partly caused by changes in flow pattern.

Also, studying curves for 6 and 8 *kg/s* of water, at 5 *g/s* of air at 2.7^o inclination, we can see that the lowest liquid flow rate gives 1.5 *kPa* pressure recovery. The highest flow rate gives approx. 9.5 *kPa* pressure recovery. The flow pattern at the expansion for these two flow rates are shown in Figure 7.12 and Figure 7.13.

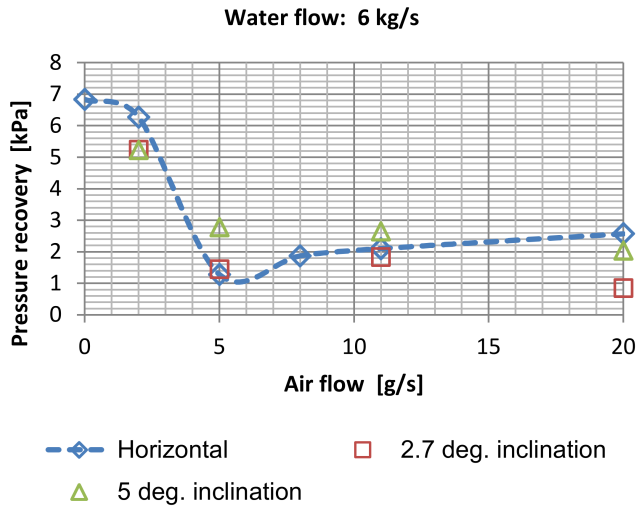

Figure 7.10: Pressure recovery with air-water two-phase flow at horizontal, 2.7 and 5^o. inclination with 6 *kg/s* water flow.

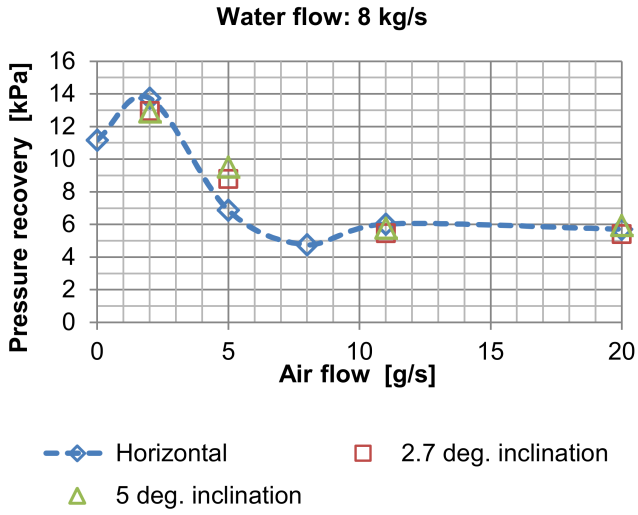

Figure 7.11: Pressure recovery with air-water two-phase flow at horizontal, 2.7 and 5^o inclination with 8 *kg/s* water flow.

For 6 *kg/s* water flow rate and 5 *g/s* air flow rate the liquid phase was concentrated in a jet stream in the center, surrounded by air, see Figure 7.12. Some 2-3 *m* downstream from the expansion the flow pattern changed to slug flow. With that flow pattern, the downstream pressure sensor was not in contact with the liquid, and it therefore measured a pressure equal to or slightly less than the pressure at the upstream sensor. At 8 *kg/s* water flow rate the whole pipe cross section was filled with turbulent water-air mixture as shown in Figure 7.13. The pressure recovery increased to 9 *kPa* across the sudden expansion.

Figure 7.12: Flow pattern after expansion. Water flow rate 5.8 *kg/s*, air flow rate 5 *g/s*. 2.7^o inclination.

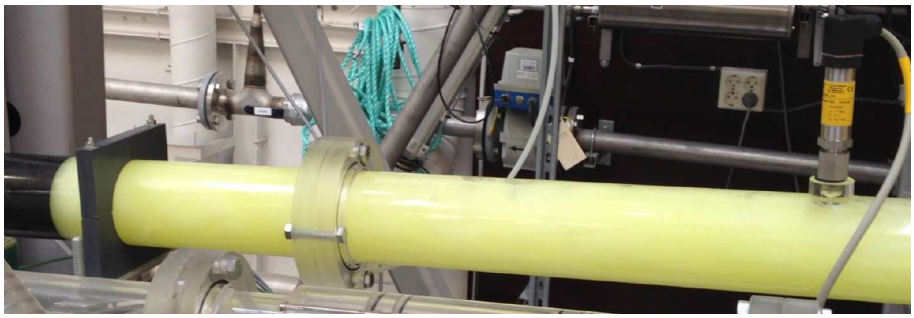

Figure 7.13: Flow pattern after expansion. Water flow rate 8.5 *kg/s*, air flow rate 5 *g/s*. 2.7^o inclination.

Figure 7.5, 7.6 and 7.7 shows that the Richardson (1958) correlation is closest to the measured values for pressure recovery. In Figure 7.14 this correlation is plotted together with the measured values for pressure recovery at different flow rates. However the correlation is not able to capture qualitatively the trends when increasing the flow rate.

A jet-like flow pattern was also reported by Chen et al. (2010). As in this work, a connection between this flow pattern and reduced pressure recovery was described, limited to a flow quality range of 0.7-1% and a mass flux of 100 $kg/(m^2s)$. Their experiments were performed with an upstream diameter of 3 *mm*, with expansion

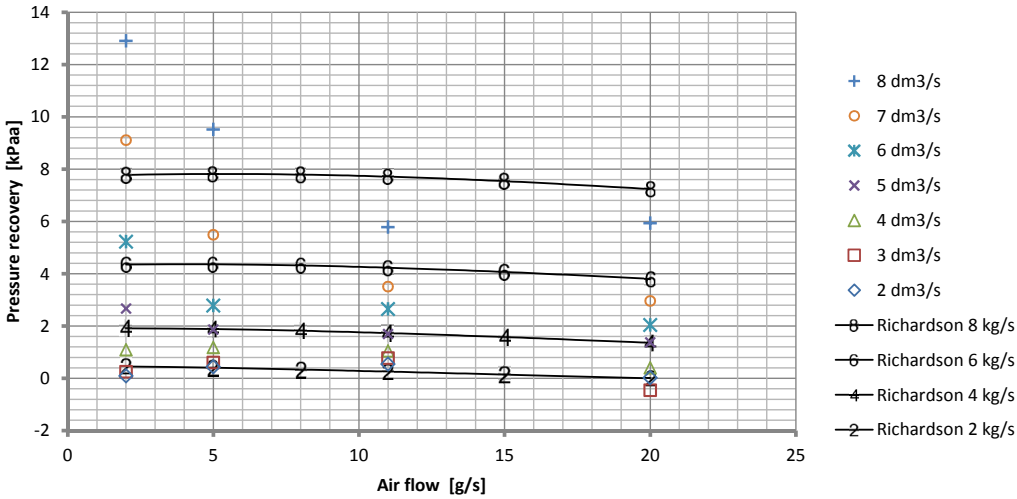

Figure 7.14: Richardson (Richardson 1958) correlation and measured pressure recovery values at different flow rates.

to rectangular channels of 3x6 mm^2 or 3x9 mm^2.

For this work, the experimental results shows a different behavior. The results of the present work are plotted as function of flow quality and mass flux in Figure 7.15. The recovered pressure is dropping for all mass fluxes up to a flow quality of 0.1%, and it increases again a little up to about $x = 0.2\%$. After that it seems to be independent of flow quality. For mass fluxes of 1258 and 1415 $kg/(m^2 s$ there is a maximum recovered pressure for a flow quality of approximately 0.05%.

The Richardson pressure recovery simulation was performed using the void fraction correlation by Thom (1964). The Drift Flux model for void fraction calculation gives a higher void fraction and a much higher predicted pressure recovery.

A possible explanation of the observed pressure recovery trends might be that the liquid has some capability of dissolving gas. This is motivated by the fact that the highest water flow rates of 8 and 9 *kg/s* have a maximum pressure recovery for an air flow rate of 2 *g/s*. For lower water flow rates the maximum is found at liquid flow only. For air flows over some limit the gas is separated from the liquid at the outlet and a central liquid jet stream is formed. The loss of pressure recovery is found to happen when this jet stream appears.

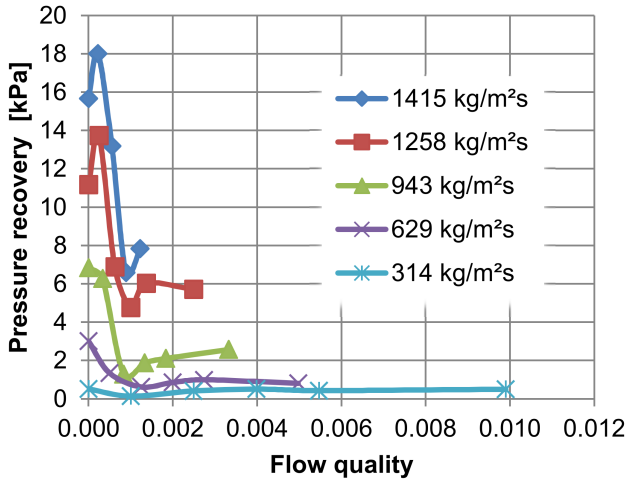

Figure 7.15: Pressure recovery as function of flow quality and mass flux.

7.5 Conclusion

With two-phase flow of air and water, the 40 to 90 *mm* diameter sudden expansion section shows an unexpectedly low rate of pressure recovery. For flow qualities up to only $x = 0.05\%$ there is an increase in pressure recovery for the highest flow rates. A minimum pressure recovery is found at a flow quality of $x = 0.1\%$. Above this flow quality there is little change for the flow qualities investigated here.

As demonstrated here, the two-phase pressure recovery cannot be modeled using the momentum equation with an average homogeneous density as in Equation 7.6. The trend for this equation together with the Lottes correlation (Equation 7.10) and the Chisholm and Sutherland correlation (Equation 7.14) shows an increased pressure recovery for increasing gas flow rate, and this is not according to the observations in the present study. The Schmidt-Friedel correlation (Equation 7.19) is close to observed values only at very low air flow rates and gives too high values at higher flow qualities. The Romie (Equation 7.8) and the Attou and Bolle correlations (Equation 7.11) gives lower values that are closer to the observed values and almost independent of air flow rate. At higher air flow rates the best of the existing correlations is the Richardson model (Equation 7.28), provided that the Thom‘s void fraction correlation is used. However, the only correlation that approximately captures the falling pressure recovery trend is the Delhaye correlation (Equation 7.29). The accuracy for this correlation is best at flow qualities around 0.025% and above 0.25%.

The amount of test data available is found to be insufficient for making a proposal for a new correlation. A new series of experiments should be performed with a possibility of having an increased system pressure. If the maximum pressure recovery depends on the liquids capacity of dissolving gas, this mechanism will be detected by increasing the downstream pressure while having constant flow rates.

Chapter 8

1-D model and two-phase flow

In this chapter the 1-D model is extended for solving a two-phase flow with minor losses. Frictional and minor losses are treated separately element by element. As described in Chapter 3, the frictional losses can be calculated with flow pattern independent correlations or with mechanistic models. The different flow models are here evaluated and compared to experimental data. For the minor losses there are no good examples in the literature and different approaches are tested and compared to experimental results. For simulation of compressible flow, the flow is regarded as isothermal. In addition to water, oil of type Exxsol D80 was used in the tests, with a density of 798 *kg/m*^{3} and a viscosity of 0.0018 *Ns/m*^{2} at 20°*C*.

8.1 Two-phase momentum balance equation

The general momentum balance for a slab Δx of a flow in a tube is given by

$$\rho v A_p \frac{\partial v}{\partial x}\Delta x \quad = \quad -A_p \frac{\partial P}{\partial x}\Delta x - \tau_w \pi D_i \Delta x \tag{8.1}$$

where ρ is density, v is velocity, A_p is pipe cross-section area, x is distance along the pipe, P is static pressure and D_i is pipe internal diameter. The term on the left-hand side is the momentum change caused by convective acceleration from density change and change in cross-section. The first term on the right-hand side is the force from change in statical pressure along the slab ΔP, and the last term is force on the slab Δx by friction along the tube wall. By rearranging we get that

$$\frac{\partial P}{\partial x} = -\rho v \frac{\partial v}{\partial x} - \frac{4\tau_w}{D_i} \tag{8.2}$$

For singularities, also called minor losses we have that

$$\frac{\partial P}{\partial x} = -\rho v \frac{\partial v}{\partial x} - K_L \rho \frac{v^2}{2} \tag{8.3}$$

The convective acceleration will here be calculated from average density ρ_H and average velocity v_H for some chosen void fraction model. The average density is calculated from the liquid holdup H_L:

$$\rho_H = \rho_L H_L + \rho_G (1 - H_L) \tag{8.4}$$

The average velocity is calculated from total mass flow $\dot{m}_{total}$ and pipe cross section A_p as

$$v_H = \frac{\dot{m}_{total}}{A_p \rho_H} \tag{8.5}$$

There are several correlations for the liquid holdup, in addition to the assumption of equal phase velocities. The derivative of average velocity $\frac{\partial v}{\partial x}$ is calculated from geometrical relationships. All changes of section are here simplified as they are regarded as conical sections. For elements of length ΔL with change of cross section, the average velocity $v_{H(i)}$ is calculated for each of the P internal nodes with index (i). The derivative is then calculated as

$$\frac{\partial v_H}{\partial x} = \frac{v_{H(P)} - v_{H(1)}}{\Delta L} \tag{8.6}$$

For flow with frictional losses the two-phase flow will be modeled as

$$\frac{\partial P}{\partial x} = -\rho_H v_H \frac{\partial v_H}{\partial x} - \frac{dP_{TF}}{\partial x} \tag{8.7}$$

where dP_{TF} is two-phase frictional pressure drop. In case of elements with minor losses it will be modeled as

$$\frac{\partial P}{\partial x} = -\rho_H v_H \frac{\partial v_H}{\partial x} - K_L \rho_H \frac{v_H^2}{2} \tag{8.8}$$

The different sections of the internal flow in the valve will now be investigated. Calculated values for convective acceleration pressure loss, minor pressure loss and frictional pressure loss will be compared separately to experimental data. Calculations will be performed for different void fraction models.

8.2 Convective acceleration pressure loss

A section of the valve with convective acceleration can be found inside the valve ports, between pressure sensor PT-1 and PT-3. This part contains only a 40° conical contraction, with well rounded transitions. For single phase flow the minor loss factor is found to be close to zero, and the pressure loss across this part will therefore be caused by convective acceleration only. Three different void fraction models will be evaluated here. For homogeneous flow with equal phase velocities we have that

$$H_L = \lambda_L = \frac{v_{SL}}{v_{SL} + v_{SG}} \tag{8.9}$$

$$\alpha = 1 - H_L \tag{8.10}$$

The drift flux void fraction model is reco*mm*ended by Thome (2014) and is given by

$$C_0 = 1 + 0.12(1 - x) \tag{8.11}$$

$$\bar{U}_{GU} = 1.18(1 - x)\left[\frac{g\sigma(\rho_L - \rho_G)}{\rho_L^2}\right]^{1/4} \tag{8.12}$$

$$\alpha = \frac{x}{\rho_G}\left[C_0\left(\frac{x}{\rho_G} + \frac{1-x}{\rho_L}\right) + \frac{\bar{U}_{GU}}{G}\right]^{-1} \tag{8.13}$$

Dalkilic et al. (2008) have evaluated a number of void fraction correlations using experimental data, and Thom‘s void fraction model (Thom 1964) was recommended:

$$\alpha = \frac{\gamma x}{1 + x(\gamma - 1)} \tag{8.14}$$

$$\gamma = Z^{1.6} \tag{8.15}$$

$$Z = \left(\frac{\rho_L}{\rho_G}\right)^{0.555}\left(\frac{\mu_G}{\mu_L}\right)^{0.111} \tag{8.16}$$

It is generally accepted that the gas phase moves faster than the liquid phase, and the last two models assumes a slip velocity. These three different void fraction models will therefore give different average density and average velocity v_H. The convective acceleration pressure loss will therefore depend on the chosen void fraction model. In Figure 8.1 experimental and calculated pressure drops for convective acceleration are compared. The diagram reveals that calculated pressure drop corresponds most closely to experimental pressure drop if the phase velocities are assumed to be equal. The pressure drop caused by two-phase convective acceleration should therefore be calculated using the homogeneous void fraction model.

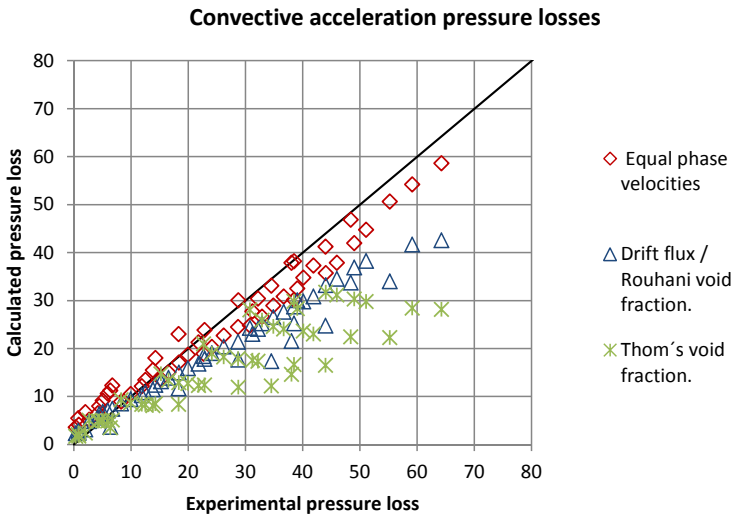

Figure 8.1: Pressure loss by convective acceleration with two-phase flow of water and air. Tube diameter is 40 *mm*, liquid flow is 0-10 *kg/s* and air flow is 0-50*g/s*.

8.3 Minor losses

The shut-in valve has a minor loss constituted by a short section of the internal 40 *mm* channel. The diameter is here increased to 50 *mm*, and four bolts are protruding into the flow. For single phase flow the minor loss coefficient is found to be 0.15. The minor loss will now be calculated using Equation (8.8) with void fraction models as above. Calculated and experimental data are compared in Figure 8.2. The homogeneous void fraction model with equal phase velocities appears to be suitable also for minor losses.

8.4 Two-phase frictional losses

8.4.1 Unified Comprehensive Model

The two-phase frictional losses can be predicted in two different ways. The first option is using the flow-pattern independent correlations given in Section 3.1. The second option is using the Unified Comprehensive Model (UCM) formulation given in Section 3.2. The solution algorithm will be as depicted in Figure 8.3 in both cases. The use of flow pattern independent correlations is quite straight forward, e.g. by applying Equation (3.35). The use of the UCM formulation is more complicated, and an evaluation algorithm must be applied in order to identify the correct flow pattern. The evaluation algorithm used in this work is shown in Fig-

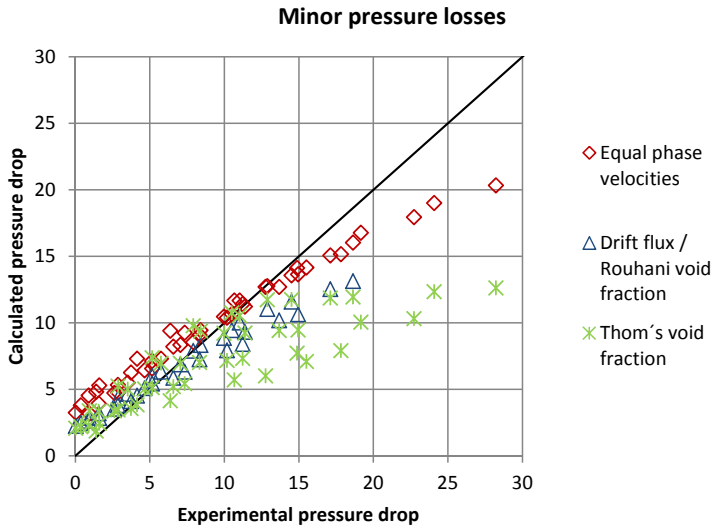

Figure 8.2: Minor pressure loss with two-phase flow of water and air. Tube diameter is 40 *mm*, liquid flow is 0-10 *kg/s* and air flow is 0-50*g/s*.

ure 8.4. The bubble flow pattern is not evaluated, as it occurs only for pipes with inclination above $60°$. As explained, the dispersed flow pattern is assumed for elements with minor losses. The reason is that the flow model for this flow pattern includes equal phase velocities. It is shown above that this will give the best prediction of the convective acceleration pressure losses and minor losses.

The UCM formulation can also be used for making maps of predicted flow patterns, and some examples are given here for different fluids in the valve inlet pipe with 84.9 *mm* diameter. These maps are given in terms of superficial velocities:

$$v_{SG} = \frac{\dot{m}_G}{A\rho_G} \tag{8.17}$$

$$v_{SL} = \frac{\dot{m}_L}{A\rho_L} \tag{8.18}$$

Figure 8.5 shows predicted flow pattern for air-water flow. Figure 8.6 shows predicted flow pattern for air-oil flow with oil type Exxsol D80. Figure 8.7 shows predicted flow pattern for air-oil flow with oil type Nexbase 3080. The predicted flow patterns were confirmed by observations.

A straight section inside the shut-in valve between pressure sensors PT-4 and PT-5 has been used for validating calculations of frictional pressure loss. In Figure

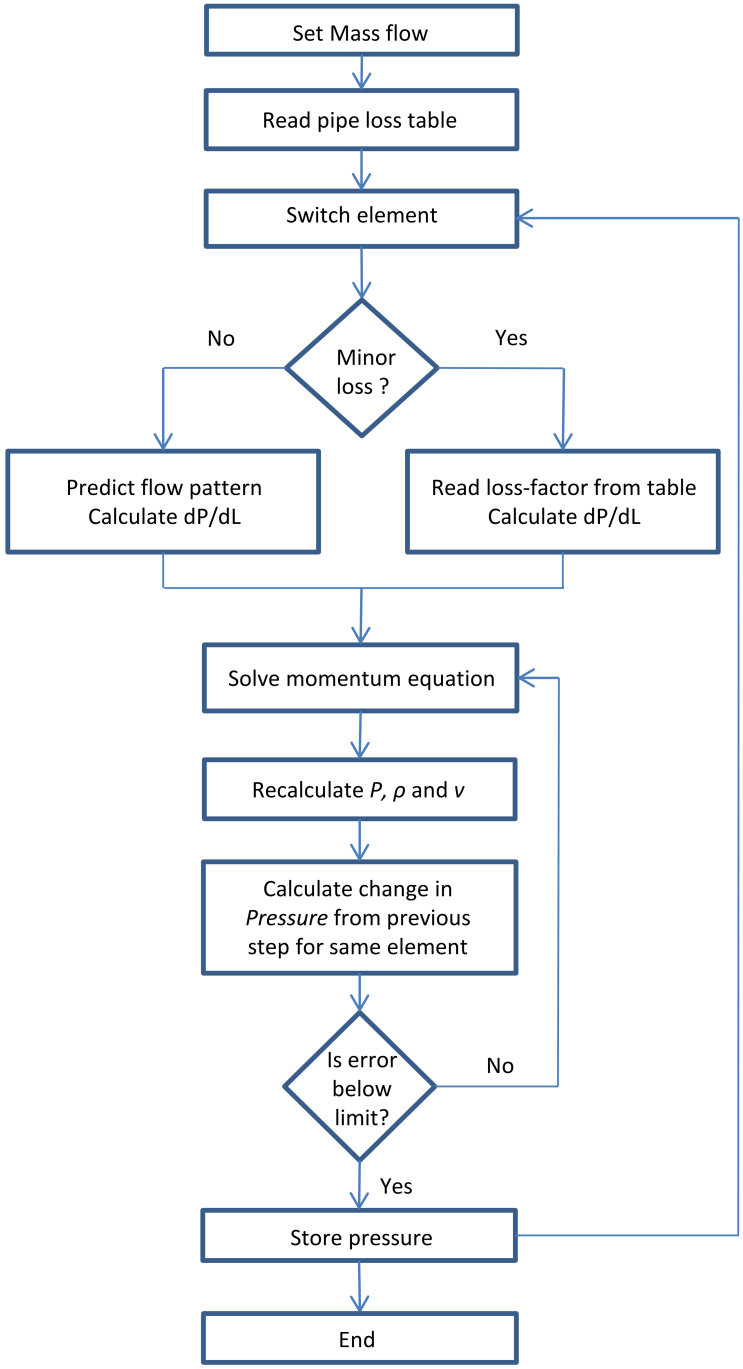

Figure 8.3: Solution algorithm for two-phase flow.

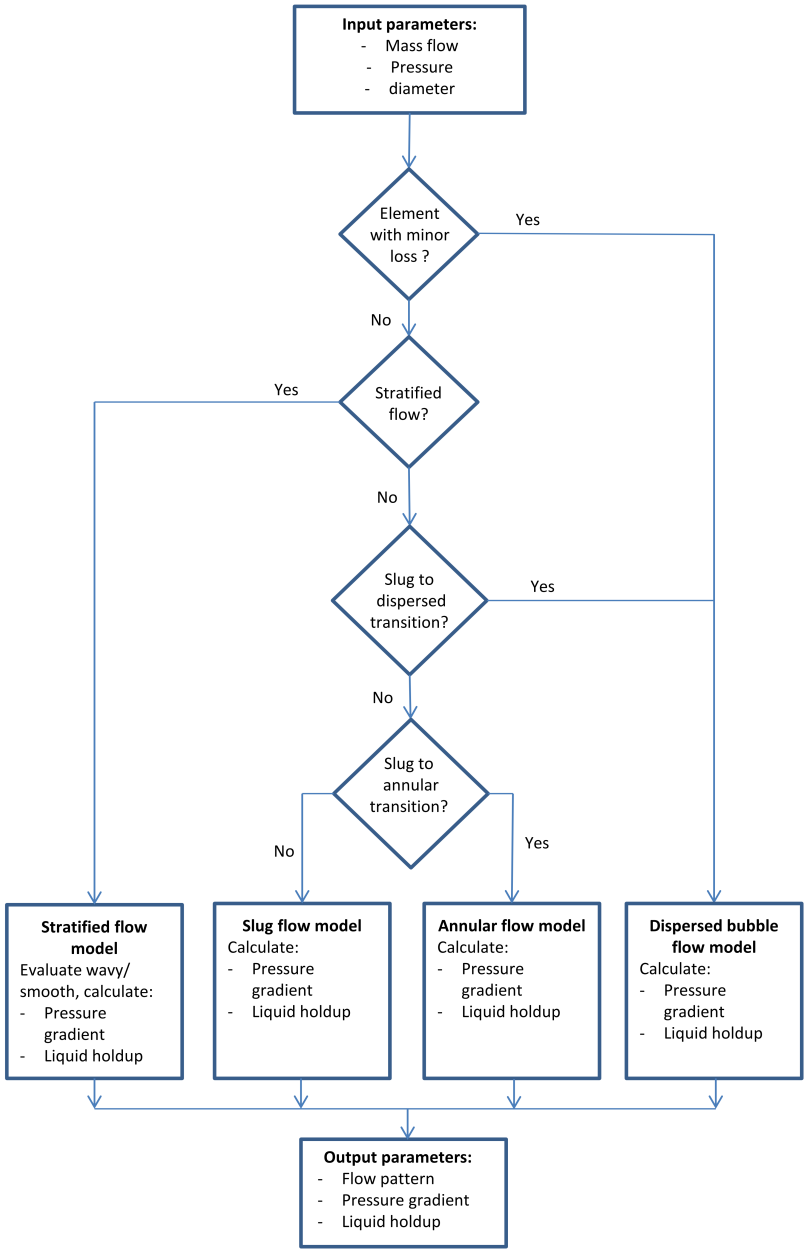

Figure 8.4: Evaluation algorithm for flow patterns according to the UCM formulation.

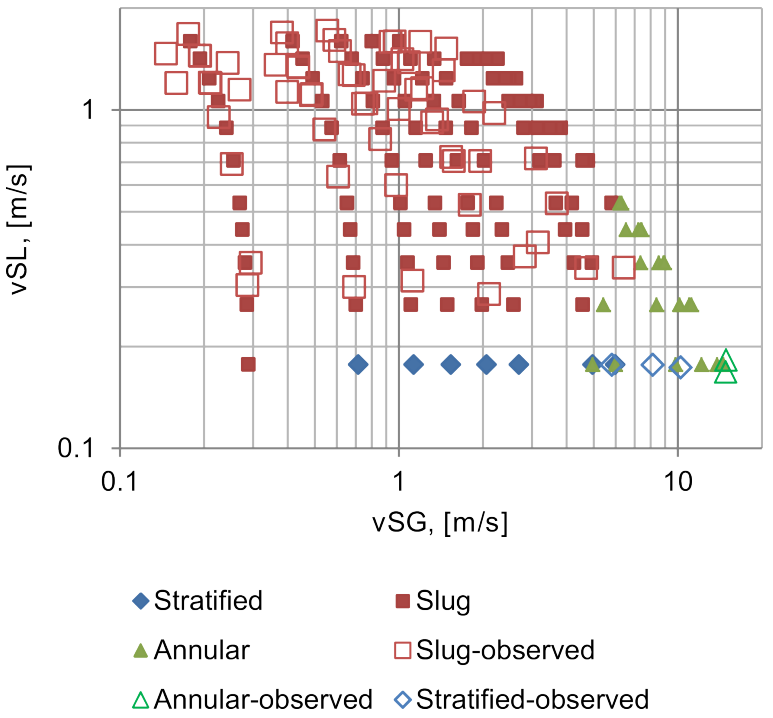

Figure 8.5: Flow pattern at inlet with air-water two-phase flow.

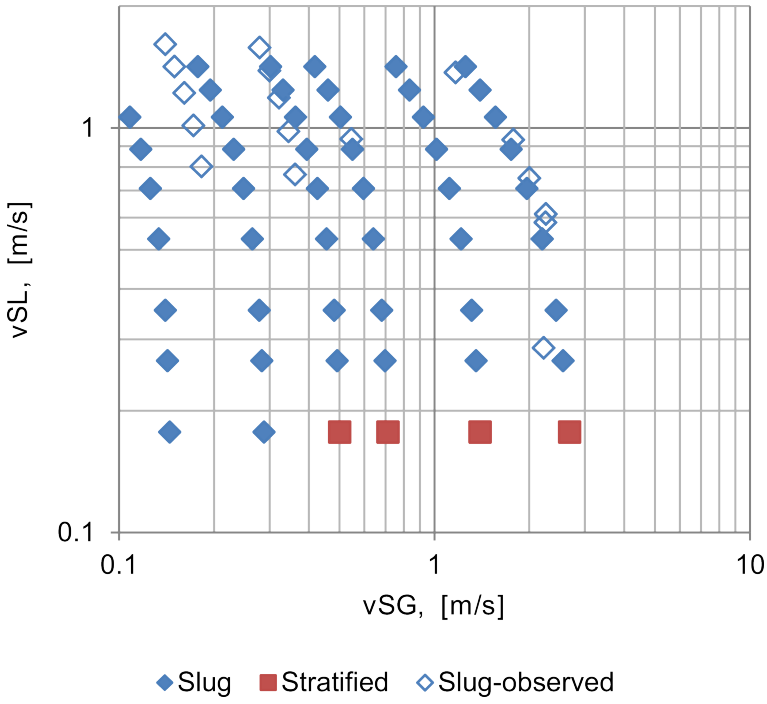

Figure 8.6: Flow pattern at inlet with air-Exxsol D80 two-phase flow.

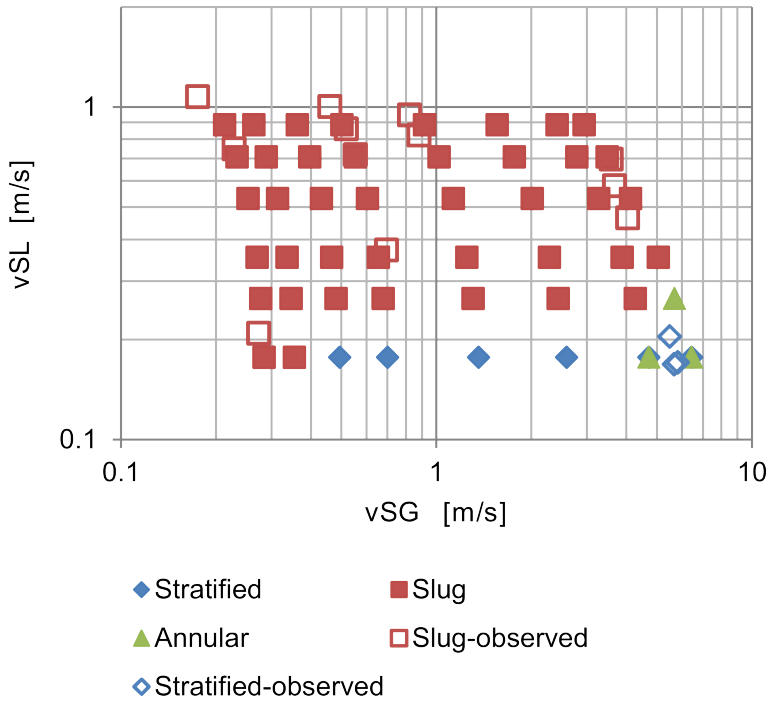

Figure 8.7: Flow pattern at inlet with air-NEXBASE 3080 two-phase flow.

8.8 calculated data for the UCM formulation and some correlations are compared to experimental data. The diagram shows the results for the original UCM for-

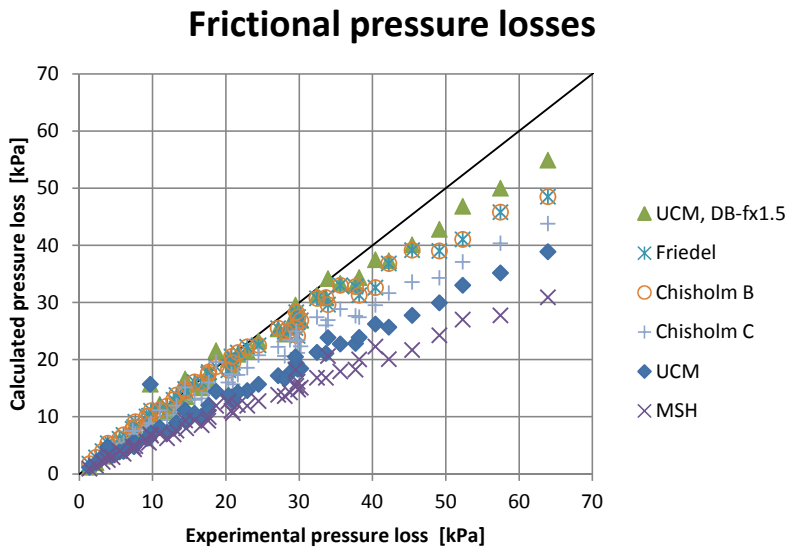

Figure 8.8: Frictional pressure loss [*kPa*] in 40 *mm* pipe with air-water two-phase flow. Liquid flow is 0-10 *kg/s* and air flow is 0-50*g/s*. UCM, DB-fx1.5 is UCM with modified friction factor for dispersed bubble flow.

mulation together with a modified model where the friction factor for dispersed bubble flow is multiplied with 1.5. In Figure 8.9 the same data are given for experimental pressure losses up to 30 *kPa*. A closer study of this diagram reveals that the first points from 0-5 *kPa* pressure drop is more accurately predicted than the rest. These points represents the air-water flow combinations resulting in slug flow in the section between pressure sensor PT-4 and PT-5, and they are plotted separately in Figure 8.10. We can see that for slug flow the calculated pressure drop is within $\pm 20\%$. A dispersed bubble flow pattern is predicted for all other flow combinations.

This observation of different deviation for slug flow and dispersed bubble flow motivates a separate multiplication factor for dispersed bubble flow. The modified UCM formulation produces the most accurate frictional pressure drops. This test section is however downstream a flow section with a minor pressure loss, see right side of detail C in Figure 4.5. Four bolts are protruding into the flow, and locally the diameter is increased from 40 to 50 *mm*. This singularity will generate more turbulence and that can possibly increase the flow friction. It is also clear that the

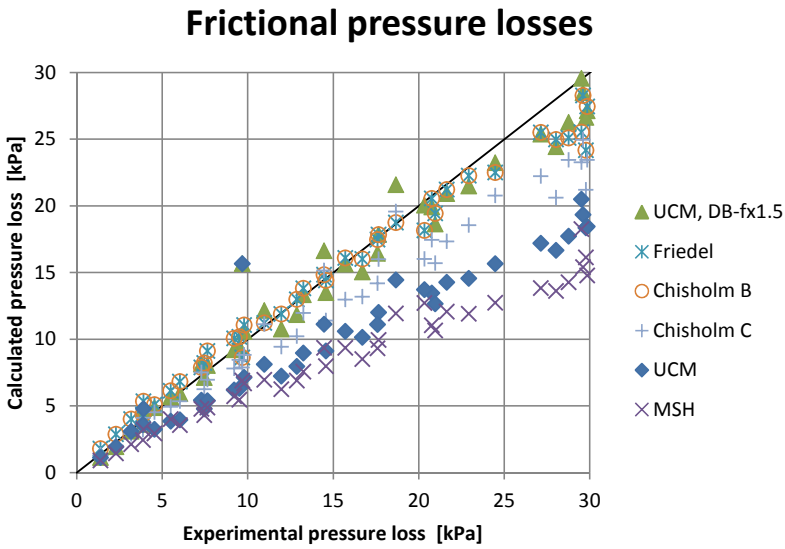

Figure 8.9: Frictional pressure loss [*kPa*] in 40 *mm* pipe with air-water two-phase flow. Liquid flow is 0-10 *kg/s* and air flow is 0-50*g/s*. UCM, DB-fx1.5 is UCM with modified friction factor for dispersed bubble flow.

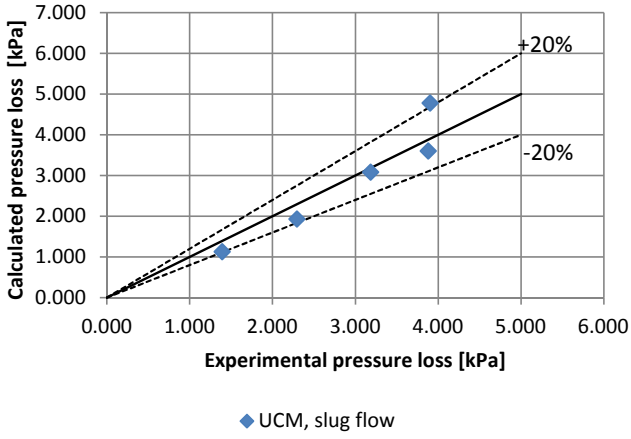

Figure 8.10: Experimental and calculated pressure drop in 40 *mm* pipe between sensors PT-4 and PT-5.

Friedel correlation and the Chisholm B coefficient correlation gives low deviation at lower pressure drops.

8.4.2 Two-phase flow patterns

At the inlet section of the shut-in valve there is a transparent pipe, where the flow pattern can be inspected. The upstream pipe is made of stainless steel, with inner diameter 0.0849 *m* and length 4.8 *m*. At the connection with the transparent LEXAN (polycarbonate) tube, there is a conical section from 0.084 to 0.094 *m* diameter, with an angle of 16^o. Observed flow patterns are shown with open symbols, and they are mainly as predicted. However, stratified flow was observed with 0.001 *kg/s* of water and 0.046-0.114 *kg/s* of air, or a superficial air velocity of 5.3-7.9 *m/s*, and here annular flow was expected. Annular flow pattern was observed with 15 *m/s* superficial air velocity. These velocities were calculated from the prevailing pressures, and that is why the diagram is twisted to the left in the top. Higher mass flow rates caused higher back pressures due to pressure drop across the valve. With oil flow, the maximum air mass flow rate was reduced to 0.020 *kg/s*, and only slug flow was observed, in accordance with the pattern predicted by the UCM formulation. For oil type Nexbase 3080, both slug flow and stratified flow was observed according to the flow map.

For the lower part of the valve (inlet side), there is an annular section up to the valve ports, see detail C in Figure 4.5. For all three liquid-air two-phase flows, the flow pattern breaks up and transforms into a homogeneous mixture in this zone. As the cross sectional area is reduced compared to the downstream pipe, the flow accelerates. The gas bubbles breaks up and are gradually distributed as smaller bubbles all around the circumference. At stratified flow, the nose of the valve body generates waves that reaches the top of the pipe.

For the central tube with inner diameter 0.04 *m*, the flow can easily be taken as homogeneous, or dispersed bubble flow, due to the high mixing upstream in the valve ports. Inspection of the flow through the transparent pipe also strengthen this impression. However, the UCM flow pattern map and high speed filming reveals that annular and slug flow can exist, even with the high-viscosity NEXBASE 3080 with a density of 845 kg/m^3 and a viscosity of 0.065 Ns/m^2, see Figure 8.11.

At high gas rate and low liquid rate, the video shows a slow moving liquid film on the pipe wall, with fast-moving droplets behind. The flow pattern map is thereby confirmed for annular flow. Pictures of two-phase air-water flow pattern in the central 40 *mm* tube are given in Figure 8.12, 8.13 and 8.14. The pictures were taken some 30 *cm* downstream pressure sensor PT-4. Observe the higher number of gas bubbles in the slug front compared to the slug tail.

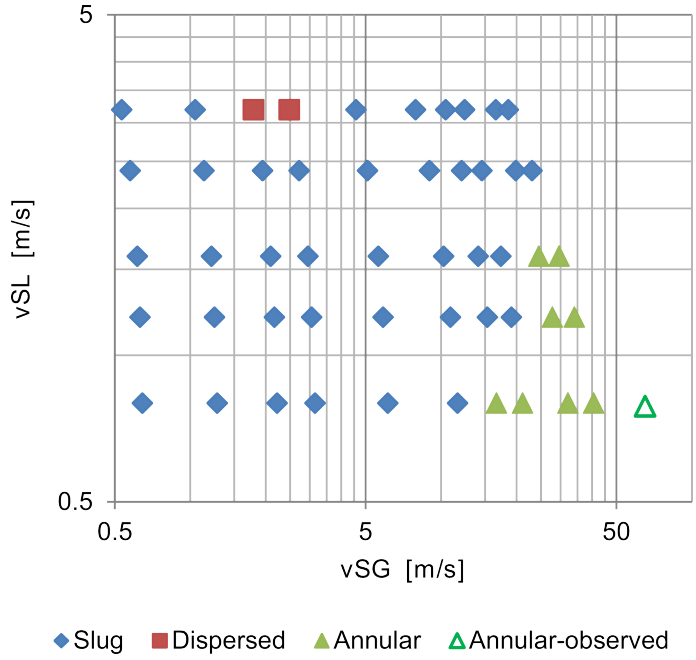

Figure 8.11: Flow pattern at 0.04 *m* diameter central section with NEXBASE 3080-air two-phase flow

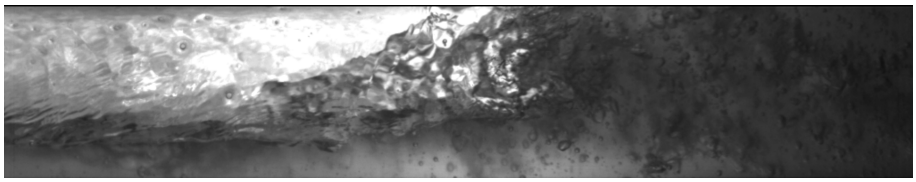

Figure 8.12: Slug body front in 40 *mm* pipe, with 2 *kg/s* water flow and 2*g/s* air flow.

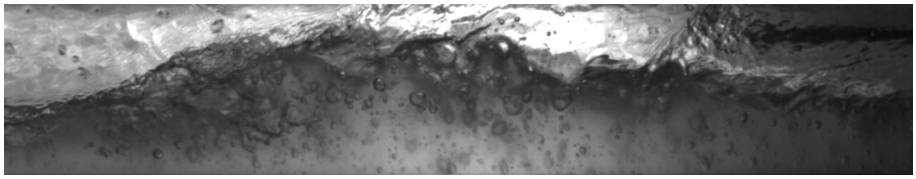

Figure 8.13: Wavy flow between two slugs, with 2 *kg/s* water flow and 2*g/s* air flow.

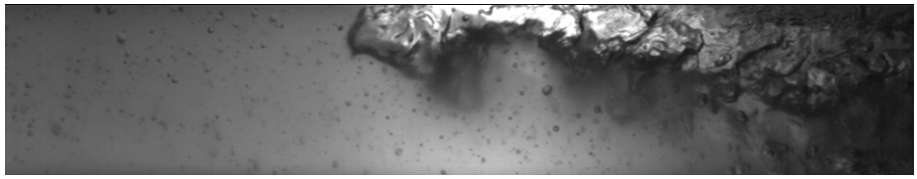

Figure 8.14: Slug body tail in 40 *mm* pipe, with 2 *kg/s* water flow and 2*g/s* air flow.

At the outlet section, an inverse annular flow can be observed at high combined flow rates. The two-phase mixture leaves the upper valve section as a jet stream in the center of the pipe. After some distance a normal flow pattern is developed. The test section was not long enough to capture these characteristics in full.

8.4.3 Pressure drop calculation

8.4.3.1 Overall prediction performance

Two-phase flow simulations are performed using the 1-D least squares spectral element model, with two-phase flow friction modeled with the Unified Comprehensive Model formulation and the various correlations described in chapter 3. Pressure losses caused by convective acceleration and singularities are modeled assuming equal phase velocities as explained above. Figure 8.15 shows a comparison of experimental and simulated results for air-water flow.

A similar comparison for two-phase flow of Exxsol D80 and air is shown in Figure 8.16.

The results are summarized in Table 8.1. E_1 is average deviation, E_2 is average absolute deviation, and E_3 is standard deviation defined as

$$E_1 = \frac{1}{n}\sum_{i=1}^{n}\frac{\Delta P_{calculated}(i) - \Delta P_{experimental}(i)}{\Delta P_{experimental}(i)} \tag{8.19}$$

$$E_2 = \frac{1}{n}\sum_{i=1}^{n}\left|\frac{\Delta P_{calculated}(i) - \Delta P_{experimental}(i)}{\Delta P_{experimental}(i)}\right| \tag{8.20}$$

$$E_3 = \sqrt{\frac{1}{n}\sum_{i=1}^{n}\left[\frac{\Delta P_{calculated}(i) - \Delta P_{experimental}(i)}{\Delta P_{experimental}(i)} - E_1\right]^2} \tag{8.21}$$

A low average deviation E_1 is good, but the deviation can still be high with the data points evenly distributed on both sides of the correct value. A low average absolute deviation E_2 indicates that the calculated values are close to the correct value. The standard deviation quantifies the variation in the data sets. The mod-

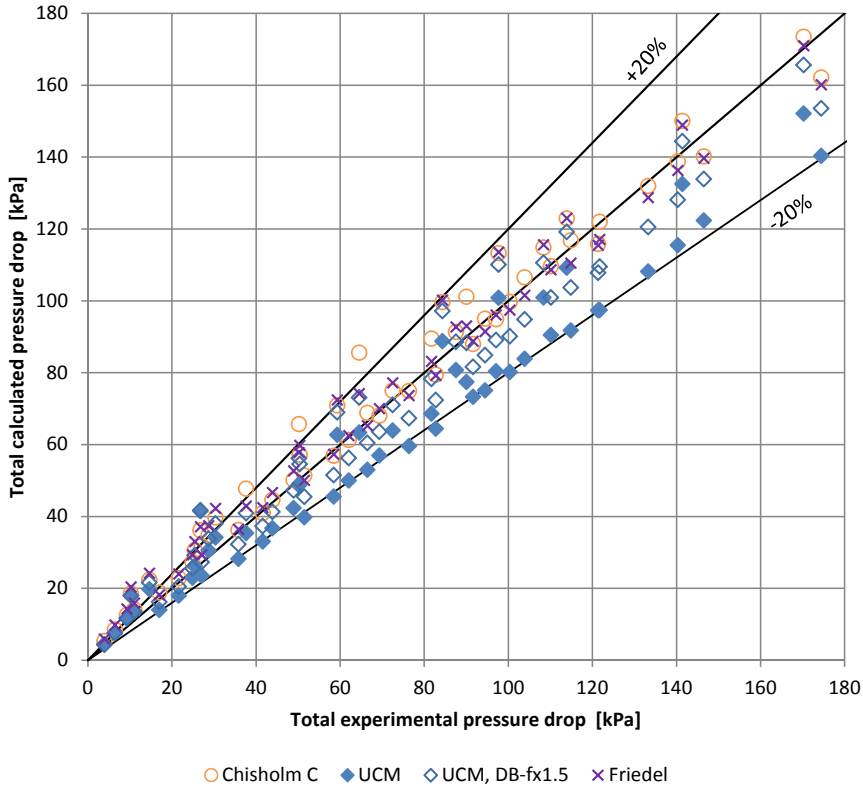

Figure 8.15: Simulated vs. experimental pressure drop for air and water. Liquid flow is 0-10 *kg/s* and air flow is 0-50*g/s*.

Table 8.1
Comparison of different two-phase flow calculation models for shut-in valve.

Method	Air-Water			Air-Exxsol D80		
	E_1 (%)	E_2 (%)	E_3	E_1 (%)	E_2 (%)	E_3
Unified Comprehensive Model formulation	-6.22	16.80	0.20	-1.55	11.18	0.19
Unified Comprehensive Model formulation, dispersed bubble flow model friction factor multiplied by 1.5	3.12	12.57	0.18	3.62	10.16	0.19
Friedel correlation	12.66	14.89	0.21	15.24	15.99	0.30
Chisholm B coefficient method	12.78	13.73	0.17	3.68	10.46	0.23
Chisholm C coefficient method	11.43	12.87	0.17	2.04	10.70	0.22
Müller Steinhagen and Heck correlation	-28.58	28.58	0.08	-20.82	24.74	0.17

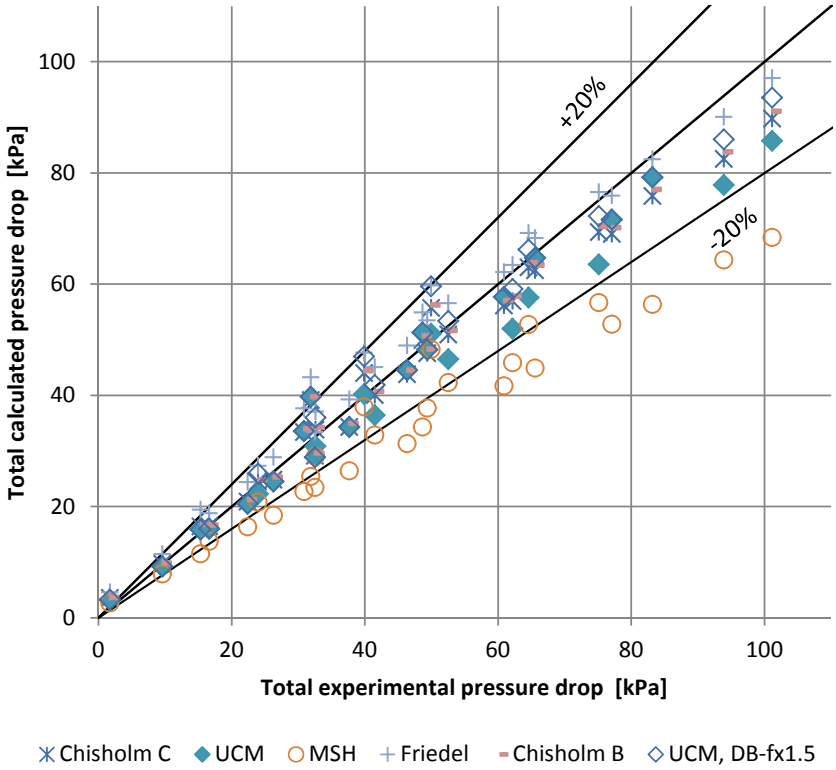

Figure 8.16: Simulated vs. experimental pressure drop for air and Exxsol D80.

ified UCM formulation gives the best overall performance with only 3.1 - 3.6% average deviation for both fluid combinations. The Chisholm B and C coefficient correlations gives equally good performance for oil and air only.

The modified UCM formulation has the lowest average absolute deviation for both fluid combinations, and the standard deviation is also among the best. It must therefore be concluded that the modified UCM formulation is to be preferred.

8.4.3.2 Detailed prediction performance

The detailed pressure drop along the shut-in valve was simulated using the atmospheric outlet pressure as boundary condition. The pressure profile along the valve for a water flow of 5.39 *kg/s* and an air-flow of 0.002 *kg/s* is indicated in Figure 8.17.

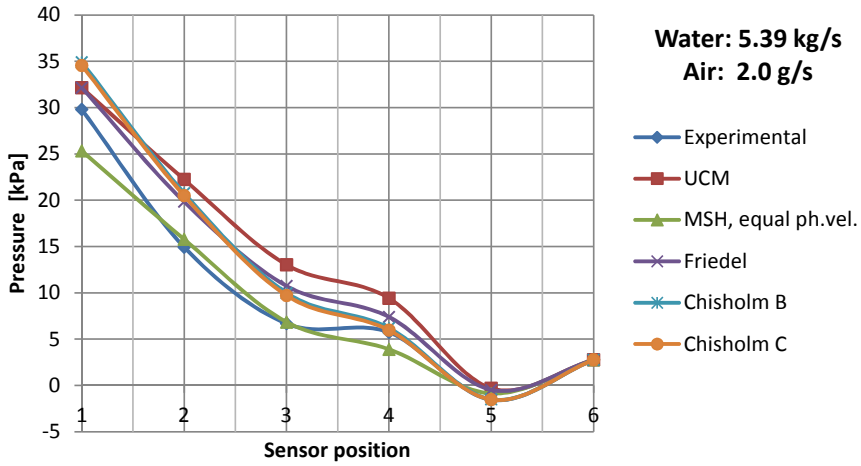

Figure 8.17: Pressure profile through shut-in valve for two-phase air-water flow.

This curve is precise only at the markers for each pressure sensor, and the curves between the points are only sketchy. The experimental results shows a very low pressure drop for the minor loss between sensor 3 and 4, but it believed that these pressure readings might be disturbed by a vena contracta effect at relatively lower flow rates due to the conical contraction in front of sensor 3. The UCM formulation predicts dispersed bubble flow pattern throughout the valve at this flow rate combination. The pressure profile along the valve for a water flow of 9.5 *kg/s* and an air-flow of 0.002 *kg/s* is indicated in Figure 8.18.

Now the predicted minor loss between sensors 3 and 4 is approximately equal to

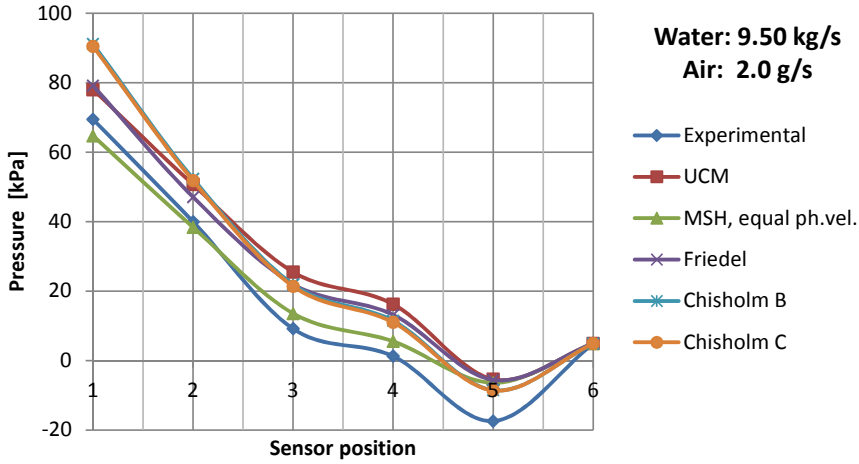

Figure 8.18: Pressure profile through shut-in valve for two-phase air-water flow.

the experimental result, but the experimental measurement of the pressure at sensor 5 is some 10 *kPa* lower than predicted. The explanation is that the chosen correlation for pressure recovery at this sudden expansion does not capture the pressure recovery maximum observed for low air flow rates, see Figure 7.14. Pressure profile curves for higher flow rates of air and water are given in the Figure 8.19 to Figure 8.26.

From these curves we can see that the believed vena contracta effect on the pressure at sensor 3 is present at low liquid flow rate for air flow rates up to 0.015 *kg/s*. At a water flow of 9.03 *kg/s* and air flow of 0.015 *kg/s* the 1-D simulation with the UCM formulation follows closely the experimental pressures. At air flow rates above 0.035 *kg/s* the frictional pressure drop between sensor 4 and 5 seems to be a little under predicted by all models and correlations. At the highest air flow rates it is also clear that the pressure recovery at the sudden expansion between sensor 5 and 6 is higher than predicted with the chosen Richardson correlation. Similar pressure profile curves for two-phase flow of air and Exxsol D80 is shown in Figure 8.27 to Figure 8.32.

The pressure prediction performance is here best at the maximum air flow rate of 0.020 *kg/s*. The pressure gradient between sensor 4 and 5 for maximum liquid and air flow rate is a little lower than the experimental values. The predicted flow pattern is in this case dispersed bubble flow. At an oil flow rate of 3.51 *kg/s* and an air flow rate of 0.020 *kg/s* the calculated pressure profile with the UCM formulation is very close to the experimental pressure values. The predicted flow pattern between

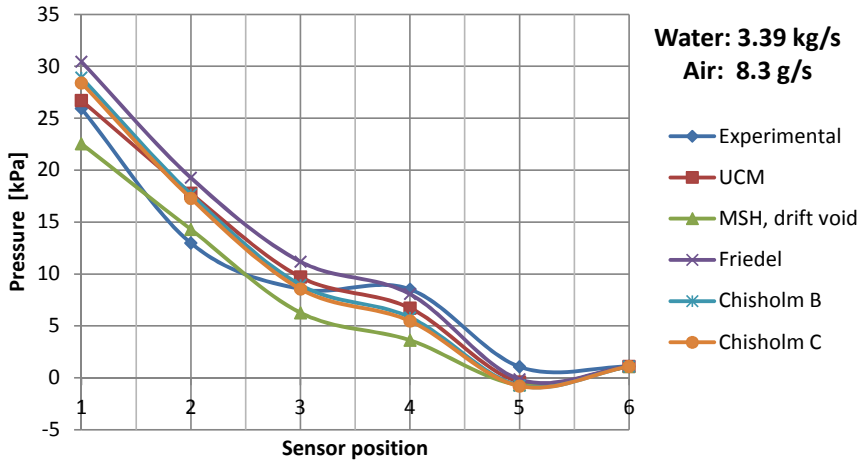

Figure 8.19: Pressure profile through shut-in valve for two-phase air-water flow.

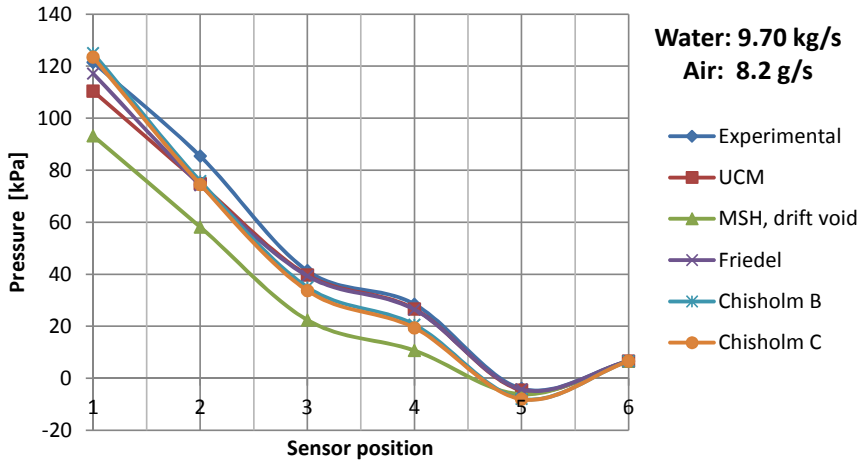

Figure 8.20: Pressure profile through shut-in valve for two-phase air-water flow.

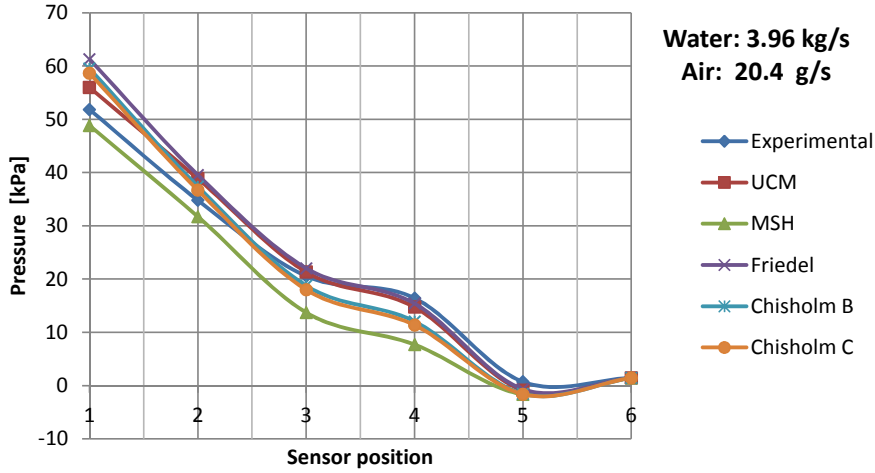

Figure 8.21: Pressure profile through shut-in valve for two-phase air-water flow.

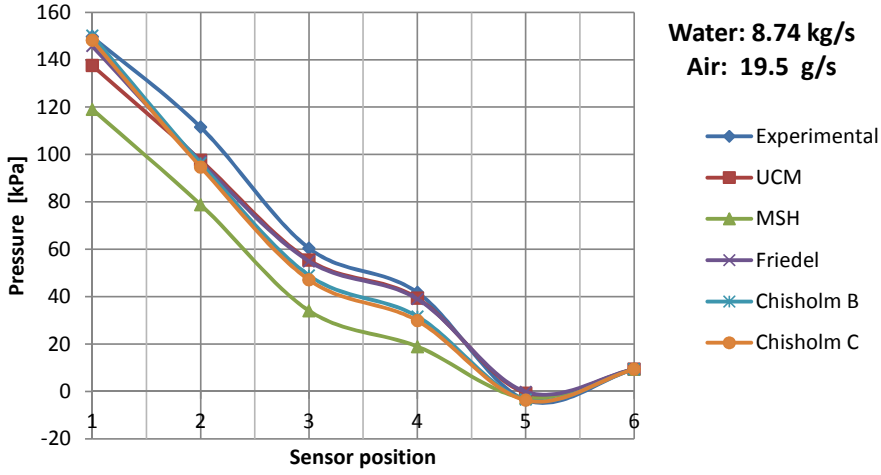

Figure 8.22: Pressure profile through shut-in valve for two-phase air-water flow.

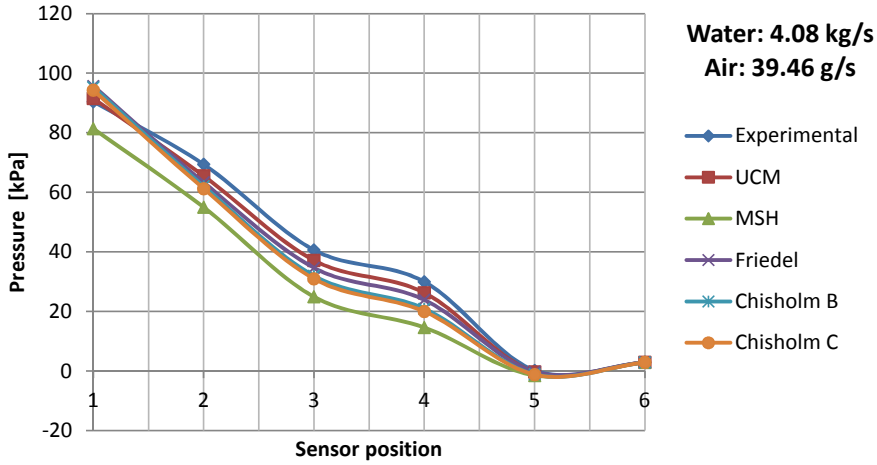

Figure 8.23: Pressure profile through shut-in valve for two-phase air-water flow.

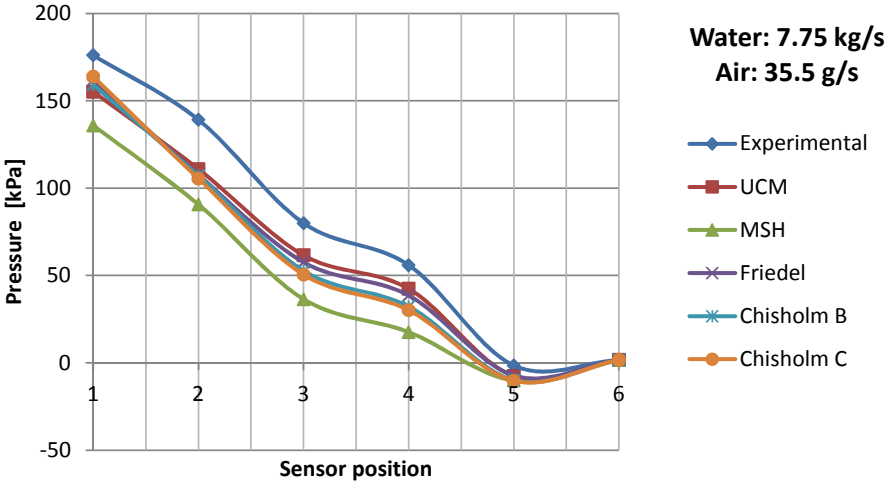

Figure 8.24: Pressure profile through shut-in valve for two-phase air-water flow.

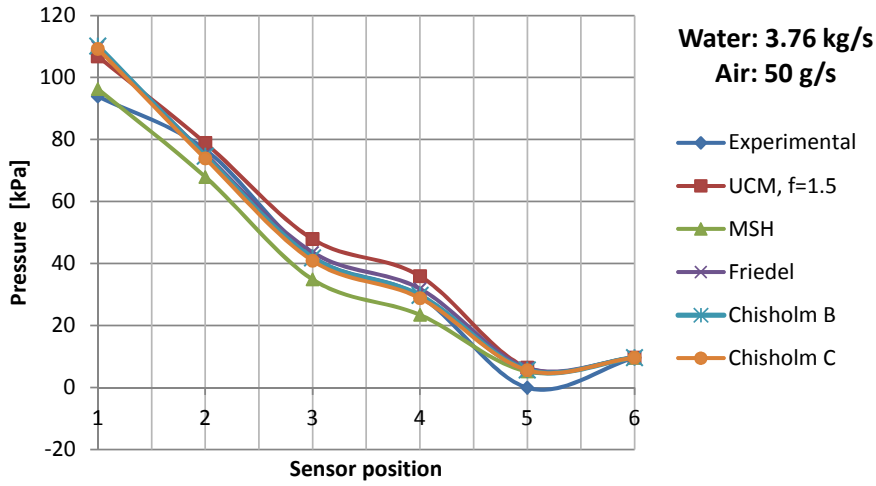

Figure 8.25: Pressure profile through shut-in valve for two-phase air-water flow.

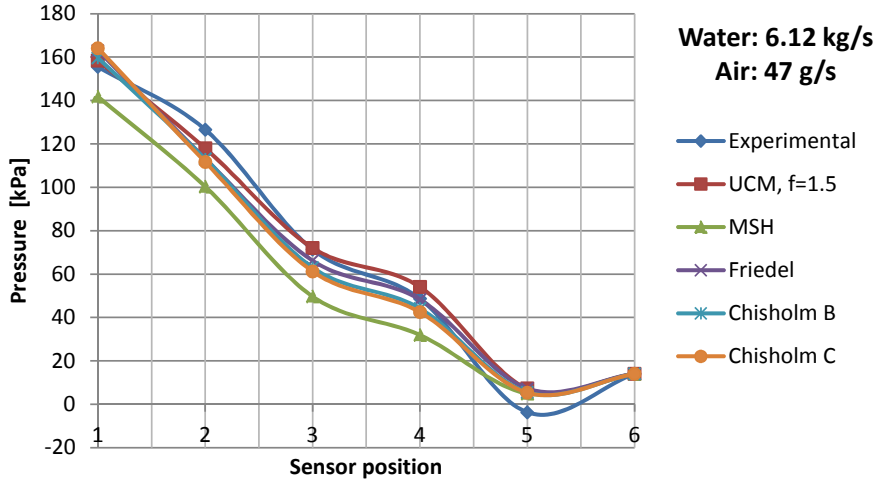

Figure 8.26: Pressure profile through shut-in valve for two-phase air-water flow.

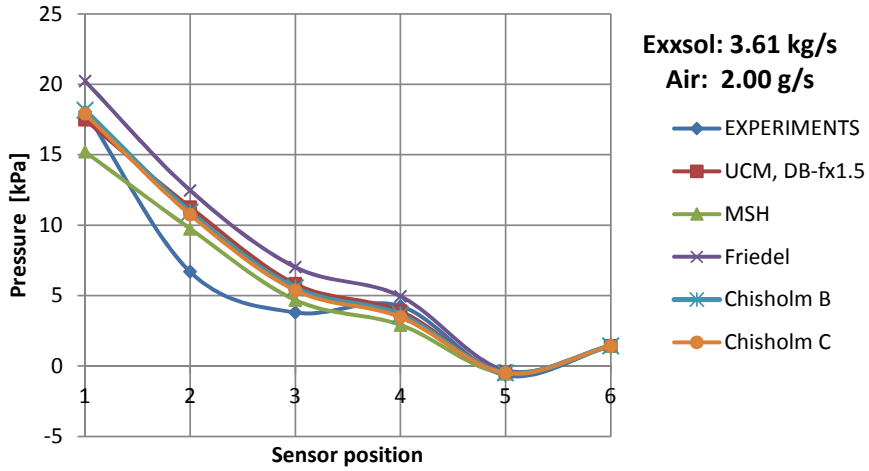

Figure 8.27: Pressure profile through shut-in valve for two-phase air-Exxsol D80 flow.

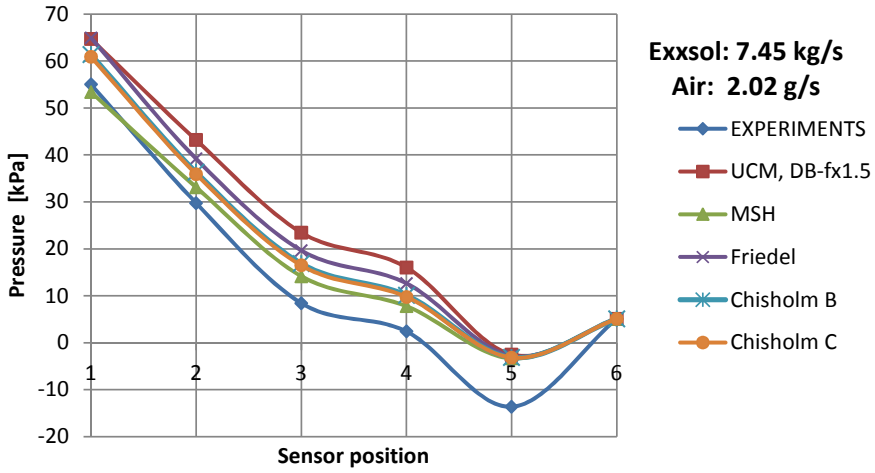

Figure 8.28: Pressure profile through shut-in valve for two-phase air-Exxsol D80 flow.

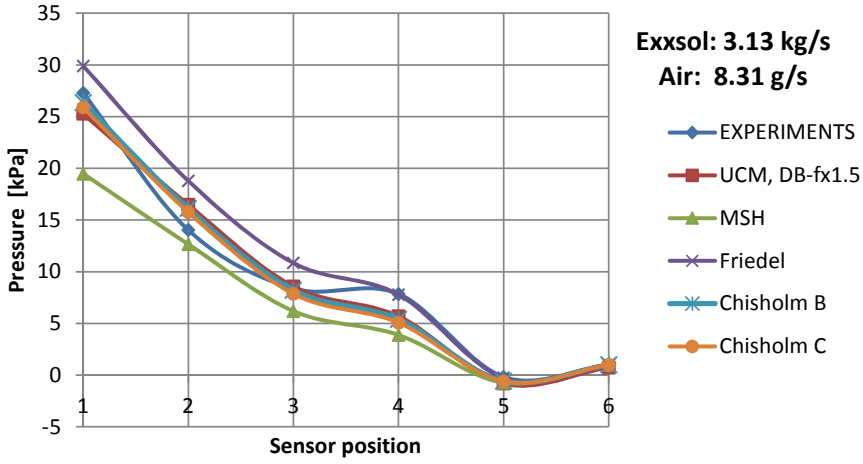

Figure 8.29: Pressure profile through shut-in valve for two-phase air-Exxsol D80 flow.

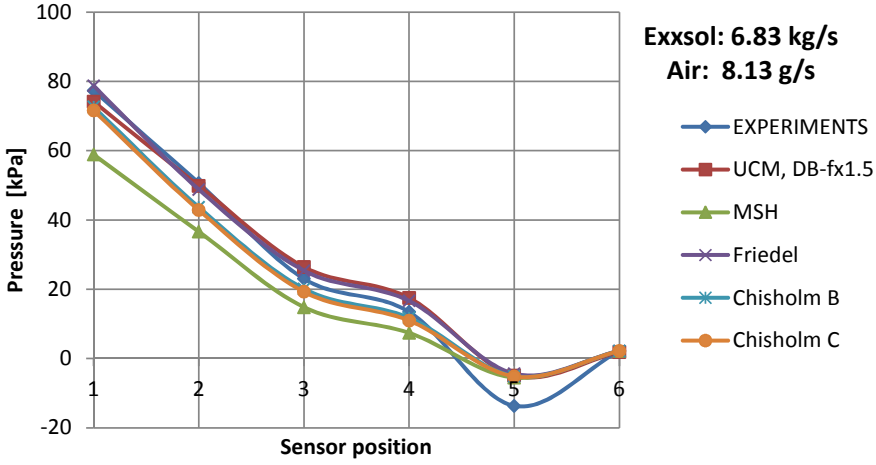

Figure 8.30: Pressure profile through shut-in valve for two-phase air-Exxsol D80 flow.

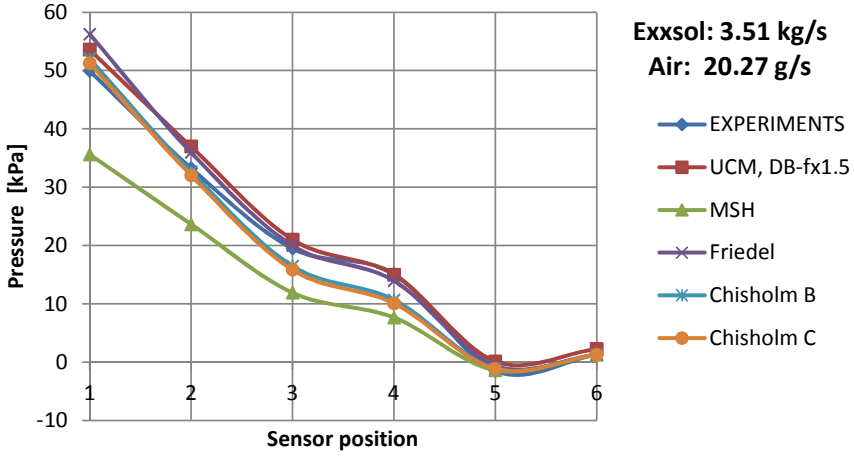

Figure 8.31: Pressure profile through shut-in valve for two-phase air-Exxsol D80 flow.

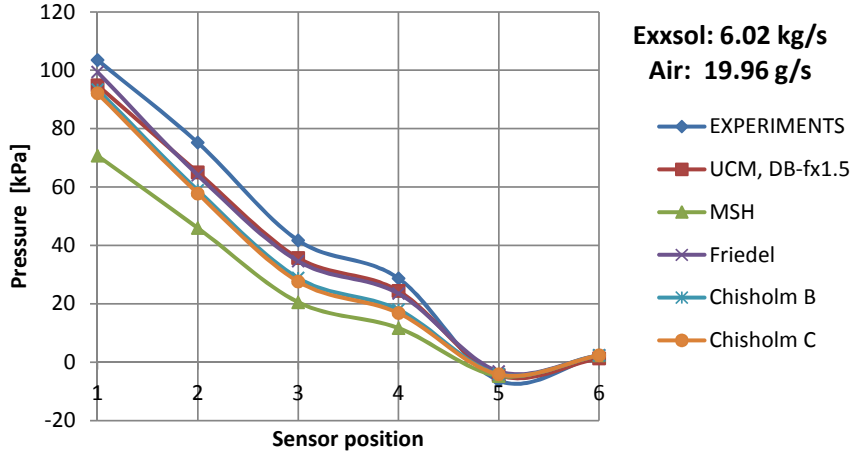

Figure 8.32: Pressure profile through shut-in valve for two-phase air-Exxsol D80 flow.

sensor 4 and 5 is now slug flow.

8.5 Conclusions

The main finding here is that it is possible to predict two-phase pressure drop in a valve section with good precision. A one-dimensional model has been developed for two-phase flow through a shut-in valve. Minor losses are derived from a CFD-simulation of incompressible flow, and the model uses the least squares method with spectral elements. In this work, the 1-D model is combined with the Unified Comprehensive Model formulation for two-phase flow. Flow patterns generated with this formulation are confirmed by experiments, and the overall pressure drop is simulated with an average deviation of -6.22% for air-water flow and -1.55% for air-Exxol D80 flow. A modified version of the UCM formulation has also been simulated, where the friction factor for dispersed bubble flow is increased with 50%. This version gives an average deviation of 3.12% for air-water flow and 3.62% for air-oil flow. The Chisholm correlations gives low deviation for air-oil flow but high deviation for air-water flow. The modified UCM formulation gives the best overall performance. The two-phase minor losses are well predicted by using homogeneous velocity and density, combined with loss factors derived from single-phase CFD simulations. The outlet sudden expansion pressure recovery is well predicted by using the Richardson correlation. There is however a maximum pressure recovery for low air flow rates that is not represented by the Richardson correlation. More research is needed in order to understand the mechanisms governing two-phase pressure recovery at sudden expansions.

Another important achievement here is the understanding of how to treat the different types of singularities in case of two-phase flow. For singularities with obstacles and for convective acceleration the flow can be regarded as homogeneous with equal phase velocities.

High-speed videos have also confirmed that the two-phase flow pattern develops very fast. Even at superficial air velocities of 50 *m/s* the characteristic slug flow pattern develops in a few pipe diameters. The use of the UCM formulation should therefore be justified.

The dispersed bubble flow pattern friction factor in the 40 *mm* pipe is found to be 50% higher than expected. More research on pressure drop and liquid holdup with this flow pattern is needed. It was assumed that the phase velocities were equal for dispersed bubble flow, but the deviation in pressure drop indicates that this is not the case here. If bubbles are concentrated near the pipe centerline, the average bubble velocity can be higher than the average liquid velocity. Studies of high-speed videos can be useful in this research.

Chapter 9

Oil-gas two-phase flow

Two-phase flow of oil and gas are simulated, using the developed 1-D-model. The standard fluid categories defined by Cronquist (1979) are used, and fluid properties are calculated with the computer program PVTsim (PVT). Some examples of two-phase oil-gas flow pressure drop are presented.

9.1 Petroleum reservoir classifications

Petroleum reservoir fluids are normally divided into five categories as defined by Cronquist (1979): dry gas, wet gas, gas condensate, volatile oil and black oil. Some typical compositions and properties for these fluids are provided by Whitson, see Table 9.1 The first three fluids are in a gaseous state in the reservoir. Gas condensate wells can produce small amounts of liquid (condensate), and the flow at the bottom of the well can be two-phase with the gas as the continuous phase. Volatile oil and black oil reservoirs can produce a two-phase flow at the well bottom if the pressure falls below the bubble-point pressure. Based on the given compositions, phase envelopes were calculated for volatile oil and black oil with the PVTsim software, see Figure 9.1 and Figure 9.2.

These phase envelopes were generated using the Soave-Redlich-Kwong (SRK) Peneloux equations of state (Dandekar 2006, p.410). With a typical reservoir temperature of 100^oC, the bubble point line for black oil tells that two-phase flow will exist below 215 *bar*. As the pressure is dropping below this pressure, more and more of the dissolved gas is liberated. For volatile oil, the bubble point pressure is approximately 280 *bar* at 100^oC.

Table 9.1
Typical compositions in mol % for reservoir fluids

Component / property	Dry Gas	Wet Gas	Gas Condensate	Volatile Oil	Black Oil
CO_2	0.1	1.41	2.37	1.82	0.02
N_2	2.07	0.25	0.31	0.24	0.34
C_1	86.12	92.46	73.19	57.6	34.62
C_2	5.91	3.18	7.8	7.35	4.11
C_3	3.58	1.01	3.55	4.21	1.01
iC_4	1.72	0.28	0.71	0.74	0.76
nC_4	-	0.24	1.45	2.07	0.49
iC_5	0.5	0.13	0.64	0.53	0.43
nC_5	-	0.08	0.68	0.95	0.21
C_{6s}	-	0.14	1.09	1.92	1.16
C_{7+}	-	0.82	8.21	22.57	56.4
GOR (SCF/STB)		69000	5965	1465	320
OGR (STB/MMSCF)	0	15	165	680	3125
γ_{API}		65	48.5	36.7	23.6
M_{7+}		132	184	240	274
γ_{7+}		0.75	0.816	0.864	0.92

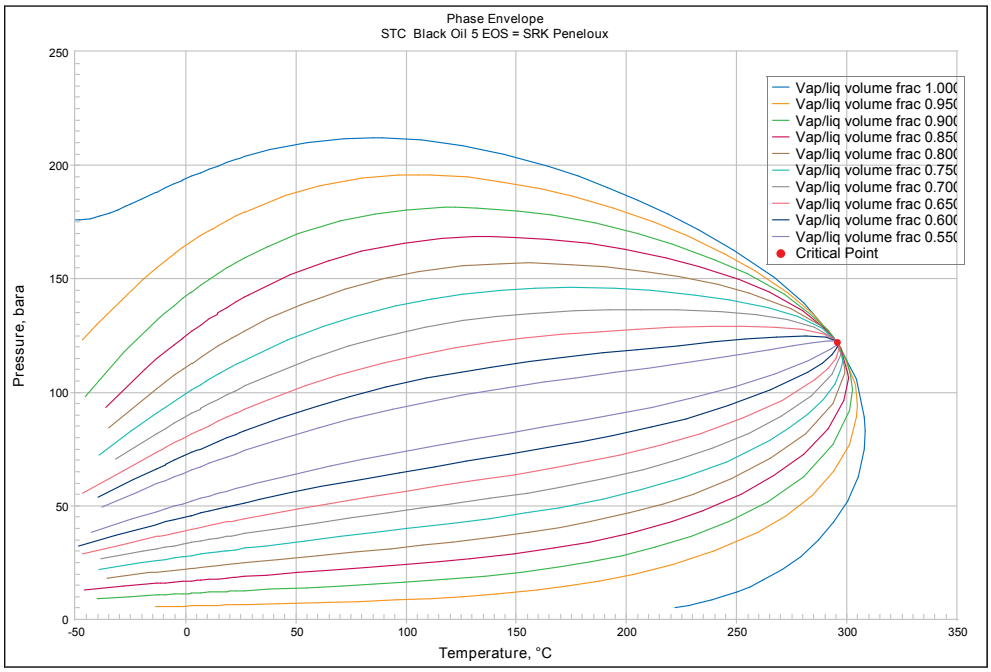

Figure 9.1: Black oil phase envelope.

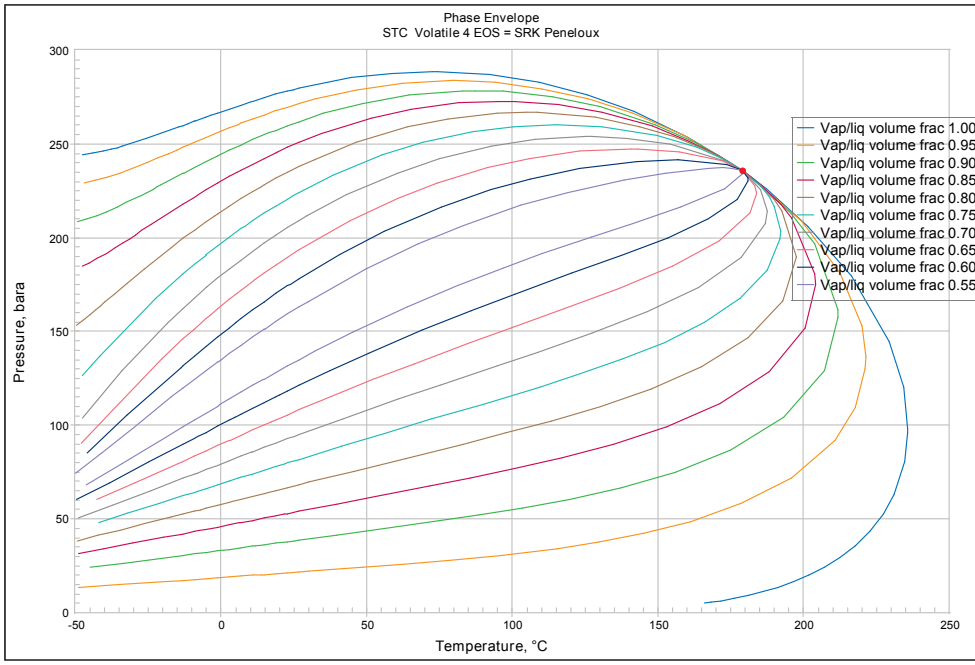

Figure 9.2: Volatile oil phase envelope.

9.2 Simulation setup

The simulation model is identical with the one used in the previous chapters. The 4.852m long valve model is here divided into 109 elements, and element lengths are less than 3 times the hydraulic diameter. As shown in Figure 6.4 for the verification of the simulation model the relative error is less than 1×10^{-4} in a case with only 3 elements per meter. The pipe diameter was in that case between 0.2 and 0.1 m. For the present simulations the order of approximation is 4.

9.3 Flow simulations

The 1-D model developed in this work depends on data for flow quality (vapor mass fraction), viscosity, density and surface tension. In order to simulate different types of crude oil flow, tables for each of these quantities were generated with the PVTsim software for a range of temperatures and pressures. The tables are exported from PVTsim as text-files, which are subsequently imported into a spreadsheet in Excel. These Excel-files are finally read by the MATLAB program with the 1D least squares spectral element model. Values for densities, viscosities and flow quality are then interpolated from the tables for each updated pressure in the iteration loop.

Some simulation results are provided here. In the first case flow of black oil is simulated. It is here assumed that the fluid entering the well has a composition as given in Table 9.1. Total pressure drop is calculated for a mass flow rate of 20 *kg/s* at different inlet temperatures and pressures, see Table 9.2. The valve section is assumed to be horizontal. The first simulation at each temperature is at

Table 9.2
Simulation of black oil flow in shut-in valve. Total mass flow rate is 20 *kg/s*.

	INLET					Outlet					
	Pressure	Mass flow		Density		Pressure	Mass flow		Density		ΔP
		Gas	Oil	Gas	Oil		Gas	Oil	Gas	Oil	
Temp:	[*kPa*]	[*kg/s*]		[*kg/m3*]		[*kPa*]	[*kg/s*]		[*kg/m3*]		[*kPa*]
50 °C	22500	0.000	20.000	175	782	22189	0.000	20.000	173	782	311
50 °C	21000	0.004	19.996	166	780	20660	0.024	19.976	164	781	340
50 °C	15000	0.531	19.469	116	805	14608	0.565	19.435	113	806	392
50 °C	10000	0.951	19.049	75	828	9494	0.993	19.007	71	830	506
100 °C	22500	0.000	20.000	157	732	22169	0.000	20.000	155	732	331
100 °C	21000	0.023	19.977	147	731	20636	0.065	19.935	144	733	364
100 °C	15000	0.683	19.317	102	761	14562	0.726	19.274	99	763	438
100 °C	10000	1.159	18.841	67	787	9412	1.213	18.787	63	790	588

pressures above the bubblepoint line, and is therefore a simulation of liquid flow. The experiments with air and water were performed with a density ratio at the inlet of minimum 500 at an inlet pressure of 1.7 *bar*. With black oil, the density ratio is only 780/166=4.7 at 50^oC and 210 *bar* inlet pressure. At 100 *bar* inlet pressure and 50^oC the density ratio has increased to 828/75=11.0. The pressure drop has now increased from 3.4 *bar* in the first case to 5.06 *bar*. Table 9.2 also shows that the mass flow of gas increases and the liquid flow decreases from inlet to outlet of the shut-in valve. The mass transfer from liquid to gas is higher for flow simulations at 100^oC, and the maximum pressure drop at 100 *bar* inlet pressure is 5.88 *bar*. The predicted flow pattern is dispersed bubble flow for all two-phase flows.

Simulations with volatile oil are presented in Table 9.3. The total mass flow is still 20 *kg/s*. The table shows that the liquid density of volatile oil varies more than the liquid density of black oil, and the mass fraction of gas increases more than for black oil. The pressure drop is also higher, with a maximum of 12.89 *bar* in the given table at 150^oC at 150 *bar* inlet pressure. The pressure level along the valve is shown in Figure 9.3. The flow pattern is here predicted to annular throughout the valve. The pressure profile at 250 *bar* inlet pressure is shown in Figure 9.4. The flow pattern is here predicted to be dispersed bubble flow. After the valve the flow pattern changes to slug flow.

From the Tables 9.2 and 9.3 we can see that volatile oil releases more gas than black oil, and this gives a much higher pressure drop for volatile oil. The gas/oil

Table 9.3
Simulation of volatile oil flow in shut-in valve. Total mass flow rate is 20 *kg/s*.

	INLET					Outlet					
	Pressure	Mass flow		Density		Pressure	Mass flow		Density		ΔP
		Gas	Oil	Gas	Oil		Gas	Oil	Gas	Oil	
Temp:	[*kPa*]	[*kg/s*]		[*kg/m3*]		[*kPa*]	[*kg/s*]		[*kg/m3*]		[*kPa*]
20 °C	30000	0.00	20.00	343.7	592.6	29593	0.00	20.00	343.2	591.8	407
20 °C	25000	1.42	18.58	300.9	611.5	24527	1.59	18.41	294.3	615.2	473
50 °C	30000	0.00	20.00	324.1	556	29567	0.00	20.00	322.1	554.9	433
50 °C	27500	0.91	19.09	300.5	565.6	27008	1.22	18.78	293.1	570.7	492
100 °C	30000	0.00	20.00	314	490.3	29509	0.00	20.00	311.2	488.5	491
100 °C	27500	1.52	18.48	284.9	502.4	26930	2.09	17.91	274.6	511.1	570
100 °C	15000	5.53	14.47	126.6	632.9	13884	5.68	14.32	115.8	642.4	1116
150 °C	30000	0.00	20.00	330.9	422.9	29431	0.00	20.00	328.8	420	569
150 °C	25000	4.49	15.51	279.3	438.5	24277	5.36	14.64	261.8	454.8	723
150 °C	20000	6.96	13.04	190.6	521	19050	7.13	12.87	178.1	532.7	950
150 °C	15000	7.70	12.30	131.9	577.6	13711	7.87	12.13	118.9	590.9	1289

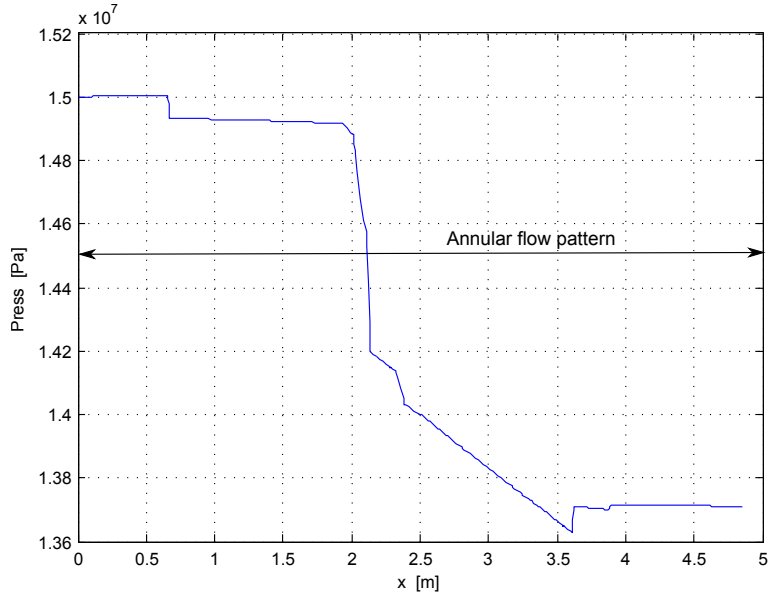

Figure 9.3: Pressure profile for STC shut-in valve at 20 *kg/s* of total mass flow rate with volatile oil. 150 *bar* inlet pressure.

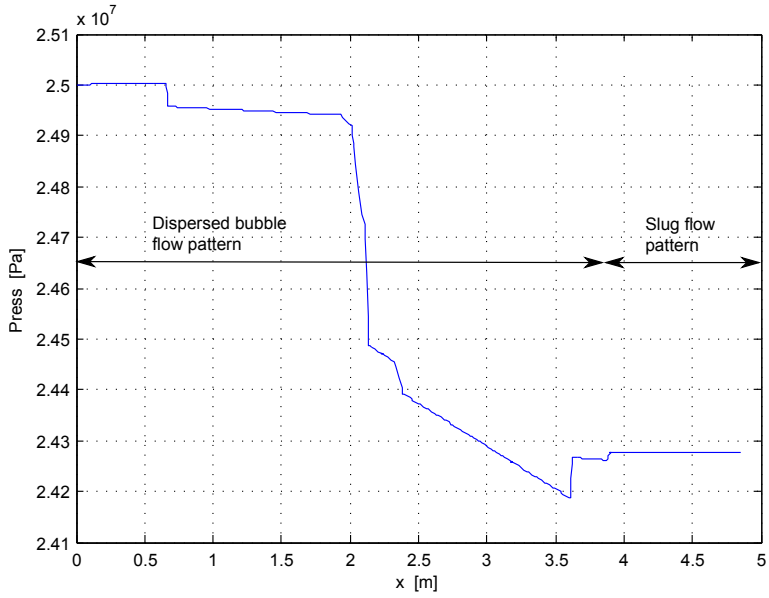

Figure 9.4: Pressure profile for STC shut-in valve at 20 *kg/s* of total mass flow rate with volatile oil. 250 *bar* inlet pressure.

mass balance however changes very little, even for volatile oil.

In Figure 9.5 the total pressure drop across the STC shut-in valve is given for a total mass flow of volatile oil of 20 *kg/s*. The pressure drop is given for various pressures and temperatures together with predicted flow patterns. The trend here is that high temperature and low pressure gives the highest pressure drop. From Figure 9.2 we can see that this condition gives the highest gas flow rate, and as expected this leads to an annular flow pattern. The curve for 100^oC shows a dip in pressure drop at 20000 *kPa*, and here slug flow is predicted trough the whole valve section. At 25000 *kPa* the gas flow rate is lower, but the overall pressure drop is a little higher as dispersed flow pattern is predicted. At 30000 *kPa* the fluid is liquid only at all temperatures. From Table 9.3 we can see that the oil density at 30000 *kPa* changes from 596 kg/m^3 at 20^oC to only 423 kg/m^3 at 150^oC, and that is the reason why the pressure drop increases with increasing temperature even if the viscosity is lower at higher temperatures.

9.4 Conclusions

The two-phase flow of oil and gas in the shut-in valve can be simulated using the 1-D least squares spectral element model. Properties of crude oil and gas can be imported as tables prepared with a PVT software program. Simulations show that

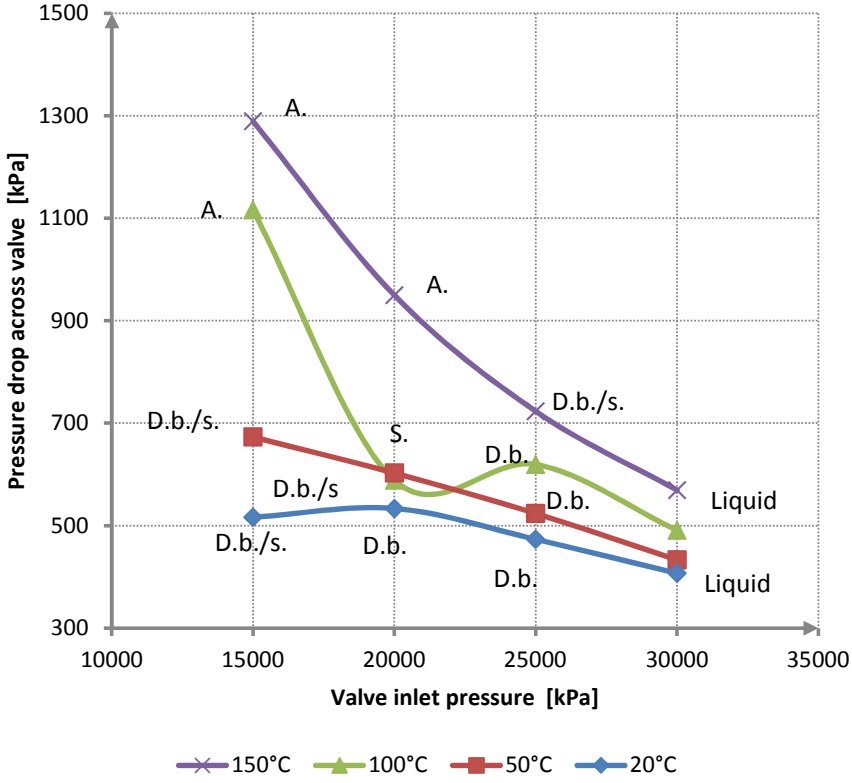

Figure 9.5: Pressure drop across STC shut-in valve for a total mass flow of volatile oil of 20 *kg/s*. Flow pattern abbrevations: A: Annular, D.b./s.: Dispersed bubble/slug, S.: Slug, D.b.: Dispersed bubble.

flow of volatile oil will give larger pressure drops than flow of black oil at equal total mass flow rate. The reason is that volatile oil releases more gas as pressure decreases. The liquid density of volatile oil is also lower than the liquid density of black oil.

Chapter 10

Summaries of papers and articles

Two papers and three articles have been written during this PhD project, and a brief presentation of them are given here.

10.1 Paper: Two-phase flow in a down-hole valve

S.Edvardsen, C.A.Dorao and O.J.Nydal. *The 9th North American Conference on Multiphase Technology*, Banff, Canada 11th-13th June 2014. 2014-H1 BHR Conference paper -2014.

In this paper the total pressure drop over the shut-in valve is simulated using CFD software ANSYS Fluent. Results are compared to experimental values, and for liquid flow the deviation is only 3-6%. Airflow pressure drop was simulated with a deviation of 7% at the highest flow rates. Two-phase flow pressure drop was estimated using several flow pattern independent correlations. The Chisholm B-coefficient correlation and the Müller-Steinhagen and Heck correlation provided the best comparison with a deviation of 20-30%

My contribution: All experimental and theoretical work. I also presented the paper at the conference. Professor Nydal contributed with inspiration and guidance on the experimental setup.

10.2 Article: Experimental and numerical study of single-phase pressure drop in downhole shut-in valve

S.Edvardsen, C.A.Dorao and O.J.Nydal. Journal of Natural Gas Science and Engineering 22 (2015) 214-226. http://dx.doi.org/10.1016/j.jngse.2014.11.034

A 1D model for single phase flow in the shut-in valve is developed. Minor loss

coefficients for partial pressure losses are derived from 3-dimensional CFD simulations. The realizable $k-\varepsilon$ turbulence model was found to give the best results for the single phase pressure drop. The 1-D model is based on a least squares spectral element model. Simulated total as well as partial pressure losses provides good comparison with experimental results.

My contribution: All experimental and theoretical work. The mathematical framework for the least-squares spectral element model was provided by Professor C.A. Dorao.

10.3 Paper: Multiphase flow in complex valve geometry

S.Edvardsen, C.A.Dorao and O.J.Nydal. *3rd Trondheim Gas Technology Conference*, 4-5 June 2014. Published in *Elsevier Energy Procedia*.

In this work the developed 1D model is applied to simulation of two-phase flow in the shut-in valve. Two-phase pressure drop is calculated using well-known flow-pattern independent correlations like the Chisholm correlations, the Friedel correlation and the Müller-Steinhagen and Heck correlation. With the assumption of equal phase velocities, the last correlation gave two-phase pressure drop with only 10.5% deviation for air-water flow and only 12% deviation for air-oil two-phase flow.

My contribution: All experimental and theoretical work. I also presented the paper at the conference.

10.4 Article: Sudden expansion and two-phase flow pattern transition in pressure recovery zone

S.Edvardsen, C.A.Dorao and O.J.Nydal. Submitted

The two-phase pressure recovery after a sudden expansion is studied in this article. The pressure recovery is investigated theoretically, and a number of known correlations are tested for predicting the downstream pressure buildup. Theoretical pressure recovery values are compared to experimental results obtained with a full scale mock-up, with tube diameter 40 *mm* with expansion to 90 *mm*, and liquid Reynolds numbers between 64000 and 255000. Above a specific gas flow rate the pressure recovery is reduced, and at the same time the downstream flow pattern is changed into a liquid jet stream surrounded by air. The Richardson correlation is found to give the best prediction of the two-phase pressure recovery.

My contribution: All experimental and theoretical work.

10.5 Article: Experimental and numerical study of two-phase pressure drop in downhole shut-in valve; Unified Comprehensive Model formulation

S.Edvardsen, C.A.Dorao and O.J.Nydal. Journal of Natural Gas Science and Engineering 23 (2015) 440-449. http://dx.doi.org/10.1016/j.jngse.2015.02.024

The 1D least squares spectral element model is here combined with the Unified Comprehensive Model formulation (UCM) for two-phase flow. The UCM formulation for two-phase flow identifies first the flow pattern, and applies subsequently the appropriate pressure drop calculation. The 1D-UCM formulation simulations provides good comparison with the experimental data. The average deviation for pressure drop is -8.6% for air-water flow and -9.3% for air-oil flow.

My contribution: All experimental and theoretical work.

Chapter 11

Conclusions and outlook for future work

In this work, a methodology for estimating the two-phase pressure drop along a complex geometry like a downhole shut-in valve was developed. In order to solve this problem a novel 1-D model has been established based on CFD simulations. The two phase flow behavior in the different sections of the valve has been studied and the results are incorporated in the 1-D model. The methodology developed here for two-phase flow has been validated by performing an extensive experimental study. Some concluding remarks will here be given together with recommendations for further research.

11.1 Conclusions

The single phase flow of gas or liquid can be simulated with a CFD program like ANSYS Fluent. Good precision can be attained provided that the mesh is carefully designed and that the *realizable k-ε* turbulence model is used. A representative pressure profile along the valve can be found by calculating cross-section average pressures. This pressure profile can subsequently be used for calculating minor pressure loss factors across singularities like bends, contractions and orifices. The 1-D model developed here uses a novel 1-D least-squares spectral element method. It was validated with single phase flow experiments on a full scale valve mock-up. The simulations converges algebraically for increasing numbers of elements and they converge exponentially for increasing approximation order.

The 1-D model can be combined with flow pattern independent correlations. The overall two-phase pressure loss can be calculated with a deviation of 10-12% by

using the Müller-Steinhagen and Heck correlation.

An important achievement of this study is the findings regarding two-phase minor losses. Two-phase pressure losses across singularities can be expressed by the same minor loss factors as for single phase flow by taking the density as the no-slip average density. Convective acceleration can be calculated in the same manner. The prediction of two-phase pressure recovery at sudden expansions is however more complicated and not fully understood. The Richardson correlation is found to give the best approximation of pressure recovery.

The pressure drop for dispersed bubble flow pattern was found to be some 50% larger than expected. One reason for this discrepancy might be that the phase velocities are not equal as assumed. For horizontal flow equal phase velocities is only possible if the gas bubbles are evenly distributed over the pipe cross section. The results from this study indicates that the average bubble velocity is lower than the average liquid velocity.

The Unified Comprehensive Model formulation gives the best precision for the frictional pressure losses. This model formulation unifies flow models for horizontal, inclined and vertical flow. It is called comprehensive because it has both a flow pattern prediction part and flow models for each flow pattern. Predicted flow patterns at the valve inlet were confirmed by experiments.

The least squares spectral element model was found to be an effective model for solving the 1-D equations. Element refinement can easily be achieved by increasing the element order.

The main achievement is the complete methodology for simulating two-phase pressure drop in complex geometries. As such this methodology should be applicable to all kinds of flow geometries. With the implementation of real oil and gas properties this 1-D model should be suitable for the simulation of well flow with tools and singularities.

Simulations with real oil and gas properties for volatile oil and black oil shows that the liquid/gas density ratio is low compared to density ratio for oil and air used in laboratory experiments. The pressure drop across the valve section will cause a mass transfer from liquid to gas known as *flashing*. The pressure drop is higher for volatile oil than for black oil at equal mass flow rates due to a larger gas content.

11.2 Outlook for future work

The sudden expansion at the valve outlet is a special source of two-phase pressure loss. The pressure recovery increases with increasing air flow up to a specific limit and then it drops again to a lower level for higher air flows. This behavior

was observed for horizontal and slightly inclined flow. Pressure recovery at sudden expansion should also be studied for inclined and vertical flow. The effect of increased system pressure should also be investigated.

Simulations of oil and gas flow should be validated by experiments. Such experiments should also investigate whether the Richardson correlation for pressure recovery at sudden expansion can be used for oil and gas or not.

The dispersed bubble flow pattern also needs more attention. The common approach for horizontal flow is to calculate the liquid holdup as if the phase velocities are equal. This might not be the case if for instance the bubble volume concentration is highest along the pipe wall. A more detailed study of dispersed bubble flow is necessary.

Bibliography

Pvtsim nova. URL www.calsep.com.

Openteach 3d visualizer of molecular structure demonstration. Web, December 2014. URL http://competentum.com/chemml/demo/.

3d cad, 2014. URL http://www.solidworks.com/.

Claudio Alimonti, Gioia Falcone, and Oladele Bello. Two-phase flow characteristics in multiple orifice valves. *Experimental Thermal and Fluid Science*, 34(8):1324 – 1333, 2010. ISSN 0894-1777. doi: http://dx.doi.org/10.1016/j.expthermflusci.2010.06.004. URL http://www.sciencedirect.com/science/article/pii/S0894177710001160.

I.M Alves, E.F. Caetano, K. Minami, and O. Shoham. Modeling annular flow behavior for gas wells. *SPE Production Engineering*, 6(SPE-20384-PA):435–440, 1991. doi: http://dx.doi.org/10.2118/20384-PA.

R. Amirante, G. Del Vescovo, and A. Lippolis. Evaluation of the flow forces on an open centre directional control valve by means of a computational fluid dynamic analysis. *Energy Conversion and Management*, 47:1748 – 1760, 2006. ISSN 0196-8904. doi: http://dx.doi.org/10.1016/j.enconman.2005.10.005. URL http://www.sciencedirect.com/science/article/pii/S0196890405002542.

ANSYS. Ansys fluent theory guide, 2014 .

A. Attou and L. Bolle. A new correlation for the two-phase pressure recovery downstream from a sudden enlargement. *Chemical Engineering & Technology*, 20(6):419–423, 1997. ISSN 1521-4125. doi: 10.1002/ceat.270200610. URL http://dx.doi.org/10.1002/ceat.270200610.

S.G. Bankoff. A simple friction pressure drop correlation for two-phase flow in pipes. *Chem. Engn. Progr.*, 20:297–308, 1960.

D. Barnea, O. Shoham, Y. Taitel, and A.E. Dukler. Gas-liquid flow in inclined tubes: Flow pattern transitions for upward flow. *Chemical Engineering Science*, 40(1):131 – 136, 1985. ISSN 0009-2509. doi: http://dx.doi.org/10.1016/0009-2509(85)85053-3. URL http://www.sciencedirect.com/science/article/pii/0009250985850533.

Kjell H. Bendiksen. An experimental investigation of the motion of long bubbles in inclined tubes. *International Journal of Multiphase Flow*, 10(4):467 – 483, 1984. ISSN 0301-9322. doi: http://dx.doi.org/10.1016/0301-9322(84)90057-0. URL http://www.sciencedirect.com/science/article/pii/0301932284900570.

I.Y. Chen, S. Wongwises, B.C. Yang, and C.C. Wang. Two-phase flow across small sudden expansions and contractions. *Heat Transfer Engineering*, 31 (4):298–309, 2010. doi: 10.1080/01457630903312056. URL http://www.tandfonline.com/doi/abs/10.1080/01457630903312056.

Ezequiel Manavela Chiapero. *Two-phase flow instabilities and flow maldistribution in parallel channels*. PhD thesis, Norwegian University of Science and Technology, 2013.

D. Chisholm. A theoretical basis for the lockhart-martinelli correlation for two phase flow. *Int. J. Heat Mass Transfer*, 10:1767–1778, 1967.

D. Chisholm. *Two-phase flow in pipelines and heat exchangers*. George Godwin, London, 1983.

D. Chisholm and L.A. Sutherland. Prediction of pressure gradients in pipeline system during two-phase flow. In *Proceedings of the Institution of Mechanical Engineers, Conference Proceedings 184:24*, volume 184, Pt. 3C, pages 24–32, 1969.

A. Cicchitti. Two-phase cooling experiments - pressure drop, heat transfer, and burnout measurements. *Energie Nucleare*, 7(6):407–425, 1960.

John Wesley Coleman. An experimentally validated model for two-phase sudden contraction pressure drop in microchannel tube headers. *Heat Transfer Engineering*, 25(3):69–77, 2004. doi: 10.1080/01457630490280335. URL http://www.tandfonline.com/doi/abs/10.1080/01457630490280335.

C. Cronquist. Evaluating and producing volatile oil reservoirs. *World Oil*, pages 159–166, April 1979.

A.S. Dalkilic, S. Laohalertdecha, and S. Wongwises. Effect of void fraction models on the two-phase friction factor of r134a during condensation in vertical downward flow in a smooth tube. *Int. Commun. Heat Mass Transfer*, 35:921–927, 2008.

Abhijit Y. Dandekar. *Petroleum Reservoir Rock and Fluid Properties*. Taylor and Francis Group, 2006. ISBN 0-8493-3043-2. URL `http://www.taylorandfrancis.com`.

J.M. Delhaye. *Singular pressure drop, in: Two-Phase and Heat Transfer in the Power and Process Industries*. Hemisphere, Washington, DC,, 1981.

S. Edvardsen, C.A. Dorao, and O.J. Nydal. Two-phase flow in a down-hole shut-in valve. In *The 9th North American Conference on Multiphase Technology, Bannf, Canada*, 2014.

N. Eskin and E. Deniz. Pressure drop of two-phase flow through horizontal channel with smooth expansion. In *International Refrigeration and Air Conditioning Conference*, number Paper 1255, 2012. URL `http://docs.lib.purdue.edu/iracc/1255`.

L. Friedel. Improved friction pressure drop correlations for horizontal and vertical two-phase pipe flow. *European Two-Phase Flow Group Meeting, Ispra, Italy*, June 1979.

L.E. Gomez, O. ShoO. Shoham. Schmidt, R.N. Chokshi, and T. Northug. Unified mechanistic model for steady-state two-phase flow: Horizontal to vertical upward flow. In *SPE65705*, 2000.

Rodolfo Phillips Guerrero and Jacques Lessi. Fast shut-in tools improve near wellbore characterisation from build-up test interpretation. *Fast Shut-in Tools*, pages 163–197, May 2007. URL `http://www.onepetro.org/mslib/app/search.do`.

A. R. Hasan and C. S. Kabir. A study of multiphase flow behavior in vertical wells. . *SPE Production Engineering*, 3:263–272, 1988. doi: http://dx.doi.org/10.2118/15138-PA.

William H. Henstock and Thomas J. Hanratty. The interfacial drag and the height of the wall layer in annular flows. *AIChE Journal*, 22(6):990–1000, 1976. ISSN 1547-5905. doi: 10.1002/aic.690220607. URL `http://dx.doi.org/10.1002/aic.690220607`.

G.F. Hewitt and P.B. Whalley. *Multiphase Flow and Pressure drop, Heat Exchanger Design Handbook*, volume 2. Hemisphere, Washington D.C., 1980, 1983.

M. Ishii. One dimensional drift-flux model and constitutive equations for relative motion between phases in various two-phase flow regimes. Technical Report Report ANL-77-47, Argonne National Laboratory, Argonne, IL, October 1977.

JGCM/WG1. Evaluation of measurement data - guide to the expression of uncertainty in measurement, 1995. JCGM 100:2008 (GUM 1995).

Seungjin Kim, Gunol Kojasoy, and Tangwen Guo. Two-phase minor loss in horizontal bubbly flow with elbows: 45 deg. and 90 deg. elbows. *Nuclear Engineering and Design*, 240(2):284 – 289, 2010. ISSN 0029-5493. doi: 10.1016/j.nucengdes.2008.08.019. URL http://www.sciencedirect.com/science/article/pii/S0029549308004640. Twelfth International Topical Meeting on Nuclear Reactor Thermal Hydraulics (NURETH-12).

B.E. Launder and D.B. Spalding. The numerical computation of turbulent flows. *Computer Methods in Applied Mechanics and Engineering*, 3:269–89, 1974.

Z. Leutwyler and C. Dalton. A cfd study of the flow field, resultant force, and aerodynamic torque on a symmetric disk butterfly valve in a compressible fluid. *Journal of Pressure Vessel Technology*, 130(2):021302–021302, Mars 2008. ISSN 0094-9930. doi: 10.1115/1.2891929. URL http://dx.doi.org/10.1115/1.2891929.

R.W. Lockhart and R.C. Martinelli. Proposed correlation of data for isothermal two-phase two-component flow in pipes. *Chem. Engn. Progr.*, 45(1):39–48, 1949.

P.A. Lottes. Expansion losses in two-phase flow. *Nucl. Sci. Engn.*, 9:26–31, 1961.

H. Müller-Steinhagen and K. Heck. A simple friction pressure drop correlation for two-phase flow in pipes. *Chem. Engn. Progr.*, 20:297–308, 1986.

B.R. Munson, D.F. Young, and T.H. Okiishi. *Fundamentals of Fluid Mechanics*. John Wiley & Sons, Inc., 5th edition, 2006.

Shut-in Tool. Omega Completion Technology Ltd., January 2015. URL http://www.sparteksystems.com.

L.B. Ouyang and K.Aziz. Development of new wall friction factor and interfacial friction factor correlations for gas-liquid stratified flow in wells and pipelines.

In *PE Western Regional Meeting, 22-24 May, Anchorage, Alaska*, number SPE-35679-MS, 1996. ISBN 978-1-55563-427-8. doi: http://dx.doi.org/10.2118/35679-MS.

M.M.J. Proot and M.I. Gerritsma. Least-squares spectral eelement applied to the stokes problem. *Journal of Comp. Phys.*, 181(2):454–477, 2002. doi: 10.1006/jcph.2002.7137.

B. Richardson. *Some Problems in Horizontal Two-Phase, Two-Component Flow*. PhD thesis, University Chicago, Chicago, IL, 1958.

F. Romie. (american standard co.). Private communication to Lottes, 1958.

Manmatha K. Roul and Sukanta K. Dash. Two-phase pressure drop caused by sudden flow area contraction and expansion in small circular pipes. *International Journal for Numerical Methods in Fluids*, 66(11):1420–1446, 2011. ISSN 1097-0363. doi: 10.1002/fld.2322. URL `http://dx.doi.org/10.1002/fld.2322`.

J. Schmidt and L. Friedel. Two-phase flow pressure change across sudden expansions in duct areas. *Chem. Eng. Comm.*, 141-142:175–190, 1996.

J. Schmidt and L. Friedel. Two-phase pressure drop across sudden contractions in duct areas. *International Journal of Multiphase Flow*, 23(2):283 – 299, 1997. ISSN 0301-9322. doi: 10.1016/S0301-9322(96)00056-0. URL `http://www.sciencedirect.com/science/article/pii/S0301932296000560`.

S.L. Scott, O. Shoham, and J.P. Brill. Prediction of slug length in horizontal large-diameter pipes. In *SPEPE*, page 335, August 1989.

T-H. Shih, WW. Liou, A. Shabbir, Z. Yang, and J. Zhu. A new kŰe eddy-viscosity model for high reynolds number turbulent flows Ű model development and validation. *Comput Fluids*, 24:227–38, 1995.

Ovadia Shoham. *Mechanistic Modeling of Gas-Liquid Two-Phase Flow in Pipes*. Society of Petroleum Engineers Inc., 2006.

Shut-in Tool. Spartek Systems, Jan. 2015. URL `http://www.omega-completion.com`.

F. Sporleder. *Simulation of Chemical Reactors using the Least-Squares Spectral Element method*. PhD thesis, Norwegian University of Science and Technology, 2011.

P.K. Swamee and A.K. Jain. Explicit equations for pipe-flow problems. *Journal of the Hydraulics Division*, 102(5):657–664, May 1976.

J.R.S. Thom. Prediction of pressure drop during forced circulation boiling of water. *Int. J. Heat Mass Transfer*, 7:709–724, 1964.

John R. Thome. *Engineering Data Book III*. Faculty of Engineering Science and Technology, Swiss Federal Institute of Technology Lausanne (EPFL), CH-1015 Lausanne, Switzerland, 2014. URL www.wlv.com.

The Pennsylvania State University. Png 520, phase relations in reservoir engineering. viewed June 16. 2011, 2008. URL https://www.e-education.psu.edu/png520/resources/l1.html.

K. van Terzaghi. Die berechnung der durchlassigkeitsziffer des tones aus dem verlauf der hydrodynamishen spannungserscheinungen. *Sber. Akad. Wiss.*, 130 (105), 1923.

M. Wadle. A new formula for the pressure recovery in an abrupt diffusor. *International Journal of Multiphase Flow*, 15(2):241 – 256, 1989. ISSN 0301-9322. doi: http://dx.doi.org/10.1016/0301-9322(89)90073-6. URL http://www.sciencedirect.com/science/article/pii/0301932289900736.

G.B. Wallis. *One-dimensional two-phase flow*. McGraw-Hill, 1969. URL http://books.google.no/books?id=xvFQAAAAMAAJ.

C.H. Whitson. *Development Geology Reference Manual*. The American Association of Petroleum Geologists, Tulsa, Oklahoma, U.S.A. AAPG Methods in Exploration Series, No. 10.

Curtis H. Whitson and Michael R. Brulé. *Phase Behavior*. Society of Petroleum Engineers Inc., Richardson, Texas, 2000. ISBN 1-55563-087-1.

V. Yakhot and S.A. Orszag. Normalization group analysis of turbulence. i. basic theory. *Journal of Scientific Computing*, 1:1–51, 1986.

L. Zhuo, Y. Jian, and M. ChongFang. Characteristics of pressure drop for single-phase and two-phase flow across sudden contraction in microtubes. *Science in China Series E: Technological Sciences*, 51:162–169, 2008. ISSN 1006-9321. URL http://dx.doi.org/10.1007/s11431-007-0030-4. 10.1007/s11431-007-0030-4.

Anatoly B. Zolotukhin and Jann-Rune Ursin. *Introduction to Petroleum Reservoir Engineering*. Høyskoleforlaget, 2000. URL http://www.hoyskoleforlaget.no.

N. Zuber and J. Findlay. Average volumetric concentration in two-phase flow systems. *J. Heat Transfer*, 87:453, 1965.

Two-phase flow in a down-hole shut-in valve

S Edvardsen, C A Dorao, O J Nydal
Norwegian University of Science and Technology, Department of Energy and Process Engineering, Norway

ABSTRACT

Oil and gas reservoirs are tested by performing a shut-in test. A new down-hole shut-in valve has been installed in a multiphase flow loop and the pressure drop over the valve has been investigated for single phase and two phase flows. The flow path through the valve is a 3 meter long narrow channel, partially annular and partially circular, with several minor losses. CFD simulations of single phase liquid flow correspond well with experimental data. Two-phase pressure loss estimates based on common two-phase pressure loss multipliers are compared with experimental data. The absolute average percent error was 20-30% for some of the correlations.

Nomenclature

Symbols

p	pressure	(Pa)
Δp	pressure drop	(Pa)
X	Lockhart-Martinelli parameter	(-)
x	flow quality (gas mass flow / total mass flow)	(-)
$\varphi_{(\ )}$	pressure drop multiplier	(-)
C	Chisholm C-parameter	
B	Chisholm B-parameter	
n	Blasius exponent for friction factor equation	
ρ	density	$(\frac{kg}{m^3})$
μ	viscosity	$(\frac{N}{m^2 s})$
Γ	physical properties coefficient	
G	mass flux	$(\frac{kg}{m^2 s})$
f	friction factor	
g	acceleration of gravity	(m/s²)
v	flow velocity	(m/s)
A	cross sectional area	(m²)
z	coordinate along the flow path	(m)

Subscripts

L	liquid
Total	sum of liquid and gas
G	gas
TF	two-phase
FL	frictional-liquid
FL0	frictional, assuming total mass flux as liquid
FG	frictional-gas
FG0	frictional, assuming total mass flux as gas
H	homogeneous
Loss	overall loss factor for minor losses

1 INTRODUCTION

Well testing is necessary in order to establish a reservoir model. This model can among other things provide data about initial reservoir pressure, area being drained, permeability and mechanical skin factor. During a well test, pressure and temperature at reservoir level in the well are recorded for a sequence of different flow rates (1).

Because of flow resistance in the porous and permeable rock formation, well bottom pressure will decrease with increasing flow rate. In the pressure drawdown test, the well is producing at a given flow rate, and the well bottom pressure will after some time approach a minimum level. In the pressure build-up test, the well is shut-in, either at the wellhead or with a valve downhole. The curve of pressure vs. time (or flow rate) for a pressure drawdown test followed by a shut-in test is of vital interest for the reservoir engineer. Downhole shut-in tests have proved to give more precise information about the oil bearing rock formation (2). If the well is shut-in at the surface, the whole volume of the wellbore must also be pressurized by oil and gas flowing from the reservoir. Well pressure will therefore increase at a slower pace, and vital information about the near-wellbore region can be lost. However, more information is needed about multiphase pressure drop in the new shut-in valve in order to determine the impact on the well-test.

The well flow will in many cases be multiphase, with water, oil, gas and particles. Figure 1 : Phase envelope and reservoir shows a phase envelope, with the typical reservoir types.

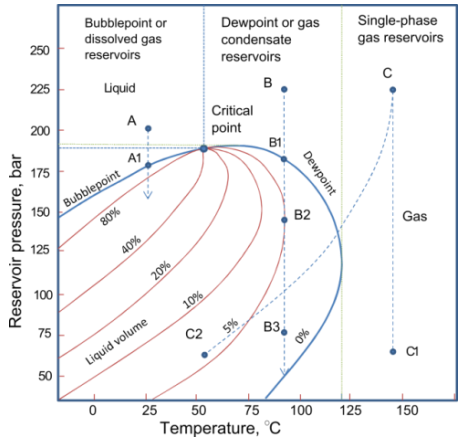

Figure 1 : Phase envelope and reservoir types

For combinations of pressure and temperature that is inside the envelope, the flow will be two-phase with oil and gas. The shape of the envelope is unique for every reservoir fluid composition. Curve A-A1 shows a typical black oil reservoir depletion curve. The reservoir temperature is below the critical temperature, and pressure in the reservoir is above the bubble point. As the formation rock has a limited permeability (3), pressure will decrease as the oil is approaching the wellbore. Consequently, the pressure might fall below the bubble point even before leaving the reservoir and entering the production tubing. The pressure depletion curve can also be like B-B1-B2-B3 for gas condensate reservoirs, where the flow is gas from the reservoir, with some condensate formed within

the production tubing. It can also be a wet gas as curve C-C2 or dry gas, curve C-C1. In the last case, the production path is always outside the phase envelope, above the cricondentherm.

A downhole shut-in valve will therefore most likely be exposed to a multiphase flow, as explained above. As this valve is open during the pressure drawdown test, information is wanted about pressure drop as function of flow rate and multiphase composition. A downhole shut-in valve type X3M350STC in use by Well Intervention Services AS is shown in Figure 2, together with a retrievable packer.

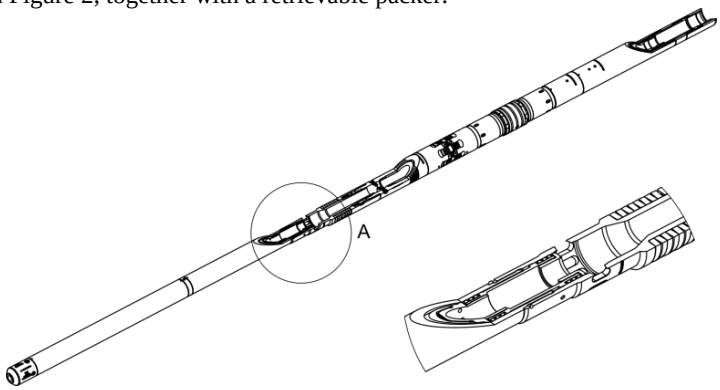

Figure 2 : Shut-in valve

A detail of the slide valve is shown with a partial cross section view. When installed in a well, the fluid is flowing outside the lower part of it, and enters inside through the valve ports (detail A). These valve ports have a total flow area equal to the annular space up stream, and this valve can therefore not be compared to a choke valve. Downstream the valve there is a long narrow channel through the packer, causing frictional pressure drop. The flow exits at the top of the packer. A full scale plastic copy of this valve and packer assembly has been the subject of single phase and two phase experiments, using water, oil and air. In this paper the results will be presented, together with single phase and two phase flow analysis. The purpose is to seek for a valid pressure drop correlation. This work is motivated due to the lack of experimental results for similar valve designs. Correlations in form of two-phase multipliers will be combined with the single phase pressure loss data from CFD simulations.

In section 2, a review of pressure drop correlations are given, with a short summary of related experiments. Results from single phase CFD simulations are also given. Section 3 describes the experimental setup and testing procedure, and in section 4 the results are presented.

2 TWO-PHASE PRESSURE DROP

A number of different two-phase pressure drop correlations will be evaluated for the total pressure drop across the shut-in valve. These correlations are developed for frictional pressure drop, but are now assumed to be valid for the total pressure drop which is partly frictional and partly due to minor losses.

2.1 Chisholm C-correlation

The first systematically study of two-phase flow was presented by Lockhart and Martinelli (4). Their correlations have been the starting point for the greater part of subsequent work in this area. They expressed the two-phase pressure drop Δp_{TF} as a function of the single phase gas or liquid pressure drop:

$$\Delta p_{TF} = \varphi_{FL}^2 \Delta p_L \tag{1}$$

$$\Delta p_{TF} = \varphi_{FG}^2 \Delta p_G \tag{2}$$

The two-phase multipliers φ_{FL} and φ_{FG} were correlated with flow quality x, densities ρ and viscosities μ without considering the flow pattern. The Lockhart-Martinelli parameter X is defined as $X = \left(\frac{\Delta p_L}{\Delta p_G}\right)^{1/2}$, and they plotted the two-phase multipliers to a base of X. Later, Chisholm (5) developed analytic expressions representing these curves:

$$\varphi_{FL}^2 = 1 + \frac{C}{x} + \frac{1}{x^2} \tag{3}$$

$$\varphi_{FG}^2 = 1 + CX + X^2 \tag{4}$$

This will therefore be called the *Chisholm C-correlation*. For Reynolds numbers from 2000 to 100000, with $\lambda = \frac{0.314}{R_e^{0,25}}$ and n=0.25 is the Blasius exponent we get that

$$X = \left(\frac{\mu_L}{\mu_G}\right)^{n/2} \left(\frac{1-x}{x}\right)^{(2-n)/2} \left(\frac{\rho_G}{\rho_L}\right)^{1/2} \tag{5}$$

For turbulent flow of both the liquid and the gas, setting C=21 will give a two-phase pressure drop multiplier equal to the curves presented by Lockhart and Martinelli.

2.2 Chisholm B-correlation

An alternative definition for two-phase pressure drop multipliers was given by Chisholm (5):

$$\varphi_{FL0}^2 = 1 + (\Gamma^2 - 1)\left[Bx^{(2-n)/2}(1-x)^{(2-n)/2} + x^{2-n}\right] \tag{6}$$

And the physical coefficient

$$\Gamma = \frac{\Delta p_{FG0}}{\Delta p_{FL0}} = \left(\frac{\mu_G}{\mu_L}\right)^n \frac{\rho_L}{\rho_G} \tag{7}$$

The notation Δp_{FG0} means the pressure drop assuming the sum of liquid and gas mass flux flowing as gas. When Γ >8.9 as here, the Chisholm B-coefficient is given by

$$B = \frac{21\Gamma - 2^{2-n} + 2}{\Gamma^2 - 1} \tag{8}$$

Chisholm gives approximate B coefficients for different valves, and a value of 2.5 has been chosen for this valve.

2.3 Friedel correlation

For viscosity ratios $\frac{\mu_L}{\mu_G} < 1000$ and mass velocities below $2000\frac{kg}{ms}$ the Friedel correlation (6) is recommended by Whalley (7):

$$\varphi_{FR}^2 = E + \frac{3.24FH}{Fr_H^{0.045} We_L^{0.035}} \tag{9}$$

$$\mathrm{Fr}_H = \frac{G_{total}^2 d_i}{\sigma \rho_H} \tag{10}$$

$$\mathrm{E} = (1-x)^2 + x^2 \frac{\rho_L f_G}{\rho_G f_L} \tag{11}$$

$$\mathrm{F} = x^{0.78}(1-x)^{0.224} \tag{12}$$

$$\mathrm{H} = \left(\frac{\rho_L}{\rho_G}\right)^{0.91} \left(\frac{\mu_G}{\mu_L}\right)^{0.19} \left(1 - \frac{\mu_G}{\mu_L}\right)^{0.7} \tag{13}$$

$$We_L = \frac{G_{total}^2}{g d_i \rho_H^2} \tag{14}$$

The homogeneous density ρ_H is based on the flow gas quality and no slip velocity:

$$\rho_H = \left(\frac{x}{\rho_G} + \frac{1-x}{\rho_L}\right)^{-1} \tag{15}$$

2.4 Homogeneous theory

The classical method for evaluating two-phase pressure drop has been using the homogeneous theory. The homogeneous density is calculated according to equation (15) and the overall pressure drop is

$$\Delta p_H = K_{Loss} \rho_H \frac{v_H^2}{2} \tag{16}$$

where $v_H = \frac{G}{A\rho_H}$.

2.5 Slip model

The pressure drop is here calculated as for homogeneous flow, but a slip ratio is calculated as (5)

$$K = \left[1 + x\left(\frac{\rho_L}{\rho_G} - 1\right)\right]^{1/2}$$

The effective density used includes the effect of liquid entrainment (8):

$$\frac{1}{\rho_e} = \left[x\frac{1}{\rho_G} + K(1-x)\frac{1}{\rho_L}\right] \times \left\{x + \frac{1-x}{K}\left[1 + \frac{(K-1)^2}{\left(\rho_L/\rho_G\right)^{1/2} - 1}\right]\right\}$$

2.6 Bankoff correlation

The Bankoff correlation (9) for two-phase multiplier is given by:

$$\varphi_{BF} = \frac{1}{1-x}\left(1 - \gamma\left(1 - \frac{\rho_G}{\rho_L}\right)\right)^{3/7}\left(1 + x\left(\frac{\rho_L}{\rho_G} - 1\right)\right) \tag{17}$$

where

$$\gamma = \frac{0.71 + 2.35\left(\frac{\rho_G}{\rho_L}\right)}{1 + \left(\frac{1-x}{x}\right)\left(\frac{\rho_G}{\rho_L}\right)} \tag{18}$$

The two-phase pressure drop is then given as

$$\Delta p_{TF} = \varphi_{BF}^{7/4} \Delta p_{L0} \tag{19}$$

where

$$\Delta p_{L0} = f_L \frac{\Delta z}{d_i} \frac{G_{Total}^2}{2\rho_L} \tag{20}$$

$$f_L = \frac{0.314}{Re_L^{0.25}} \tag{21}$$

$$Re_L = \frac{G_{Total} d_i}{\mu_L} \tag{22}$$

2.7 Müller-Steinhagen and Heck correlation

This is an empirical correlation (10) given by:

$$\left(\frac{dp}{dz}\right)_{TF} = G(1-x)^{1/3} + Bx^3 \tag{23}$$

where

$$G = A + 2(B - A)x \tag{24}$$

and

$$A = \left(\frac{dp}{dz}\right)_L = f_L \frac{G_{Total}^2}{2 d_i \rho_L} \tag{25}$$

The liquid friction factor f_L is given by equation (21). Similarly,

$$B = \left(\frac{dp}{dz}\right)_G = f_G \frac{G_{Total}^2}{2 d_i \rho_G} \tag{26}$$

and

$$f_G = \frac{0.314}{Re_G^{0.25}} \tag{21}$$

$$Re_G = \frac{G_{Total} d_i}{\mu_G} \tag{22}$$

2.8 Previous work

Experimental single- and two-phase pressure drop for the shut-in valve will be compared to the above given correlations. The total pressure loss is assumed to be mostly due to minor losses, and a summary of research on minor pressure losses for two-phase flow is given in Table 1.

Table 1 Experimental work with multiphase flow in restrictions

Diameter [mm]	Author	Fluids	System
50	(11)	Water/air	Multiple orifice
0.8-1.6	(12)	Water/air	Expansion, contraction
0.33-0.85	(13)	Nitrogen/water	Expansion, contraction
0.83	(14)	R134a	Minor loss, contraction
50	(15)	Water/air	Minor loss, elbows
<60	(16)	Water, air, R12, glycerol	Minor loss, contraction

Schmidt and Friedel (16) give an improved model for two-phase flow in contractions, but for relatively high flow qualities with annular flow. It is worth noting that they prove that there is no vena contracta (streamline concentration) downstream a sudden contraction, unlike the case for single phase flow. Kim et al. (15) gives an interesting model for overall two-phase pressure loss in a system with minor losses. An alternative two-phase pressure loss multiplier is calculated with an extra term for minor losses. However, they calculated a minor loss factor that differs from recommended values for single phase flow. They also showed that the overall pressure loss could be predicted using the Chisholm C-correlation with C=30, instead of using the normal value of C=21 for turbulent gas/turbulent liquid flow. Coleman (14) investigated experimentally the minor losses for contractions in micro tubes with 0.83mm hydraulic diameter. He found the pressure loss to be larger than expected from common correlations, and established a simple mathematical model for the mass flux in the vena contracta without taking slip into consideration. Zhou et al. (13) also investigated single- and two-phase flow in contractions, and found that introducing a slip-ratio of $S = \left({\rho_L}/{\rho_G}\right)^{1/3}$ gave predicted pressure drops corresponding to experimental values. Roul and Dash (12) also performed experiments with abrupt area changes in mini-channels, and concluded that the same slip-ratio applies. In agreement with Schmidt and Friedel, it is observed that a vena contracta do not exist in two-phase flow. Alimonti et al. (11) performed experiments with multiple orifice valves, and correlated multiphase pressure drop with a measured void fraction. However, they did not correlate flow quality and void fraction, and information on slip ratio is therefore missing.

2.9 CFD simulation of single phase flow

The external-internal flow path across the shut-in valve is represented by the 3D-model shown in Figure 3. This is a symmetric half of the valve, and the valve ports are shown in a detail view. The flow path at the inlet to the left and at the top outlet to the right is tubular or annular, with some contractions and expansions. The single phase pressure drop is quite well defined for these parts by recommended minor loss factors. The flow through the valve ports is however more complicated, and simulations with computational fluid dynamic (CFD) programme ANSYS Fluent was performed for a symmetric half of the complete valve setup. The purpose of the Fluent simulations was to determine the single phase flow pressure loss for the fluids used in the laboratory experiments.

A detail of the unstructured mesh generated in ANSYS Workbench is shown in Figure 4. As indicated, an inflated mesh was used, with two boundary layers. The mesh was refined in steps to seek for a mesh-independent simulation. With a maximum face size of 5mm, maximum element size of 6mm and a totally 931104 element and 258831 nodes the average element quality was 0.747. Details on setup of the Fluent simulations are given in Table 2. Results from experiments and CFD simulations with water and oil flow are given in Figure 5.

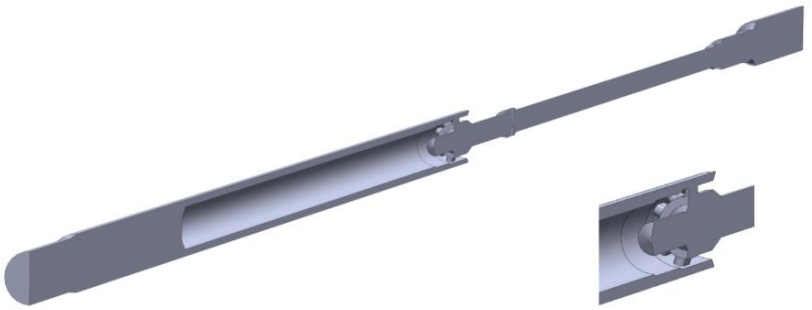

Figure 3 : 3D-model of shut-in valve

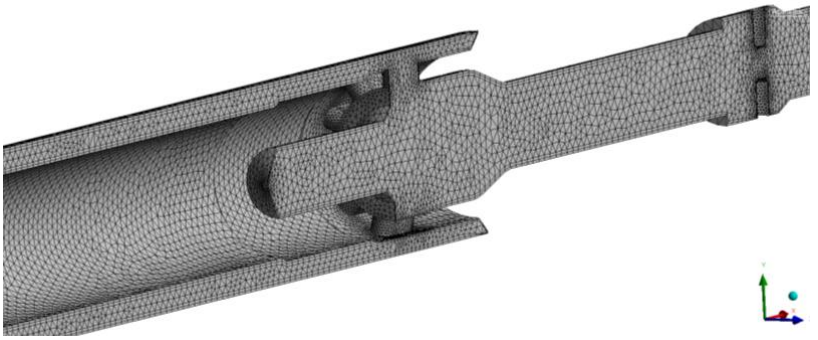

Figure 4 : Mesh for CFD simulation

Table 2 CFD setup

Setup for CFD simulation with ANSYS Fluent – liquid flow			
Solver:	Pressure based		
Time:	Steady		
Viscous model:	RNG k-e	Turbulence intensity:	5%
		Turbulent length scale:	0.00594 m
Fluids:	Water	Viscosity: 0.001 Pa-s	Density: 998 kg/m³
	Exxol D80	Viscosity: 0.0018 Pa-s	Density: 798 kg/m³
Pressure-velocity coupling			
Scheme:	Simple		
Spatial discretization			
Gradient	Least squares cell based		
Pressure	Presto		
Momentum	Second order upwind		
Turbulent kinetic e.	Second order upwind		
Turbulent dissipation rate	First order upwind		

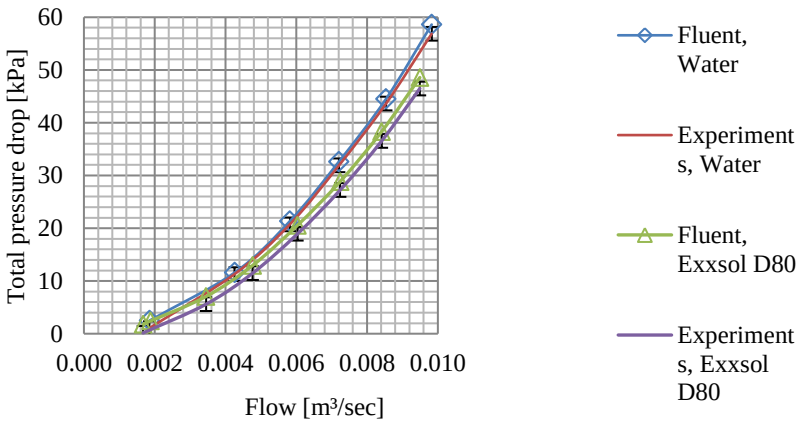

Figure 5 : Experiments and CFD simulations

The pressure measurements are marked with vertical error bars of ±1.3 kPa. The volume measurement error is very small: ±0.05 litres/s for water and ±0.019 litres/s for oil.

For water flow, the deviation between experiments and CFD simulations are only 2-3%, and for oil flow about 4-6% at the highest flow rates.

ANSYS simulations of airflow were also done, with air as a real gas with SRK equations of state, see Figure 6. The spatial discretization was second order as for incompressible flow, and a change to QUICK spatial momentum discretization scheme did not improve the accuracy. The simulated pressure drop was approximately 70% higher than measured at low flow, and approximately 7% too high at high flow.

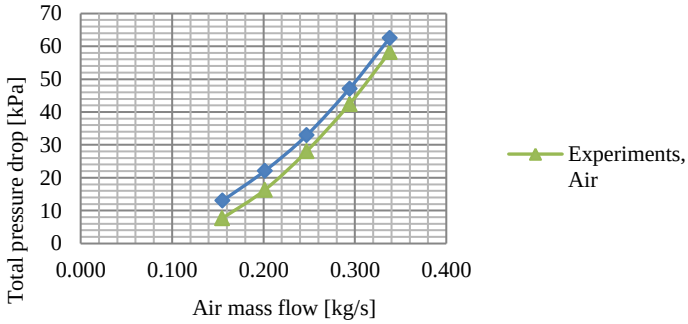

Figure 6 Pressure drop for air flow.

3 EXPERIMENTAL SETUP AND TESTING PROCEDURE

The experimental setup is shown in Figure 7 , and the laboratory valve mock-up is shown in Figure 8. Flow meters are specified in Table 3.

Table 3 Flow meters

Flow meter	Type	Range	Uncertainty	Repeatability
Air, small	Coriolis	0-0.0222 kg/s	±0.1% of rate combined	
Air, large	Vortex	0.004- 0.110 m³/s	±1% of rate	±0.25% of rate
Water	Electromagnetic	0-10 kg/s	±0.5%	±0.15% of rate
Oil	Coriolis	0-10 kg/s	±0.15% of rate combined	

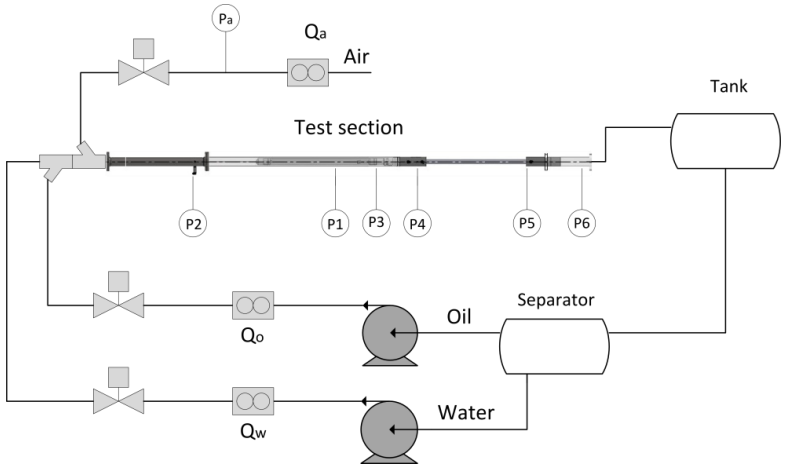

Figure 7 : Experimental setup

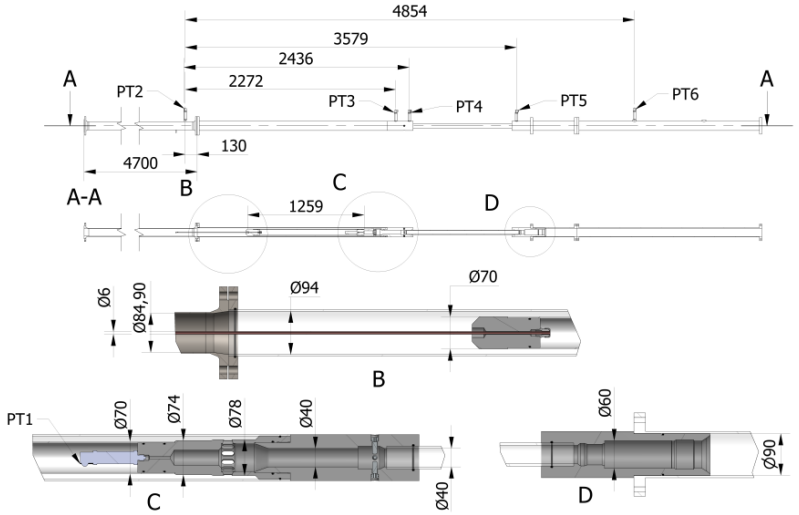

Figure 8 : Laboratory valve mock-up

Pressure sensors are specified in Table 4.

Table 4 Pressure sensors

Sensor	Type	Range	Uncertainty	Repeatability
P1-P3	Piezoresistant	0-600 kPa	±0.2%	0.05%
P4-P6	Piezoresistant	-100 to +100 kPa	±0.2%	0.05%

For the total pressure loss the resulting combined accuracy is ±1.3kPa. At two-phase flow experiments, the separator allowed for continuous, recycling flow of water and air or oil and air. Two-phase flow with oil and water is also possible. At high flow rates for long periods there is a risk of poor separation, and two-phase flow experiments were therefore limited to a few minutes.

4 RESULTS AND DISCUSSION

The flow limits for multiphase tests were 0-9.83 kg/s for water, 0-7.58 kg/s for oil type Exxol D80 and 0-0.338 kg/s for airflow. Maximum pressure drop over the shut-in valve was 235 kPa at water flow of 2 kg/s with air flow of 0.250 kg/s. A maximum flow quality of 0.21 was achieved with a water flow of 1 kg/s with air flow of 0.250 kg/s. With homogeneous flow, the maximum void fraction was 0.99. Minimum homogeneous void fraction was 0.096 at flow quality 0.00021, with a water flow of 9.5 kg/s and an air flow of 0.002 kg/s.

In Figure 9, the test results are plotted in terms of pressure drop multiplier versus flow quality. The curves show that both the Chisholm C-correlation (C=21), the Chisholm B-correlation (B=2.5) and the homogeneous theory under predicts, especially at higher flow qualities. The Bankoff correlation over predicts with more than 100%. The Friedel correlation over predicts the multiphase pressure drop below 10% flow quality, and under predicts more and more above 10%. The correlation named Chisholm / Xe is the Chisholm C-correlation with C=21, but the Lockhart-Martinelli parameter X is here based on known single phase pressure drop for water and air. It has been demonstrated that the pressure drop for single phase flow of liquid can be determined with high accuracy. The CFD simulation of compressible flow of air gives pressure drop values approximately 7-70% higher than experimental values. The CFD simulation results for single phase flow is therefore an interesting basis for the Lockhart-Martinelli factor X.
The Müller-Steinhagen and Heck correlation shows good overall result. This is a correlation between two extreme situations, with the total mass flow as liquid in the one end and as gas in the other end. The friction coefficients are based on the simple Blasius equation.

In Figure 10 a diagram is given for flow qualities up to 1.4%. Here we can see that both the selected correlations under predicts the two-phase pressure loss below 1%. It is worth noting that 0.4% flow quality corresponds to 60-70% void fraction, assuming homogeneous flow. The predicted multiplier is then approximately 3.25, and laboratory experiment gives a multiplier of 4.5. Multiphase pressure drop multiplier for air and Exxol D80 is given in Figure 11. Here the maximum airflow is limited to 20 g/s, and maximum flow quality is 0.8%. As for water and air there are several correlations that perform equally well in this quality range. The flow is assumed to be homogeneous, due to the intense mixing observed during experiments.

The most appropriate pressure drop correlation for water and air multiphase flow seems to be the Müller-Steinhagen and Heck. It is also among the best for oil and air flow, but here it under predicts. In these calculations the total pressure loss across the shut-in valve has been treated as one single minor loss, and this assumption might be too simple. Another approach might be to divide it into separate steps for every change in flow cross section.

Average percent error *E1*, absolute average percent error *E2* and standard deviation *E3* is given in Table 5 for the best correlations.

Table 5 Error analysis

	Water			**Oil**		
Model	E_1 (%)	E_2 (%)	E_3 (%)	E_1 (%)	E_2 (%)	E_3 (%)
Müller-Steinhagen and Heck	-17.0	20.3	1.6	-23.0	26.7	2.1
Friedel	45.7	50.9	3.5	117.5	117.5	8.8
Chisholm B=2.5	4.7	30.2	3.6	10.1	16.2	3.1
Chisholm Xe	-20.4	21.6	1.2	-35.6	37.0	2.3

5 CONCLUSION

Results from multiphase flow experiments with a shut-in valve have been compared to a set of correlations for pressure drop multipliers. For single phase flow with liquid, the CFD programme ANSYS Fluent is capable of predicting the pressure loss with an accuracy of 3%. For CFD air flow simulations the deviation is approximately 7-70%. For multiphase flow with air and water, a Chisholm B-correlation with B=2.5 and the Müller-Steinhagen and Heck correlation is closest to the experimental values. This trend is the same for water-air and oil-air experiments. The correlation with slip flow gave larger deviation than correlation with homogeneous flow. Based on the procedure presented here, the two-phase pressure loss in complex flow geometry can be estimated with an absolute average error of 20-30%.

The existing information from these experiments could be used for a more detailed simulation, where each sub-step of the flow across the valve is calculated separately.

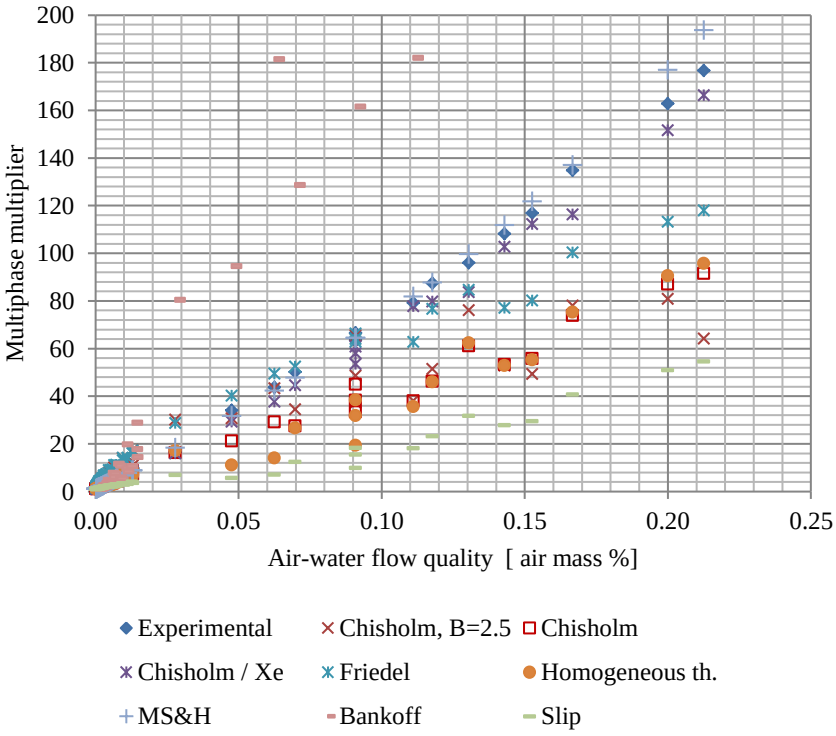

Figure 9 : Multiphase flow of water and air

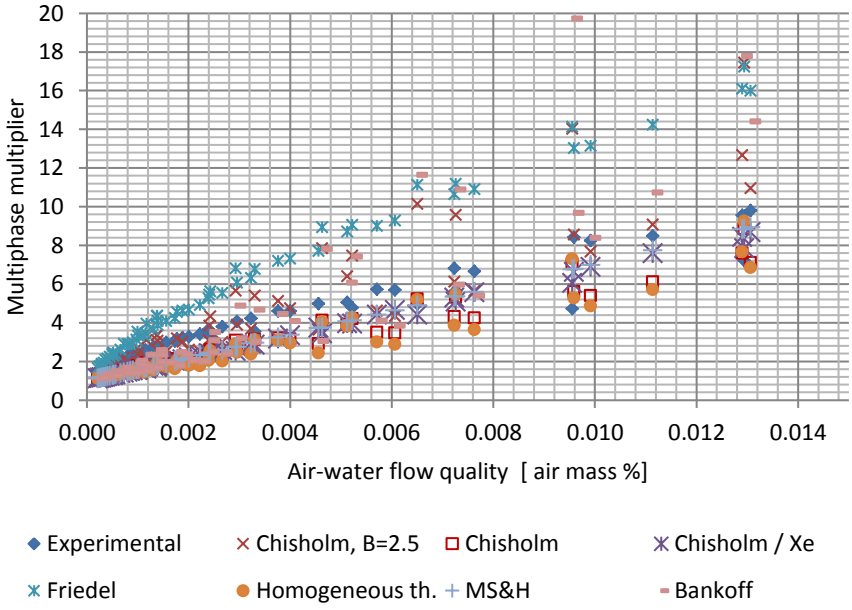

Figure 10 : Water-air multiphase flow at low quality

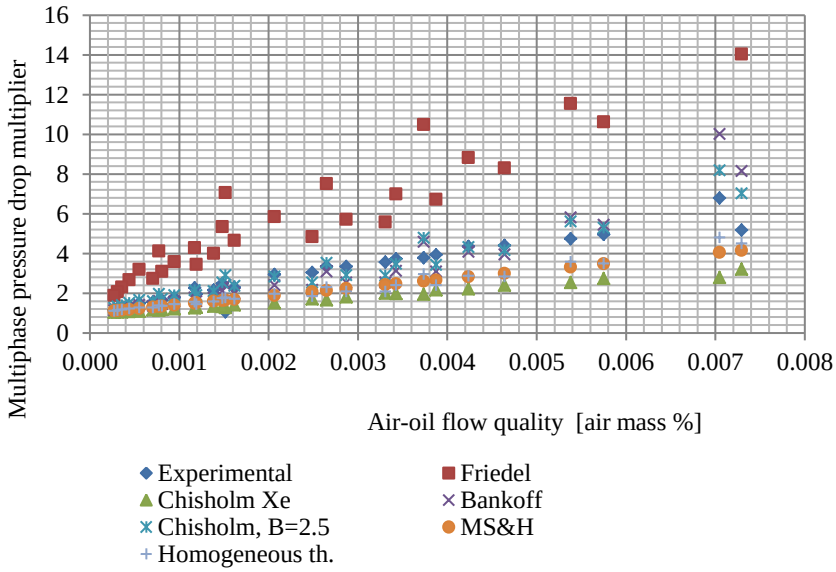

Figure 11 : Pressure drop multiplier for air and Exxol D80 versus flow quality

REFERENCES

1. **Zolotukhin, Anatoly B. and Ursin, Jann-Rune.** *Introduction to Petroleum Reservoir Engineering.* s.l. : Høyskoleforlaget, 2000.

2. *Fast Shut-in Tools Improve Near Wellbore Characterisation from Build-up Test Interpretation.* **Guerrero, Rodolfo Phillips and Lessi, Jacques.** s.l. : Society of Petroleum Engineers, SPE 110941, May 2007, pp. 163-197.

3. **Dandekar, Abhijit Y.** *Petroleum Reservoir Rock and Fluid Properties.* s.l. : Taylor and Francis Group, 2006. ISBN: 0-8493-3043-2.

4. *Proposed correlation of data for isothermal two-phase two-component flow in pipes.* **Lockhart, R.W. and Martinelli, R.C.** 1949, Chem. Engn. Progr., Vol. 45(1), pp. 39-48.

5. **Chisholm, D.** *Two-phase flow in pipelines and heat exchangers.* London : George Godwin, 1983.

6. *Improved Friction Pressure Drop Correlations for Horizontal and Vertical Two-Phase Pipe Flow.* **Friedel, L.** June 1979, European Two-Phase Flow Group Meeting, Ispra, Italy.

7. **Whalley, P.** *See Hewitt, G.F. (1983). Multiphase Flow and Pressure drop, Heat Exchanger Design Handbook.* Washington, D.C. : Hemisphere, 1980. pp. 2.3.2-11. Vol. 2.

8. *Compressible Gas-Liquid Flow through Pipeline Restrictions.* **Morris, S.D.** 1991, Chem. Eng. Process., Vol. 30, pp. 39-44.

9. *A Variable Density Single-Fluid Model for Two-Phase Flow with Particular Reference to Steam-Water.* **Bankoff, S.G.** 1960, J.Heat Transfer, Vols. II, Series B, pp. 265-272.

10. *A simple Friction Pressure Drop Correlation for Two-Phase Flow in Pipes.* **Müller-Steinhagen , H. and Heck, K.** 1986, Chem. Eng, Processing, Vol. 20, pp. 297-308.

11. *Two-phase flow characteristics in multiple orifice valves* . **Alimonti, Claudio, Falcone, Gioia and Bello, Oladele.** 8, 2010, Experimental Thermal and Fluid Science , Vol. 34, pp. 1324-1333. ISSN: 0894-1777 DOI: http://dx.doi.org/10.1016/j.expthermflusci.2010.06.004.

12. *Two-phase pressure drop caused by sudden flow area contraction and expansion in small circular pipes.* **Roul, Manmatha K. and Dash, Sukanta K.** 11, s.l. : John Wiley \& Sons, Ltd., 2011, International Journal for Numerical Methods in Fluids, Vol. 66, pp. 1420-1446. ISSN: 1097-0363 DOI: 10.1002/fld.2322.

13. *Characteristics of pressure drop for single-phase and two-phase flow across sudden contraction in microtubes.* **Zhuo, Li, Jian, Yu and ChongFang, Ma.** s.l. : Science China Press, co-published with Springer, 2008, Science in China Series E: Technological Sciences, Vol. 51, pp. 162-169. 10.1007/s11431-007-0030-4. ISSN: 1006-9321.

14. *An Experimentally Validated Model for Two-Phase Sudden Contraction Pressure Drop in Microchannel Tube Headers.* **Coleman, John Wesley.** 3, 2004, Heat Transfer Engineering, Vol. 25, pp. 69-77. DOI: 10.1080/01457630490280335.

15. *Two-phase minor loss in horizontal bubbly flow with elbows: 45 deg. and 90 deg. elbows.* **Kim, Seungjin, Kojasoy, Gunol and Guo, Tangwen.** 2, 2010, Nuclear Engineering and Design, Vol. 240, pp. 284-289. Twelfth International Topical Meeting on Nuclear Reactor Thermal Hydraulics (NURETH-12). ISSN: 0029-5493 DOI: 10.1016/j.nucengdes.2008.08.019.

16. *Two-phase pressure drop across sudden contractions in duct areas.* **Schmidt, J. and Friedel, L.** 2, 1997, International Journal of Multiphase Flow, Vol. 23, pp. 283-299. ISSN: 0301-9322 DOI: 10.1016/S0301-9322(96)00056-0.

Available online at www.sciencedirect.com

ScienceDirect

Energy Procedia 00 (2014) 000–000

Energy Procedia

www.elsevier.com/locate/procedia

3rd Trondheim Gas Technology Conference, TGTC-3

Multiphase flow in complex valve geometry

S. Edvardsen*, C.A. Dorao, O.J. Nydal

Norwegian University of Science and Technology, Kolbjørn Hejes vei 2, 7491 Trondheim, Norway

Abstract

Downhole shut-in valves are used for testing of oil and gas reservoirs. The internal flow geometry is complex, and contains annulus flow, annular contractions, sharp angles, valve ports and sudden expansions. A new procedure for calculating two-phase pressure loss in a downhole shut-in valve is proposed. Two-phase flow correlations that are independent of flow patterns are used here with a one-dimensional model of the valve in order to simulate two-phase flow. The one-dimensional model is solved using a least squares spectral element method. Two-phase flow experiments with air/water and air/oil mixtures are performed on a full-scale shut-in valve mock-up. Experimental two-phase flow pressure drop values are then compared to simulations with different correlations. The Müller Steinhagen and Heck correlation is found to be the best choice, giving an average deviation of 12% assuming homogeneous flow.

Peer-review under responsibility of the Scientific Committee of TGTC-3.

Keywords: Single phase; Multiphase; Spectral elements; Least squares; Simulation; Validation

1. Introduction

Downhole shut-in valves are used when testing oil and gas reservoirs. Fig.1 presents a typical shut-in valve. The study of the pressure build-up curve after a sudden downhole shut-in (closing) of a flowing well provides important information about the oil and gas reservoir characteristics, in particular the size and near wellbore region. This information is obtained from gauges hanging below the shut-in valve. Traditionally, shut-in operations are

* Corresponding author. Tel.: +47 98296939; fax: +47 73593580.
E-mail address: svein.edvardsen@ntnu.no

Peer-review under responsibility of the Scientific Committee of TGTC-3.

performed by operating a valve at the wellhead, but due to the wellbore storage effect errors are introduced in the reservoir estimates.

Nomenclature

A	cross-sectional area	(m²)
B	Chisholm B-parameter	
C	Chisholm C-parameter	
f	friction factor, Darcy	
g	acceleration of gravity	(m/s²)
G	mass flux	$(\frac{kg}{m^2 s})$
K	minor loss factor	
$\dot{m}$	mass flow rate	
n	Blasius exponent for friction factor equation	
P	pressure	(Pa)
Δp	pressure drop	(Pa)
v	flow velocity	(m/s)
x	flow quality (gas mass flow / total mass flow)	(-)
X	Lockhart-Martinelli parameter	(-)
z	coordinate along the flow path	(m)

Greec Symbols

α	void fraction	
Γ	physical properties coefficient	
μ	viscosity	$(\frac{N}{m^2 s})$
ρ	density	$(\frac{kg}{m^3})$
τ	shear stress	$(Pa = \frac{N}{m^2})$
$\varphi_{(\ )}$	pressure drop multiplier	(-)

Subscripts

FG	frictional-gas
FG0	frictional, assuming total mass flux as gas
FL	frictional-liquid
FL0	frictional, assuming total mass flux as liquid
G	gas
H	homogeneous
i	inner
L	liquid
Loss	overall loss factor for minor losses
TF	two-phase
Total	sum of liquid and gas
w	wall

If a downhole shut-in operation is performed, this source of error can be reduced. The downhole shut-in valve will however give a pressure drop in the wellbore, and the multiphase flow resistances in a downhole shut-in valve have

to be examined theoretically and experimentally in order to improve the analysis of the test results. The value of this pressure drop can also be used as an indicator of the flow across the shut-in valve.

The flow path through the valve-packer assembly is complex, with a series of minor losses such as contractions, expansions, sharp angles and obstructions. The first part is annular, between the lower part of the valve and the production tubing. After the valve ports at detail A, Fig.1, there is a chamber, followed by a contraction and a long channel through the packer. The total pressure drop across the valve-packer assembly will be simulated here by a novel one-dimensional finite element method using the least-squares method with spectral element approximation [1].

Similar flow conditions with turbulent multiphase flow can be expected to occur in other parts of subsea oil and gas production systems. One example is the flow through a well plug during pressure equalization before removal of the plug. The flow path through the plug can be compared to a shut-in valve, and knowledge about the flow rate at different pressures is important to avoid problems when operating wireline equipment.

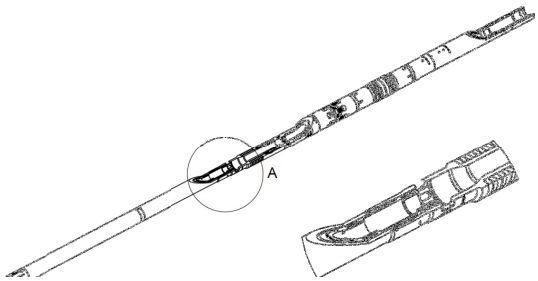

Fig.1. Shut-in valve.

2. Theoretical background

The approach here is to calculate the multiphase pressure drop by using various multiphase flow correlations:

$$\Delta P_{twophase} = \varphi^2 \Delta P_{single\ phase} \tag{1}$$

Many different empirical correlations exist for the multiplier, φ, starting with the classical Lockhart-Martinelli [2] correlations. Here only "black box models", that are independent of flow pattern will be evaluated. Finding the two-phase pressure drop will therefore be a two-fold problem: The single-phase pressure drop must be determined as precisely as possible, and then a suitable correlation must be applied. The flow path is too complex to use standard minor loss factors, so the best option for predicting single-phase pressure loss is using CFD simulation on a 3-dimensional model. Edvardsen et al. [3] have shown that the overall pressure drop can be determined with a CFD simulation with an error of only 3%. Applying a two-phase multiplier directly to the total single phase pressure loss resulted in a two-phase pressure drop error of 20-30%.

In order to improve the accuracy of the prediction, a 1-D model for single phase compressible and incompressible flow through the valve-packer assembly was made based on the CFD simulations [4]. The frictional and minor losses like contractions, expansions and orifices for this model are given in Table 1.

The two phase flow through the valve can be modeled with the Navier-Stokes Equation. For 1-dimensional, steady state horizontal flow, the following equations can be derived for a slab Δz of the flow:

$$(1-\alpha)\rho_l v_l \frac{\partial v_l}{\partial z}\Delta z + \alpha \rho_g v_g \frac{\partial v_g}{\partial z}\Delta z = -\frac{\partial P}{\partial z}\Delta z - \frac{4}{D_i}\tau_w \Delta z \tag{2}$$

In this momentum balance equation τ_w [Pa] is shear stress at tube wall, α is void fraction and P [Pa] is pressure. The total force from the shear stress τ_w acting along the slab ∂z is divided here by the tube cross section. The resulting pressure drop can also be expressed by the Darcy formula for the case of single-phase flow:

$$\Delta P = \rho f \frac{\Delta z}{D}\frac{v^2}{2} = \frac{4\tau_w \pi D \Delta z}{\pi D^2} = \frac{4\tau_w \Delta z}{D} \tag{3}$$

And therefore

$$\tau_w = \rho f \frac{v^2}{8} \tag{4}$$

Pressure drop across singularities are expressed by the minor loss coefficients K from Table 1:

$$\Delta P = \rho K \frac{v^2}{2} = K \frac{G^2}{2\rho} \tag{5}$$

Table 1. Frictional and minor losses in the STC downhole valve.

No.	Description	Length (m)	Minor loss coeff.	Diameter (m)	Hydraulic diameter (m)
1	Circular	0.100		0.0849	0.0849
2	Diffuser, 16°	0.030	0.036	0.0849 < 0.094	
3	Circular, at inlet	0.525		0.094	0.094
4	Annular contraction, 90°	0.015	0.366	0.094 >	0.024
5	Annular	1.259		0.094 x 0.070	0.024
6	Annular contraction, 90°	0.004	0.095		0.024 > 0.020
7	Annular	0.075		0.094 x 0.074	0.02
8	Annular contraction, 90°	0.006	0.071		0.020 > 0.016
9	Annular	0.020		0.094 x 0.078	0.016
10	Valve opening	0.075	1.759		0.016 > 0.060
11	Contraction, 40°	0.030	0	0.060 < 0.040	
12	Circular	0.192		0.04	0.04
13	Equalizing central	0.058	0.284		
14	Circular, through packer	1.220		0.04	0.04
15	Expansion	0.288	0.255	0.040 < 0.090	
16	Circular	0.958		0.09	0.09

For two-phase flow a multiplier is introduced in Eq. (3). It has been shown [3] that the Müller Steinhagen and Heck correlation [5] and the Chisholm B-correlation [6] give the best prediction for the overall pressure drop, when applying the two-phase multiplication factor to the total single-phase pressure drop. Both correlations will be tested, together with the Friedel correlation. The Chisholm B-correlation is given by:

$$\varphi_{FLo}^2 = 1 + (\Gamma^2 - 1)\left[Bx^{(2-n)/2}(1-x)^{(2-n)/2} + x^{2-n}\right] \tag{6}$$

where x is flow quality: $x = \dot{m}_G/(\dot{m}_G + \dot{m}_L)$. The physical coefficient Γ is

$$\Gamma = \frac{\Delta P_{FG0}}{\Delta P_{FL0}} = \left(\frac{\mu_G}{\mu_L}\right)^n \frac{\rho_L}{\rho_G} \tag{7}$$

The meaning of the notation ΔP_{FG0} is the pressure drop assuming total mass flux as gas. Chisholm recommends a B-value of 2.3 for globe valves, and for this valve B is set to 2.5. Then, for two-phase flow the shear stress

$$\tau_w = \rho f_{L0} \frac{v^2}{8} \varphi_{FLo}^2 \tag{8}$$

The Müller, Steinhagen and Heck correlation is given by

$$\left(\frac{dP}{dx}\right)_{TF} = G_{MS}(1-x)^{1/3} + Bx^3 \tag{9}$$

where $G_{MS} = A + 2(B-A)x$, A = $\left(\frac{dP}{dx}\right)_L = f_L \frac{G_{Total}^2}{2D_i\rho_L}$, $f_L = \frac{0.314}{Re_L^{0.25}}$, $Re_L = \frac{G_{Total}D_i}{\mu_L}$, $B = \left(\frac{dP}{dx}\right)_G = f_G \frac{G_{Total}^2}{2D_i\rho_G}$, $f_G = \frac{0.314}{Re_G^{0.25}}$ and $Re_G = \frac{G_{Total}D_i}{\mu_G}$.

A two-phase multiplier can then be calculated from $\varphi_{FLo}^2 = \left(\frac{dP}{dx}\right)_{TF} / A$ The Friedel correlation [7] is given by

$$\varphi_{FR}^2 = E + \frac{3.24FH}{Fr_H^{0.045} We_L^{0.035}} \tag{10}$$

where $\mathrm{Fr}_H = \frac{G_{total}^2 d_i}{\sigma \rho_H}$, E = $(1-x)^2 + x^2 \frac{\rho_L f_G}{\rho_G f_L}$, F = $x^{0.78}(1-x)^{0.224}$, H = $\left(\frac{\rho_L}{\rho_G}\right)^{0.91} \left(\frac{\mu_G}{\mu_L}\right)^{0.19} \left(1-\frac{\mu_G}{\mu_L}\right)^{0.7}$ and $We_L = \frac{G_{total}^2}{g d_i \rho_H^2}$.

The two-phase multiplier is only applied to frictional pressure losses. Due to the high turbulence intensity, the phase velocities are believed to be equal. The homogeneous void fraction is then [8]:

$$\alpha = (x\rho_L)/(x\rho_L + (1-x)\rho_G) \tag{11}$$

2.1. Least squares method

The dynamic equation for momentum, Eq. 2, is solved using the least-squares method with spectral element approximation. This method was also used by Ciapero [9] and Sporleder [10]. The use of the least-squares method involves the minimization of a norm-equivalent functional. We have that

$$L\mathbf{u} = \mathbf{g} \text{ in } \Omega$$
$$B\mathbf{u} = \mathbf{h} \text{ on } \partial\Omega$$

where Ω and ∂Ω are the domain and the boundary of the domain respectively. *L* is a linear operator and *B* is the trace operator. With the requirement that the system is well-posed and that the operators *L* and *B* are continuous mappings between the function space X(Ω) onto the solution space Y(Ω)×Y(∂Ω), the norm equivalent functional becomes

$$I(u) = \frac{1}{2}\|L\mathbf{u} - \mathbf{g}\|_{Y(\Omega)}^2 + \frac{1}{2}\|B\mathbf{u} - \mathbf{h}\|_{Y(\partial\Omega)}^2$$

Variational analysis gives

$$\lim_{\epsilon \to 0} \frac{d}{d\epsilon} I(\mathbf{u} + \epsilon\, \mathbf{v}) = 0 \;\forall\; \mathbf{u} \in \mathrm{X}(\Omega)$$

I can now be minimized with the following necessary condition: Find $\mathbf{u}\in X(\Omega)$ such that

$$A(\mathbf{u},\mathbf{v}) = F(\mathbf{v})\ \forall\ \mathbf{v}\in X(\Omega)$$

and

$$A(\mathbf{u},\mathbf{v}) = \langle L\mathbf{u}, L\mathbf{v}\rangle_{Y(\Omega)} + \langle B\mathbf{u}, B\mathbf{v}\rangle_{Y(\partial\Omega)}$$
$$F(\mathbf{v}) = \langle \mathbf{g}, L\mathbf{v}\rangle_{Y(\Omega)} + \langle \mathbf{h}, B\mathbf{v}\rangle_{Y(\partial\Omega)}$$

$A:X\times X\rightarrow \mathbb{R}$ is a symmetric, continuous bilinear form. $F:X\rightarrow \mathbb{R}$ is a continuous linear form.

2.2. Spectral element formulation

As for finite element formulations, the computational domain Ω is divided into N_e non-overlapping sub-domains Ω_e such that

$$\Omega = \bigcup_{e=1}^{N_e}\Omega_e \ \text{ with } \Omega_e\cap\Omega_k = \emptyset,\ e\neq k$$

The unknown function u_h^e is approximated in each element Ω_e by the set of all polynomials P_Q of degree$\leq Q$. The global approximation u_h in Ω is

$$u_h = \bigcup_{e=1}^{N_e} u_h^e$$

Within each element, the solution is expanded in Φ_i basis functions

$$u_h^e(x) = \sum_{n=0}^{i} u_n^e \Phi_i(\xi)$$

with $(\xi) = X_e^{-1}(x)$ the local coordinate of (x) in the parent element, with $-1\leq\xi\leq 1$, and u_h^e being the coefficients in the expansion.

2.3. Linearization

The least-squares method with spectral elements requires linear equations, and the term $v\,\partial v/\partial x$ for convective acceleration can be linearized using the Newton-Raphson linearization:

$$u_{k+1} = u_k + \delta u$$
$$u\frac{\partial u}{\partial z} = (u_k+\delta u)\left(\frac{\partial u_k}{\partial z}+\frac{\partial \delta u}{\partial z}\right)$$
$$u\frac{\partial u}{\partial z} = u_k\frac{\partial u_{k+1}}{\partial z} + u_{k+1}\frac{\partial u_k}{\partial z} - u_k\frac{\partial u_k}{\partial z}$$

2.4. Numerical solution

No mass transfer takes place between the phases here, and for elements with a change in cross-section *A* we have that

$$\frac{\partial u}{\partial z} = \frac{\partial u}{\partial A}\frac{\partial A}{\partial z} = \frac{\partial}{\partial A}\left(\frac{\dot m}{A\rho}\right)\frac{\partial A}{\partial z} \quad \text{and} \quad \frac{\partial u}{\partial z} = -\left(\frac{\dot m}{A^2\rho}\right)\frac{\Delta A}{\Delta z}$$

The differential equation $L\mathbf{u} = \mathbf{g}$ can now be written as follows for multiphase flow:

$$\begin{Bmatrix} \frac{\partial}{\partial z} & 0 & 0 \\ 0 & \frac{\partial}{\partial z} & 0 \\ v_G^* \frac{\partial}{\partial z} + \frac{\partial v_G^*}{\partial z} & v_L^* \frac{\partial}{\partial z} + \frac{\partial v_L^*}{\partial z} & \frac{\partial}{\partial z} \end{Bmatrix} \begin{Bmatrix} \alpha \rho_G v_G \\ (1-\alpha)\rho_L v_L \\ P \end{Bmatrix} = \begin{Bmatrix} -\left(\frac{\dot{m}_G}{A^2}\right)\frac{\partial A}{\partial z} \\ -\left(\frac{\dot{m}_L}{A^2}\right)\frac{\partial A}{\partial z} \\ -\varphi^2 \frac{4}{D_i}\tau_w - v_G^* \left(\frac{\dot{m}_G}{A^2}\right)\frac{\partial A}{\partial z} - v_L^* \left(\frac{\dot{m}_L}{A^2}\right)\frac{\partial A}{\partial z} \end{Bmatrix} \quad (12)$$

The superscript asterisk indicates that this is a value from the previous iteration. If the element has a minor loss factor, the right-hand side is

$$\begin{Bmatrix} \frac{\partial}{\partial z} & 0 & 0 \\ 0 & \frac{\partial}{\partial z} & 0 \\ v_G^* \frac{\partial}{\partial z} + \frac{\partial v_G^*}{\partial z} & v_L^* \frac{\partial}{\partial z} + \frac{\partial v_L^*}{\partial z} & \frac{\partial}{\partial z} \end{Bmatrix} \begin{Bmatrix} \alpha \rho_G v_G \\ (1-\alpha)\rho_L v_L \\ P \end{Bmatrix} = \begin{Bmatrix} -\left(\frac{\dot{m}_G}{A^2}\right)\frac{\partial A}{\partial z} \\ -\left(\frac{\dot{m}_L}{A^2}\right)\frac{\partial A}{\partial z} \\ -K \frac{G^2{}_{Total}}{2\rho_L} - v_G^* \left(\frac{\dot{m}_G}{A^2}\right)\frac{\partial A}{\partial z} - v_L^* \left(\frac{\dot{m}_L}{A^2}\right)\frac{\partial A}{\partial z} \end{Bmatrix} \quad (13)$$

The term $\partial A/\partial z \approx \Delta A/\Delta x$ can be found from geometrical relationships, as all cross-section changes are simplified to conical contractions or conical expansions.

3. Experimental setup and testing procedure

A full-scale model of a shut-in valve was installed in the multiphase test loop at NTNU, see Fig. 2.

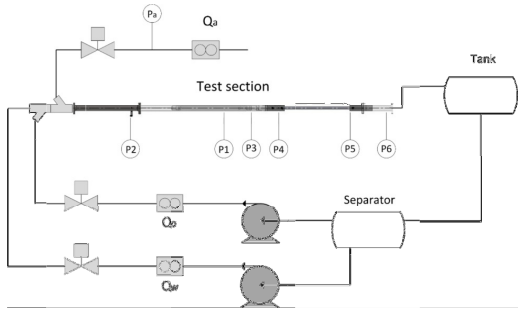

Fig. 2. Valve model in multiphase test loop.

The separator allows continuous circulation of multiphase flow. The test section has pressure sensors at six different locations, in order to identify the pressure drop in as much detail as possible, see Fig. 2. For the total pressure loss the resulting combined accuracy is ±1.3kPa. The dimensions of the valve mock-up are shown in Fig. 3, and experimental conditions are given in Table 2. Flowmeter and sensor specifications are given in Table 3.

Table 2. Experimental conditions, 20°C.

Fluid	Flow range	Density	Viscosity
Air	0-0.27 kg/s with water / 0-0.02 kg/s with oil	1.2 kg/m^3 at 1 bar	1.8E-5 Pa-s
Water	0-10 kg/s	998 kg/m^3	0.001 Pa-s
Oil, Exxsol D80	0-10 kg/s	798 kg/m^3	0.0018 Pa-s

Table 3. Flowmeters and sensors.

Flow meter / sensor	Type	Range	Uncertainty	Repeatability
Air, small	Coriolis	0-0.0222 kg/s	±0.1% of	
Air, large	Vortex	0.004- 0.110 m³/s	±1% of rate	±0.25% of
Water	Electromagnetic	0-10 kg/s	±0.5%	±0.15% of
Oil	Coriolis	0-10 kg/s	±0.15% of	
P1-P3	Piezoresistant	0-600 kPa	±0.2%	0.05%
P4-P6	Piezoresistant	-100 to +100 kPa	±0.2%	0.05%

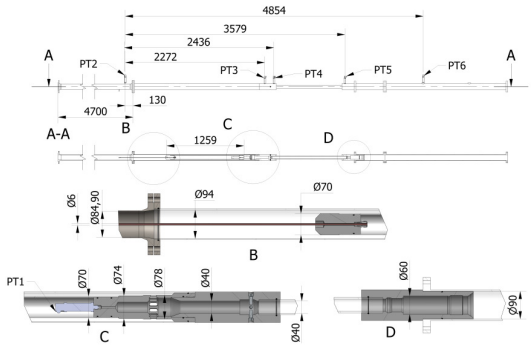

Fig. 3. Shut-in valve mock-up

4. Results and discussion

The numerical simulation of two-phase flow was performed using element lengths that are approximately equal to the local diameter, in total 76 5th order elements. Smaller elements did not improve the accuracy. The atmospheric outlet pressure was used as boundary condition, and element pressures were calculated by solving Eq. (12) for elements with frictional pressure drop, or Eq. (13) for elements with a minor loss coefficient. Pressures were calculated for one element at a time, countercurrent to the fluid flow. Air density was updated at each element. The one-dimensional mesh was based on Table 1. The above-mentioned correlations for multiphase flow were tested one by one by simulating the full range of flow conditions given in Table 2. The minor losses were calculated as if total mass flow was liquid, without multiphase multiplier. Two-phase air-water and air-oil flow experiments were also performed with the same range of flow conditions.

In order to compare the simulated and experimental results, overall multiphase multiplication factors $\varphi_{overall\_corr}$ were calculated for each correlation by dividing simulated total multiphase pressure drop $\Delta P_{TF\_simulated}$ with total experimental liquid flow pressure drop $\Delta P_{L\_experimental}$.

$$\varphi_{overall\_corr} = \frac{\Delta P_{TF\_simulated}}{\Delta P_{L\_experimental}} \tag{14}$$

The corresponding experimental overall multiphase multiplication factors $\varphi_{overall\_exp}$ were calculated from the experimental two-phase pressure drop $\Delta P_{TF\_experimental}$:

$$\varphi_{overall\_exp} = \frac{\Delta P_{TF\_experimental}}{\Delta P_{L\_experimental}} \tag{15}$$

The overall multiphase multiplication factors $\varphi_{overall\_corr}$ will consequently also contain a small deviation from single phase liquid flow pressure drop simulation, which is about -1.2% [4]. The deviations for the for air-water flow simulation results are given in Table 4. Average deviation E_1 and standard deviation E_3 are defined as

$$E_1 = \left[\frac{1}{n}\sum_{i=1}^{n}\frac{\varphi_{overall\_corr(i)}-\varphi_{overall\_exp(i)}}{\varphi_{overall\_exp(i)}}\right] \text{ and } E_3 = \sqrt{\frac{1}{n}\sum_{i=1}^{n}\left\{\left[\frac{\varphi_{overall\_corr(i)}-\varphi_{overall\_exp(i)}}{\varphi_{overall\_exp(i)}}\right]-E_1\right\}^2}$$

Experimental and simulation results are plotted as a function of flow quality $x = \dot{m}_G/(\dot{m}_G + \dot{m}_L)$ in Fig. 4. The overall multiphase pressure drop multiplier $\varphi_{overall}$ is the ordinate in Figs. 4 and 5. The Müller Steinhagen and Heck correlation gives simulation results that are closest to the experimental values, as the error analysis in Table 4 shows only 10.5% average deviation.

Table 4. Air-water flow error analysis.

Correlation	Friedel	Chisholm B	Müller Steinhagen and Heck
Average deviation E_1	22.5%	27.1%	10.5%
Standard deviation E_3	17.3%	19.4%	13.9%

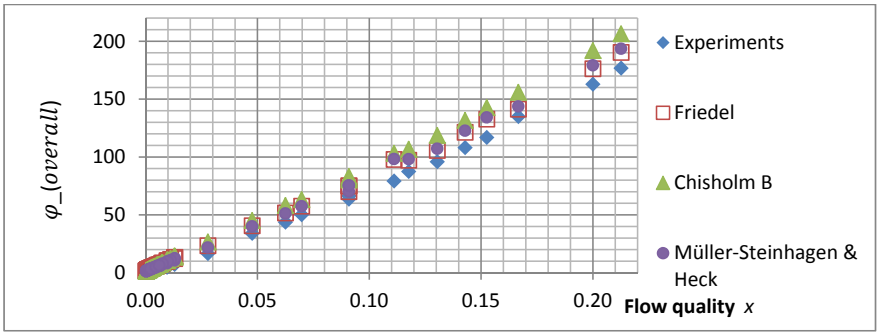

Fig. 4. Air-water flow in shut-in valve mock-up.

The results for air-oil flow are illustrated in Fig. 5, and error analysis is given in Table 5. Here the trend is the same, showing that the Müller Steinhagen and Heck correlation gives the best results, with only 12.1% average deviation.

Table 5. Air-oil flow error analysis.

Correlation	Friedel	Chisholm B	Müller Steinhagen and Heck
Average deviation E_1	29.3%	29.6%	12.1%
Standard deviation E_3	35.4%	32.1%	26.3%

5. Conclusions

In this work, a one-dimensional least squares spectral element method was used to predict the two-phase flow pressure drop in a downhole shut-in valve. The one-dimensional mesh had 76 5th order elements and was based on a formerly qualified model for liquid flow [4]. With the outlet pressure as the boundary condition, element pressure drops were calculated one by one countercurrent to the fluid flow. The two-phase pressure drop was calculated as a product of the single-phase liquid flow pressure drop and a multiphase flow multiplier. Minor pressure losses were calculated as if total mass flow was liquid. The total pressure drop was determined with only 10.5-12% average deviation compared to experimental values, using the Müller, Steinhagen and Heck correlation for the two-phase multiplier with void fraction calculated for equal phase velocities.

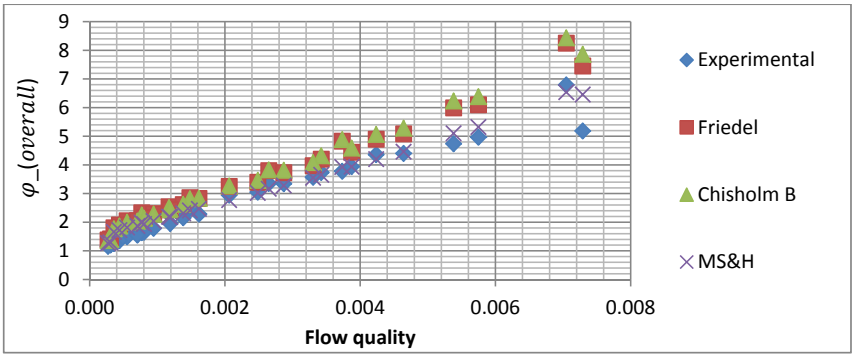

Fig. 5. Air-oil flow tests.

References

[1] Proot M, Gerritsma M. Least-squares spectral eelement applied to the Stokes problem. *Journal of Comp. Phys.* 2002; 181(2): 454-477

[2] Lockhart R, Martinelli R. Proposed correlation of data for isothermal two-phase two-component flow in pipes. *Chem. Engn. Progr* 1949; 45(1): 39-48

[3] Edvardsen S, Dorao C, Nydal OJ. Two-phase flow in a down-hole shut-in valve. *9th North American Multiphase Technology Conference*. 2014 June 11-13. Banff, Canada

[4] Edvardsen S, Dorao C, Nydal OJ. Single-phase flow in downhole shut-in valve. 2014: Submitted

[5] Müller-Steinhagen H, Heck K. A Simple Friction Pressure Drop Correlation for Two-Phase Flow in Pipes. *Chem. Engn. Progr* 1986;20: 297-308

[6] Chisholm D. *Two-phase flow in pipelines and heat exchangers*. London: George Godwin; 1983.

[7] Friedel L. Improved Friction Pressure Drop Correlations for Horizontal and Vertical Two-Phase Pipe Flow. *European Two-Phase Flow Group Meeting, Ispra, Italy* 1979 June

[8] Thome J. *Engineering Data Book III*, Lausanne: Swiss Federal Institute of Technology Lausanne; 2010.

[9] Chiapero EM. *Two-phase flow instabilities and flow mal-distribution in parallel channels*. PhD Thesis, Trondheim: Norwegian University of Science and Technology; 2013.

[10] Sporleder F. *Simulation of Chemical Reactors using the Least-Squares Spectral Element method*. PhD Thesis, Trondheim: Norwegian University of Science and Technology; 2011.

Journal of Natural Gas Science and Engineering 22 (2015) 214–226

Contents lists available at ScienceDirect

Journal of Natural Gas Science and Engineering

journal homepage: www.elsevier.com/locate/jngse

Experimental and numerical study of single-phase pressure drop in downhole shut-in valve

Svein Edvardsen*, Carlos Alberto Dorao, Ole Jørgen Nydal

Department of Energy and Process Technology, Norwegian University of Science and Technology, Kolbjørn Hejes vei 2, 7491 Trondheim, Norway

ARTICLE INFO

Article history:
Received 8 September 2014
Received in revised form
22 November 2014
Accepted 24 November 2014
Available online

Keywords:
Shut-in valve
Single-phase flow
CFD simulation
Turbulence models
1-Dimensional Navier–Stokes model

ABSTRACT

In this work an experimental and numerical analysis of single-phase pressure drop in a downhole shut-in valve is performed. The main goal was to develop a 1D numerical model suitable for both compressible and incompressible flow. For the experimental study a mock-up of the shut-in valve was built and instrumented with pressure sensors and flowmeters. The pressure drop along the different sections of the valve were recorded for various flow rates using water, oil and air as working fluids. For the numerical analysis a two-step approach was used. First a commercial CFD package was used for 3D simulations of the flow, and different turbulence models were compared. Then a 1D model was developed based on a spectral element method, with minor loss factors derived from the CFD simulations. Both the 3D CFD simulations and the 1D model simulations provided a good comparison with the experimental data. The small difference in the simulation results can be attributed to the difference in the frictional coefficient which showed a discrepancy of about 20% compared with the measurements. Minor loss factors derived from CFD simulations of incompressible flow are found to be valid also for 1D simulation of compressible flow of air. The 1D model is developed for future simulation of compressible multiphase flow.

1. Introduction

Downhole shut-in valves are used when testing oil and gas wells. The purpose of a shut-in test is to find the flow capacity and the size of the reservoir. The shut-in test consists of a pressure drawdown test period with an open valve, and a pressure buildup test period (pressure at wellbore perforation) with a closed valve (Zolotukhin and Ursin, 2000). During the first test with the valve open, the well starts to produce, and the well bottom pressure is reduced in time, see Fig. 1. The second test period starts by closing the shut-in valve, recording the following pressure buildup with memory gauges hanging below the shut-in valve.

There are two options for the test. These are known as the wellhead and downhole shut-in tests. In the wellhead shut-in test, the valve is located at the wellhead. This configuration avoids the costs and complications of installing a downhole valve, but the drawback is the problems of interpreting the data from the pressure buildup test. The measurement of pressure drawdown can be considered accurate, but pressure buildup is affected by the wellbore storage effect (Guerrero and Lessi, 2007). This effect is related to the two-phase volume of the wellbore above the pressure sensor and its unknown compressibility. An alternative to this is placing the shut-in valve downhole and thus avoid wellbore storage.

This work focuses on the fluid flow in the STC downhole shut-in valve. CFD has been used for similar purposes by a number of authors, as given in Table 1.

Amirante et al. (2006) used CFD for the simulation of fluid forces on a hydraulic directional control valve spool and validated the numerical results with experiments. Amirante et al. (2007) simulated the flow in a hydraulic proportional valve and found that the results matched the experimental data from the valve manufacturer. Chattopadhyay et al. (2012) investigated compressible flow in a spool type pressure regulating valve using CFD. Different turbulence models were evaluated, concluding that the realizable k-e model was the best option for turbulence modeling. Compressible flow in a butterfly valve was modeled with CFD by Leutwyler and Dalton (2008), and the torque on valve disc was validated with experimental values. Valdes et al. (2008) modeled equations for predicting flow and fluid forces in a hydraulic valve on basis of CFD simulations.

* Corresponding author.
E-mail address: svein.edvardsen@ntnu.no (S. Edvardsen).

http://dx.doi.org/10.1016/j.jngse.2014.11.034
1875-5100/

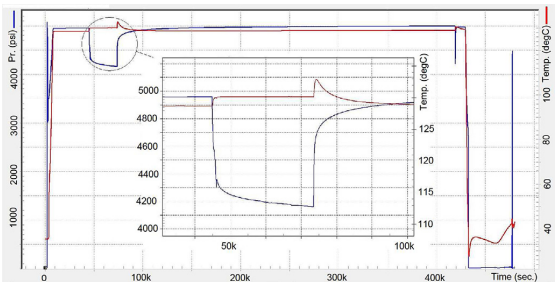

Fig. 1. Pressure and temperature curves from downhole shut-in operation.

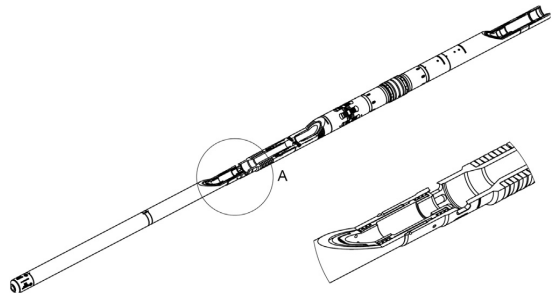

Fig. 2. Qinterra Technologies shut-in valve type STC on an RPD type retrievable packer.

Table 1
CFD simulation of flow in valves.

Author	Software	Type	Main observations
Amirante et al. (2006)	Fluent	3D section	Flow forces, validated
Amirante et al. (2007)	Fluent	3D section	Flow forces, validated
Chattopadhyay et al. (2012)	Fluent	2D/3D	Flow vs. pressure drop
Leutwyler and Dalton (2008)	CFX 10	3D section	Flow forces, validated
Valdes et al. (2008)	Fluent	2D/3D	Flow rates and flow forces

The flow through the shut-in valve can be regarded as flow through a series of different sections, with various shapes and interconnections. The different partial losses will be frictional (viscous) and so-called minor losses, which are dominated by inertia effects. The objective of this work is to investigate the single-phase pressure drop across the downhole shut-in valve, and develop a one-dimensional (1D) simulation model. This model will later serve as a basis for future work on two-phase flow. The approach here is to use 3-dimensional (3D) computational fluid dynamics (CFD) simulations with the Fluent package as a tool for predicting the internal axial pressure profile curve in the shut-in valve. Minor pressure loss factors for the 1D model will be derived from this curve.

It is assumed that a valid 1D model must be able to simulate both compressible and incompressible flow. The simulations will be validated by experiments on a full-scale valve mock-up. The laboratory tests will be performed using water, oil and air as the working fluid. Two-phase correlations are normally valid only for approximately incompressible flow, and it is therefore necessary to divide the total pressure drop into partial frictional and minor losses along the valve.

The shut-in valve is mounted onto a packer, that constitutes the seal and anchor between the valve and the well casing. Fig. 2 illustrates a typical shut-in sleeve valve, assembled with a retrievable packer. A common downhole assembly used by Aker Well Service with packer, shut-in valve, shock absorber and memory gauges hanging below the shut-in valve is shown in Fig. 3. A typical shut-in valve will have a complicated internal flow path, and it cannot be separated into standard minor losses such as sudden contraction, nozzles and bends. Reliable values for single-phase pressure loss can only be found by performing full-scale tests in a laboratory.

The lower part of the valve assembly contains a valve movement mechanism and a timer. When the packer is “set” in hole, a rubber element on the packer is compressed, giving an increase in the diameter of the rubber element, and this forms a seal between the valve-packer assembly and the production tubing (well casing). Setting the packer also forces the slips to move radially outwards,

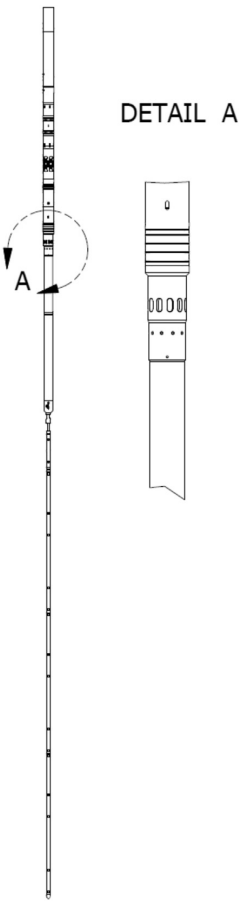

Fig. 3. Downhole assembly for shut-in valve (Qinterra Technologies AS).

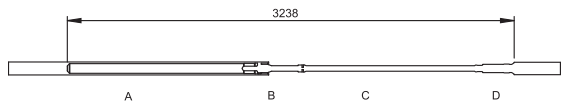

Fig. 4. Main parts of the flow path through the STC shut-in valve.

thus holding the assembly in place against axial movement in the well.

The flow path over and through the valve can be divided into four main parts, see Fig. 4: A: Annular inlet around the lower part, B: radial inlet through valve ports, C: narrow circular flow through the packer, and D: outlet at the top.

As mentioned, this work is designed to develop a 1D model for compressible and incompressible single-phase flow in a downhole shut-in valve. Additionally, CFD simulation of flow in this complex geometry will be validated. First the experimental setup will be presented. The theoretical part then presents the fundamental equations for the 1D model, together with an explanation of the least squares spectral element method. Then the CFD simulation setup is presented with the derivation of minor loss factors. The theoretical part is concluded with the numerical solution. Finally the results from single-phase flow experiments and simulations are presented and discussed.

2. Experimental setup and testing procedure

The experimental tests were performed in the Multiphase Flow Laboratory at the Dept. of Energy and Process Engineering, Norwegian University of Science and Technology (NTNU). The flow loop consists of a supply system for oil, water and air, and has a separator for continuous recirculation of oil and water. Flow control valves and pumps with speed adjustment ensure that the flow rate can be set as required. A logging system records all flow rates and pressures continuously. Water and oil are circulated by centrifugal pumps, and air is supplied by a compressor with a control pressure of 400 kPa (=4 bar). The flow rate of water was measured with an electromagnetic flowmeter with a range of 0–10 kg/s, and flow rate of oil (Exxol D80) was measured with a Coriolis flowmeter with a range of 0–10 kg/s. The air flow was set by control valves and measured with a Coriolis flowmeter with range of 0–0.022 kg/s for small airflows. For large airflows, a vortex flowmeter with range 0.004–0.11 m^3/s at system pressure of 400 kPa was used, corresponding to a mass flow of 0.024–0.612 kg/s. The flowmeter specifications are given in Table 2.

The Coriolis type of oil flowmeter can also detect liquid density.

The test section consists of a full-scale mock-up of a shut-in valve, made in POM (polyoxymethylene, or acetal) and polycarbonate tubes. Roughness for the plastic tubes in the laboratory model is about 5×10^{-6} m. The main parts of the valve are the inlet section with circular flow, a section with annular flow, a section with radial inward flow through valve ports to a central chamber, a narrow circular channel through the upper part and an outlet part with expansion. Pressure was measured at six different points with pressure sensors to get total pressure loss as well as partial losses across the different parts.

A sketch of the Multiphase Flow Loop is shown in Fig. 5.

In addition to water, oil type Exxsol D80 was used, with density 798 kg/m^3 and viscosity 1.8 cp at 20 °C. The pressure drop across the valve model was measured at six different locations, in order to find the individual pressure drops for the different sections inside the valve. The locations of the piezoresistant pressure transmitters are indicated in Figs. 4 and 5. Note that sensor number 1 is also called PT-2.

Table 2
Flowmeters.

Flowmeter	Type	Range	Uncertainty	Repeatability
Air, small	Coriolis	0–0.022 kg/s	±0.1% of rate combined	
Air, large	Vortex	0.024 –0.612 kg/s	±1% of rate	±0.25% of rate
Water	Electromagnetic	10 kg/s	±0.5% of rate	±0.15% of rate
Oil	Coriolis, liquid	10 kg/s	±0.15% of rate combined	

The range of the pressure sensors PT1, PT2 and PT3 is 0–6 bar, and range of sensors PT4, PT5 and PT6 is −1 to 1 bar. The accuracy for pressure transmitters are 0.2% of full scale, and the resulting measurement uncertainties are given in Table 3.

The values for flow and pressure were sampled with a frequency of 5 kHz, and average values logged to a data file 5 times per sec.

For uncorrelated input quantities the combined uncertainty is $u_c^2(y) = \sum_{i=1}^{N} \left(\frac{\partial f}{\partial x_i}\right)^2 u^2(x_i)$, or $[u_c(y)/y]^2 = \sum_{i=1}^{N} [p_i u(x_i)/x_i]^2$, where $y = cX_1^{p1}X_2^{p2}\ldots X_N^{pN}$ (JGCM/WG1, 1995). For a total pressure difference from PT2 to PT6 we have that $u_c^2(y) = 1.2^2 + 0.4^2$ and then the uncertainty is $u_c(y) = \pm 1.3$ kPa.

Fig. 6 shows the laboratory mock-up of the shut-in valve, with details causing minor losses that have to be modeled. The details of the flow path are given in Fig. 7.

3. Mathematical modeling

3.1. 1D model

The objective of this work is to generate a representative 1D finite element model of the shut-in valve. The requirements are that the 1D model must reproduce correct partial and total pressure losses for compressible and incompressible flow. The flow of fluid through the valve can be modeled with the Navier–Stokes equation. If the flow is represented with a 1-dimensional, steady state horizontal flow we get for a slab Δx of the flow that.

$$\rho v \frac{\partial v}{\partial x}\Delta x = -\frac{\partial P}{\partial x}\Delta x - \frac{4}{D_i}\tau_w \Delta x \tag{1}$$

$$\rho v \frac{\partial v}{\partial x} = -\frac{\partial P}{\partial x} - \frac{4}{D_i}\tau_w \tag{2}$$

where ρ [kg/m^3] is density, v [m/s] is velocity, x [m] is distance along the pipe, P [Pa] is pressure and D_i [m] is pipe internal diameter. The term on the left-hand side, $\rho v(\partial v/\partial x)$, is pressure change caused by convective acceleration, or change in velocity due to change in cross-section area. The first part on the right-hand side, $-\partial P/\partial x$, is the static pressure along the pipe. The last term on the right-hand side is the pressure loss caused by the shear stress τ_w [N/m^2] along the pipe wall. In case of a minor pressure loss, we have that $\Delta P = K_L \rho(v^2/2)$, where K_L is a minor loss factor. In that case the momentum equation is

$$\rho v \frac{\partial v}{\partial x} = -\frac{\partial P}{\partial x} - K_L \rho \frac{v^2}{2} \tag{3}$$

There are several changes in cross-section along the flow path in the STC shut-in valve, and for this simulation the area changes will be approximated as conical sections. The derivative of velocity with respect to distance is therefore

$$\frac{\partial v}{\partial x} = \frac{\partial v}{\partial A}\frac{\partial A}{\partial x} = \frac{\partial}{\partial A}\left(\frac{\dot{m}}{A\rho}\right)\frac{\partial A}{\partial x} \tag{4}$$

$$\frac{\partial v}{\partial x} = -\frac{\dot{m}}{A^2\rho}\frac{\partial A}{\partial x} \tag{5}$$

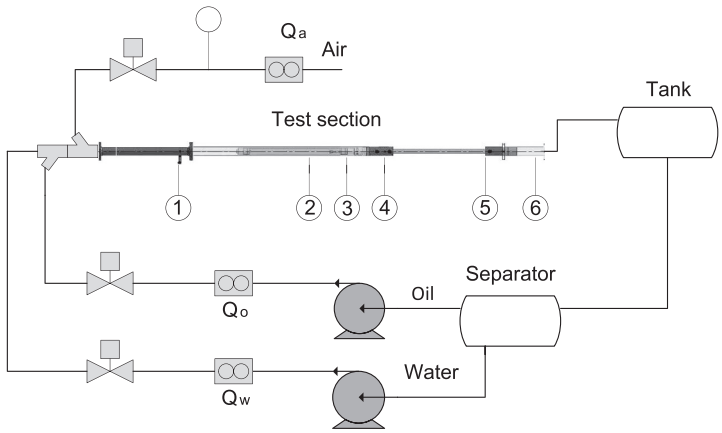

Fig. 5. Schematic of the NTNU test rig for single- and multi-phase flow.

Table 3
Measurement uncertainty.

No.	Range	Uncertainty
PT1	0–6 bar	±1.2 kPa
PT2	0–6 bar	±1.2 kPa
PT3	0–6 bar	±1.2 kPa
PT4	−1/+1 bar	±0.4 kPa
PT5	−1/+1 bar	±0.4 kPa
PT6	−1/+1 bar	±0.4 kPa

For simulation of compressible flow, the flow is regarded as isothermal. The density change is therefore proportional to the pressure change:

$$\rho_2 = \rho_1 \frac{P_2}{P_1} \tag{6}$$

The frictional losses can be expressed as $\Delta P = f(l/D)\rho(v^2/2)$, and we get that

$$\tau_w = f\rho\frac{v^2}{8} \tag{7}$$

here $f = f(R_e, \varepsilon/D)$ is the Darcy friction factor, $R_e = \rho v D/\mu$ is the Reynolds number, μ [Pa s] is dynamic viscosity, ε [m] is pipe roughness and D is pipe diameter. The friction factor can be approximated by the formula by Swamee and Jain (1976):

$$f = \frac{0.25}{\left(\log\left(\frac{\varepsilon}{3.7D} + \frac{5.74}{R_e^{0.9}}\right)\right)^2} \tag{8}$$

The plastic tubes and parts in this laboratory model are assumed to be smooth; $\varepsilon = 0$. The pressure drop equation will be solved using the least-squares method with spectral elements. This method

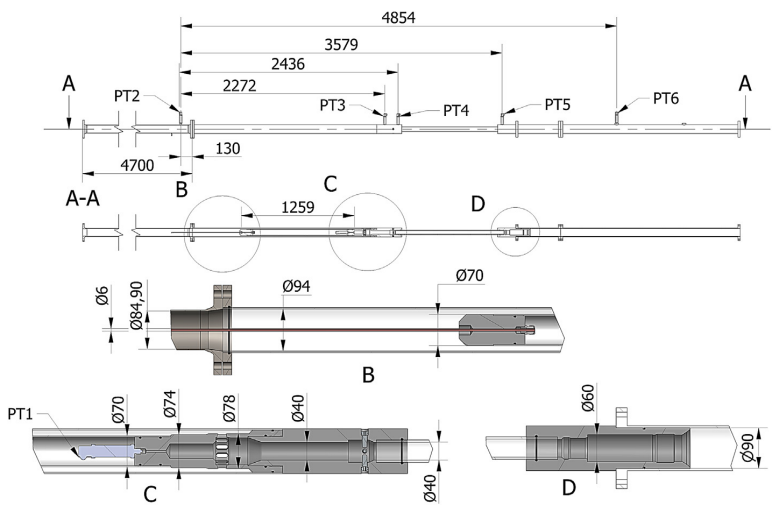

Fig. 6. Laboratory mock-up of STC shut-in valve.

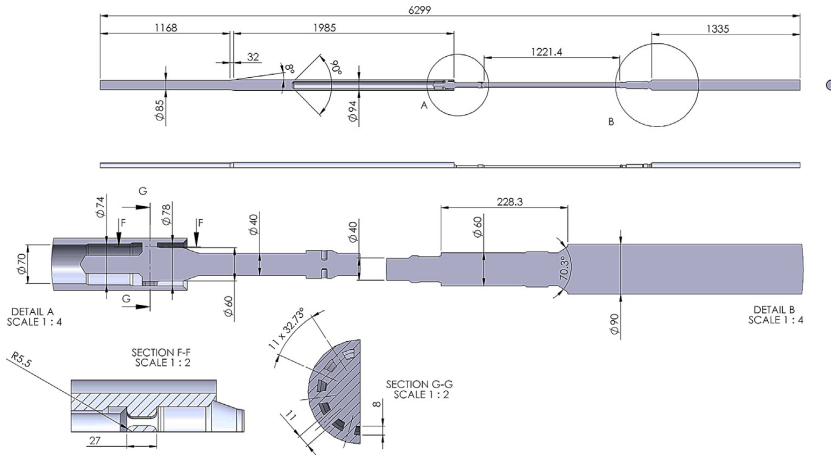

Fig. 7. Flow path details of STC shut-in valve mock-up.

requires linear equations, and the term $v\partial v/\partial x$ can be linearized using Newton–Raphson linearization. With k defining the step in an iteration we have that.

$$u_{k+1} = u_k + \delta u \tag{9}$$

$$u\frac{\partial u}{\partial x} = (u_k + \delta u)\left(\frac{\partial u_k}{\partial x} + \frac{\partial \delta u}{\partial x}\right) \tag{10}$$

$$u\frac{\partial u}{\partial x} = u_k\frac{\partial u_{k+1}}{\partial x} + u_{k+1}\frac{\partial u_k}{\partial x} - u_k\frac{\partial u_k}{\partial x} \tag{11}$$

here step k is the known value from the previous iteration step, and $k+1$ is the new value.

The flow volume around and through the shut-in valve is depicted in Fig. 8. For the purpose of a finite element simulation of the flow, the whole shut-in valve is divided into discrete elements. Detail A in Fig. 8 gives example of how the valve is divided into 1D elements.

This is the inlet section, showing a cylindrical section and a concentric expansion. The latter has also a loss factor, indicated as K_{L-2}. Straight sections are divided into several elements. The total test section length of 4.851 m was divided into a total of 79 elements, with element lengths between 0.033 m and 0.074 m. For the laboratory experiments, the outlet pressure was constant and equal to atmospheric pressure. The mass flow and outlet pressure were therefore chosen as boundary conditions for the simulations. The spectral element method is a higher order method, and the order O is given as $O = P - 1$, where P is number of nodes per element including end nodes. Refinement tests were run with different orders, and the final simulations were performed with $P = 6$ nodes per element.

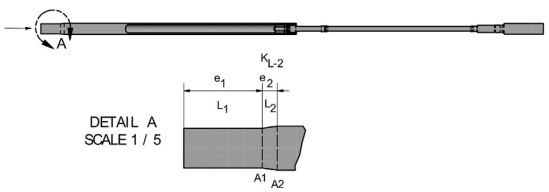

Fig. 8. Flow volume around and through the shut-in valve, with indication of finite element representation.

The following information is provided for each element, see Table 4:

Type: Frictional or minor loss type. This parameter is read and interpreted by the computer program. The set of equations to be used will depend on the element type.
Length: Length of element.
Inlet hydraulic diameter: Calculated from $D_h = 4A/p$, where A is flow cross-section and p is perimeter. For annular flow $D_h = D_{\text{outer}} - D_{\text{inner}}$.
Outlet hydraulic diameter: Calculated as above.
Inlet flow cross-section: This area is pre-calculated, as the flow cross-section is not circular everywhere.
Outlet flow cross-section: Calculated for circular and annular sections.
Minor loss coefficient: This value will be given only for elements of type “minor”.

3.2. Least squares method

The dynamic equations for two-phase flow are solved using the least-squares method with spectral element approximation (Proot and Gerritsma, 2002). This method has also been used successfully by Chiapero (2013) for the simulation of two-phase flow instabilities, and by Sporleder (2011) for simulation of chemical reactors.

The advantages of the least-squares method include low numerical diffusion, generic implementation and that it involves the minimization of a norm-equivalent functional. Generally we have that

$$L\boldsymbol{u} = \boldsymbol{g} \quad \text{in } \Omega \tag{12}$$

$$B\boldsymbol{u} = \boldsymbol{h} \quad \text{on } \partial\Omega \tag{13}$$

where Ω and $\partial\Omega$ are the domain and the boundary of the domain respectively. With the requirement that the system is well-posed and that the operators L and B are continuous mappings between

Table 4
Frictional and singular losses in the STC downhole valve.

No.	Description	Length S [m]	Minor loss coeff.	Hydraulic diameter 1 [m]	Hydraulic diameter 2 [m]	Flow cross-section in [m^2]	Flow cross-section out [m^2]
1	Friction	0.1		0.085	0.085	5.675E-03	5.675E-03
2	Diffuser, 16°	0.03	0.067	0.085	0.094	5.675E-03	6.940E-03
3	Friction	0.525		0.094	0.094	6.940E-03	6.940E-03
4	Annular contraction, 90°	0.015	0.28	0.094	0.024	6.940E-03	3.091E-03
5	Friction	1.261		0.024	0.024	3.091E-03	3.091E-03
6	Annular contraction, 90°	0.079	0.037	0.024	0.02	3.091E-03	2.639E-03
7	Annular contraction, 90°	0.02	0.044	0.02	0.016	2.639E-03	2.161E-03
8	Valve inlet	0.075	1.74	0.016	0.06	2.161E-03	2.827E-03
9	Contraction, 40°	0.03	0	0.06	0.04	2.827E-03	1.257E-03
10	Friction	0.192		0.04	0.04	1.257E-03	1.257E-03
11	Equalizing central	0.058	0.15	0.04	0.04	1.257E-03	1.257E-03
12	Friction	1.22		0.04	0.04	1.257E-03	1.257E-03
13	Expansion	0.288	0.255	0.04	0.09	1.257E-03	6.362E-03
14	Friction	0.958		0.09	0.09	6.362E-03	6.362E-03
	Total length	4.851					

the function space $X(\Omega)$ onto the solution space $Y(\Omega) \times Y(\partial\Omega)$, the norm equivalent functional becomes

$$I(u) = \frac{1}{2}||L\mathbf{u} - \mathbf{g}||^2_{Y(\mathbf{\Omega})} + \frac{1}{2}||B\mathbf{u} - \mathbf{h}||^2_{Y(\partial\mathbf{\Omega})} \tag{14}$$

Variational analysis gives that

$$\lim_{\varepsilon \to 0} \frac{\mathrm{d}}{\mathrm{d}\varepsilon} I(\mathbf{u} + \varepsilon\mathbf{v}) = \mathbf{0} \ \forall \ \mathbf{u} \in \mathbf{X}(\mathbf{\Omega}) \tag{15}$$

I can now be minimized with the following necessary condition: Find $\mathbf{u} \in \mathbf{X}(\mathbf{\Omega})$ such that

$$A(\mathbf{u}, \mathbf{v}) = \mathbf{F}(\mathbf{v}) \ \forall \ \mathbf{v} \in \mathbf{X}(\mathbf{\Omega}) \tag{16}$$

and

$$A(\mathbf{u}, \mathbf{v}) = \langle L\mathbf{u}, \mathbf{L}\mathbf{v} \rangle_{Y(\mathbf{\Omega})} + \langle B\mathbf{u}, \mathbf{B}\mathbf{v} \rangle_{Y(\partial\mathbf{\Omega})} \tag{17}$$

$$F(\mathbf{v}) = \langle \mathbf{g}, \mathbf{L}\mathbf{v} \rangle_{Y(\mathbf{\Omega})} + \langle \mathbf{h}, \mathbf{B}\mathbf{v} \rangle_{Y(\partial\mathbf{\Omega})} \tag{18}$$

$A : X \times X \to \mathbb{R}$ is a symmetric, continuous bilinear form. $F : X \to \mathbb{R}$ is a continuous linear form.

3.3. Spectral element formulation

As for finite element formulations, the computational domain Ω is divided into N_e non-overlapping sub-domains Ω_e such that

$$\Omega = \cup_{e=1}^{N_e} \Omega_e \text{ with } \Omega_e \cap \Omega_k = \varnothing, \ e \neq k \tag{19}$$

The unknown function u_h^e is approximated in each element Ω_e by the set of all polynomials P_Q of degree $\leq Q$. The global approximation u_h in Ω is.

$$u_h = \cup_{e=1}^{N_e} u_h^e \tag{20}$$

Within each element, the solution is expanded in Φ_i basis functions

$$u_h^e(x) = \sum_{n=0}^{i} u_n^e \Phi_i(\xi) \tag{21}$$

with $(\xi) = X_e^{-1}(x)$ th local coordinate of (x) in the parent element, with $-1 \leq \xi \leq 1$, and u_h^e the coefficients in the expansion.

3.4. CFD simulation

A full 3-dimensional CFD simulation was used as a tool for establishing the minor losses for the 1D model. In order to reduce the computational cost only incompressible simulations were performed, and the governing equations to be solved are the continuity equation:

$$\nabla \cdot (\rho \overline{v}) = 0 \tag{22}$$

and the momentum equation:

$$\nabla \cdot (\rho \overline{v}\overline{v}) = -\nabla P + (\mu + \mu_t)\nabla^2 \overline{v} + \rho \overline{g} \tag{23}$$

where μ is absolute viscosity and μ_t is turbulent viscosity.

The absolute viscosity of water is dependent on the temperature. It changes from 1.0 cP at 20 °C to 0.5 cP at 55 °C. The maximum possible temperature rise can be calculated from the technical work W_t performed by the flow per mass unit. The maximum pumping pressure available in the laboratory setup is 3 bar. For a volume of 0.001 m^3 we get that $W_t = V(P_1 - P_2) = 0.001 * 300{,}000 = 300$ J. The heat capacity of water at 20 °C is 4180 J/Kg K, and maximum temperature rise for water flow is therefore $\Delta T = 300/4180 = 0.07$ K. Here it is assumed that all technical work is transformed into heat by frictional work on the fluid. The absolute viscosity is therefore regarded to be constant since the temperature change will be very little.

Specific heat capacity for oil type Exxsol D80 has not been found, but for kerosene and light oils the heat capacity is approximately 2000 J/Kg K. With a density of 798 kg/m^3 and a pressure drop of 3 bar we get $\Delta T = 300/(2000 * 0.798) = 0.19$ K. The possible temperature rise is higher for oil than for water, but it is still very low.

Three different turbulence models were tested: standard k-ε model, the RNG k-ε model and the realizable k-ε model. In the standard semi-empirical 2-equation k-ε model by Launder and Spalding (1974), the turbulent viscosity μ_t is given by turbulent kinetic energy k and turbulent dissipation rate ε as $\mu_t = \rho C_\mu (k^2/\varepsilon)$, where $C_\mu = 0.09$ is a constant. The RNG k-ε turbulence model by Yakhot and Orszag (1986) is derived from the Navier–Stokes equations using the re-normalization group theory. The equation for turbulent dissipation rate ε has an extra term for rapidly strained flows, and the effect of swirl on turbulence is added. The Prandtl number is given by an analytical formula, and the calculation of the effective viscosity is done with respect to both high and low Reynolds numbers. This turbulence model is recommended by Amirante et al. (2006).

In the realizable k-ε model by Shih et al. (1995), the number C_μ in the equation for turbulent viscosity is a function of the mean strain and rotation rates, the turbulence fields and the angular velocity of the system rotation. This model has been tested and found to perform better than the standard k-ε model in many cases, e.g. channel flow, as demonstrated by Leutwyler and Dalton (2008).

A 3-dimensional model of the flow volume was created with the SOLIDWORKS package and loaded into ANSYS Fluent, and a part of the generated unstructured mesh is shown in Fig. 9.

The first part of the simulations was performed on a symmetrical half-section. The mesh was refined until the simulated pressure drop did not change with further refinement. The final mesh had maximum 0.005 m cell size, with maximum 0.004 m face size. As shown on the figure, a mesh with prismatic boundary elements was selected In order to limit the total number of cells, the final mesh had 6 inflated layers, and automatic adjustable wall functions were used. In order to allow for build-up of turbulence, the inlet section to the valve was extended 1 m in front of the first pressure sensor. Turbulence intensity at inlet was set to 5%.

A maximum normalized residual of 10^{-4} was used as convergence criteria for all equations. CFD simulations were also performed on a full cross-section model.

3.5. Results from CFD simulations and determination of minor losses

Simulation results are presented together with experimental results for total pressure loss for water and oil flow in Fig. 10. These simulations were done on a symmetrical half-section model, using the RNG k-ε turbulence model. For water flow the deviation between simulations and experimental values is 2–3%. For oil flow, the deviation is 4–6% at high flow rates. As the simulated pressures in both cases are so close to the experimental pressure values, the water flow simulations were chosen for calculating representative partial pressure drops inside the STC shut-in valve.

Fig. 11 shows the flow velocity inside the shut-in valve along a symmetry plane, for a water mass flow of 9.83 kg/s. This flow rate corresponds to the maximum flow rate for the laboratory experiments.

From the inlet at the left-hand side we can see that the flow first changes to annular flow, and that the annular cross-section is reduced in two steps towards the valve inlet at detail A. Inside the valve ports there is complicated turbulent flow, and in the right-hand part of detail A we can see the equalizing section. The function of this part is connected to the release of a closed valve from the well-bore. Detail B illustrates the outlet at the top of the valve, with a two-step expansion. Above the valve there is a wake section with turbulence which is similar to an oscillating Karman vortex street wake.

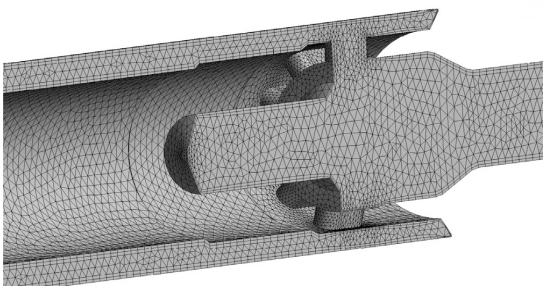

Fig. 9. Unstructured mesh for CFD simulation.

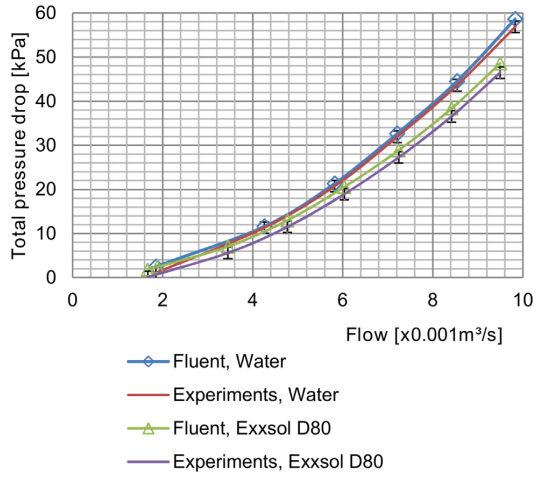

Fig. 10. CFD simulation results and experimental results for total pressure drop over STC shut-in valve. Error bars of ±1.3 kPa are indicated.

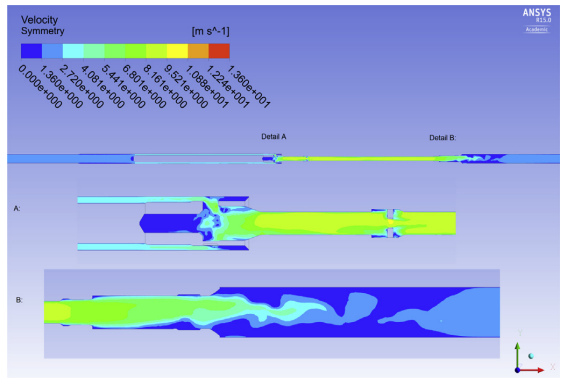

Fig. 11. Velocity plot of ANSYS CFD simulation for high rate water flow, 9.83 kg/s.

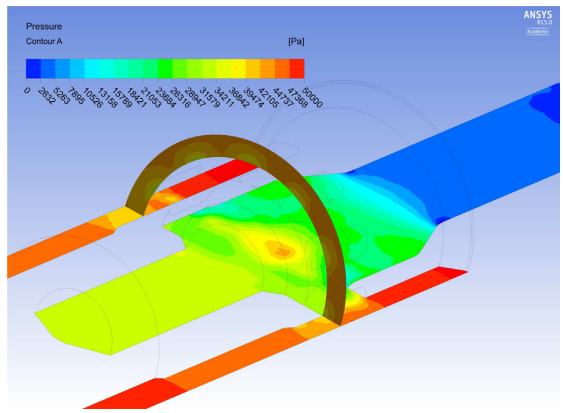

Fig. 12. Cross-sectional pressure profile at valve ports at high water flow rate.

The pressures in Fig. 12 are average pressures over the cross-sections along the valve, calculated with a built-in ANSYS program function. In this figure there are two pressure profiles. One profile is transversal, just upstream of the valve ports. The second profile is along the symmetry plane in the center of the valve. The two pressure profiles have the same pressure color scale.

The pressure profile along the shut-in valve is shown in Fig. 13 for three different simulation cases. All pressure values are taken from ANSYS cross-section average calculations. Simulations were performed on both symmetrical half-sections and full cross-section.

Several valve features can be observed from the pressure-position curve. The coordinate system used has its origin at 22 mm below the valve openings, with lowest valve point at −1.355 m and the top outlet at 1.883 m. The test section has inlet at −3.08 m, and outlet at 3.0 m. At −1.91 m there is a conical expansion from 84.9 to 94 mm diameter due to practical reasons in the laboratory. A small increase in pressure can be observed due to the reduced velocity. Annular flow occurs over the lower section of the valve, and a sudden pressure drop can be observed at the valve nose at −1.35 m. At −0.079 m there is an annular contraction, with a corresponding pressure drop. Another annular contraction follows at position 0, closely followed by the valve ports. The flow cross-section of the valve ports is 2981 mm^2, which is a little larger than the narrowest annular section. The outside pressure of 46 kPa drops to about 24 kPa inside the turbulent valve chamber. As the flow is guided further into the 40 mm diameter central section, pressure drops further. An additional pressure drop can be observed across the equalizing central. The outlet expansion section is between 1.595 m and 1.883 m, but the pressure continues to increase to about position 2.35 m. In other words, the pressure increases to a position about 0.45 m above the valve outlet, where a fully developed turbulent velocity profile can be expected.

The minor losses for each location along the valve can now be determined from the pressure curve, by applying the following equation:

$$P_1 + \rho\frac{v_1^2}{2} - K_L\rho\frac{v_1^2}{2} = P_2 + \rho\frac{v_2^2}{2} \tag{24}$$

The velocities v_1 and v_2 downstream of and upstream the minor loss location are calculated at the same positions as P_1 and P_2. Fig. 14 shows how the pressure profile curve can be used for the calculation of a minor loss factor at the valve outlet. As can be seen from Figs. 11 and 13, the two expansions at the outlet must be treated as

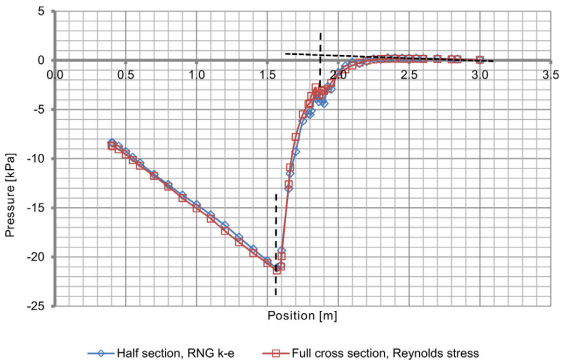

Fig. 13. Pressure profile along the shut-in valve as simulated with ANSYS Fluent for half-section and full cross-section.

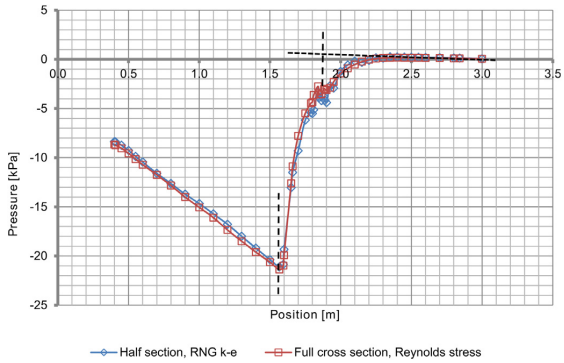

Fig. 14. Pressure profile and calculation of valve outlet loss factor.

one single loss factor. There are in fact several diameter changes at the outlet, with distances down to fractions of the local diameter. See also Detail D in Fig. 6. The expansion occurs between positions 1.595 m and 1.883 m, and this is marked with dashed lines in Fig. 14. The linear pressure profile trend downstream of position 2.35 m is extrapolated back to the position of the valve outlet. The intersection with the vertical dashed line at position 1.883 m will now give the outlet pressure P_2 for calculation of a local minor loss factor. The pressure P_1 is taken from the intersection of the simulated pressure profile and the vertical dashed line at position 1.595 m, which is the start of the first expansion.

For the inlet expansion at −1.9 m from 84.9 mm to 94 mm diameter, the loss factor from the CFD simulation is calculated to 0.067, and this value is used in the simulations. The next minor loss is at −1.35 m with a contraction to an annular section, with 70 mm inner diameter, and the minor loss factor is calculated to 0.285. The minor loss factors for the two following annular contractions are calculated in the same manner to respectively 0.037 and 0.044. For the pressure drop across the valve inlet ports, the stagnation pressure P_s, as measured with sensor PT-1, was used in the following way:

$$P_1 + \rho\frac{v_1^2}{2} - K_L\rho\frac{v_1^2}{2} = P_s \tag{25}$$

The valve inlet minor loss coefficient is found to be 1.74. The next change is a contraction from circular flow 60 mm–40 mm diameter. As can be seen from detail C in Fig. 5, there is a well rounded transition at the start and end of this contraction. From the CFD simulation results it can be concluded that the minor loss coefficient here is approximately zero. The reason might be that there is a heavy turbulence right in front of it, and that a contraction will help converting a part of the turbulent energy into kinetic energy in the flow direction.

The equalizing section has a short part with an increased diameter, and four screws are protruding into the chamber. The minor loss coefficient across it is found to be 0.154. Treated as one single minor loss as described above, the minor loss factor at the valve outlet is found to be 0.255. The complete list of calculated minor loss coefficients K_L is given in Table 4.

3.6. Numerical solution of 1D model

The calculation of total pressure drop with the 1D model was accomplished as an iteration for one element at a time, with frictional and minor losses as given by Table 4. As explained above, the

least-squares method with spectral elements was used. Spectral elements are higher order elements, with internal nodes. The solution for each element will therefore be a column vector with pressure at each node in the element. The set of equations given above can now be formulated as $L\mathbf{u} = \mathbf{g}$ in Ω. The linear partial differential operator is

$$L = \left\{\frac{\partial}{\partial x}\right\} \tag{26}$$

and

$$L\mathbf{u} = v_k\frac{\partial v_{k+1}}{\partial x} + v_{k+1}\frac{\partial v_k}{\partial x} + \frac{\partial P}{\partial x} \tag{27}$$

$$\mathbf{g} = -\frac{4}{D_i}\tau_w + v_k\frac{\partial v_k}{\partial x} \tag{28}$$

and for minor pressure losses

$$\mathbf{g} = -\frac{1}{\partial x}K_L\rho\frac{v^2}{2} + v_k\frac{\partial v_k}{\partial x} \tag{29}$$

The last term in the expression for g comes from the linearization of $v(\partial v/\partial x)$, and as given above we have that $\partial v/\partial x = -(\dot{m}/A^2\rho)(\partial A/\partial x)$.

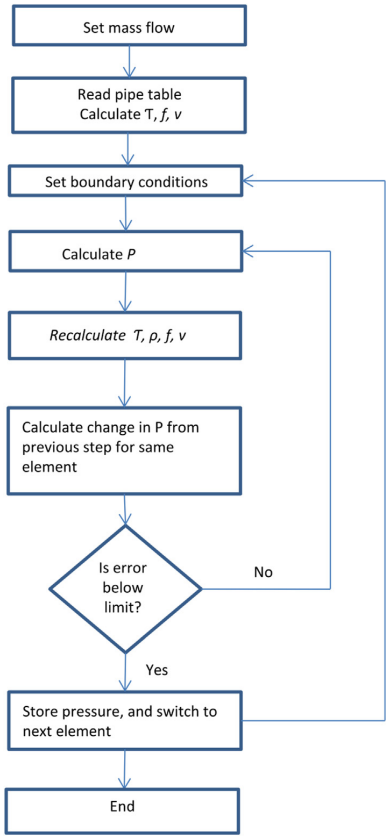

Fig. 15. Solution algorithm for single-phase liquid flow.

The boundary term will be omitted here, and the boundary condition will be enforced strongly. The simulations will be compared to laboratory experimental results, where the valve outlet is at atmospheric pressure. Consequently, the outlet pressure will be specified and the element pressures will be calculated counter current from outlet to inlet. A solution algorithm is given in Fig. 15.

The procedure is applicable to compressible flow of air as well, as the density ρ is recalculated at each iteration step. The error evaluated in the decision step is in fact the change in calculated pressure. If the calculated pressure changes more than a decided limit, a new iteration loop is done, with recalculated pressure based upon updated density, velocity and friction factor.

4. Results and discussions

4.1. Single-phase flow calibration

The single-phase pressure drop in a straight section between pressure sensors PT-4 and PT-5 on the mock-up was used for single-phase flow calibration, see Fig. 16. The tube has 40 mm inside diameter and smooth surface, and it is made of PMMA (Polymethyl methacrylate, or acrylic glass). With an estimated roughness of $\varepsilon = 0.004\cdot10^{-3}$ m, we have that $D_h/\varepsilon = 10{,}000$.

The experimental friction factor is compared with the well-known Colebrook correlation.

$$\frac{1}{\sqrt{f}} = -2\log\left(\frac{2.51}{Re\sqrt{f}} + \frac{\varepsilon}{3.7D_h}\right) \tag{30}$$

The experimental friction factor can be calculated from the following relation:

$$\Delta p = f\frac{l}{D_h}\rho\frac{v^2}{2}$$
$$\Updownarrow$$
$$f = \frac{2D_h\Delta p}{\rho l v^2}$$

Calibration tests were done with Reynolds numbers from 135,600 to 312,900 for water, and with Reynolds numbers from 23,500 to 133,990 for oil. The results are given in Figs. 17 and 18.

The uncertainty in friction factor measurement depends on the flow rate. At low flow rates, e.g. 2 kg/s, with about 3 kPa pressure drop the combined uncertainty is $u_c(y)/y = \sqrt{(-2(0.005{*}10/2))^2 + (1.3/3)^2} = 44\%$, assuming there is no uncertainty in diameter measurement for the valve inlet. At high flow rates it is typically $u_c(y)/y = \sqrt{(-2(0.005{*}10/10))^2 + (1.3/55)^2} = 2.6\%$. As can be seen from Figs. 15 and 16, the experimental friction factor is about 10–20% higher than the theoretical values for both oil and water.

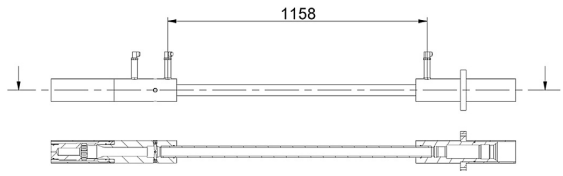

Fig. 16. Central straight section of shut-in valve mock-up used for flow calibration.

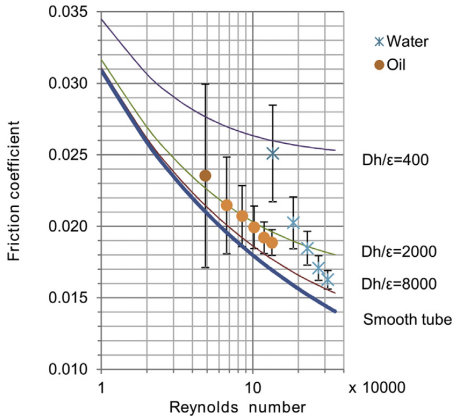

Fig. 17. Experimental friction factor compared to the Colebrook correlation.

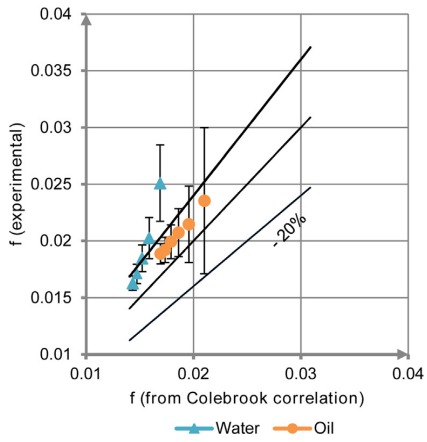

Fig. 18. Comparison of experimental friction factor with result from the Colebrook correlation.

Oil flow tests were done with flow rates from 1.67 to 9.5 kg/s, and water flow tests with rates from 4.26 to 9.83 kg/s.

For the tests with water at low flow rates (low Reynolds numbers), experimental friction factors were more than 20% higher than the Colebrook correlation theoretical values. The main part of the friction factor uncertainty comes from the relative uncertainty in the measurement of the pressure. For the lowest flow rates the pressure at the sensor location might be disturbed due to the contraction upstream, as depicted in Fig. 19. The pressure sensor tap is only 35 mm downstream a 50 deg. conical contraction. A reduction in effective flow area (vena contracta) can be expected, giving a reduced pressure where the pressure sensor is located. For low flow rates and low overall pressure drop, a small addition to the pressure drop will have a huge impact on the calculated friction factor. For oil flow, the higher viscosity is believed to reduce the effect of flow contraction behind the conical contraction.

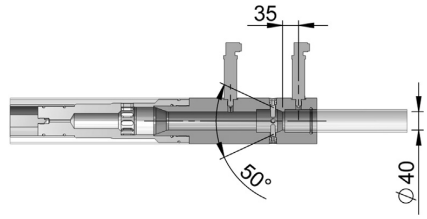

Fig. 19. Internal details of STC shut-in valve.

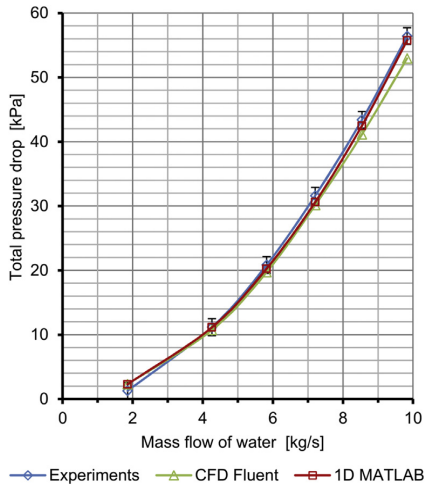

Fig. 20. Experimental water flow pressure drop compared to CFD simulation and 1D MATLAB model.

4.2. Single-phase flow study – water

The experimental pressure drop for single-phase flow of water is presented in Fig. 20, together with (3D) CFD simulated pressure

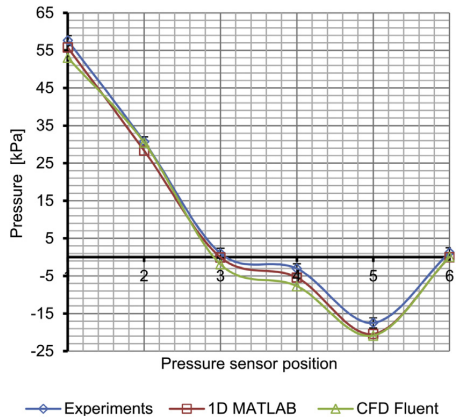

Fig. 21. Pressure drop along the STC shut-in valve. Water flow experimental results compared to 3D CFD full cross-section simulations and 1D simulations. Measurement error bars of ±1.3 kPa indicated.

drop and the 1D model simulation. The curves reveal first of all that the pressure drop from the CFD simulation of incompressible liquid flow is very close to the experimental values. The deviation is −6.1% for the highest flow rate. This CFD simulation was performed with a full cross-section 3D model and the realizable k-ε turbulence model.

Second, the curves show that the 1D model also predicts the pressure loss quite accurately. The friction factor used in all MATLAB simulations was calculated with the Haaland equation, with an extra 10% due to the results from the calibration tests, see Fig. 18. The deviation is −0.6 kPa, or −1.2% at the highest flow rate. The deviation is therefore of the same order as the measurement uncertainty of ±1.3 kPa.

The procedure used for deriving the minor loss factors from the CFD simulations must therefore be correct, and the 1D model as such is also working satisfyingly for liquid flow. The small deviation between the CFD simulation and the 1D model might partly be due to the increased frictional coefficient.

In Fig. 21 the experimental pressure profile along the STC shut-in valve mock-up is shown together with simulation results from ANSYS Fluent and 1D simulation results from MATLAB. The water flow rate is 9.83 kg/s. These curves are only correct at the sensor positions 1–6, and are only sketchy between these points.

Although the overall pressure loss is simulated with high accuracy, there are some small internal inaccuracies for both the CFD and the MATLAB 1D simulations. Between sensor PT3 and sensor PT4 the experimental results found a lower pressure drop. It is therefore believed that the complex flow geometry in the central part is not completely recreated with the CFD model. An even finer mesh resolution or some tuned turbulence parameters would probably be the solution.

The initial CFD simulations were performed on a 3-dimensional symmetrical half-section of the valve, but the simulated pressure drop across the equalizing section between PT3 and PT4 was much higher than the experimental value. A change to simulations on a 3D model with full cross-section improved the results. The new model had about 3.3 million elements. Different turbulence models were also tested. Using the realizable k-ε model (Shih et al., 1995) gave an overall pressure drop closer to experimental values than the k-e model and the Reynolds stress model. Fig. 21 shows the results from the final CFD simulations with realizable k-ε turbulence model on the full cross-section model.

4.3. Single-phase flow study – oil type Exxsol D80

Experiments and 1D simulations with oil type Exxsol D80 found the same trend as with water, see Fig. 22. Here the pressure drop is over-predicted at low flow rates, and under-predicted by 2.3 kPa or 5% at the highest flow rate. The pressure profile along the valve for Exxol D80 is shown in Fig. 23, and it reveals some interesting details. For the first part from the inlet to the valve chamber (PT1) the experimental pressure drop is a little higher than the 1D MATLAB simulated value. This trend was not seen with water, which has a lower viscosity and higher density. The pressure drop from PT1 to PT3 is however lowest for the experimental value, and here the minor loss factor for the 40° contraction is found to be zero. This shows that the pressure drop across the valve ports from the MATLAB 1D model is too low, or that the annular section in front of the valve ports creates a higher pressure drop than expected with oil flow. This trend is not seen with water flow.

4.4. Single-phase flow study – air

The 1D flow model that is developed here will be used also for compressible two-phase flow, and it is therefore necessary to validate it for compressible flow of air. For experiments with air flow, the total pressure drop between sensors PT2 and PT6 was measured with a 0–100 kPa differential pressure transmitter, and the pressure drop from PT4 to PT5 was measured with a 0–10 kPa differential pressure transmitter. The first one had an accuracy of 0.5%, and the second one an accuracy of 1%.

The simulated pressure drop for airflow is shown together with the experimental results in Fig. 24.

Experiments with the full-scale valve mock-up gave a total pressure drop of 24.4 kPa at maximum air flow rate of 0.212 kg/s. The 1D model understate the pressure drop by 10.5% at maximum flow rate, and this trend is constant over the whole range of flows.

The pressure profile inside the valve mock-up for an airflow of 0.212 kg/s is given in Fig. 25.

The most noticeable difference here is the pressure drop across the central section, where the experimental results find a higher pressure drop than the 1D MATLAB simulations. This difference is the opposite of the result for water flow. One explanation might be that sensor PT4 is influenced by a vena contracta effect downstream of the central section. If that is the case, the increased experimental frictional pressure drop between sensors PT4 and PT5 can also be

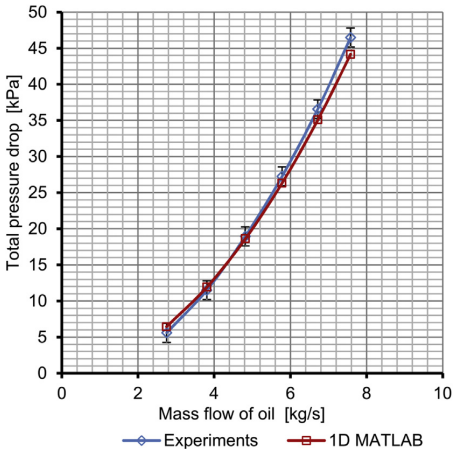

Fig. 22. Experimental oil flow pressure drop compared to 1-D MATLAB model.

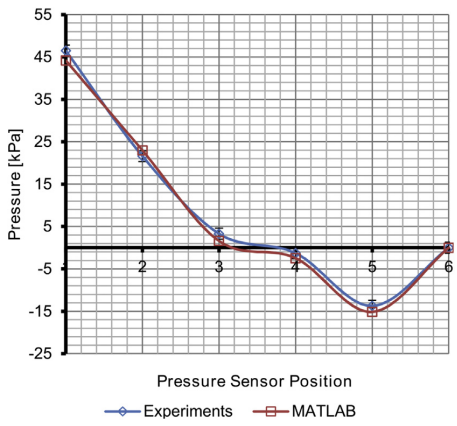

Fig. 23. Experimental oil flow pressure drop compared to 1D MATLAB model.

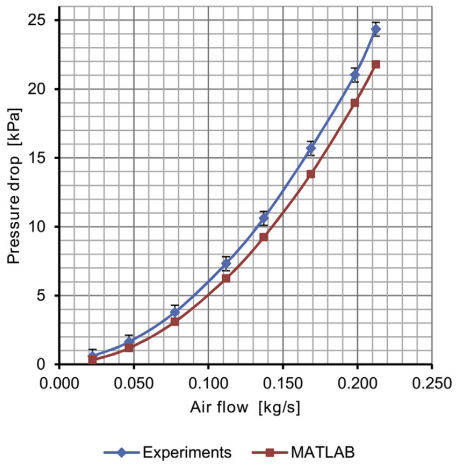

Fig. 24. 1D model simulated total pressure drop for airflow.

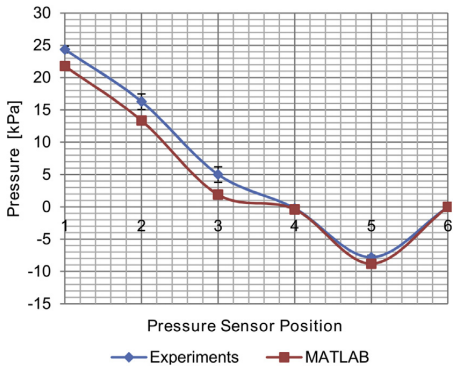

Fig. 25. Pressure profile inside shut-in valve for airflow of 0.212 kg/s.

explained. For all air flow simulations the friction factor was as calculated from Equation (8), with 10% additional friction.

5. Conclusion

A downhole shut-in valve represents a complex flow geometry. The total pressure loss for single-phase water flow was simulated using the ANSYS Fluent CFD package. When comparing these simulations with the experimental results, it is proved that incompressible liquid flow can be simulated with a high degree of precision using a full cross-section 3-dimensional model. The realizable k-ε turbulence model was found to perform better than the RNG k-ε and the Reynolds stress turbulence model. At the highest flow rate the CDF simulated total pressure drop is less than 2% lower than experimental values. CFD simulations on a 3-dimensional symmetrical half-section were found to give too high pressure drop in some areas with high velocity and turbulence intensity.

In order to be able to simulate multiphase pressure drop, a 1-dimensional model is convenient. From the CFD-simulation, the axial pressure profile graph can be used for determination of all internal minor losses. Simulation of liquid flow with a novel 1D least-squares spectral element method gives total pressure loss deviation comparable to the CFD simulation. The 1D model can also be used for simulation of compressible flow, by regarding the flow as isothermal. At maximum air flow rate, the 1D model understates the total pressure drop by 10% compared to experimental values.

Acknowledgment

We thank Stig Karlsen, Manager of Plugs and Packers, Qinterra Technologies, Narvik, for permission to publish the work. We are also thankful to The Research Council of Norway 208174 for financial support.

Nomenclature

A	cross-section area [m^2]
c	constant
c_p	specific heat capacity at constant pressure
D	diameter [m]
f	friction coefficient
g	gravitational acceleration [m/s^2]
G	mass flux [kg/m^2 s]
h	enthalpy
k	turbulent kinetic energy
K_L	minor loss coefficient
l	length [m]
$\dot{m}$	mass flow rate [kg/s]
P	pressure [Pa]
R_e	Reynolds number
T	temperature [K]
u	internal energy
v	velocity [m/s]
V	volume [m^3]
x	length coordinate

Greek symbols

ε	turbulent dissipation rate
ϵ	surface roughness
μ	dynamic viscosity [Pa s]
μ_t	turbulent viscosity
ρ	density
τ_w	wall shear stress [Pa]

Subscripts

h	hydraulic
s	stagnation
w	wall

Abbreviations

CFD	computational fluid dynamics
RNG	re-normalization group

References

Amirante, R., Moscatelli, P., Catalano, L., 2007. Evaluation of the flow forces on a direct (single stage) proportional valve by means of a computational fluid dynamic analysis. Energy Convers. Manag. 48 (3), 942–953. http://dx.doi.org/10.1016/j.enconman.2006.08.024. http://www.sciencedirect.com/science/article/pii/S0196890406002949.

Amirante, R., Vescovo, G.D., Lippolis, A., 2006. Evaluation of the flow forces on an open centre directional control valve by means of a computational fluid dynamic analysis. Energy Convers. Manag. 47, 1748–1760. http://dx.doi.org/10.1016/j.enconman.2005.10.005. http://www.sciencedirect.com/science/article/pii/S0196890405002542.

Chattopadhyay, H., Kundu, A., Saha, B.K., Gangopadhyay, T., 2012. Analysis of flow structure inside a spool type pressure regulating valve. Energy Convers. Manag. 53 (1), 196–204. http://dx.doi.org/10.1016/j.enconman.2011.08.021. http://www.sciencedirect.com/science/article/pii/S0196890411002354.

Chiapero, E.M., 2013. Two-phase Flow Instabilities and Flow Mal-distribution in Parallel Channels. Norwegian University of Science and Technology (Ph.D. thesis).

Guerrero, R.P., Lessi, J., 2007. Fast Shut-in Tools Improve near wellbore characterisation from build-up test interpretation. Fast Shut-in Tools, pp. 163–197. http://www.onepetro.org/mslib/app/search.do.

JGCM/WG1, 1995. Evaluation of Measurement Data – Guide to the Expression of Uncertainty in Measurement. JCGM 100:2008 (GUM 1995).

Launder, B., Spalding, D., 1974. The numerical computation of turbulent flows. Comput. Methods Appl. Mech. Eng. 3, 269–289.

Leutwyler, Z., Dalton, C., 2008. A CFD study of the flow field, resultant force, and aerodynamic torque on a symmetric disk butterfly valve in a compressible fluid. J. Press. Vessel Technol. 130 (2) http://dx.doi.org/10.1115/1.2891929, 021302–021302.

Proot, M., Gerritsma, M., 2002. Least-squares spectral element applied to the stokes problem. J. Comp. Phys. 181 (2), 454–477. http://dx.doi.org/10.1006/jcph.2002.7137.

Shih, T.H., Liou, W., Shabbir, A., Yang, Z., Zhu, J., 1995. A new ke Eddy-viscosity model for high Reynolds number turbulent flows model development and validation. Comput Fluids 24, 227–238.

Sporleder, F., 2011. Simulation of Chemical Reactors Using the Least-squares Spectral Element Method. Norwegian University of Science and Technology (Ph.D. thesis).

Swamee, P., Jain, A., 1976. Explicit equations for pipe-flow problems. J. Hydraul. Div. 102 (5), 657–664.

Valdes, J.R., Miana, M.J., Nunez, J.L., Putz, T., 2008. Reduced order model for estimation of fluid flow and flow forces in hydraulic proportional valves. Energy Convers. Manag. 49 (6), 1517–1529. http://dx.doi.org/10.1016/j.enconman.2007.12.010. http://www.sciencedirect.com/science/article/pii/S0196890407004153.

Yakhot, V., Orszag, S., 1986. Normalization group analysis of turbulence. I. Basic theory. J. Sci. Comput. 1, 1–51.

Zolotukhin, A.B., Ursin, J.R., 2000. Introduction to Petroleum Reservoir Engineering. Høyskoleforlaget. http://www.hoyskoleforlaget.no.

Sudden expansion and two-phase flow pattern transition in pressure recovery zone

Svein Edvardsen[1], Carlos Dorao, Per Arne Sundsbø

Department of Energy and Process Technology, Norwegian University of Science and Technology, Kolbjrn Hejes vei 2, 7491 Trondheim, Norway

Abstract

In this study, the two-phase flow in a downhole shut-in valve is investigated, with attention to pressure recovery after a section comparable to a sudden expansion. The pressure recovery is investigated theoretically, and a number of known correlations are tested for predicting the downstream pressure buildup. Theoretical pressure recovery values are compared to experimental results obtained with a full scale mock-up, with tube diameter 40mm with expansion to 90mm, and liquid Reynolds numbers between 64000 and 255000. The air/water flow quality was between $1 \times 10^{-3}m$ and $1 \times 10^{-2}m$. Experiments were performed with horizontal and slightly inclined tubes, and some important findings were made. In particular, experimental work has shown that the pressure recovery downstream of a sudden enlargement changes abruptly for some flow conditions. Above a certain gas flow rate, the pressure recovery is reduced. At the same time, the downstream flow pattern changes from bubbly turbulent to inversed annular with a jet-like water stream in the center, surrounded by gas. Experimental values for single phase liquid flow pressure recovery provided very good comparison with theoretical values.

Keywords: Shut-in valve, Two-phase flow, Sudden enlargement,

[1]Corresponding author. Tel.: +47 97566601; E-mail address: svein.edvardsen@ntnu.no (S. Edvardsen)

1. Introduction

When analyzing two-phase flow in a conduit, minor losses have to be taken into consideration together with frictional losses. Two-phase flow minor losses like sudden expansions are far more complex than single phase minor losses. In the last case, the local pressure loss can be calculated from the flow velocity and a loss factor. For two-phase flow in singularities, the flow quality, flow patterns and void fractions upstream and downstream also have to be taken into consideration. Typical singularities are bends, valves, orifices, sudden contractions and sudden enlargements. The number of studies on two-phase minor losses are limited. In this work, the pressure recovery downstream a sudden enlargement in a downhole shut-in valve will be analyzed. Downhole shut-in valves are used in oil wells , and are located close to the oil reservoir. The purpose of the valve is to create a sudden pressure buildup in the well after a period of pressure draw down during well flow. During a test sequence of pressure draw down and shut-in, temperature and pressure are recorded with memory gages hanging below the valve. The logged pressure buildup curves are used for reservoir analysis giving estimates of recoverable amounts of hydrocarbons. When performing such tests, information is needed about the pressure drop across the valve. Detailed knowledge on two-phase pressure drop across the shut-in valve can also be used for calculating real-time downhole flow rates during shut-in tests, and this will enhance the precision of the reservoir analysis. In Fig. 1, a shut-in valve is shown mounted onto a packer and placed in an oil well. A cut-out in the top end shows the internal flow geometry at the outlet. This section can be compared to a two-step sudden expansion.

A cross-section of the sudden expansion in the outlet is given in Fig. 2. The shape of this section is governed by the functional parts of the retrievable packer.

The valve/packer outlet has one sudden expansion step from 40 to 59mm, and one step from 59 to 90mm. Due to the short distance between the steps, the flow will not be fully developed before the last step. The single phase pressure recovery is therefore expected to deviate from a sudden expansion from 40 to 90mm.

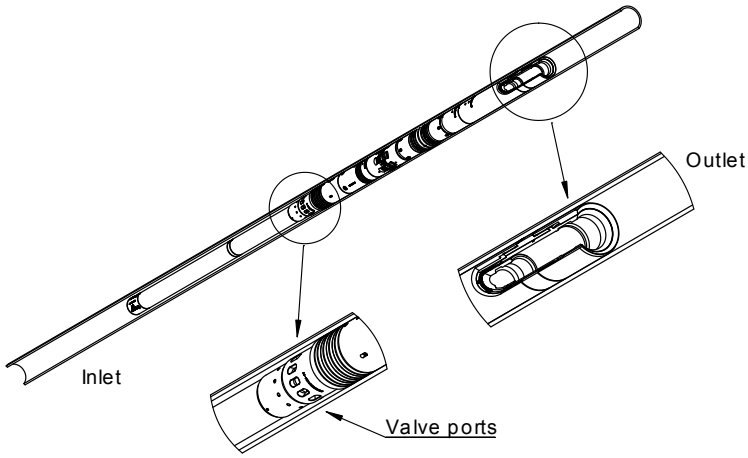

Figure 1: Shut-in valve in oil well.

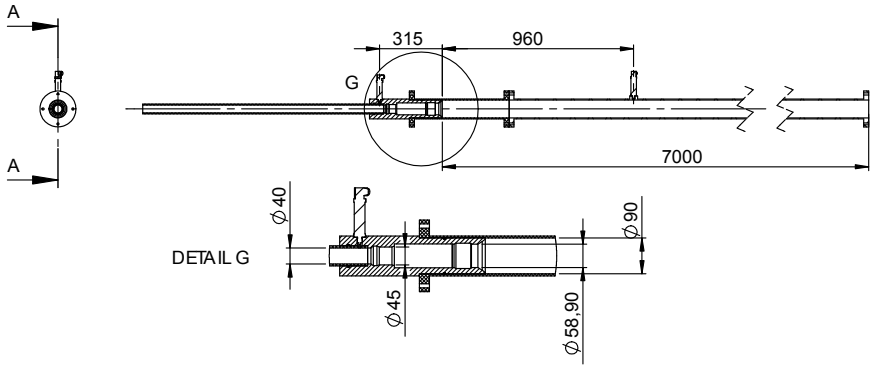

Figure 2: Sudden expansion in shut-in valve outlet.

2. Theoretical background

2.1. Single phase

The flow of incompressible liquid through a sudden expansion can be modeled from two different view points. The first one is assuming that only the momentum is preserved, and that implies a loss of energy. The retardation of the flow at the expansion can in that case be compared to an inelastic collision, where kinetic energy is lost. The second view point is to assume that no energy is lost, so that the reduction in kinetic energy is equal to increased pressure "energy". It is reasonable to assume that some energy will be lost, and the pressure recovery can be deduced by combining the equation for mass conservation:

$$A_1\mathbf{u_1} = \mathbf{A_3}\mathbf{u_3} \tag{1}$$

and the momentum equation:

$$p_1 A_3 - p_3 A_3 = \rho A_3 \mathbf{u_3}(\mathbf{u_3} - \mathbf{u_1}) \tag{2}$$

and the mechanical energy equation with energy loss:

$$p_1 + \rho\frac{\mathbf{u_1^2}}{2} = p_3 + \rho\frac{\mathbf{u_3^2}}{2} + K_L\rho\frac{\mathbf{u_1^2}}{2} \tag{3}$$

Here ρ is density, $\mathbf{u}$ is velocity and p is pressure. By rearranging these equations it can be shown that the loss factor for incompressible liquid flow in a sudden expansion is $K_L = (1-\sigma_A)^2$. This formula is approved by experimental data (Munson et al., 2006). For the pressure drop over the expansion with momentum conservation we also have that:

$$p_3 - p_1 = \frac{\sigma_A\,(1-\sigma_A)\,G^2}{\rho} \tag{4}$$

As a further simplification, the radial pressure profile is assumed to be plane, and the pressure on the axial face at the expansion is taken as p_1.

If we have a kind of expansion without mechanical energy loss, we get from the energy conservation equation that:

$$p_3 - p_1 = \frac{(1-\sigma_A^2)\,G^2}{2\rho} \tag{5}$$

2.2. Nomenclature

p pressure [Pa]

A cross section area [m^2]

u velocity [m/s]

g gravitational acceleration [m/s^2]

x quality [mass flow of gas / total mass flow]

z height

l length [m]

D diameter [m]

R_e Reynolds number

$\dot{m}$ mass flow rate [kg/s]

G mass flux [kg/m^2s]

σ_A area ratio, $\frac{A_1}{A_2}$

2.2.1. Greek symbols

ρ density

ε surface roughness

τ_w wall shear stress

μ_t turbulent viscosity

2.2.2. Subscripts

o oil

w water

a air

2.2.3. Abbreviations

CFD computational fluid dynamics

RNG re-normalization group

2.3. Two phase pressure recovery

The pressure recovery for a two-phase flow can be modeled by calculating an average two-phase density, and in its simplest form it is without slip velocity (Wadle, 1989):

$$p_3 - p_1 = \frac{\sigma_A \left(1 - \sigma_A\right) G^2}{\rho_h} \tag{6}$$

where the homogeneous density is

$$\frac{1}{\rho_h} = \frac{x}{\rho_G} + \frac{1 - x}{\rho_L} \tag{7}$$

A model by Lottes (1961) and attributed to Romie (1958) uses the void fraction for calculating the pressure recovery. In this formulation the void fraction at inlet and outlet is assumed to be equal.

$$p_3 - p_1 = \frac{\sigma_A \left(1 - \sigma_A\right) G^2}{\rho_s} \tag{8}$$

where the slip density is

$$\frac{1}{\rho_s} = \frac{x^2}{\rho_G \alpha} + \frac{\left(1 - x\right)^2}{\rho_L \left(1 - \alpha\right)} \tag{9}$$

Lottes (1961) also proposed a simplified model where loss in dynamic pressure in the gas phase is not included:

$$p_3 - p_1 = \sigma_A \left(1 - \sigma_A\right) G^2 \left[\frac{1}{\rho_L \left(1 - \alpha\right)^2}\right] \tag{10}$$

The model by Attou and Bolle (1997) is based on the momentum balance, where the jet emerging from the sudden expansion is treated as a conical section:

$$p_3 - p_1 = G^2 \sigma_A \left(1 - \sigma_A\right) \left[\Phi \theta^r + \frac{\left(1 - \theta^r\right)}{\rho_L}\right] \tag{11}$$

where

Chisholm and Sutherland (1969) gives a general procedure for calculating pressure drop in pipeline components. The two-phase pressure drop is given as a function of the single phase liquid flow pressure drop:

$$\frac{\Delta p_{TP}}{\Delta p_L} = 1 + \frac{C}{X} + \frac{1}{X^2} \tag{12}$$

where

$$X = \left(\frac{1-x}{x}\right)\sqrt{\frac{\rho_G}{\rho_L}} \tag{13}$$

and

$$C = \left[1 + (C_2 - 1)\left(\frac{\rho_L - \rho_G}{\rho_L}\right)^{0.5}\right]\left(\sqrt{\frac{\rho_L}{\rho_G}} + \sqrt{\frac{\rho_G}{\rho_L}}\right) \tag{14}$$

For a pipe enlargement the factor $C_2 = 0.5$. Starting with the momentum equation we have that

$$p_3 - p_1 = \sigma\left(1-\sigma\right)G^2\left(1-x\right)^2\left[1 + \frac{C}{X} + \frac{1}{X^2}\right]\frac{1}{\rho_L} \tag{15}$$

Wadle (1989) also proposed a model which is not based on the momentum equation. The pressure recovery is here given as a fraction of the reduction in dynamic pressure head:

$$p_3 - p_1 = \left(1-\sigma^2\right)\frac{G^2}{2}K\left[\frac{x^2}{\rho_G} + \frac{\left(1-x\right)^2}{\rho_L}\right] \tag{16}$$

The factor K was experimentally found to be 0.83.

Schmidt and Friedel (1996) presented a model for two-phase flow pressure recovery considering also the liquid entrainment in the gas phase:

$$p_3 - p_1 = \frac{G^2\left[\frac{\sigma_A}{\rho_{eff}} - \frac{\sigma_A^2}{\rho_{eff}} - f_e\rho_{eff}\left(\frac{x}{\rho_G\alpha} - \frac{(1-x)}{\rho_L(1-\alpha)}\right)^2\left(1-\sigma_A^{0.5}\right)^2\right]}{1-\Gamma_e\left(1-\sigma_A\right)} \tag{17}$$

where

$$\frac{1}{\rho_{eff}} = \frac{x^2}{\rho_G\alpha} + \frac{\left(1-x\right)^2}{\rho_L\left(1-\alpha\right)} + \frac{\alpha_E\rho_L\left(1-\alpha\right)}{1-\alpha_E}\left[\frac{x}{\rho_G\alpha} - \frac{1-x}{\rho_L\left(1-\alpha\right)}\right]^2 \tag{18}$$

$$\alpha = 1 - \frac{2\left(1-x\right)^2}{1-2x+\sqrt{1+4x\left(1-x\right)\left(\frac{\rho_L}{\rho_G}-1\right)}} \tag{19}$$

$$\alpha_E = \frac{1}{S}\left[1 - \frac{1-x}{1-x\left(1-0.05We^{0.27}Re^{0.05}\right)}\right] \tag{20}$$

$$S = \frac{x}{1-x}\frac{\left(1-\alpha\right)}{\alpha}\frac{\rho_L}{\rho_G} \tag{21}$$

$$We = G^2x^2\frac{d}{\rho_G\sigma}\frac{\left(\rho_L-\rho_G\right)}{\rho_G} \tag{22}$$

$$Re = \frac{G\left(1-x\right)d}{\mu_L} \tag{23}$$

$$\Gamma_e = 1 - \sigma_A^{0.25} \tag{24}$$

$$f_e = 4.9\times10^{-3}x^2\left(1-x\right)^2\left(\frac{\mu_L}{\mu_G}\right)^{0.7} \tag{25}$$

One of the earliest pressure recovery equations is presented by Richardson (1958). He includes only the liquid phase in his equation, modeling the real liquid velocity:

$$p_3 - p_1 = \frac{\sigma_A\left(1-\sigma_A^2\right)G^2}{2\rho_L}\left[\frac{\left(1-x\right)^2}{\left(1-\alpha\right)}\right] \tag{26}$$

Another equation by Delhaye (1981) is also based on the mechanical energy balance, but here the gas phase is included, with slip velocity:

$$p_3 - p_1 = \frac{G^2\left(1-\sigma_A^2\right)}{2}\left[\frac{\left(1-x\right)^3}{\rho_L^2\left(1-\alpha\right)^2} + \frac{x^3}{\rho_G^2\alpha^2}\right]\left[\frac{\left(1-x\right)}{\rho_L} + \frac{x}{\rho_G}\right]^{-1} \tag{27}$$

In most cases the gas velocity is larger than the liquid velocity, and several models exist for the calculation of the void fraction. The Drift Flux model by Zuber and Findlay (1965) is a well known model for void fraction prediction,

and also Wallis (1969) and Ishii (1977) have taken part in its development. The general drift flux void fraction equation is given by

$$\alpha = \frac{x}{\rho_G}\left[C_\circ\left(\frac{x}{\rho_G}+\frac{1-x}{\rho_L}\right)+\frac{\bar{U}_{GU}}{G}\right]^{-1} \tag{28}$$

where $\bar{U}_{GU}$is the weighed mean drift velocity. For horizontal flow it is given by

$$\bar{U}_{GU} = 1.18\,(1-x)\left[\frac{g\sigma\,(\rho_L-\rho_G)}{\rho_L^2}\right] \tag{29}$$

where $C_\circ = 1 + c_\circ\,(1-x)$ and $c_\circ = 0.12$. This void fraction correlation is recommended by Thome (2014).

A number of void fraction correlations have been evaluated by Dalkilic et al. (2008), and one of the best was that by Thom (1964):

$$\alpha = \frac{\gamma x}{1 + x\,(\gamma - 1)} \tag{30}$$

where

$$\gamma = Z^{1.6}, Z = \left(\frac{\rho_L}{\rho_G}\right)^{0.555}\left(\frac{\mu_G}{\mu_L}\right)^{0.0.111} \tag{31}$$

3. Experimental setup and testing procedure

Two-phase air-water and air-oil experiments were performed with air flow rate from 0-0.020 kg/s, water flow rate 0-9 kg/s and oil flow rate 0-8 kg/s. Air-oil experiments were performed with horizontal tubes, while air-water experiments were performed with horizontal and 2.7 and 5deg. inclined tubes.

The two-phase flow experiments were performed in the Multiphase flow laboratory at NTNU, Trondheim, and this work is a part of the study of two-phase flow in a downhole shut-in valve. The laboratory setup is shown in Fig. 3, and the sudden expansion illustrated in Fig. 2 is located between pressure sensor 5 and 6.

The flow meter specifications are given in Table 1, and the fluids used in the experiments are listed in Table 2 together with their physical properties.

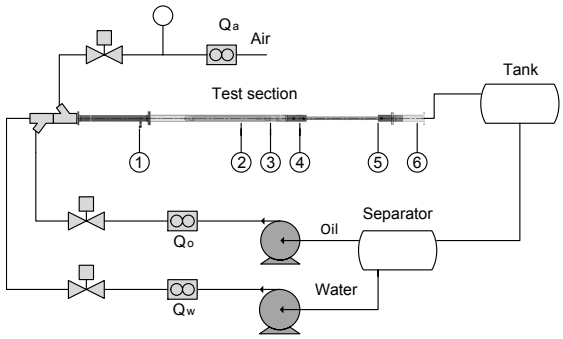

Figure 3: Schematic of the NTNU test rig for single- and multiphase flow

Table 1
Flowmeters

Flowmeter	Type	Range	Uncertainty	Repeatability
Air, small	Coriolis	0-0.022 kg/s	±0.1% of rate combined	
Air, large	Vortex	0.024-0.612 kg/s	±1% of rate	±0.25% of rate
Water	Electromagnetic	10 kg/s	±0.5% of rate	±0.15% of rate
Oil	Coriolis, liquid	10 kg/s	±0.15% of rate combined	

Table 2
Two-phase flow fluids

Fluid	Density, 1 atm, 20°C [kg/m³]	Viscosity at 20°C [Pa-s]	Surface tension in air [N/m]
Air	1.2	1.79E-05	
Water	998	1.00E-03	7.20E-02
Exxsol D80	798	1.80E-03	2.63E-02

4. Validation and results

4.1. Single phase flow

First single phase flow experiments will be examined, and then two phase flow study will be performed with different gas and liquid ratios. Since the outlet section has a design that deviates from a sharp sudden expansion, single phase liquid test results are compared to theoretical values. The outlet is here regarded as a two-step expansion, with the first step from 40 to 59mm diameter, and the last step from 59 to 90mm diameter.

Fig. 4 shows the experimental pressure recovery for water flow, compared to values calculated with the momentum equation, Eq. (4). The experimental pressure recovery is very close to the values calculated with the momentum equation. Similar curves for oil type Exxsol D80 is shown in Fig. 5.

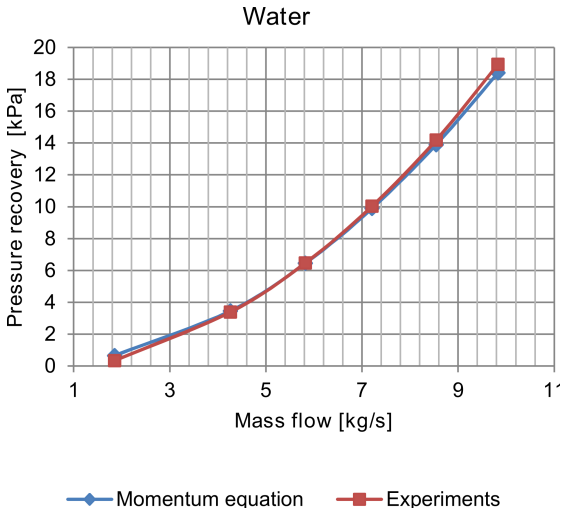

Figure 4: Pressure recovery with water flow

The theoretical pressure recovery is still close to experimental values. It is therefore justified to regard the shut-in valve outlet as a two-step sudden expansion, despite the short distance between the steps.

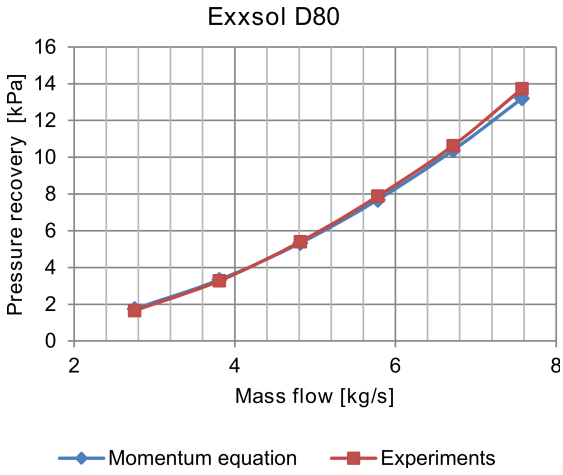

Figure 5: Pressure recovery with oil flow, Exxsol D80

4.2. Two-phase flow

The upstream and downstream flow conditions will now be described before the data analysis. The sudden expansion studied here was a part of a valve section mock-up as shown in Fig. 3. The 40 mm diameter upstream pipe in this study was therefore a mid-section of a large assembly. The two-phase flow was mixed at the inlet to a 5 meter long 85 mm pipe upstream the valve mock-up. Slugs that were formed in this pipe could be tracked through the rest of the test section. The expected flow pattern in the 40mm diameter upstream pipe was predicted by using the Unified Comprehensive Mechanistic (UCM) model for steady-state two-phase flow by Gomez et al. (2000). This is a comprehensive model with both flow pattern prediction and separate flow models for each identified flow pattern. Fig. 6 gives the predicted flow pattern for the upstream pipe together with some observations by high-speed video filming.

Pictures of slug flow at 2 kg/s water flow and 2 g/s air flow are given in Fig. 7, 8 and 9. At higher air flows there is more liquid film on the pipe walls, and flow between slugs reminds of annular flow. Behind the slowly moving liquid film fast moving air drops can be observed. For the downstream pipe only slug flow was observed, as also predicted by the UCM model. The pressure just downstream the sudden expansion was calculated using the

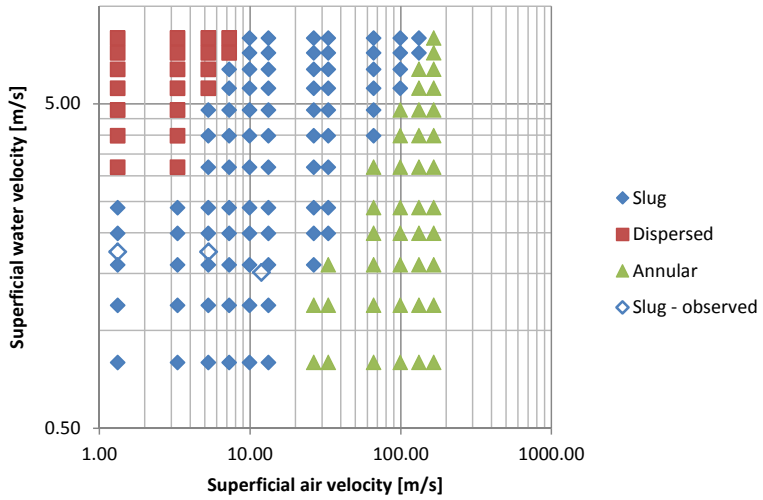

Figure 6: Predicted and observed flow patterns for 40mm upstream pipe

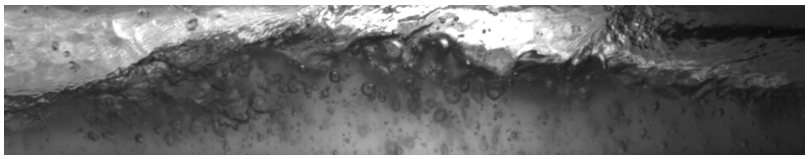

Figure 7: Wavy flow between to slugs, 40mm pipe with 2 kg/s water flow and 2 g/s air flow

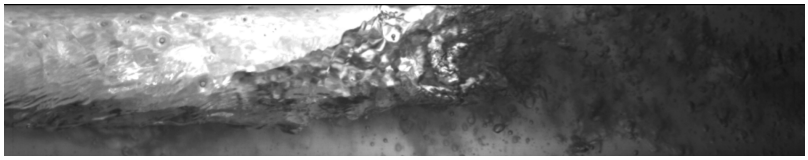

Figure 8: Slug body front, 40mm pipe with 2 kg/s water flow and 2 g/s air flow

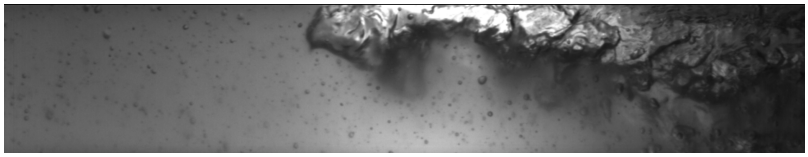

Figure 9: Slug body tail, 40mm pipe with 2 kg/s water flow and 2 g/s air flow

same UCM method.

In Fig. 10 the measured pressure recovery is compared to the above described correlations. The liquid flow rate is here 4 kg/s, and pressure recovery is plotted as function of air flow rate. Similar comparison for water flow rates of 6 and 8 kg/s are given in Fig. 11 and 12.

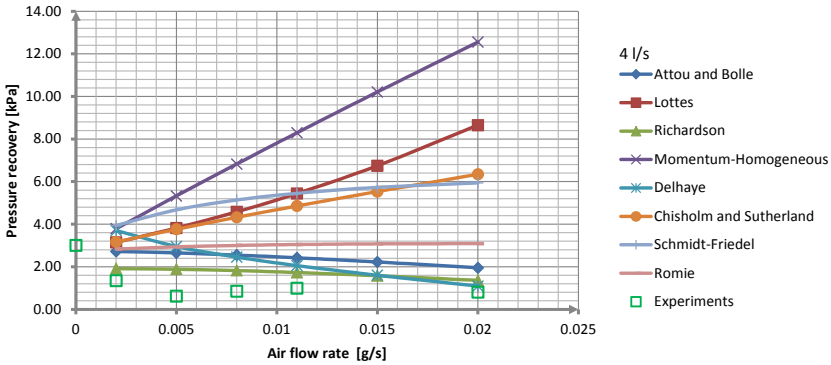

Figure 10: Measured and predicted pressure recovery as function of air flow rate, with constant water flow rate of 4 kg/s

At a water flow rate of 8 kg/s and air flow rate of 2 g/s, corresponding to a flow quality of 2.5×10^{-4}, the measured pressure recovery is approximately 14 kPa, close to the value predicted by the Schmidt and Friedel (1996) correlation. For higher gas flow rates, the pressure recovery drops to 5-6 kPa. The drop in pressure recovery is surprising, and in order to get a better understanding of this phenomenon the measured pressure recovery is given below for the different liquids and different flow rates. For horizontal tubes, the measured pressure recovery for air-water flow is given in Fig. 13, and for air-oil flow in Fig. 14.

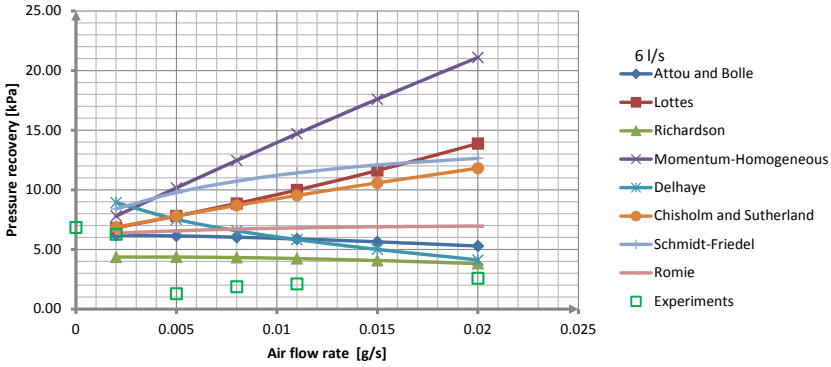

Figure 11: Measured and predicted pressure recovery as function of air flow rate, with constant water flow rate of 6 kg/s

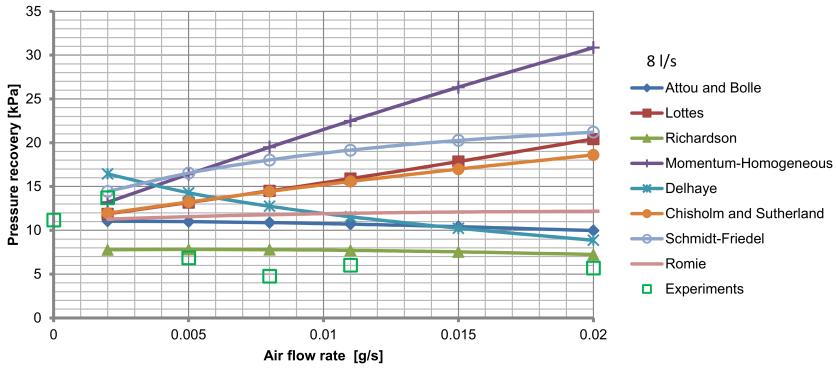

Figure 12: Measured and predicted pressure recovery as function of air flow rate, with constant water flow rate of 8 kg/s

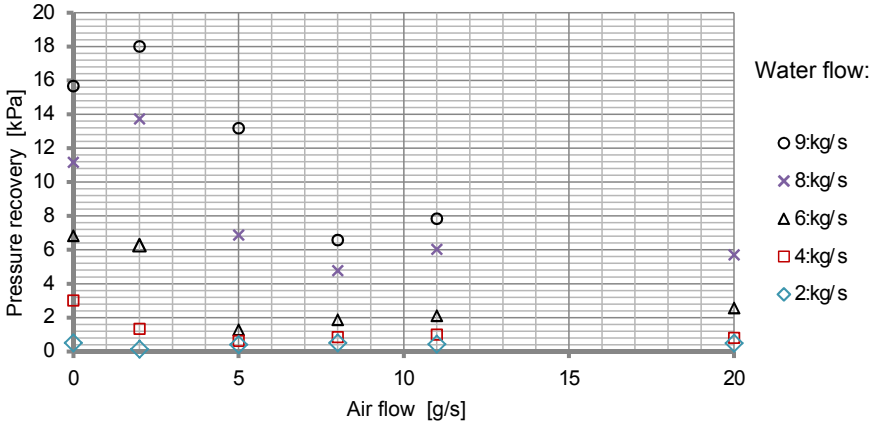

Figure 13: Pressure recovery with air-water two-phase flow, horizontal pipes

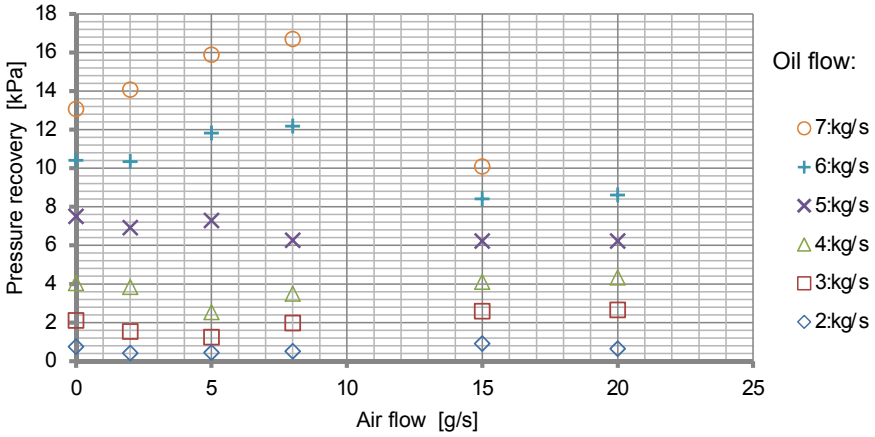

Figure 14: Pressure recovery with air-oil two-phase flow, horizontal pipes

For oil flow of 2-5 kg/s, the pressure recovery is almost independent of air flow rate. For oil flow of 6 and 7 kg/s, there is a local maximum for pressure recovery at 8 g/s air flow rate. For air-water two-phase flow with horizontal tubes, the pressure recovery is reduced to a stable minimum for air flow rates above 8-11 g/s, only dependent on liquid flow rate. The same trend can be observed for oil flow. For oil flow of 2-7 kg/s, the pressure recovery is almost stable above 15 g/s air flow rate.

Pressure recovery was also studied for inclined pipe flow. Curves for pressure recovery vs. flow rates for air-water flow with horizontal pipes are given together with corresponding pressure recovery values at 2.7 deg. and 5 deg. inclination in Fig. 15 and Fig. 16 for 6 and 8 kg/s water flow. The curves shows that the pressure recovery is changing little with these inclination angels.

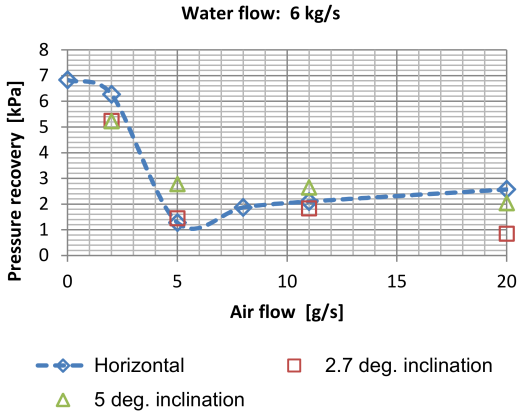

Figure 15: Pressure recovery with air-water two-phase flow at horizontal, 2.7 and 5 deg. inclination with 6 ks/s water flow.

Also, studying curves for 6 and 8 kg/s of water, at 5 g/s of water at 2.7 deg. inclination, we can see that the lowest liquid flow rate gives 1.5 kPa pressure recovery. The highest flow rate gives app. 9.5 kPa pressure recovery. The flow pattern at the expansion for these two flow rates are shown in Fig. 17 and Fig. 18.

For 6 kg/s water flow rate and 5 g/s air flow rate the liquid phase was concentrated in a jet stream in the center, surrounded by air, see Fig. 17.

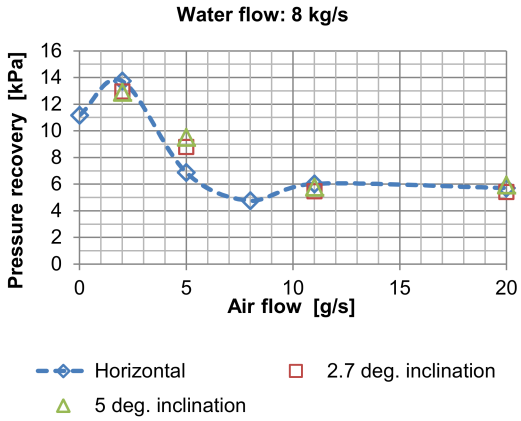

Figure 16: Pressure recovery with air-water two-phase flow at horizontal, 2.7 and 5 deg. inclination with 8 kg/s water flow.

Some 2-3 meter downstream from the expansion the flow pattern changed to slug flow. With that flow pattern, the downstream pressure sensor was not in contact with the liquid, and it therefore measured a pressure equal to or slightly less than the pressure at the upstream sensor. At 8 kg/s water flow rate the whole pipe cross section was filled with turbulent water-air mixture as shown in Fig. 18. The pressure recovery increased to 9 kPa across the sudden expansion.

Figure 17: Flow pattern after expansion. Water flow rate 5.8 kg/s, air flow rate 5 g/s. 2.7 deg. inclination.

Fig. 10, 11 and 12 shows that the Richardson (1958) correlation is closest to the measured values for pressure recovery. In Fig. 19 this correlation is plotted together with the measured values for pressure recovery at different

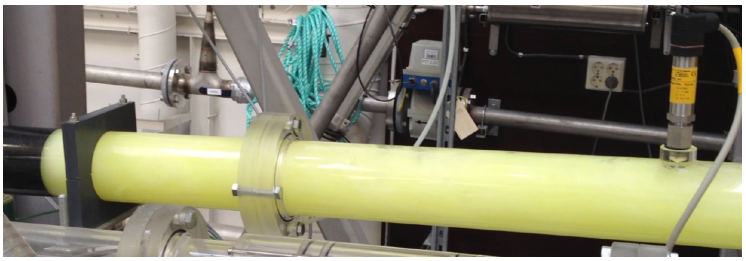

Figure 18: Flow pattern after expansion. Water flow rate 8.5 kg/s, air flow rate 5 g/s. 2.7 deg. inclination.

flow rates.

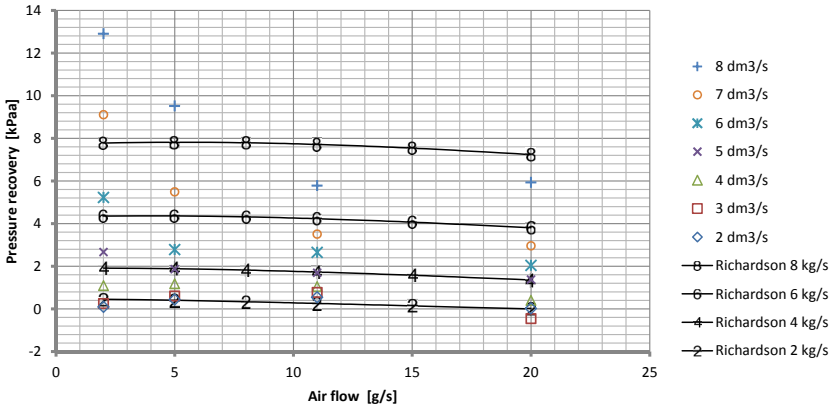

Figure 19: Richardson Richardson (1958) correlation and measured pressure recovery values at different flow rates.

A jet-like flow pattern was also reported by Chen et al. (2010). As in this work, a connection between this flow pattern and reduced pressure recovery was described, limited to a flow quality range of 0.7-1% and a mass flux of 100 $kg \cdot m^{-2} \cdot s^{-1}$. Their experiments were performed with an upstream diameter of 3mm, with expansion to rectangular channels of 3x6 mm or 3x9 mm.

For this work, the experimental results shows a different behavior. The

results of the present work are plotted as function of flow quality and mass flux in Fig. 20. The recovered pressure is dropping for all mass fluxes up to a flow quality if 0.1%, and it increases again a little up to about $x = 0.2\%$. After that it seems to be independent of flow quality. For mass fluxes of 1258 and 1415 $kg \cdot m^{-2} \cdot s^{-1}$ there is a maximum recovered pressure for a flow quality of approximately 0.05%.

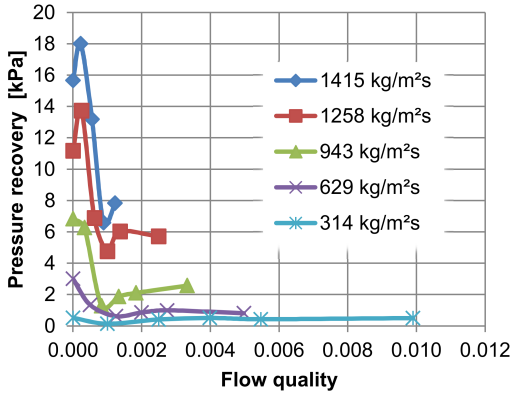

Figure 20: Pressure recovery as function of flow quality and mass flux.

The Richardson pressure recovery simulation was performed using Thom‘s void fraction correlation. The Drift Flux model for void fraction calculation gives a higher void fraction and a much higher predicted pressure recovery.

5. Conclusion

With two-phase flow of air and water, the 40 to 90mm diameter sudden expansion section shows an unexpectedly low rate of pressure recovery. For flow qualities up to only $x = 0.05\%$ there is an increase in recovered pressure. A minimum pressure recovery is gained at a flow quality of $x = 0.1\%$. Above this flow quality there is little change for the flow qualities investigated here. The best of the existing correlations is the Richardson model, provided that the Thom‘s void fraction correlation is used.

Acknowledgment

We thank Manager Stig Karlsen, Plugs and Packers, Qinterra Tecnologies, Narvik, for permission to publish the work. We are also thankful to The Research Council of Norway for financial support.

References

Attou A, Bolle L. A new correlation for the two-phase pressure recovery downstream from a sudden enlargement. Chemical Engineering & Technology 1997;20(6):419–23. URL: http://dx.doi.org/10.1002/ceat.270200610. doi:10.1002/ceat.270200610.

Chen I, Wongwises S, Yang B, Wang C. Two-phase flow across small sudden expansions and contractions. Heat Transfer Engineering 2010;31(4):298–309. URL: http://www.tandfonline.com/doi/abs/10.1080/01457630903312056. doi:10.1080/01457630903312056.

Chisholm D, Sutherland L. Prediction of pressure gradients in pipeline system during two-phase flow. In: Proceedings of the Institution of Mechanical Engineers, Conference Proceedings 184:24. volume 184, Pt. 3C; 1969. p. 24–32.

Dalkilic A, Laohalertdecha S, Wongwises S. Effect of void fraction models on the two-phase friction factor of r134a during condensation in vertical downward flow in a smooth tube. Int Commun Heat Mass Transfer 2008;35:921–7.

Delhaye J. Singular pressure drop, in: Two-Phase and Heat Transfer in the Power and Process Industries. Hemisphere, Washington, DC,, 1981.

Gomez L, Schmidt OSS, Chokshi R, Northug T. Unified mechanistic model for steady-state two-phase flow: Horizontal to vertical upward flow. In: SPE65705. 2000. .

Ishii M. One Dimensional Drift-Flux Model and Constitutive Equations for Relative Motion between Phases in Various Two-Phase Flow Regimes. Technical Report Report ANL-77-47; Argonne National Laboratory; Argonne, IL; 1977.

Lottes P. Expansion losses in two-phase flow. Nucl Sci Engn 1961;9:26–31.

Munson B, Young D, Okiishi T. Fundamentals of Fluid Mechanics. 5th ed. John Wiley & Sons, Inc., 2006.

Richardson B. Some Problems in Horizontal Two-Phase, Two-Component Flow. Ph.D. thesis; University Chicago, Chicago, IL; 1958.

Romie F. (american standard co.). Private communication to Lottes; 1958.

Schmidt J, Friedel L. Two-phase flow pressure change across sudden expansions in duct areas. Chem Eng Comm 1996;141-142:175–90.

Thom J. Prediction of pressure drop during forced circulation boiling of water. Int J Heat Mass Transfer 1964;7:709–24.

Thome JR. Engineering Data Book III. Faculty of Engineering Science and Technology, Swiss Federal Institute of Technology Lausanne (EPFL), CH-1015 Lausanne, Switzerland, 2014. URL: www.wlv.com.

Wadle M. A new formula for the pressure recovery in an abrupt diffusor. International Journal of Multiphase Flow 1989;15(2):241 –56. URL: http://www.sciencedirect.com/science/article/pii/0301932289900736. doi:http://dx.doi.org/10.1016/0301-9322(89)90073-6.

Wallis G. One-dimensional two-phase flow. McGraw-Hill, 1969. URL: http://books.google.no/books?id=xvFQAAAAMAAJ.

Zuber N, Findlay J. Average volumetric concentration in two-phase flow systems. J Heat Transfer 1965;87:453.

Journal of Natural Gas Science and Engineering 23 (2015) 440–449

Contents lists available at ScienceDirect

Journal of Natural Gas Science and Engineering

journal homepage: www.elsevier.com/locate/jngse

Experimental and numerical study of two-phase pressure drop in downhole shut-in valve with Unified Comprehensive Model formulation

Svein Edvardsen*, Carlos Alberto Dorao, Ole Jørgen Nydal

Department of Energy and Process Technology, Norwegian University of Science and Technology, Kolbjørn Hejes vei 2, 7491 Trondheim, Norway

ARTICLE INFO

Article history:
Received 5 December 2014
Received in revised form
19 February 2015
Accepted 19 February 2015
Available online

Keywords:
Shut-in valve
CFD simulation
Two-phase flow
1-dimensional Navier Stokes model
Least squares spectral elements
Unified Comprehensive Model

ABSTRACT

The Unified Comprehensive Model (UCM) formulation for two-phase flow identifies first the flow pattern, and applies subsequently the appropriate pressure drop calculation. In this work the UCM has been extended for dealing with the complex two phase flow in a shut-in valve. In particular, local two phase pressure drops were included where the loss coefficients were obtained from full 3D CFD simulations. The final mathematical model was solved by a least squares spectral element method. Two-phase flow simulations with the extended UCM were validated with experiments performed on a full scale mock-up of the valve. The suggested models provide a good estimation of the pressure drop. The predicted flow patterns from the UCM are also confirmed by the experiments.

1. Introduction

Valves and equipment in wells are exposed to two-phase flow of oil and gas, and it is a challenge to calculate the multiphase pressure drop with high precision. Downhole shut-in valves are used for testing reservoirs, and will during operation be placed close to the casing perforations. This is where the oil and gas flows from the reservoir into the well. Due to flow resistance in the rock formation, the bottom of hole pressure will be lower than the reservoir initial pressure when oil or gas are flowing. If the flow is suddenly stopped, the bottom of hole pressure will build up again with a pace determined by the permeability of the formation. This mechanism is utilized when interpreting shut-in pressure curves. In order to improve the quality of shut-in well tests, the pressure drop over the shut-in valve should be known as precise as possible.

For common singularities like globe valves, gate valves and plug valves some recommendations for two-phase flow calculation exist (Chisholm, 1983). In this work two-phase flow in a downhole shut-in valve was modeled and simulated. The geometry of the flow channel across the shut-in valve is complex, and it has details that cannot by compared to standard pipe components. In order to find the single phase flow loss coefficients in this valve, full 3D CFD simulations were performed by Edvardsen et al. (2015). Experiments with water and oil flow in a shut-in valve mock-up gave total and partial pressure losses close to values from CFD simulations. The Unified Comprehensive Model formulation by Gomez et al. will here be extended with two-phase pressure loss in singularities based on single phase loss coefficients. An example of a well shut-in pressure curve is given in Fig. 1. This pressure curve is recorded by gages hanging below a shut-in valve, and shows the recorded pressure before, during and after the shut-in test.

The detail in the center of the curve shows first a pressure draw-down period, initiated by opening a surface valve to let the well flow. At approximately 74 k sec., the shut-in valve has been closed, causing a pressure build-up below the valve. The shape of this build-up curve is the essential part for the test analysis. However, during the pressure draw-down period, the shut-in valve is open, and a detailed understanding of the pressure drop at two-phase flow can be useful. The measured pressure drop can be used to calculate a corresponding flow rate, and hence the flow through the shut-in valve can be recorded real-time and close to the bottom of the well. This will improve the quality of the test interpretation.

Abbreviations: CFD, computational fluid dynamics.

* Corresponding author.
E-mail address: svein.edvardsen@ntnu.no (S. Edvardsen).

http://dx.doi.org/10.1016/j.jngse.2015.02.024
1875-5100/

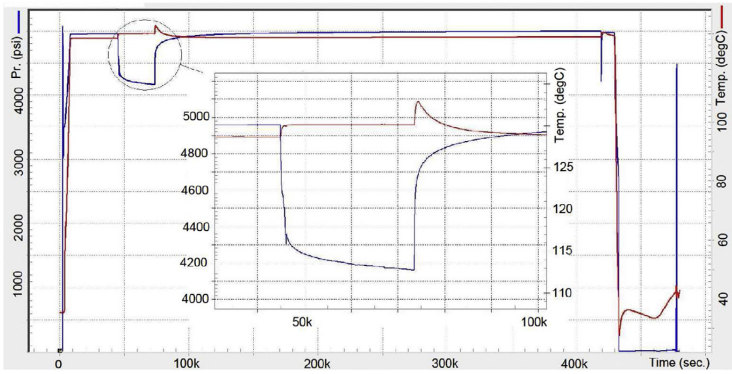

Fig. 1. Pressure and temperature curves from downhole shut-in operation.

The shut-in valve in question has been investigated experimentally and numerically for single phase flow by Edvardsen et al. (2015), and a 1-dimensional simulation model was developed. In Fig. 2, the valve is shown together with a packer.

This model is based on the Navier-Stokes equation for steady state flow, using the least squares method with spectral elements. The minor (or singular) losses for this model were calculated from 3-dimensional CFD simulations. This 1D simulation model provided good comparison with experimental data for both incompressible and compressible flow. Two-phase flow in this shut-in valve has also been simulated by Edvardsen et al. (2014a), using various two-phase correlations by Chisholm (1983), Mller-Steinhagen and Heck (1986) and Friedel (1979). The deviations in pressure drop prediction for these simulations were about 12%.

In this work, the Unified Mechanistic Model for steady-state two-phase flow by Gomez et al. (2000) will be implemented in an attempt to improve the precision at two-phase pressure drop calculations. In mechanistic modeling, flow patterns as stratified, slug or annular are predicted from analysis of two-phase physical phenomena. Individual models are then applied for the identified flow pattern for prediction of the liquid holdup and the pressure gradient. Models for two-phase flow pattern prediction have been developed by Taitel and Dukler (1976) and Barnea et al. (1985) amongst others, and separate models have been proposed for horizontal and vertical flow. There are also a number of studies on specific flow pattern transitions like Shoham and Taitel (1984), Cheremisinoff and Davis (1979) and Issa (1988). In this context, a comprehensive model contains both a flow pattern prediction part and a flow model part for liquid holdup and pressure gradient calculation. Unified models are models that can be applied to horizontal, inclined and vertical flow. A comprehensive mechanistic model for horizontal flow was proposed by Xiao et al. (1990), and similar comprehensive models for vertical flow was proposed by Ozen et al. (1987), Hasan and Kabir (1988) and Ansari et al. (1994). The unified, comprehensive model formulation by Gomez et al. (2000) is therefor an attractive model, capable of flow pattern prediction at all inclination angels. With flow models provided for all flow patterns, it is well suited for combination with the 1D Least Squares Spectral Element model.

The goal of the work presented was to develop a versatile tool for the prediction of the flow behavior in complex geometries, like a downhole shut-in valve. First the experimental setup will be presented. The theoretical part then presents the 1-D model, together with an explanation of the Least Squares Spectral Element method. The Unified Comprehensive Model formulation by Gomez et al. is presented in detail, and details from implementation in the 1-D model are given. The numerical solution is also described together with the solution algorithm. Finally the results from two-phase flow experiments and simulations are presented and discussed.

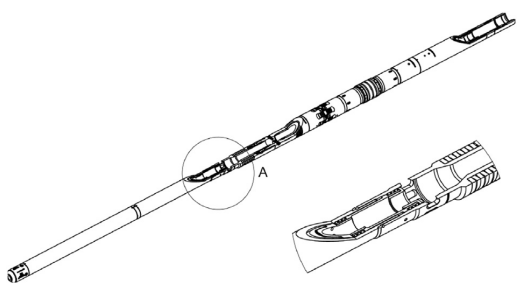

Fig. 2. Qinterra Technologies shut-in valve type STC on an RPD type retrievable packer.

2. Experimental setup and testing procedure

The experimental tests were performed in the Multiphase Flow Laboratory at the Dept. of Energy and Process Engineering, NTNU. The flow loop consists of a supply system for oil, water and air, and has a separator for continuous recirculation of oil and water. Flow control valves and pumps with speed adjustment ensure that the flow rate can be set as wanted. A logging system records all flow rates and pressures continuously. Water and oil are circulated by centrifugal pumps, and air is supplied by a compressor. Flow rate of water was measured with an electromagnetic flowmeter with a range of 0–10 kg/s, and flow rate of oil (Exxsol D80) was measured with a Coriolis flowmeter with a range of 0–10 kg/s. Air flow was set by control valves and measured with a Coriolis flowmeter with range of 0–0.022 kg/s for small airflows. For large airflows, a vortex flowmeter with range 0.004–0.11 m^3/s at system pressure of 400 kPa was used, corresponding to a mass flow of 0.024–0.612 kg/s. The flowmeter specifications are given in Table 1.

The coriolis type oil flowmeter can also detect liquid density.

The test section consists of a full-scale mock-up of a shut-in valve, made in POM (polyoxymethylene, or acetal) and polycarbonate tubes. Roughness for the plastic tubes in the laboratory

Table 1
Flowmeters.

Flowmeter	Type	Range	Uncertainty	Repeatability
Air, small	Coriolis	0–0.022 kg/s	±0.1% of rate combined	
Air, large	Vortex	0.024–0.612 kg/s	±1% of rate	±0.25% of rate
Water	Electromagnetic	10 kg/s	±0.5% of rate	±0.15% of rate
Oil	Coriolis, liquid	10 kg/s	±0.15% of rate combined	

model is about $5 \times 10\ m^6$. The main parts of the valve are the inlet section with circular flow, a section with annular flow, a section with radial inward flow through valve ports to a central chamber, a narrow circular channel through the upper part and an outlet part with expansion. Pressure was measured at six different points with pressure sensors to get total pressure loss as well as partial losses across the different parts.

A sketch of the Multiphase Flow Loop is shown in Fig. 3.

In addition to water, two oil types were used in the test: Exxsol D80 with a density of 798 kg/m^3 and a viscosity of 0.0018 Ns/m^2 at 20° C, and NEXBASE 3080 with a density of 845 kg/m^3 and a viscosity of 0.065 Ns/m^2. The pressure drop across the valve model was measured at six different locations, in order to find the individual pressure drops for the different sections inside the valve. The locations of the piezoresistant pressure transmitters are shown in Figs. 3 and 5. Note that sensor number 1 is also called PT-2.

The range of the pressure sensors PT1, PT2 and PT3 is 0–6 bar, and range of sensors PT4, PT5 and PT6 is −1 to 1 bar. The accuracy for pressure transmitters are 0.2% of full scale, and the resulting measurement uncertainties are given in Table 2.

The values for flow and pressure were sampled with a frequency of 5 kHz, and average values logged to a data file 5 times per. sec.

For uncorrelated input quantities the combined uncertainty is. $u_c^2(y) = \sum_{i=1}^{N} \left(\frac{\partial f}{\partial x_i}\right)^2 u^2(x_i)$,or $\left[\frac{u_c(y)}{y}\right]^2 = \sum_{i=1}^{N} [p_i u(x_i)/x_i]^2$, where $y = cX_1^{p1}X_2^{p2}\ldots X_N^{pN}$ (JGCM/WG1, 1995) For a total pressure difference from PT2 to PT6 we have that $u_c^2(y) = 1.2^2 + 0.4^2$ and then the uncertainty is $u_c(y) = \pm 1.3\ kPa$.

Fig. 4 shows the laboratory mock-up of the shut-in valve, with details causing minor losses that have to be modeled.

3. Mathematical modeling

The original UCM is intended for steady state two-phase flow in horizontal, inclined or vertical pipes. The 3.24 m long flow path across the shut-in valve can be divided into four different parts, see Fig. 5: A: Annular flow around the lower part. B: Flow through valve ports, internal chamber, contraction and flow obstacle. C: Internal narrow channel. D: Sudden expansion with downstream pressure recovery. Except from part C, these flow parts are not covered by the UCM, and had to be modeled.

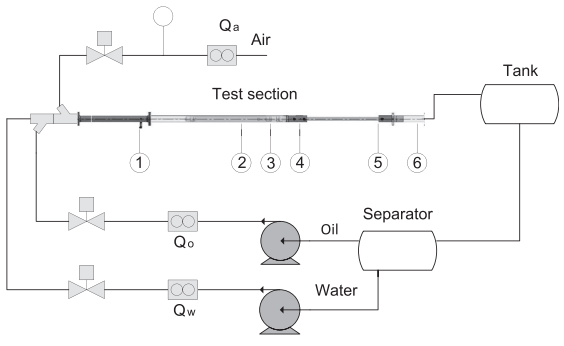

Fig. 3. Schematic of the NTNU test rig for single- and multiphase flow.

3.1. 1D model

The 1-D model developed by Edvardsen et al. (2015) is based on the Navier-Stokes Equation. If the flow is a 1-dimensional, steady state horizontal flow we get for a slab Δz of the flow that

$$\rho v \frac{\partial v}{\partial z}\Delta z = -\frac{\partial P}{\partial z}\Delta z - \frac{4}{D_i}\tau_w \Delta z \tag{1}$$

where ρ [kg/m^3] is density, v [m/s] is velocity, z [m] is distance along the pipe, P [Pa] is static pressure and D_i [m] is pipe internal diameter. The left hand side here is momentum change caused by convective acceleration. The first term on the right hand side is the derivative of the static pressure along the pipe, and the last term is the pressure loss caused by the shear stress τ_w [N/m^2] along the pipe wall. The convective acceleration will here be calculated from homogeneous properties based on equal phase velocities. The minor and frictional losses for the valve model were determined by use of CFD simulations, and the 1D model elements are given in Table 3. By rearranging Equation (1) we get that

$$\frac{\partial P}{\partial z} = -\rho_H v_H \frac{\partial v_H}{\partial z} - \frac{dP_{TF}}{dz} \tag{2}$$

For two-phase flow the frictional term $-\frac{4}{D_i}\tau_w \Delta z$ will be replaced by the two-phase pressure gradient dP_{TF} calculated by the UCM formulation. For the 1D model elements from Table 3 with a minor loss coefficient caused by a singularity, the equation to be solved is

$$\frac{\partial P}{\partial z} = -\rho_H v_H \frac{\partial v_H}{\partial z} - K_L \rho_H \frac{v_H^2}{2} \tag{3}$$

where K_L is the minor loss factor from the table. The homogeneous density ρ_H and velocity v_H are also used for calculating minor losses, and they are given by

$$\rho_H = \rho_L(1-\alpha) + \rho_G \alpha \tag{4}$$

$$v_H = \frac{\dot{m}_L + \dot{m}_G}{A\rho_H} \tag{5}$$

where α is void fraction and A is flow cross-section. The homogeneous void fraction is given by the superficial velocities of gas and liquid as

$$\alpha = \frac{v_{SG}}{v_{SG} + v_{SL}} \tag{6}$$

and

$$v_{SG} = \frac{\dot{m}_G}{A\rho_G} \tag{7}$$

$$v_{SL} = \frac{\dot{m}_L}{A\rho_L} \tag{8}$$

There are several changes in cross section along the flow path in the STC shut-in valve, and area changes are approximated as conical sections. The derivative of velocity with respect to distance is therefore

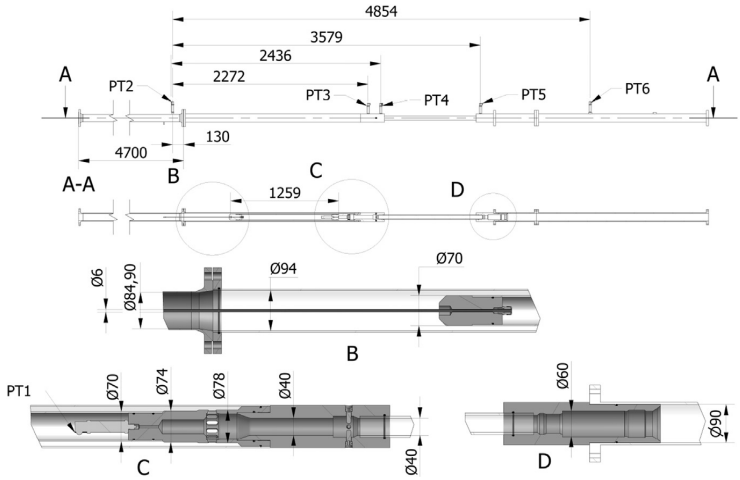

Fig. 4. Laboratory mock-up of STC shut-in valve. Dimensions in millimeter [mm].

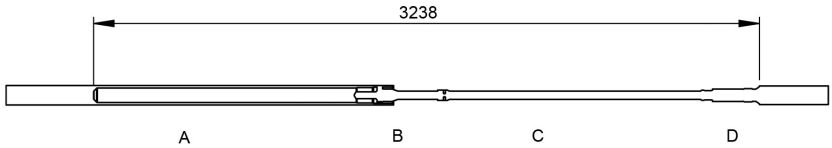

Fig. 5. Flow path across shut-in valve. Dimensions in millimeter [mm].

Table 2
Measurement uncertainty.

No.	Range	Uncertainty
PT1	0–6 bar	±1.2 kPa
PT2	0–6 bar	±1.2 kPa
PT3	0–6 bar	±1.2 kPa
PT4	−1/+1 bar	±0.4 kPa
PT5	−1/+1 bar	±0.4 kPa
PT6	−1/+1 bar	±0.4 kPa

$$\frac{\partial v}{\partial z} = \frac{\partial v}{\partial A}\frac{\partial A}{\partial z} = \frac{\partial}{\partial A}\left(\frac{\dot{m}}{A\rho}\right)\frac{\partial A}{\partial z} \tag{9}$$

$$\frac{\partial v}{\partial z} = -\frac{\dot{m}}{A^2\rho}\frac{\partial A}{\partial z} \tag{10}$$

For simulation of compressible flow, the flow is regarded as isotherm.

The pressure recovery at the valve outlet was investigated by Edvardsen et al. (2014b), and it was found that the correlation by Richardson (1958) gave the best approximation for the pressure

Table 3
Frictional and singular losses in the downhole shut-in valve.

No.	Description	Length S [m]	Minor loss coeff.	Hydraulic diameter 1 [m]	Hydraulic diameter 2 [m]	Flow cross section in [m^2]	Flow cross section out [m^2]
1	Friction	0.1		0.085	0.085	5.675E-03	5.675E-03
2	Diffuser, 16°	0.03	0.067	0.085	0.094	5.675E-03	6.940E-03
3	Friction	0.525		0.094	0.094	6.940E-03	6.940E-03
4	Annular contraction, 90°	0.015	0.28	0.094	0.024	6.940E-03	3.091E-03
5	Friction	1.261		0.024	0.024	3.091E-03	3.091E-03
6	Annular contraction, 90°	0.079	0.037	0.024	0.02	3.091E-03	2.639E-03
7	Annular contraction, 90°	0.02	0.044	0.02	0.016	2.639E-03	2.161E-03
8	Valve inlet	0.075	1.74	0.016	0.06	2.161E-03	2.827E-03
9	Contraction, 40°	0.03	0	0.06	0.04	2.827E-03	1.257E-03
10	Friction	0.192		0.04	0.04	1.257E-03	1.257E-03
11	Equalizing central	0.058	0.15	0.04	0.04	1.257E-03	1.257E-03
12	Friction	1.22		0.04	0.04	1.257E-03	1.257E-03
13	Expansion	0.288	0.255	0.04	0.09	1.257E-03	6.362E-03
14	Friction	0.958		0.09	0.09	6.362E-03	6.362E-03
	Total length	4.851					

recovery. This correlation is given by

$$p_3 - p_1 = \frac{\sigma_A(1-\sigma_A^2)G^2}{2\rho_L}\left[\frac{(1-x)^2}{(1-\alpha)}\right] \tag{11}$$

where the area ratio is $\sigma_A = \frac{A_1}{A_2}$ and x is flow quality defined as mass flow of gas over total mass flow: $x = \dot{m}_G/(\dot{m}_G + \dot{m}_L)$. This pressure recovery correlation is used together with the Thom void fraction correlation (Thom, 1964).

3.2. Least squares method

The dynamic equations for two-phase flow are solved using the least-squares method with spectral element approximation (Proot and Gerritsma, 2002). This method has also been used successfully by Chiapero (2013) for simulation of two-phase flow instabilities, and by Sporleder (2011) for simulation of chemical reactors.

The advantages of the least-squares method are low numerical diffusion and generic implementation amongst others, and it involves the minimization of a norm-equivalent functional. Generally we have that

$$L\boldsymbol{u} = \boldsymbol{g} \quad in\ \Omega \tag{12}$$

$$B\boldsymbol{u} = \boldsymbol{h} \quad on\ \partial\Omega \tag{13}$$

where Ω and $\partial\Omega$ are the domain and the boundary of the domain respectively. With the requirement that the system is well-posed and that the operators L and B being continuous mappings between the function space $X(\Omega)$ onto the solution space $Y(\Omega) \times Y(\partial\Omega)$, the norm equivalent functional becomes

$$I(u) = \frac{1}{2}||L\mathbf{u} - \mathbf{g}||^2_{Y(\Omega)} + \frac{1}{2}||B\mathbf{u} - \mathbf{h}||^2_{Y(\partial\Omega)} \tag{14}$$

Variational analysis gives that

$$\lim_{\varepsilon\to 0}\frac{d}{d\varepsilon}I(\mathbf{u} + \varepsilon\mathbf{v}) = 0\ \forall\ \mathbf{u}\in\mathbf{X}(\boldsymbol{\Omega}) \tag{15}$$

I can now be minimized with the following necessary condition: Find $\mathbf{u}\in\mathbf{X}(\boldsymbol{\Omega})$ such that

$$A(\mathbf{u},\mathbf{v}) = \mathbf{F}(\mathbf{v})\ \forall\ \mathbf{v}\in\mathbf{X}(\boldsymbol{\Omega}) \tag{16}$$

and

$$A(\mathbf{u},\mathbf{v}) = \langle L\mathbf{u}, \mathbf{L}\mathbf{v}\rangle_{Y(\Omega)} + \langle B\mathbf{u}, \mathbf{B}\mathbf{v}\rangle_{Y(\partial\Omega)} \tag{17}$$

$$F(\mathbf{v}) = \langle \mathrm{g}, \mathbf{L}\mathbf{v}\rangle_{Y(\Omega)} + \langle \mathbf{h}, \mathbf{B}\mathbf{v}\rangle_{Y(\partial\Omega)} \tag{18}$$

$A : X \times X \to \mathbb{R}$ is a symmetric, continuous bilinear form. $F : X \to \mathbb{R}$ is a continuous linear form.

3.3. Spectral element formulation

As for finite element formulations, the computational domain Ω is divided into N_e non-overlapping sub-domains Ω_e such that

$$\Omega = \cup_{e=1}^{N_e}\Omega_e \ with\ \Omega_e \cap \Omega_k = \varnothing,\ e \neq k \tag{19}$$

The unknown function u_h^e is approximated in each element Ω_e by the set of all polynomials P_Q of degree $\leq Q$. The global approximation u_h in Ω is

$$u_h = \cup_{e=1}^{N_e} u_h^e \tag{20}$$

Within each element, the solution is expanded in Φ_i basis functions

$$u_h^e(x) = \sum_{n=0}^{i} u_n^e \Phi_i(\xi) \tag{21}$$

with $(\xi) = X_e^{-1}(x)$ th local coordinate of (x) in the parent element, with $-1 \leq \xi \leq 1$, and u_h^e the coefficients in the expansion.

4. Simulations

4.1. Unified Comprehensive Model formulation

The Unified Comprehensive Model (UCM) formulation used in this work is taken from Gomez et al. (2000) and Shoham (2006). This formulation unifies flow pattern prediction models for horizontal, inclined and vertical flow. It is called comprehensive as it has both flow pattern prediction models and also flow models for each identified flow pattern. The flow models have formulas for liquid holdup and pressure gradient.

4.2. Numerical solution of 1D model with two-phase flow

Frictional and minor losses for the 1D Least Squares Spectral Element model is given by Table 3. The set of equations given above can be formulated as $L\mathbf{u} = \mathbf{g}$ in Ω. The linear partial differential operator is

$$L = \left\{\frac{\partial}{\partial z}\right\} \tag{22}$$

and

$$L\mathbf{u} = u_k\frac{\partial u_{k+1}}{\partial z} + u_{k+1}\frac{\partial u_k}{\partial z} + \frac{\partial P}{\partial x} \tag{23}$$

$$\mathbf{g} = -\frac{dP}{dL} + u_k\frac{\partial u_k}{\partial z} \tag{24}$$

The first term on the right hand side is output from the two-phase flow model. For minor pressure losses we get that

$$\mathbf{g} = -K_L\rho\frac{v^2}{2} + u_k\frac{\partial u_k}{\partial z} \tag{25}$$

The last term in the expression for g comes from the linearization of $v\frac{\partial v}{\partial z}$, and as given above we have that $\frac{\partial v}{\partial z} = -\frac{\dot{m}}{A^2\rho}\frac{\partial A}{\partial z}$.

The boundary term will be omitted here, and the boundary condition will be enforced strongly. The simulations will be compared to laboratory experimental results, where the valve outlet is at atmospheric pressure. Consequently, the outlet pressure will be specified and the element pressures will be calculated counter current from outlet to inlet. A solution algorithm is given in Fig. 6.

The total test section length of 4.85 m is divided into 1D elements with lengths between 0.014 and 0.061 m, in total 109 5th order elements. A model refinement was achieved by simply increasing the element order, splitting each element into more sub-elements. A higher number of total elements did not enhance the accuracy.

In the annulus section of the valve, the equilibrium liquid level is calculated in the same manner as for circular sections, but equations for cross section and interfacial areas take account for the

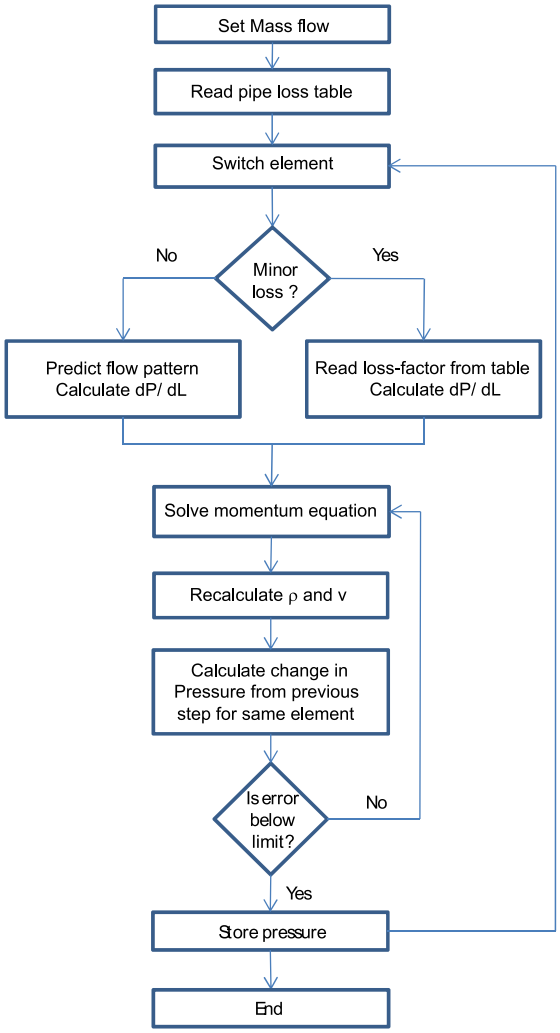

Fig. 6. Solution algorithm for two-phase flow.

inner diameter.

In these simulations, the liquid and gas velocities for the momentum equation are based on the predicted liquid holdup from the actual flow pattern.

5. Results and discussion

Flow patterns generated with the Unified Comprehensive Model formulation will now be presented and validated. Simulated pressure drop for a range of fluids and flow conditions will be compared to experimental data.

5.1. Flow patterns

At the inlet section of the shut-in valve there is a transparent pipe, where the flow pattern can be inspected, see detail B in Fig. 4. The upstream pipe is made of stainless steel, with inner diameter 0.0849 m and length 4.8 m. At the connection with the transparent LEXAN tube, there is a conical section from 0.084 to 0.094 m, with an angle of 16deg. The flow pattern seen in the tube in front of the valve is therefore calculated from a diameter of 0.0849 m. In Fig. 7, the inlet flow pattern as given by the UCM formulation is shown with filled symbols.

Observed flow patterns are shown with open symbols, and they are mainly as predicted. However, stratified flow was observed with 0.001 kg/s of water and 0.046–0.114 kg/s of air, or a superficial air velocity of 5.3–7.9 m/s, and here annular flow was expected. Annular flow pattern was observed with 15 m/s superficial air velocity. These velocities were calculated from the prevailing pressures, and that is why the diagram is twisted to the left in the top. Higher mass flow rates caused higher back pressures due to pressure drop across the valve. A similar diagram for Exxsol D80 and air is shown in Fig. 8.

The maximum air mass flow rate was reduced to 0.020 kg/s, and only slug flow was observed, in accordance with the pattern predicted by the UCM formulation. A similar map for the high viscosity NEXBASE 3080 is shown in Fig. 9.

Both slug flow and stratified flow was observed according to the flow map.

For the lower part of the valve, there is an annular section up to the valve ports, see detail C in Fig. 4. For all three liquid-air two-phase flows, the flow pattern breaks up and transforms into a homogeneous mixture in this zone. As the cross sectional are is reduced compared to the downstream pipe, the flow accelerates. The gas bubble breaks up and is gradually distributed as smaller bubbles all around the circumference. At stratified flow, the nose of the valve body generates waves that reaches the top of the pipe. The flow is therefore regarded as homogeneous here, with no slip velocity.

The valve ports and the valve chamber generate high turbulence intensity, and the flow is regarded as homogeneous. The singular losses are therefore calculated from the coefficients given in Table 3, and the velocities used are calculated using the void fraction at homogeneous flow.

For the central tube with inner diameter 0.04 m, the flow can easily be taken as homogeneous, or dispersed bubble flow, due to

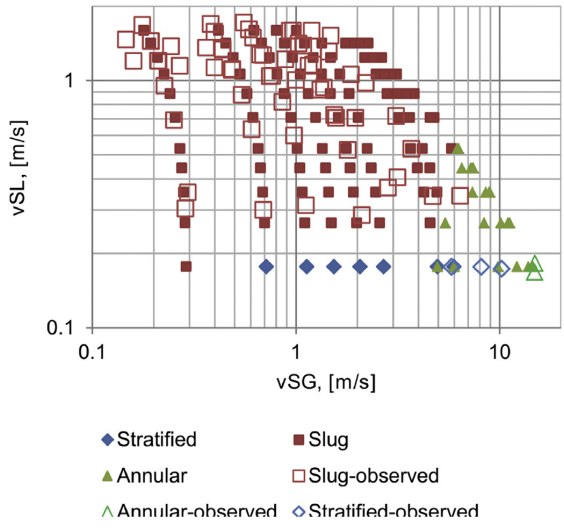

Fig. 7. Flow pattern at inlet with water–air two-phase flow.

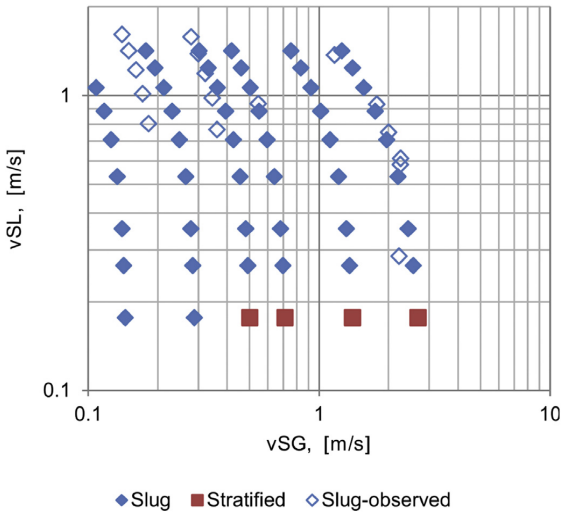

Fig. 8. Flow pattern at inlet with Exxsol D80-air two-phase flow.

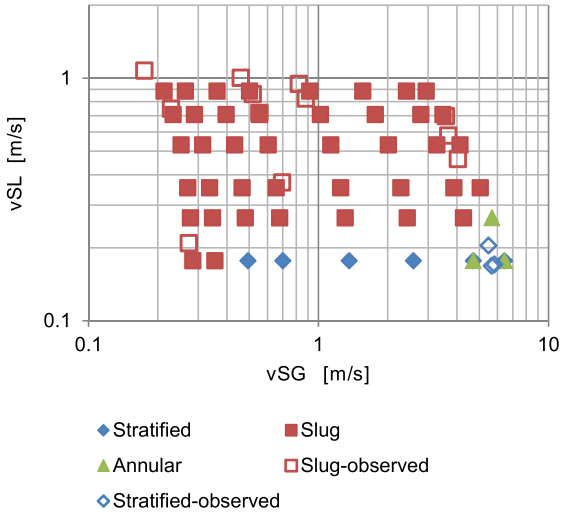

Fig. 9. Flow pattern at inlet with NEXBASE 3080-air two-phase flow.

the high mixing upstream in the valve ports. Inspection of the flow through the transparent pipe also strengthens this impression. However, the UCM flow pattern map and high speed filming reveals that annular flow can exist, even with the high-viscosity NEXBASE 3080, see Fig. 10.

At high gas rate and low liquid rate, the video shows a slow moving liquid film on the pipe wall, with fast-moving droplets behind. The flow pattern map is thereby confirmed for annular flow.

At the outlet section, an inverse annular flow can be observed at high combined flow rates. The two-phase mixture leaves the upper valve section as a jet stream in the center of the pipe. After some distance a normal flow pattern is developed. The test section was not long enough to capture these characteristics in full.

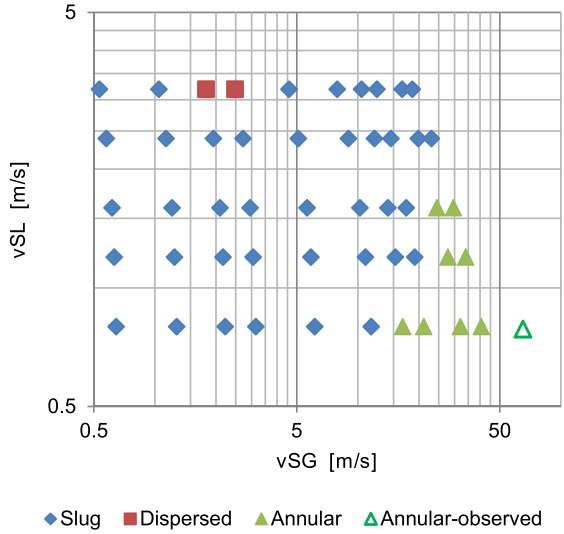

Fig. 10. Flow pattern at 0.04 m central section with NEXBASE 3080-air two-phase flow.

5.2. Pressure drop calculation

Two-phase flow simulations were performed using the 1D Least Squares Spectral Element model, with two-phase flow modeled with the Unified Comprehensive Model formulation. For minor losses, the phase velocities used in the momentum equation are based on void fraction at no-slip condition. Fig. 11 shows a comparison of experimental and simulated results for air–water flow.

The average deviation is 1.8%, and the average absolute deviation is 17.6%. A similar comparison for two-phase flow of Exxsol D80 and air is shown in Fig. 12.

The average deviation is −9.3%, and the average absolute deviation is 16.8%. Simulation of NEXBASE 3080 and air is given in

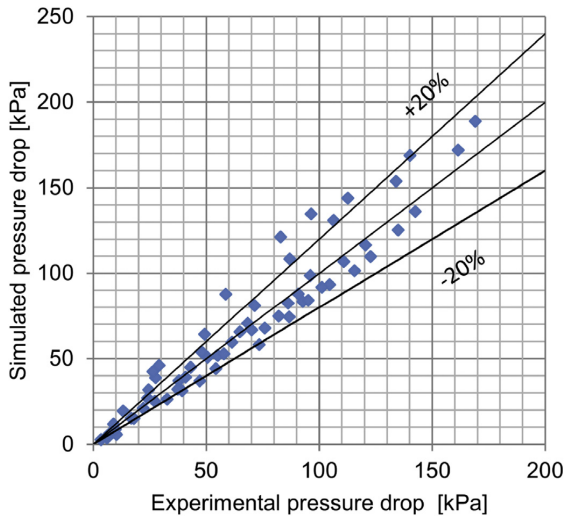

Fig. 11. Simulated vs. experimental pressure drop for air and water.

Fig. 13.

The average deviation is only 0.5%, but the average absolute deviation is 26.5%. Inspection of the individual data points reveals that the deviation is high at the lowest liquid flow rates, and also at high air flow rates.

The pressure profile along the valve for a water flow of 8.7 kg/s and an air-flow of 0.02 kg/s is indicated in 14. This curve is precise only at the markers for each pressure sensor. The curve shows that both frictional losses and minor losses are predicted with good precision at this flow rate.

A similar curve for a water flow of 4.4 kg/s and an air-flow of 0.049 kg/s is given in Fig. 15. At this higher flow quality there is a clear deviation for several sections. First, we can see that the pressure recovery at the outlet at sensor 6 is under-predicted. It is also clear that the frictional pressure loss in the narrow internal 40 mm pipe is over-predicted. The flow pattern is here in a transition zone between slug flow and dispersed bubble flow.

The dispersed bubble flow model is modified here by introducing the Thom correlation for void fraction (Thom, 1964). A slip velocity between gas and liquid is therefore allowed. The motivation is that dispersed bubble flow is predicted by the UCM formulation even at liquid holdup below 52%, when the gas phase is believed to be the continuous phase. At relatively low flow qualities this modification seems to be justified, as indicated in Fig. 14. At higher flow qualities the frictional pressure drop is over-predicted.

It can also be concluded from Figs. 14 and 15 that the minor losses are predicted with good precision. This can be seen from the pressure drop between sensor 1 and 2 across the valve ports. Between sensor 2 and 3 there is a conical contraction from 60 to 40 mm diameter, and this causes a pressure reduction that is well predicted at both flow conditions. Between sensor 3 and 4 there is an obstacle in the flow channel, and the two-phase pressure loss is well predicted.

The total pressure drop across the shut-in valve for water–air two-phase flow is shown in Fig. 16. The maximum water flow rate is 10 kg/s, and experimental and simulated pressure drop is given for 2, 8, 20 and 50 g/s of air flow. Similar curves for two-phase flow of Exxsol D80 and air is given in Fig. 17, and for Nexbase 3080 and air in Fig. 18.

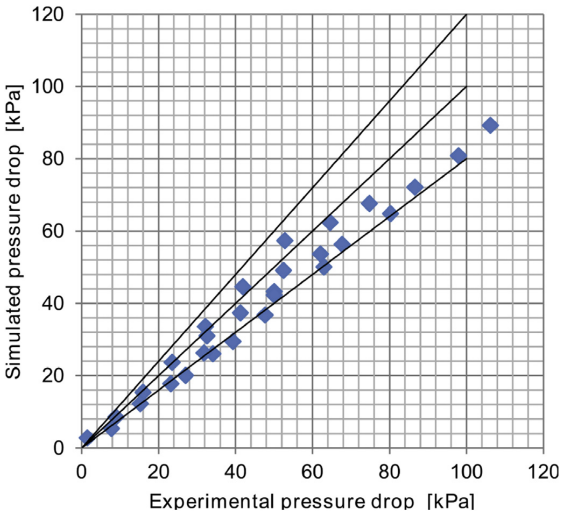

Fig. 12. Simulated vs. experimental pressure drop for air and Exxsol D80.

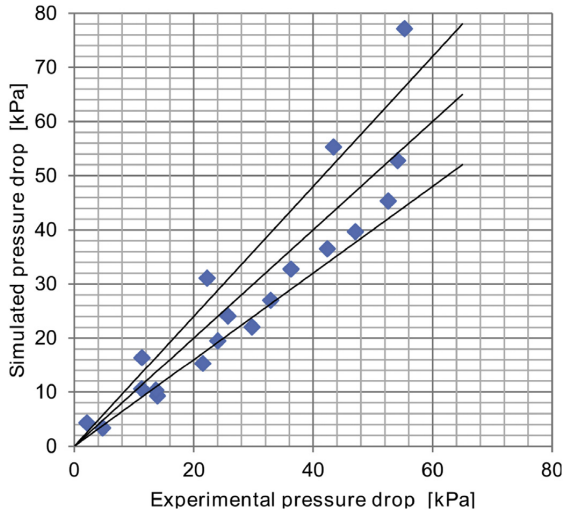

Fig. 13. Simulated vs. experimental pressure drop for air and NEXBASE 3080.

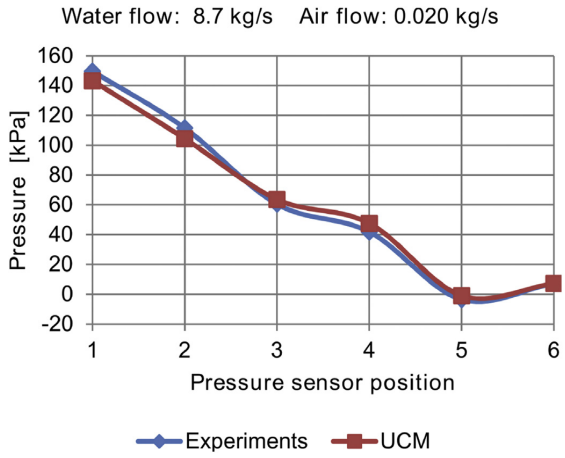

Fig. 14. Pressure profile for water flow 8.7 kg/s and air-flow 0.02 kg/s.

The curves show that the deviation between experimental and simulated pressure drop is smallest at the lowest air flow rates. At air flow rates of 20 and 50 g/s the total pressure drop is over-predicted, especially at low water flow rates. The reason for this is found in the UCM formulation of flow at transition between slug flow and dispersed bubble flow. On the one hand dispersed bubble flow can not exist as the liquid holdup is less than 52%, but on the other hand slug flow is not predicted either as the calculated slug bubble length is too short. The UCM formulation treats this situation by deciding that the flow pattern is dispersed bubble flow if the slug bubble length is shorter than the inner diameter times 1.2. The simulations here show that the pressure drop is overpredicted by 12–46% when the liquid holdup is only 35 to 15% as in the experiments with an airflow of 50 g/s.

With two-phase flow of Exxsol D80 and air the total pressure drop is underpredicted at the two higher air flow rates. In this case the lowest liquid holdup is 21%. With Nexbase 3080 and air the total

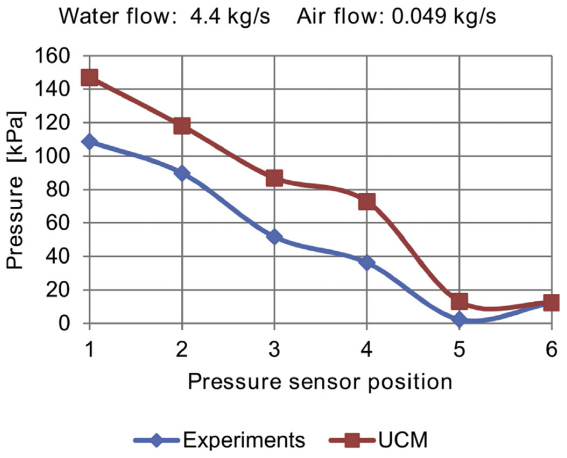

Fig. 15. Pressure profile for water flow 4.4 kg/s and air-flow 0.049 kg/s.

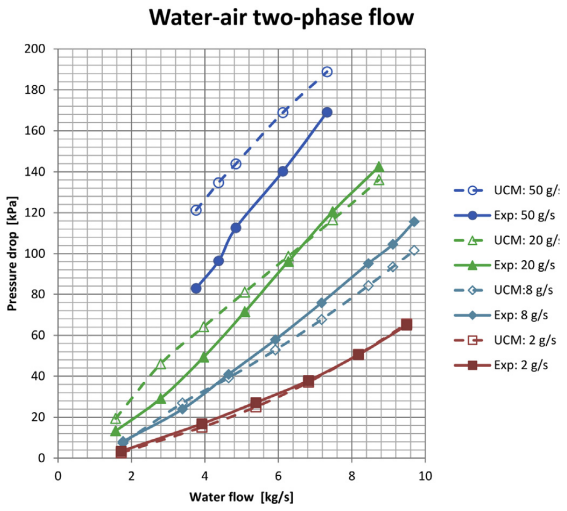

Fig. 16. Total pressure drop across the shut-in valve for water–air two-phase flow.

pressure drop is underpredicted at low air flow rates and overpredicted at high air flow rates.

The results from these simulations can now be compared to two other simulation approaches by the same authors. The total pressure drop was first approximated by applying two-phase correlations to the total single phase pressure drop (Edvardsen et al., 2014a), and then the pressure drop was simulated using the 1D Least Squares Spectral Element method with two-phase correlations. The results are summarized in Table 4. Two-phase flow with the NEXBASE 3080 high viscosity oil was not simulated with the other methods. E_1 is average deviation, E_2 is average absolute deviation, and E_3 is standard deviation defined as

$$E_1 = \frac{1}{n}\sum_{i=1}^{n}\frac{\Delta P_{calculated}(i) - \Delta P_{experimental}(i)}{\Delta P_{experimental}(i)} \quad (26)$$

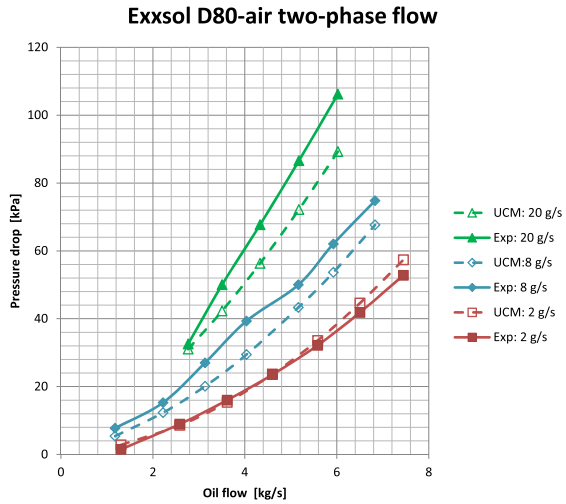

Fig. 17. Total pressure drop across the shut-in valve for Exxsol D80-air two-phase flow.

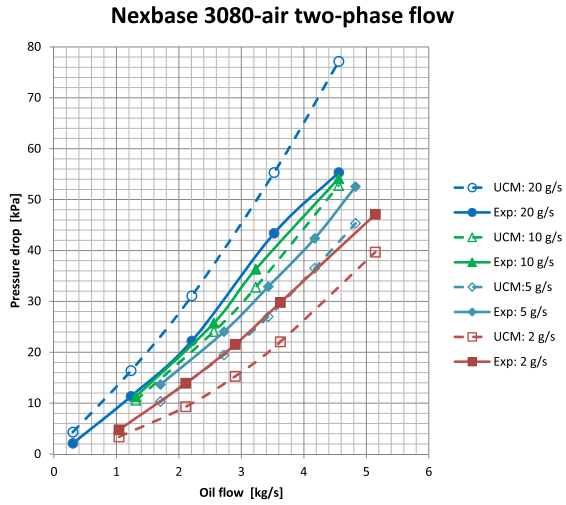

Fig. 18. Total pressure drop across the shut-in valve for Nexbase 3080-air two-phase flow.

Table 4
Comparison of different two-phase flow calculation models for shut-in valve.

Method	Air-water			Air-Exxsol D80		
	E_1 (%)	E_2 (%)	E_3	E_1 (%)	E_2 (%)	E_3
Total pressure drop and Müller-Steinhagen and Heck two-phase pipe flow correlation	−17.0	20.3	1.60	−23.0	26.7	2.10
1D LSSE model with Müller-Steinhagen and Heck two-phase pipe flow correlation	10.5	12.2	0.14	12.1	14.2	0.26
1D LSSE model with Unified Comprehensive Model formulation	1.8	17.6	0.23	−9.3	16.8	0.21

$$E_2 = \frac{1}{n}\sum_{i=1}^{n}\left|\frac{\Delta P_{calculated}(i) - \Delta P_{experimental}(i)}{\Delta P_{experimental}(i)}\right| \quad (27)$$

$$E_3 = \sqrt{\frac{1}{n}\sum_{i=1}^{n}\left[\frac{\Delta P_{calculated}(i) - \Delta P_{experimental}(i)}{\Delta P_{experimental}(i)} - E_1\right]^2} \quad (28)$$

For average deviation the present calculation method outperforms two-phase correlations models. For average absolute deviation however, the 1D least squares spectral element model with the Müller-Steinhagen and Heck correlation is better.

6. Conclusion

A 1-dimensional model has been developed for two-phase flow through a shut-in valve. Minor losses are derived from a CFD-simulation of incompressible flow, and the model uses the least squares method with spectral elements. In this work, the 1-D model is combined with the Unified Comprehensive Model formulation for two-phase flow. Flow patterns generated with this formulation are confirmed by experiments, and the overall pressure drop is simulated with an average absolute deviation of 17.6% for air–water flow, 16.8% for air-Exxsol D80 flow and 26.5% for air-NEXBASE 3080 two-phase flow. The two-phase minor losses are well predicted by using homogeneous velocity and density, combined with loss factors derived from single-phase CFD simulations. The outlet sudden expansion pressure recovery is well predicted by using the Richardson correlation.

Acknowledgment

We thank Stig Karlsen, Manager of Plugs and Packers, Qinterra Technologies, Narvik, for permission to publish the work. We are also thankful to The Research Council of Norway for financial support, project number 208174.

Nomenclature

A	cross section area [m^2]
c	constant
c_p	specific heat capacity at constant pressure
g	gravitational acceleration [m/s^2]
c	constant
D	diameter [m]
f	friction coefficient
G	mass flux [kg/m^{2}s]
h	enthalpy
l	length [m]
K_L	minor loss coefficient
$\dot{m}$	mass flow rate [kg/s]
P	pressure [Pa]
R_e	Reynolds number
u	internal energy
u_c	uncertainty
v	velocity [m/s]
v_{SL}	superficial liquid velocity [m/s]
v_{SG}	superficial gas velocity [m/s]
x	flow quality, mass flow of gas over total mass flow
z	distance along flowline

Greek symbols

α	void fraction
ε	surface roughness
μ_t	turbulent viscosity
ρ	density
σ	area ratio
τ_w	wall shear stress

Subscripts

a	air
G	gas
H	homogeneous (equal phase velocities)
L	liquid
o	oil
TF	two-phase
w	water

References

Ansari, A., Sylvester, N., Sarica, C., Shoham, O., Brill, J., 1994. A comprehensive mechanistic model for upward two-phase flow in wellbores. SPE Prod. Facil. 9, 143–151. http://dx.doi.org/10.2118/20630-PA.

Barnea, D., Shoham, O., Taitel, Y., Dukler, A., 1985. Gas-liquid flow in inclined tubes: flow pattern transitions for upward flow. Chem. Eng. Sci. 40 (1), 131–136. http://dx.doi.org/10.1016/0009-2509(85)85053-3. URL: http://www.sciencedirect.com/science/article/pii/0009250985850533.

Cheremisinoff, N.P., Davis, E.J., 1979. Stratified turbulent-turbulent gas-liquid flow. AIChE J. 25 (1), 48–56. http://dx.doi.org/10.1002/aic.690250106. URL:

Chiapero, E.M., 2013. Two-phase Flow Instabilities and Flow Mal-distribution in Parallel Channels. Norwegian University of Science and Technology. Ph.D. thesis.

Chisholm, D., 1983. Two-phase Flow in Pipelines and Heat Exchangers. George Godwin, London.

Edvardsen, S., Dorao, C., Nydal, J., 2015. Experimental and Numerical Study of Single-phase Pressure Drop in Downhole Shut-in Valve. J. Nat. Gas Sci. Eng. 22, 214–226.

Edvardsen, S., Dorao, C., Nydal, O., 2014a. Two-phase flow in a down-hole shut-in valve. In: The 9th North American Conference on Multiphase Technology, Bannf, Canada.

Edvardsen, S., Dorao, C., Sundsb, P., 2014b. Sudden Expansion and Two-phase Flow Pattern Transition in Pressure Recovery Zone.

Friedel, L., 1979. Improved friction pressure drop correlations for horizontal and vertical two-phase pipe flow. In: European Two-phase Flow Group Meeting, Ispra, Italy.

Gomez, L., Schmidt, O.S.S., Chokshi, R., Northug, T., 2000. Unified mechanistic model for steady-state two-phase flow: horizontal to vertical upward flow. In: SPE65705.

Hasan, A.R., Kabir, C.S., 1988. A study of multiphase flow behavior in vertical wells. SPE Prod. Eng. 3, 263–272. http://dx.doi.org/10.2118/15138-PA.

Issa, R., 1988. Prediction of turbulent, stratified, two-phase flow in inclined pipes and channels. Int. J. Multiph. Flow 14 (2), 141–154. http://dx.doi.org/10.1016/0301-9322(88)90002-X. URL: http://www.sciencedirect.com/science/article/pii/030193228890002X.

JGCM/WG1, 1995. Evaluation of measurement data – guide to the expression of uncertainty in measurement. JCGM 100, 2008 (GUM 1995).

Mller-Steinhagen, H., Heck, K., 1986. A simple friction pressure drop correlation for two-phase flow in pipes. Chem. Eng. Prog. 20, 297–308.

Ozen, P., Ferschneider, G., Chwetzoff, A., 1987. A new multiphase flow model predicts pressure and temperature profiles in wells. In: Offshore Europe, 8–11 September, Aberdeen, United Kingdom. Society of Petroleum Engineers. http://dx.doi.org/10.2118/16535-MS.

Proot, M., Gerritsma, M., 2002. Least-squares spectral element applied to the Stokes problem. J. Comput. Phys. 181 (2), 454–477. http://dx.doi.org/10.1006/jcph.2002.7137.

Richardson, B., 1958. Some Problems in Horizontal Two-phase, Two-component Flow. University Chicago, Chicago, IL. Ph.D. thesis.

Shoham, O., 2006. Mechanistic Modeling of Gas-Liquid Two-phase Flow in Pipes. Society of Petroleum Engineers Inc.

Shoham, O., Taitel, Y., 1984. Stratified turbulent-turbulent gas-liquid flow in horizontal and inclined pipes. AIChE J. 30 (3), 377–385. http://dx.doi.org/10.1002/aic.690300305. URL:

Sporleder, F., 2011. Simulation of Chemical Reactors Using the Least-squares Spectral Element Method. Norwegian University of Science and Technology. Ph.D. thesis.

Taitel, Y., Dukler, A., 1976. A model for predicting flow regime transition in horizontal and near horizontal gas-liquid flow. AIChE J. 22, 47.

Thom, J., 1964. Prediction of pressure drop during forced circulation boiling of water. Int. J. Heat Mass Transf. 7, 709–724.

Xiao, J.J., Shonham, O., Brill, J., 1990. A comprehensive mechanistic model for two-phase flow in pipelines. Soc. Pet. Eng. http://dx.doi.org/10.2118/20631-MS; sPE-20631-MS.

Mud Pump Valve Analysis

Svein Edvardsen
Norwegian University of Science and Technology
Department of Energy and Process Engineering
Trondheim, NO 7491, Norway

December 15, 2014

Abstract

This paper presents an analysis of the piston movement characteristics of the National Oilwell Varco HEX pump, and data are compared with a traditional pump with crank mechanism. Early valve failure has been observed especially for the suction valve, and possible causes are presented.

1 Preface

In this article, the valve function of the National Oilwell Hex pump is investigated and compared to a traditional Triplex pump. For offshore installations, early valve failure is a major problem with Hex pumps, and possible explanations are investigated.

2 Pump types

2.1 Conventional triplex pumps

A conventional triplex mud pump is shown in Figure 1. Varco (2012b).

This National Oilwell Varco mud pump type 12P-160 is a single-acting triplex type, that is, it has three pump cylinders, with horizontal axis. It is driven by two DC electric motors of 800HP each. On the picture we can see the electric motors to the left, the crank mechanism, and the fluid end to the right. The fluid end contains the pumping plunger, intake valve and discharge valve. The thick blue line is the suction line, and the red one is discharge. We can also see a vertical red line behind the pump, which must be the safety relief valve system, with return line to the suction tank. These pumps are normally feeded by a boost pump. Technical data:

Figure 1: National Oilwell Varco (NOV) Triplex mud pumps, type 12P-160

Electric motors:	1600 HP	1177 kW
Maximum capacity:	772 GPM	2921 liters per min.
Maximum pressure:	7500 psi	517 bar
Liners:	Min. 4,5”	114,3mm
	Max. 7,25”	184,2mm
Stroke:	12”	304,8mm
Maximum speed:	120 RPM	

The capacity depends on liner size, as given in Figure2, (Varco, 2011).

For the smallest liner size of 4,5” diameter, maximum pressure is 7500 psi (517 bar), and flow rate is 297 GPM = 1124 liters/min. The larger the liner, the lower is maximum pumping pressure, and this is due to the maximum input power from electric motor. The maximum speed is 120 rev/min.

2.2 Hex pumps

The Hex mud pump is developed by National Oilwell Varco, see Figure 3 (Kverneland et al., 2003). The pump plungers axis are vertical, and they are driven by rollers on a cam profile, see Figure 4 (Contractor, 2002).

This pump has six plungers, arranged in a circle with vertical axis. Suction and discharge valves are located horizontally and in line, below the plunger, with suction valve towards the pump center. The pump is driven by two AC electric motors. Technical data:

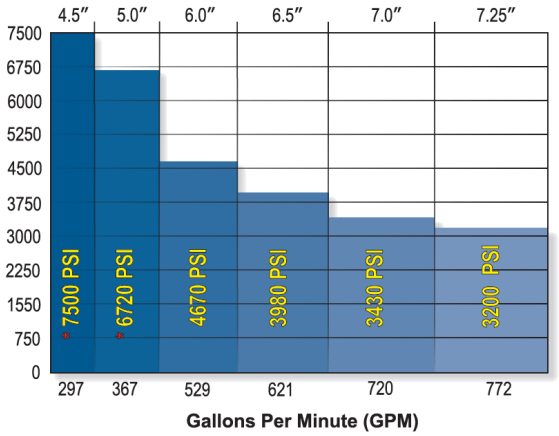

Figure 2: NOV 12P-160 capasity i GPM versus max. pumping pressure with liner from 4,5 in. to 7,25 in.

Figure 3: NOV HEX mud pump 150.

Electric motors:	1500 HP	1103 kW
Maximum capacity:	817 GPM	3092 liters per min.
Maximum pressure:	7500 psi	517 bar
Liners:	4”	101,6mm
Stroke:	11,8”	300mm
Maximum speed:	212 RPM	

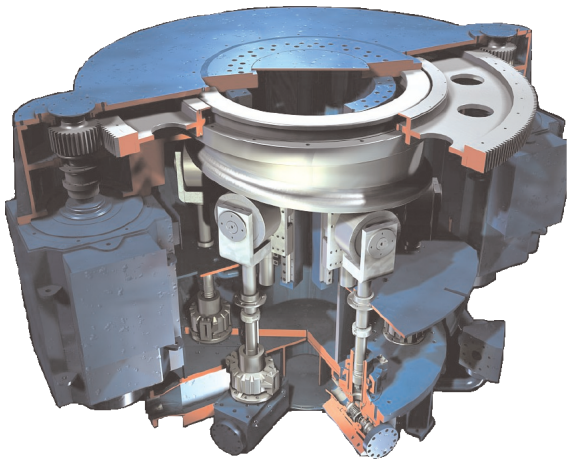

Figure 4: Section of NOV HEX mud pump 150.

3 Pump dynamics

3.1 Triplex pump piston dynamics

The plungers in the above mentioned triplex pump are driven by a crank mechanism, see Figure 5 (Varco, 2012b).

The plunger movement is illustrated in Figure 6 (Wikipedia, 2011):

For the NOV 12P-160 pump, the stroke is 12 in., so $r = 152.4mm$, and from Figure 5 we have that $l = 1120mm$. The mathematical description of the movement is given by

$$y\left(x\right) = l + r - r\cos A - \sqrt{l^2 - r^2 \cdot \left(\sin A\right)^2} \tag{1}$$

where A is crank angle. See Figure 7

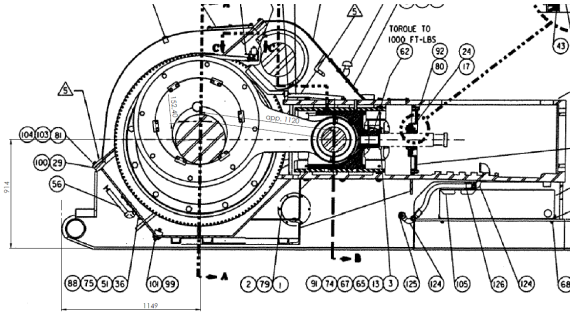

Figure 5: Crank mechanism in NOV 12P-160 mud pump.

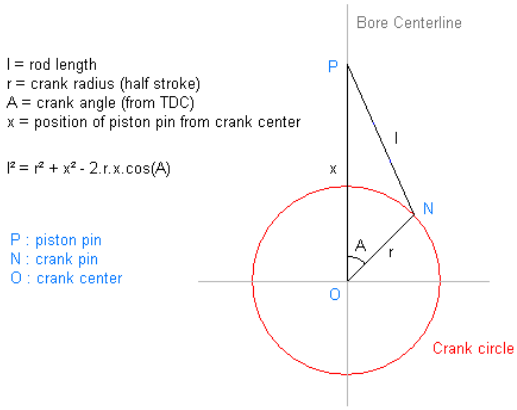

Figure 6: Mathematical description of piston movement by a crank mechanism.

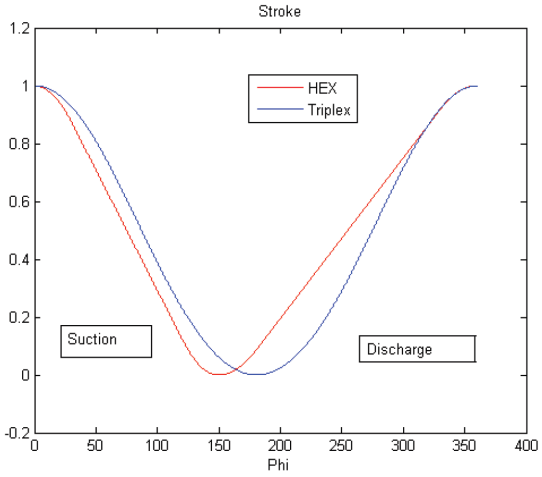

Figure 7: Triplex plunger movement, as function of absolute crank angle A from top dead center (TDC).

Black curve is plunger position, as distance from TDC (top dead center). As a comparison, the ideal sine-function $r - r \cdot \cos x$ (in red) is plotted in the same diagram. Studying the curves, we can see that the plunger movement is very close to a sine-curve, but accelerates a little faster around TDC ($y = 0$, start of suction stroke).

3.2 Hex pump piston dynamics

Information about the piston dynamics of the Hex pump is collected from a article from a drilling conference Kverneland et al. (2003). The piston movement is illustrated in Figure 8.

The movement equations are Golan (2011):

If θ¿=0 and θ ¡=30	$\frac{S}{180} \cdot \frac{1}{60} \cdot \theta^2$
If θ¿30 and θ¡=18	$\frac{S}{180} \cdot (\theta - 15)$
If θ ¿180 and θ ¡=210	$\frac{S}{180} \cdot \left(-\frac{\theta^2}{60} + 7\theta - 555\right)$
If θ¿210 and θ ¡=240	$\frac{S}{180} \cdot \left(-\frac{\theta^2}{40} + 10.5\theta - 922.5\right)$
If θ ¿240 and θ ¡=330	$\frac{S}{180} \cdot (-1.5\theta + 517.5)$
If θ¿330 and θ ¡=360	$\frac{S}{180} \cdot \left(\frac{\theta^2}{40} - 18\theta + 3240\right)$

S is stroke length.

The piston amplitudes versus crank angle are compared for the two pumps, see Figure 9 .

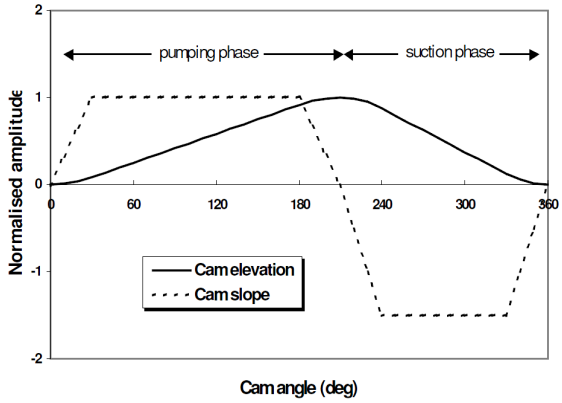

Figure 8: Piston movement in HEX mud pump.

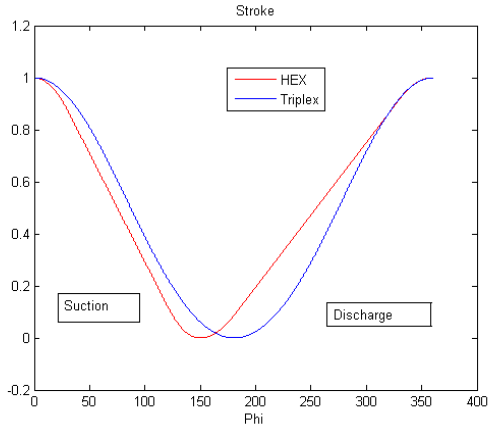

Figure 9: Normalized amplitude of HEX and Triplex pumps.

For the HEX pump, the suction stroke lasts for 150 degrees, and the pumping stroke for 210 degrees. This is possible because of the use of a rotating cam profile instead of a crank mechanism, and the outcome is a lower and more constant piston speed in the pumping period. The motivation for this design is obviously to get as low pressure pulsations on the pressure side as possible. On the other hand, at equal rotation speeds, the piston will accelerate faster in the suction period in the Hex pump than in the Triplex pump, see Figure 10 (Kverneland et al., 2003).

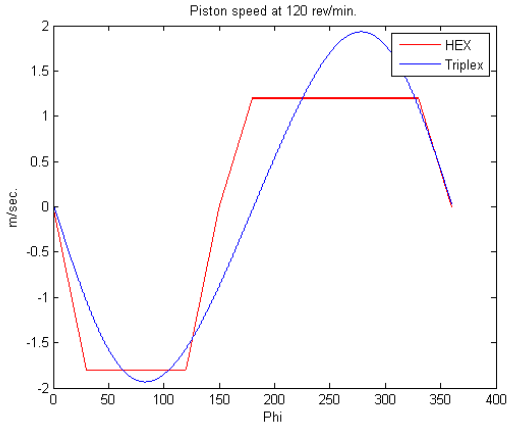

Figure 10: Piston speeds at 120 RPM for both pump types.

Also, since the Hex pump has a fixed liner size of 4", it will have to rotate faster at given combinations of pressure and pump volume. If , for instance, the necessary pressure is not more than 4670 psi, the Triplex pump can use 6" liners, giving 16,7 liters per rev (for the three plungers together). The Hex pump gives 14,6 liters/min., so the speed will have to be 14% higher to give equal volume per min. In Figure 11 the piston speeds are shown for a flow of $529GPM = 2000l/min.$, The speed is then $2000/14.6 = 137RPM$ for the HEX pump, and $2000/16.7 = 120RPM$ for the Triplex pump.

The most interesting part of the figure is the start of the suction stroke, at 0-30 deg. crank angle. We can see that the piston in the HEX pump accelerates much faster than the piston in the Triplex pump. When the flow is forced to increase at a higher rate, the force on the valve disk will also be increased, as the valve disk itself also have to accelerate harder. Consequently, there will be higher flow velocities along the beveled valve seat in the early part of the suction stroke, giving a risk for erosion in valve disk, valve seat and especially in elastomer seal. The piston acceleration for HEX and Triplex pump type is shown in Figure 12.

The plots for position, velocity and accelerations are based on the movement equations given by Golan (2011). When comparing the Triplex and the Hex pump at

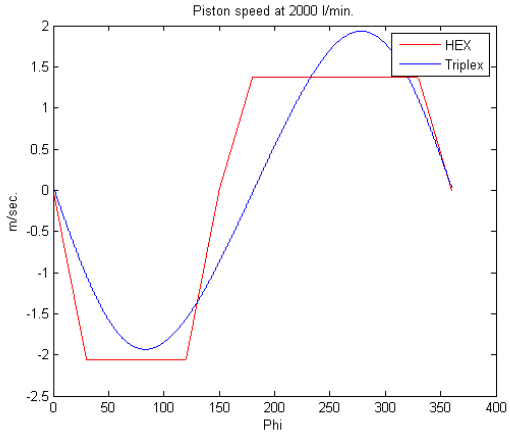

Figure 11: Piston speeds at 2000 l/min.

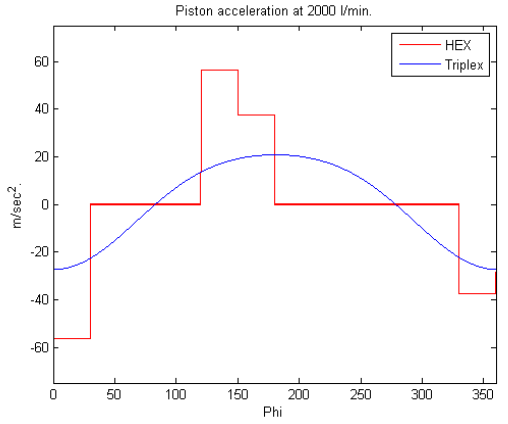

Figure 12: Piston acceleration at 2000 l/min for HEX and Triplex pump.

$2000l/\min$, we can see that the pistons in the HEX pump accelerates app. twice as much as the pistons in the Triplex pump.

4 Valve dynamics

4.1 Valve systems

4.1.1 Triplex Valves

A conventional triplex mud pump has horizontal liners, and valves that are moving vertically, see Figure 13 (Varco, 2012b):

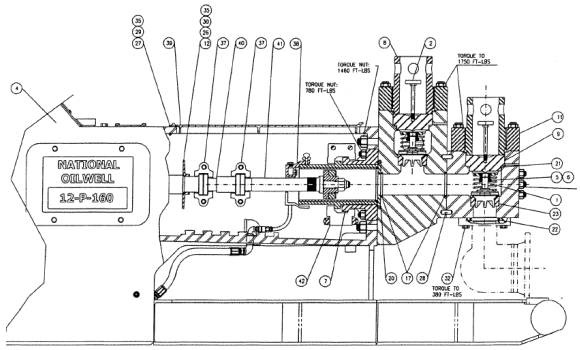

Figure 13: Fluid end of NOV 12P-160 mud pump.

The valves has beveled seats, with elastomer seals, and are guided in the lower end by four wings, see Figure 14 (Varco, 2012a):

4.1.2 HEX pump valves

The fluid end of the HEX mud pump, with pump cylinder, suction- and discharge valve is shown in Figure 15 (Varco, 2012a):

The valve seat and valve disk have been modeled 3-dimensionally for the purpose of doing CFD analysis, see Figure 16.

This valve has also a beveled seat with elastomer seal, but it is guided with stems both in top and bottom. There is a small clearance between the stem and the guidance in the seat, app. $0.4mm$. The valve disk can therefore be $0.2mm$ out of centre in horizontal position.

Figure 14: Valve seats, springs and valve disks for NOV Triplex pumps.

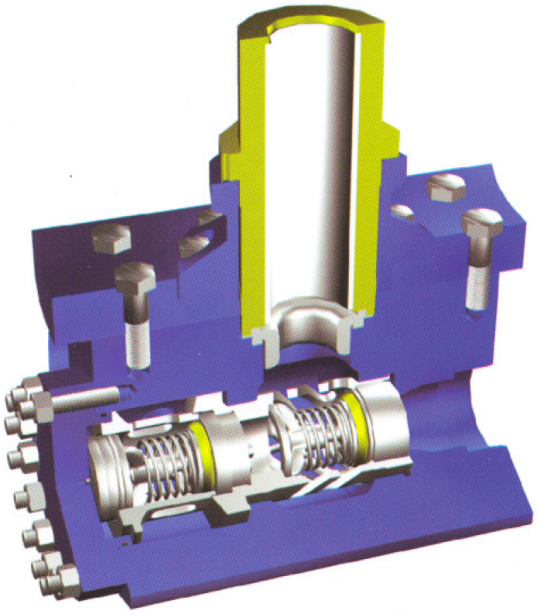

Figure 15: Fluid end of NOV HEX mud pump.

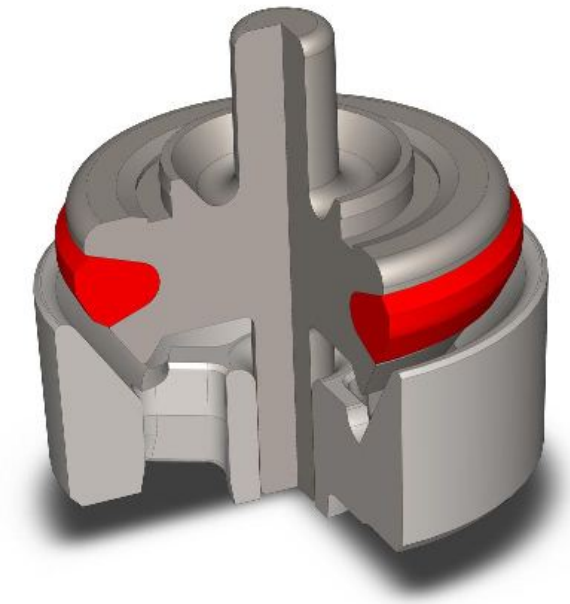

Figure 16: Valve seat and valve disk for NOV HEX pump.

4.2 Valve movement dynamics

The characteristic dimensions of the valve disk and seat are shown in Figure 17

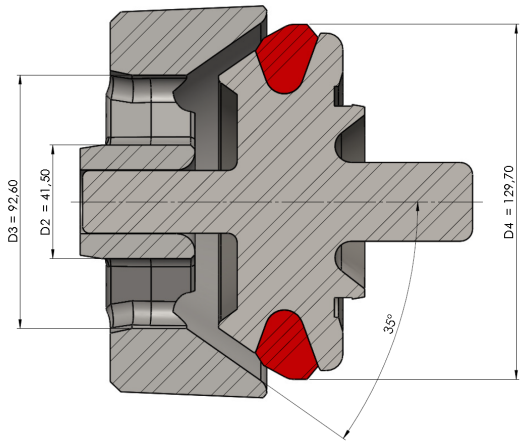

Figure 17: Bevel-face valve disk and seat for NOV HEX pump.

The areas and the pressure forces on the valve disk are:

Inlet side of valve disk $A2 = D3^2 * \frac{\pi}{4}.$, Pressure: $P2$

Outflow area, beveled face $A3 = (D4^2 - D3^2) * \frac{\pi}{4}$, Pressure: $P3$

Piston side of disk $A4 = D4^2 * \frac{\pi}{4}$, Pressure: $P4$

When the valve is lifted from the seat , flow across the valve causes a pressure drop over the beveled outflow area. This can be considered being a minor loss $\Delta p = c\rho\frac{V^2}{2}$, where ρ is density and V is flow velocity. In order to find the value of the constant c, a number of flow simulations have been performed with ANSYS Fluent. Based on an available HEX valve disk with seat, a CAD model was generated, see Figure 16, and from this model the fluid volume in the valve was generated, see Figure18

In Fluent , an inflated mesh is generated, see Figure 19.

An inflated mesh has several layers of thin cells next to surfaces where pressure levels are of interest. Such meshed models were generated for valve lifts up to 12mm, and for each combination of flow rate and valve lift the generated pressure drop across the valve disk was recorded. The fluid in these simulations is mud, with gravity 1350 kg/m^3 and viscosity 21cp. Pressures on surfaces are visualized in Figure 20.

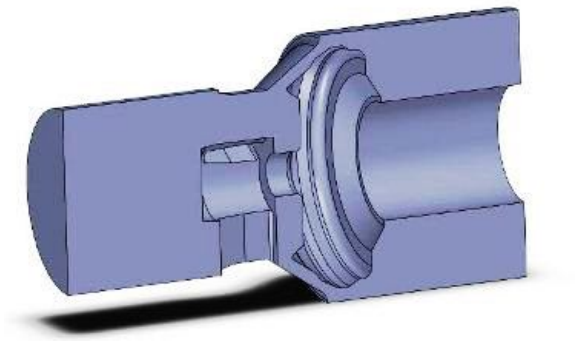

Figure 18: Fluid (mud) volume in HEX suction valve.

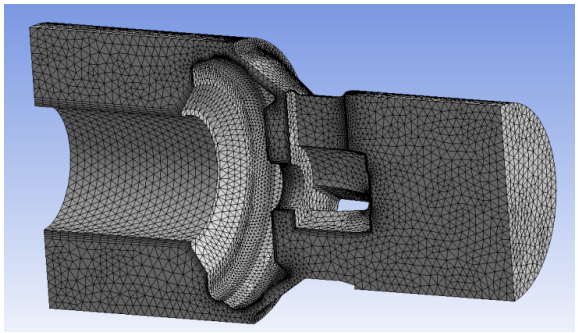

Figure 19: Meshed model of fluid volume.

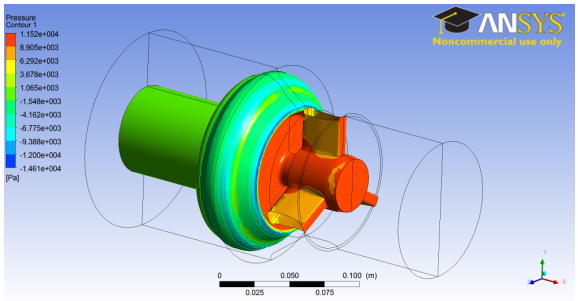

Figure 20: Pressure on valve disk with 12mm lift and 1 m/s inlet velocity. Fluid is mud, with 21 cp viscosity and 1350 kg/m^3 density.

Pressure on surfaces are indicated by color, and a pressure scale is given on the figure. As expected, the highest pressure is found in a stagnation zone at the inlet side of the valve. and this pressure is used as $P2$ in the simulations. It is also seen that the pressure is negative in some zones on the beveled part, which means that the pressure is in fact lower than on the outflow (piston) side of the valve. Flow simulations were performed for valve lifts from 5 to $12mm$, and flows from 2 to $24l/s$. Summarizing all the simulations, the minor loss coefficient can be found by calculating $c = \frac{2\Delta p}{\rho V^2}$, where Δp is pressure drop and V is the velocity at the entrance to the valve seat, where $D = D_3$, see Figure 17 and 21. See table below.

	Minor loss coefficient C					
Flow	2 l/s	4 l/s	8 l/s	12 l/s	18 l/s	24 l/s
Lift						
4	1360					
5		210	193	177		
6		92	83	81		
7		60	48	44		
8		36	32	30		
9		19	16	15		
10			16	16	16	15
12				10	10	10

The loss coefficient is expected to be independent on flow rate, and this is indeed true for the higher valve lift values.

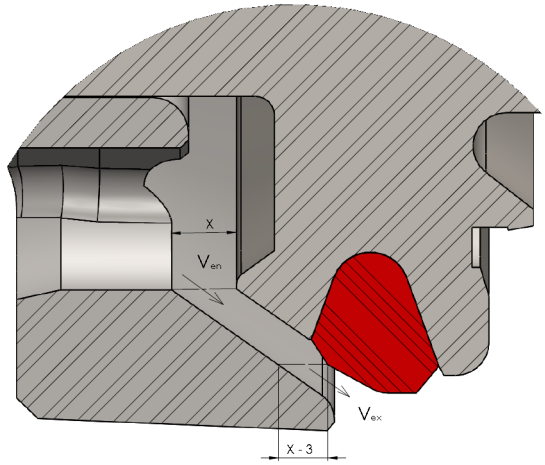

Figure 21: Illustration of valve lift and fluid velocities in valve seat.

Taking the average for each valve lift, the relation between valve lift and pressure drop coefficient c is illustrated in Figure 22.

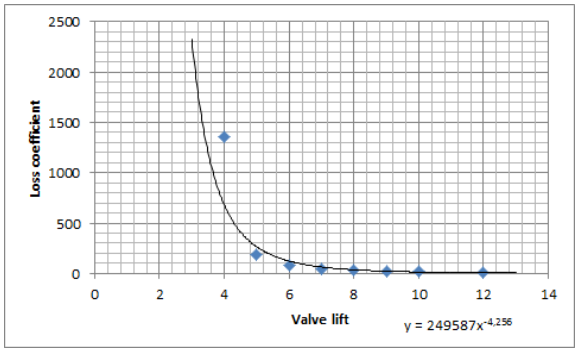

Figure 22: Loss coefficient c for pump suction valve.

The loss coefficient is (app.) $c = 249587x^{-4.256}$, where x is valve lift in mm. Then we have that

$$P_2 - P_4 = c\frac{\rho \cdot A_2}{2}V_{D3}^2 \tag{2}$$

The forces acting upon the valve disk are:

$$F_{total} = P_2A_2 + P_3A_3 - P_4A_4 - (F_0 + Rx) \tag{3}$$

Here it is assumed that the valve is moving along a horizontal axis.

Nomenclature:

A_2 area under valve disk (suction side)

A_3 axial projection of (beveled) valve seat area

A_4 area on top of valve disk (piston side)

A_s flow cross section area in valve seat

D_3 diameter of valve disk on suction side of beveled face

F_0 spring force on valve disk when closed

K_c clinging coefficient $= \left[\left(\frac{D_4}{D_3}\right)^2 + \left(\frac{D_3}{D_4}\right)^2 - 2\right]\frac{1}{8\pi(\sin\alpha)^2}$

K_i impulse coefficient, caused by flow impinging on valve disk inlet side

P_1 static pressure upstream of valve seat

P_2 static pressure on underside (suction side) of valve disk

P_3 static pressure in outflow area, along beveled face

P_4 static pressure on top of valve disk

Q_2 flow created by piston movement

R spring rate $[N/mm]$

V_{disk} valve velocity

x valve lift

α angle of beveled face of valve, see Figure 17

ρ density of fluid

To be able to simulate the movement of the valve disk, the pressure differences acting upon the valve disk must be expressed by the flow across it, Q_2. We have that $A_4 = A_2 + A_3$, so that the total force on the valve disk is

$$\begin{aligned} F_t &= P_2A_2 - (P_4A_2 + P_4A_3) + P_3A_3 - (F_0 + Rx) \quad (4) \\ F_t &= (P_2 - P_4)A_2 + (P_3 - P_4)A_3 - (F_0 + Rx) \quad (5) \end{aligned}$$

As explained by Henshaw (2009), the friction loss through the inlet valve assembly is almost only a friction loss across the valve seat. On the other hand, as it is the *static* pressure P_2 that is acting upon A_2, we must subtract the dynamic pressure in the valve seat from P_1, or

$$P_2 = P_1 - \rho \left(\frac{Q_2}{A_s}\right)^2 \frac{1}{2} \quad (6)$$

Because the high velocity in the outflow area along the beveled face, the dynamic pressure is high and the static pressure is low: $P_{total} = P_{static} + P_{dynamic}$. It can be calculated as the sum of the static pressure P_4 plus dynamic loss V_{ex} in valve outlet (exit loss) minus dynamic pressure along valve seat:

$$P_3 = P_4 + \frac{\rho}{2}\left(V_{ex}^2 - V_{en}^2\right) \quad (7)$$

Combining Equations 3 to 7 we get

$$F_t = (P_1 - P_4) A_2 - \rho \left(\frac{Q_2}{A_s}\right)^2 \frac{A_2}{2} - \frac{\rho}{2}\left(V_{en}^2 - V_{ex}^2\right) A_3 - (F_0 + Rx) \tag{8}$$

The term $\frac{\rho}{2}\left(V_{en}^2 - V_{ex}^2\right) A_3$ is the static underpressure compared to P_4 that causes a force that resist opening of the valve. By expressing V_{en} at D_3 and V_{ex} at D_4 by the flow Q_2 we get that

$$\begin{aligned} \frac{\rho}{2}\left(V_{en}^2 - V_{ex}^2\right) A_3 &= \left[\left(\frac{D_4}{D_3}\right)^2 + \left(\frac{D_3}{D_4}\right)^2 - 2\right] \frac{\rho}{8\pi \left(\sin\alpha\right)^2} \cdot \frac{Q_e^2}{x^2} & (9) \\ &= K_c \rho \left(\frac{Q_e}{x}\right)^2 & (10) \end{aligned}$$

Even it the valve disk is moving only a few mm , the velocity can be substantial, and therefore the flow velocity over the valve disk depends on the valve disk velocity:

$$Q_e = Q_2 - A_4 V_{disk} \tag{11}$$

To complete the picture, we must add one more term; the impulse force from the flow impinging on the valve bottom. Again, we must take the difference between the flow velocity and the valve velocity:

$$F_i = K_i \rho Q_2 \left(\frac{Q_2}{A_s} - V_{disk}\right) \tag{12}$$

According to Henshaw (2009) , the measured force for a bevel-seat valve is only 30% of this theoretical value, so $K_i = 0,3$. On the other hand, the ANSYS CFD (Computational Fluid Dynamic) simulations includes this force from the flow, so we must set $K_i = 0$. Then we have that

$$\begin{aligned} m_{disk} \cdot a_{disk} &= c\frac{\rho \cdot A_2}{2}\left[\frac{Q_2 - A_4 V_{disk}}{\pi D_3 x \sin\alpha}\right]^2 - \rho\left(\frac{Q_2}{A_s}\right)^2 \frac{A_2}{2} & (13) \\ &\quad - \frac{K_c \rho}{x^2}\left(Q_2 - A_4 V_{disk}\right)^2 & (14) \\ &\quad + K_i \rho Q_2 \left(\frac{Q_2}{A_s} - V_{disk}\right) - (F_0 + Rx)_{spring} & (15) \end{aligned}$$

The spring rate R has been measured on a sample spring Stanko (2012).

5 Valve movement simulations

5.1 Computer program structure

A computer program has been made in Matlab, incorporating the equations given above for valve movement. The structure of the computer program consists of the following steps:

1. Variable definitions
2. Defining tables for valve position, acceleration and velocity
3. Piston movement equations Golan (2011). Values for piston position are stored in a table. The timestep can be changed.
4. For-loop, calculating each step in a full cycle.

   - calculating flow for each timestep

   - for very low valve lift values, the valve disk movement is a direct function of the piston movement, as the valve disk has an elastomer seal with up to $3mm$ deflection.

   - calculation of valve disk acceleration based on Equation 15.

   - calculating new valve velocity and position.

The Matlab code generated is given in Appendix 1.

5.2 Simulation results

5.2.1 HEX pump valve at 120 RPM

A simulation of HEX suction valve displacement and valve velocity is shown in Figure 23. An opening lag of 5 deg. is anticipated for this and all subsequent plots.

From the graph we can see that the inlet valve has a maximum lift of app. 8,6mm, and it closes 12 deg. after the suction stroke has ended. The suction volume flow is constant from 30 to 120 deg. , and in the beginning of this period the valve is fluttering a little. Valve velocity at closing is app. $0.34m/s$.

5.2.2 Triplex pump suction valve at 120 RPM

The suction valve disk velocity for the Triplex pump at 120 RPM is show in Figure 24. In this case it is simulated with a 4" liner, as for the HEX pump, in order to see the impact of piston movement mechanism on valve seating velocity.

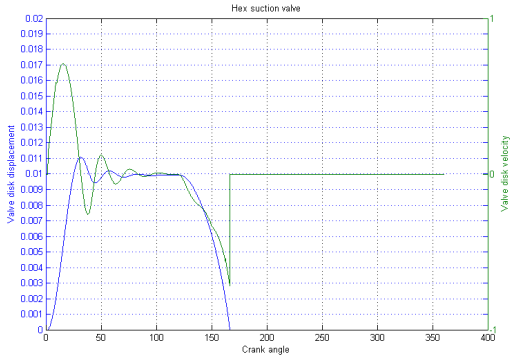

Figure 23: Hex suction valve data at 120 RPM.

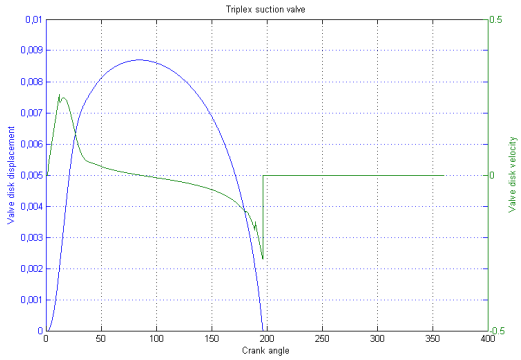

Figure 24: Triplex pump valve data at 120 RPM.

Maximum valve lift is app. $8.6mm$, and seating velocity for the Triplex suction valve is app. $0.26m/s$. Closing lag is app.15 deg . Comparing the HEX and the Triplex pump at equal velocities, with equal liner size, it is clear that the HEX pump gives a 30% higher seating velocity for the suction valve.

5.2.3 HEX pump valve at 212 RPM

The situation for the HEX pump at 212 rev./min. is shown in Figure 25.

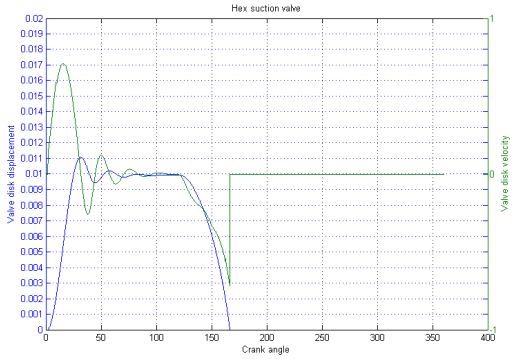

Figure 25: HEX pump valve movement data at 212 RPM.

Now the maximum valve lift is $10mm$, with fluttering up to $11mm$. Closing lag is app. $15deg.$, and seating velocity has increased to app. $0.7m/s$. This is far above the acceptable value of $0.19m/s$ given by Henshaw (2009).

5.2.4 Triplex pump valve at 120 RPM with 6" liner

For the sake of comparison at high flow rates, valve plot for conventional crank mechanism is shown in Figure 26. The speed is 120 RPM, and liner size is $6,5$" , giving $621GPM = 2340l/\min$. at $3980psi$.

The suction valve closing lag for the Triplex pump is simulated to be app. $12deg.$, and maximum valve lift is app. $11mm$. Seating velocity is app. $0.5m/s$. In this case, the Triplex pump is simulated with a valve equal to the HEX pump valves. Again, the HEX pump gives higher seating velocity.

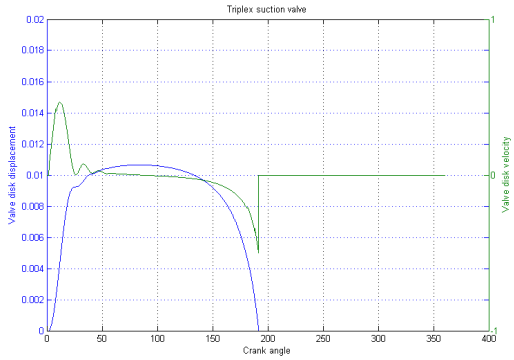

Figure 26: HTriplex pump valve movement with $6,5$" liner.

6 Summary and conclusions

The piston movement mechanism in the HEX pump causes the pistons to accelerate faster compared with a conventional pump with crank mechanism, see Figure 11. The suction part of a cycle is reduced from 180° to 150° , and the suction flow is constant from 30° to 120° . At 120 rev. per min., the cam mechanism in the HEX pump produces 30% higher seating velocity than a comparable crank mechanism, and this might be a explanation for the early valve failure experienced.

References

Contractor, D., September/October 2002. Smaller mud pump achieves near zero pulsation. Drilling Contractor.
URL `http://www.drillingcontractor.org/dc-archive/septemberoctober-2002`

Golan, M., 2011. Hex piston movement equations, file transfer.

Henshaw, T., 2009. Power pump valve dynamics - a study of the velocity and pressure distribution in outward-flow bevel-face and flat-face power pump valves. 25th International Pump Users Symposium Proceedings.
URL `http://turbolab.tamu.edu/articles/25th_international_pump_users_symposium_proceedings`

Kverneland, H., Kyllingstad, ., Moe, M., 2003. Development and performance testing of the hex mud pump. SPE/IADC Drilling Conference, 19-21 February , Amsterdam, Netherlands.
URL `http://www.onepetro.org`

Stanko, M. E., 2012. Hex pump valve spring. Spring rate measurement.

Varco, N. O., 2011. Premium p series offshore tripolex pumps, d391000236-mkt-001 rev.06, product presentation.
URL www.nov.com

Varco, N. O., 2012a. Mission Premium Product Brochure.

Varco, N. O., 2012b. Part list 12P-160 Triplex Mud Pump. National Oilwell Varco, section drawing.
URL http://www.nov.com/Drilling/Drilling_Fluid_Equipment/Mud_Pumps/12-P-160_Triplex_Mud_

Wikipedia, 2011. Piston motion equations. Internet page.
URL http://en.wikipedia.org/wiki/Piston_motion_equations

7 Appendix 1 - Matlab code

7.1 Triplex pump

7.2 HEX pump

```
% Valve disk movement calculation
% Formulas by Henshaw, T. , 2009, Power Pump Valve Dynamics -
% A study of the velocity and pressure distribution in outward-flow
% bevel-face and flat-face power pump valves 25th International Pump
% Users Symposium Proceedings

% Valve loss coefficient C calculated from CFD simulations

% Programming by S.Edvardsen   April 2012

Rev=120 ; % pump rev/min
maxstroke=0.3048;  % 0.3048 m stroke
pl_diam=0.0254*4; % 6"  plunger diameter, max. 7.25" = 2900 l/min
pl_a=pl_diam^2*pi/4

Pd=100;  %   Divides each degree in several parts
N_steps=Pd*360+1;
dt=(1/Pd)/(6*Rev);

Phi=[0:1/Pd:360];
stroke=ones(N_steps,1);
l=1120;
r=152.4;

for N=1:N_steps
   stroke(N)=(2*r-(l+r-r*cos((N/Pd-1)/360*2*pi)...
       -(l^2-r^2*(sin((N/Pd-1)/360*2*pi))^2)^0.5))/(2*r);
end

x_disk=zeros(N_steps,1);
v_disk=zeros(N_steps,1);
a_disk=zeros(N_steps,1);
q=zeros(N_steps,1);
seat_flow_vel=zeros(N_steps,1);
x_disk(1)=0;
v_disk(1)=0;
a_disk(1)=0;
m_disk=3.2;  % kg
rho=1350;    % kg/m3
D2=0.0415;
D3=0.0923;%
D4=0.13;



alfa=35/180*pi;
Kc=((D4/D3)^2+(D3/D4)^2-2)/(8*pi*(sin(alfa))^2); % Clinging coefficient
Astem=pi*(23.3*35+28.8*(26+14/2))*(10^-6); % Sliding area of valve stem
My=0.021    % Ps-s viscosity
Gap=0.0002  % Gap between valve stem and guidance

Fo=157;     % N orig.: 157
R=15780;    % N/m
Ki=0.0;     % Included in CFD simulations (=> P2) impulse coefficient
A2=pi/4*D3^2;
A4=pi/4*D4^2;
As=pi/4*(D3^2-D2^2);
```

```
Pl=500000; % Pa inlet pressure

Opening_lag=2;  % deg.
i_start=Opening_lag*Pd;
seal_deflection=0.001  %Piston elastomer has hit seat at x_disk(i) = 0.003 in new↙
condition
for i=i_start:N_steps
    q(i)=(stroke(i-1)-stroke(i))*maxstroke*pl_a/dt;

    if x_disk(i-1)<=seal_deflection && i<N_steps/4
        v_disk(i)=q(i)/(pi/4*0.13^2);
        if i==2
            a_disk(i)=v_disk(i)/dt;
            x_disk(i)=0.5*a_disk(i)*dt^2;
        else
            a_disk(i)=(v_disk(i)-v_disk(i-1))/dt;
            x_disk(i)=x_disk(i-1)+v_disk(i-1)*dt+0.5*(a_disk(i))*dt^2;
        end
    elseif x_disk(i-1)>=seal_deflection
        c=249587*(x_disk(i-1)*1000)^-4.256;  % Using V at A2 area
        a2=A2*c*rho/2*((q(i)-A4*v_disk(i-1))/A2)^2;

        if q(i)>=0
            %  "a" is sum of forces
            a=a2-rho*(q(i)/As)^2*A2/2-Kc*rho/(x_disk(i-1)^2)*(q(i)-A4*v_disk(i-1))^2+↙
...
                +Ki*rho*q(i)*(q(i)/As-v_disk(i-1))-(Fo+R*x_disk(i-1)+m_disk*9.81);
            if  a2>Pl
                a=A2*Pl-rho*(q(i)/As)^2*A2/2-Kc*rho/((x_disk(i-1)^2)*(q(i)-A4*v_disk(i-↙
1))^2)+ ...
                +Ki*rho*q(i)*(q(i)/As-v_disk(i-1))-(Fo+R*x_disk(i-1)+m_disk*9.81);
            end
        else
           a=a2-(Fo+R*x_disk(i-1)+m_disk*9.81);
        end

        f_damping=Astem*My*v_disk(i-1)/Gap;   %  viscous damping in valve stem guide

        if v_disk>0
            a=a-f_damping;
        else
            a=a+f_damping;
        end









      seat_flow_vel(i)=(q(i)-A4*v_disk(i-1))/(pi*D3*x_disk(i-1)*sin(alfa));
      a_disk(i)=a/m_disk;
      v_disk(i)=v_disk(i-1)+a_disk(i)*dt;
      %x_disk(i)=x_disk(i-1)+0.5*(v_disk(i-1)+v_disk(i))*dt;  Alternativ
      %formulation
      x_disk(i)=x_disk(i-1)+v_disk(i-1)*dt+0.5*a_disk(i-1)*dt^2;

  elseif x_disk(i-1)<seal_deflection && i>N_steps/4
          v_disk(i)=q(i)/(pi/4*0.13^2);
          seat_flow_vel(i)=0;
          x_disk(i)=x_disk(i-1)+0.5*(v_disk(i-1)+v_disk(i))*dt;
```

```
        if i>N_steps/4 && x_disk(i)<0.000
            x_disk(i)=0;
            v_disk(i)=0;
            a_disk(i)=0;
        end
    end
end
figure (1)
plot(Phi,stroke);
title('Phi, Stroke from TDC (=1)')

figure (2)
[AX,H1,H2]=plotyy(Phi,x_disk,Phi,v_disk,'plot');
set(get(AX(1),'Ylabel'),'String','Valve disk displacement');
set(get(AX(2),'Ylabel'),'String','Valve disk velocity');
xlabel('Crank angle');
title('Triplex suction valve');

figure (3)
plot(Phi,seat_flow_vel);
title('Seat flow velocity')
```

```
% Valve disk movement calculation
% Formulas by Henshaw, T. , 2009, Power Pump Valve Dynamics -
% A study of the velocity and pressure distribution in outward-flow bevel-face
% and flat-face power pump valves 25th International Pump Users Symposium Proceedings
%
% Valve loss coefficient C calculated from CFD simulations
%
% Programming by S.Edvardsen   April 2012


Rev=212; % pump rev/min,  2900 l/min = 198 RPM, 14,6 l/rev.
maxstroke=0.3;  % 300 mm stroke
pl_diam=0.1016; % 4" plunger diameter
pl_a=pl_diam^2*pi/4
Pd=200;  %   Divides each degree in several parts
N_steps=Pd*360+1;
dt=(1/Pd)/(6*Rev);

Phi=[0:1/Pd:360];
stroke=ones(N_steps,1);
for N=1:N_steps
    if (N)<=30*Pd
        stroke(N+150*Pd)=(N/Pd)^2/(180*60);
    elseif (N)>30*Pd && (N)<=180*Pd;
        stroke(N+150*Pd)=((N/Pd)-15)/180;
    elseif (N)>180*Pd && (N)<=210*Pd;
        stroke(N+150*Pd)=(-(N/Pd)^2/60+7*(N/Pd)-555)/180;
    elseif (N)>210*Pd && (N)<=240*Pd;
        stroke(N-210*Pd)=(-(N/Pd)^2/40+10.5*(N/Pd)-922.5)/180;
    elseif (N)>240*Pd && (N)<=330*Pd;
        stroke(N-210*Pd)=(-1.5*(N/Pd)+517.5)/180;
    else (N)>330*Pd && (N)<=360*Pd;
        stroke(N-210*Pd)=((N/Pd)^2/40-18*(N/Pd)+3240)/180;
    end
end

x_disk=zeros(N_steps,1);
v_disk=zeros(N_steps,1);
a_disk=zeros(N_steps,1);
seat_flow_vel=zeros(N_steps,1);
q=zeros(N_steps,1);

m_disk=3.2;  % kg
rho=1350;    % kg/m3
D2=0.0415;
D3=0.0923;%
D4=0.13;







alfa=35/180*pi;
Kc=((D4/D3)^2+(D3/D4)^2-2)/(8*pi*(sin(alfa))^2); % Clinging coefficient

Astem=pi*(23.3*35+28.8*(26+14/2))*(10^-6); % Sliding area of valve stem
My=0.021    % Ps-s viscosity
Gap=0.0002  % Gap between valve stem and guidance
```

```
Fo=157;     % N, Measured by M.E.W. Stanko
R=15780;    % N/m
Ki=0.0;     % Included in CFD simulations (=> P2), impulse coefficient
A2=pi/4*D3^2;
A4=pi/4*D4^2;
As=pi/4*(D3^2-D2^2);
P1=400000; % P1 inlet (static) pressure

Opening_lag=2;  % deg.
i_start=Opening_lag*Pd;
seal_deflection=0.001  %Piston elastomer has hit seat at x_disk(i) = 3 in new condition
for i=i_start:N_steps
    q(i)=(stroke(i-1)-stroke(i))*maxstroke*pl_a/dt;

    if x_disk(i-1)<=seal_deflection && i<N_steps/4

        v_disk(i)=q(i)/(pi/4*0.13^2);
        if i==2
            a_disk(i)=v_disk(i)/dt;
            x_disk(i)=0.5*a_disk(i)*dt^2;
        else
            a_disk(i)=(v_disk(i)-v_disk(i-1))/dt;
            x_disk(i)=x_disk(i-1)+v_disk(i-1)*dt+0.5*(a_disk(i))*dt^2;
        end

    elseif x_disk(i-1)>=seal_deflection
        c2=249587*(x_disk(i-1)*1000)^-4.256;% pressure loss constant, by S.Edvardsen
        a2=A2*c2*rho/2*((q(i)-A4*v_disk(i-1))/A2)^2;

        if q(i)>=0
            a=a2-rho*(q(i)/As)^2*A2/2-Kc*rho/(x_disk(i-1)^2)*(q(i)-A4*v_disk(i-1))^2+↙
...
                +Ki*rho*q(i)*(q(i)/As-v_disk(i-1))-(Fo+R*x_disk(i-1));
            if a2 > P1
                a=A2*P1-rho*(q(i)/As)^2*A2/2-Kc*rho/((x_disk(i-1)^2)*(q(i)-A4*v_disk(i-↙
1))^2)+ ...
                -Ki*rho*q(i)*(q(i)/As-v_disk(i-1))-(Fo+R*x_disk(i-1));
            end
        else
            a=a2-(Fo+R*x_disk(i-1));
        end
        f_damping=Astem*My*v_disk(i-1)/Gap+00;   %  viscous damping in valve stem guide









        if v_disk>0
            a=a-f_damping;
        else
            a=a+f_damping;
        end

        seat_flow_vel(i)=(q(i)-A4*v_disk(i-1))/(pi*D3*x_disk(i-1)*sin(alfa));
        a_disk(i)=a/m_disk;
        v_disk(i)=v_disk(i-1)+a_disk(i-1)*dt;
        x_disk(i)=x_disk(i-1)+0.5*(v_disk(i-1)+v_disk(i))*dt;
    %    if q(i)<0 && x_disk(i)<0.002
    elseif x_disk(i-1)<seal_deflection && i>N_steps/4
```

```
        v_disk(i)=q(i)/(pi/4*0.13^2);  % Bacause piston elastomer has hit seat
        seat_flow_vel(i)=0;
        x_disk(i)=x_disk(i-1)+0.5*(v_disk(i-1)+v_disk(i))*dt;

        if i>N_steps/4 && x_disk(i)<0.000
            x_disk(i)=0;
            v_disk(i)=0;
            a_disk(i)=0;
        end
    end
end
figure (1)
plot(Phi,stroke);
title('Phi, Stroke from TDC (=1)')

%figure (2)
%plot(Phi,q,'r-',Phi,x_disk,'b-')
%title('Suction volume/sec at 212 rev/min')
%legend('Suction volume','Valve Displacement')

figure (2)
[AX,H1,H2]=plotyy(Phi,x_disk,Phi,v_disk,'plot');
set(get(AX(1),'Ylabel'),'String','Valve disk displacement');
set(get(AX(2),'Ylabel'),'String','Valve disk velocity');
xlabel('Crank angle');
title('Hex suction valve');

figure (3)
plot(Phi,seat_flow_vel);
title('Seat flow velocity')
```